# MAPPING THE 3D ORIENTATION AND NANOSCALE DISTRIBUTION OF PICONEWTON RECEPTOR FORCES

A Dissertation
Presented to
The Academic Faculty

by

Joshua Mark Brockman

In Partial Fulfillment
of the Requirements for the Degree
Doctor of Philosophy in the
Wallace H. Coulter Department of Biomedical Engineering

Georgia Institute of Technology
Emory University
August 2020

# MAPPING THE 3D ORIENTATION AND NANOSCALE DISTRIBUTION OF PICONEWTON RECEPTOR FORCES

Approved by:

Dr. Khalid Salaita, Advisor
Chemistry
*Emory University*

Dr. Cheng Zhu
Biomedical Engineering
*Georgia Institute of Technology*

Dr. Alexa Mattheyses
Cell, Developmental and Integrative Biology
*University of Alabama at Birmingham*

Dr. Phillip Santangelo
Biomedical Engineering
*Georgia Institute of Technology*

Dr. Yonggang Ke
Biomedical Engineering
*Emory University*

Date Approved: August 6, 2020

To Samantha Elizabeth Brockman

# ACKNOWLEDGEMENTS

I am extremely grateful for many people whose support has made this work possible. First, I would like to thank my wife, Samantha, who has been with me every step of the way. I would like to thank my parents, Mark and Angela Brockman, who told me that I could do well in research long before that thought ever occurred to me. I owe my father a special thanks for helpful discussions regarding some of the mathematical modeling in this work. In twenty-three years of school, he never stopped being able to help me with my math homework.

I would like to extend a special thanks to my advisor, Prof. Khalid Salaita for taking a chance and welcoming a wayward biomedical engineer into his lab. Khalid is a never-ending source of ideas. His high standards and the excellent training he provided have pushed me further in my research career than I thought I could go.

My friends in graduate school have been the very best. I am grateful to the entire Salaita lab, but I would like to take the time to thank a few specific labmates. I would like to thank Dr. Roxanne Glazier, who started in the Salaita lab with me and who has been a friend and sounding board for the entire duration of my graduate career. I want to thank my partner in crime, Hanquan Su, who lead the tPAINT project with me. Han and I have spent uncountable hours at the microscope. We finished the final experiments of this work as Emory University prepared to close due to the Coronavirus epidemic, often staying in lab until just before sunrise. I could not have done it without him. I would also like to thank Aaron Blanchard, who is able to accomplish more with his broken laptop than most of us can with a fully functioning computer. Aaron's ability to reduce the complexity of the

world to tractable experiments has left an indelible mark on my approach to science. Finally, I want to thank Anna Kellner and Allison Ramey whose friendship (and many, many memes) have made my days much brighter.

Finally, I would like to thank my committee. Thank you for guiding me on this scientific journey. I have enjoyed my graduate career immensely.

# TABLE OF CONTENTS

# LIST OF TABLES

# LIST OF FIGURES

# LIST OF SYMBOLS AND ABBREVIATIONS

| | |
|---|---|
| bp | Base pair |
| BHQ1 | Black Hole Quencher 1 |
| CCD | Charge Coupled Device |
| CDF | Cumulative Distribution Function |
| sCMOS | Scientific complementary metal-oxide-semiconductor |
| cRGD | cylic-Arginine-Glycine-Aspartate |
| Cy3B | Cyanine 3B |
| DiI | 1, 1'-dioctadecyl-3, 3, 3', 3'-tetramethylindocarbocyanine |
| DNA-PAINT | DNA-based Point Accumulation for Imaging in Nanoscale Topography |
| dsDNA | Double-stranded DNA |
| $F_{1/2}$ | F one-half |
| FP | Fluorescence polarization |
| FPM | Fluorescence polarization Microscopy |
| FRET | Förster resonance energy transfer |
| GFP | Green fluorescent protein |
| HOMO | Highest Occupied Molecular Orbital |
| LUMO | Lowest Unoccupied Molecular Orbital |
| MEF | Mouse embryonic fibroblasts |
| MFM | Molecular Force Microscopy |
| MTFM | Molecular Tension Fluorescence Microscopy |
| nt | nucleotide |
| PALM | Photoactivation Localization Microscopy |

| | |
|---|---|
| PEG | Polyethylene-glycol |
| SIM | Structured-illumination microscopy |
| SLB | Supported Lipid Bilayer |
| SMLM | Single Molecule Localization Microscopy |
| SNR | Signal-to-Noise Ration |
| ssDNA | Single-stranded DNA |
| STED | Stimulated Emission Depletion |
| STORM | Stochastic Optical Reconstruction Microscopy |
| TDM | Transition Dipole Moment |
| TGT | Tension Gauge Tether |
| TFM | Traction Force Microscopy |
| tPAINT | Tension Point Accumulation for Imaging in Nanoscale Topography |

# SUMMARY

Molecular forces are vital to many biological systems including hemostasis, immune function, development, and cell-cell communication. The tools currently available to measure cellular forces are incapable of quantifying the 3D orientation and nanoscale distribution of piconewton receptor forces. To address this technological gap, this thesis describes the development of two mechanoimaging techniques, Molecular Force Microscopy (MFM) and tension-Point Accumulation for Imaging in Nanoscale Topography (tPAINT). The first technique, MFM, combines DNA-based molecular tension probes with fluorescence polarization microscopy to measure the 3D orientation of pN molecular forces. MFM revealed that platelets contract anisotropically, a feature missed by previous traction force microscopy measurements, and suggested that integrin forces within focal adhesions are aligned with force-transducing proteins such as talin, linking focal adhesion structure to integrin forces. The second technique, tPAINT, enables single molecule localization microscopy of receptor force events by converting DNA-based molecular tension probes into force-triggered switches that recruit fluorophores only when experiencing pN receptor force. tPAINT enabled measurement of dynamic receptor forces with ~25nm resolution. tPAINT imaging of platelet lamellipodial forces linked these forces with a peripheral ring of actin, demonstrating the capability to link receptor forces to the protein structures that produce them. MFM and tPAINT provide new capabilities to interrogate mechanobiology, and may offer a route to link structural biology and receptor mechanics.

# CHAPTER 1. INTRODUCTION

Cells are highly mechanically active. This statement seems simple at the outset. Humans are all made of cells. We can all move and exert forces on our surroundings. It therefore follows that cells must produce these forces. However, the importance of cellular forces extends far beyond simply allowing us to move. In fact, forces transmitted by cellular receptors regulate many processes, including cell migration, hemostasis, immune recognition, cancer invasion and metastasis, embryonic development, cell-cell signaling, and force generation. The study of cell-generated forces and their importance to biological function is generally known as mechanobiology.

To get a sense of the scale of the forces we will be discussing, a force of 1 newton (N) is required to lift an apple off the ground. Single cells generally generate nanonewton (nN) forces ($1x10^{-9}$ N), a remarkably small amount of force. The forces transmitted by individual protein receptors measure only piconewtons (pN) in scale ($1x10^{-12}$ N), yet these forces are critical to biology. Developing technologies to quantify the pN forces that cells use to interact mechanically with their environment is the topic of this thesis.

Chapter 2 provides background information about the field of mechanobiology, and the techniques that are commonly used to quantify receptor forces.

Chapter 3 describes Molecular Force Microscopy, a technique that combines DNA-based molecular tension probes with fluorescence polarization microscopy to measure the 3D orientation of pN receptor forces. We hypothesized that molecular tension probes would behave somewhat like a rope, aligning parallel to applied receptor forces. This force-

induced reorientation also aligns fluorescent reporters that are rigidly affixed to the probe. By employing fluorescence polarization techniques, it is possible to measure the orientation of the fluorophore, and therefore to calculate the orientation of pN receptor forces. We named this technique Molecular Force Microscopy (MFM). We leveraged MFM to quantify the 3D orientation of pN receptor forces transmitted by human platelets and mouse embryonic fibroblasts. These experiments revealed a previously unknown axis of contraction within platelets. Additionally, MFM revealed alignment between the out-of-plane-orientation of integrin forces in fibroblasts and the orientation of force-bearing proteins as measured by other investigators.

Chapter 4 describes tension-Point Accumulation for Imaging in Nanoscale Topography (tPAINT), a technique that enables the measurement of the nanoscale distribution of pN receptor forces with ~25nm resolution. tPAINT leverages DNA-based tension probes in conjunction with the stochastic super-resolution imaging modality DNA-based Point Accumulation for Imaging in Nanoscale Topography (DNA-PAINT). In DNA-PAINT, short, (~9nt) fluorophore-tagged "imager" strands hybridize transiently to complementary "dock" sites affixed to biomolecules of interest. We hypothesized that by concealing a cryptic docking site within a DNA-based tension probe, receptor forces would trigger imager hybridization, providing a means of super-resolving single molecule receptor forces. The resulting technique, tPAINT, enabled super-resolved imaging of pN receptor forces exerted by human platelet and mouse embryonic fibroblasts. Because the folding and unfolding of tPAINT probes under force is reversible, tPAINT enables live-cell dynamic measurement of the distribution of pN receptor forces. With this live-cell imaging technique, we interrogated the formation and spreading of a "ring" of tension at

the leading edge of platelet lamellipodia. We combined tPAINT with multiplexed Exchange-PAINT to sequentially visualize pN platelet receptor forces and the platelet actin architecture. These experiments linked the ring of platelet integrin forces with a ring of actin at the platelet edge. Exchange-tPAINT thus promises to link the nanoscale distribution of receptor forces with the protein structures or signaling complexes that produce those forces, offering critical insight into structure-function relationships in mechanobiology.

This thesis describes the invention of two mechanoimaging modalities, MFM and tPAINT, that enable measurement of the 3D orientation and nanoscale distribution of pN receptor forces, respectively. These imaging modalities have broad application in mechanobiology, enabling investigation of piconewton molecular forces with unprecedented detail.

# CHAPTER 2. A BRIEF HISTORY OF BIOLOGICAL FORCES AND THE TECHNIQUES USED TO MEASURE THEM

This chapter contains text adapted from Brockman, J, & Salaita, K., *Frontiers in Physics* 2019 and used with permission (CC BY 4.0).

## 2.1 Abstract

This chapter will explore the importance of mechanical forces in biology and discuss techniques to quantify those forces. Mechanical forces are critical to many biological processes including hemostasis[2-7], immune function[8-11], cancer invasion[12, 13], and development[14, 15]. Both the magnitude and the molecular orientation of receptor forces likely influence biological signaling[9, 13, 16, 17]. The gold standard technique for biological force measurement, Traction Force Microscopy (TFM) offers only nanonewton (nN) force sensitivity and micrometer (μm) spatial resolution[18-20]. In contrast, single receptor forces are piconewton (pN) in scale, three orders of magnitude smaller than the force sensitivity of TFM. Recently-developed molecular tension probes enable measurement of the magnitude of pN receptor forces, generally with diffraction-limited (~250nm) spatial resolution[21-25]. These probes represent a significant step forward in quantifying receptor forces, but they are not without their weaknesses. Specifically, molecular tension sensing approaches do not provide information regarding the orientation of receptor forces. Additionally, neither molecular tension probes nor TFM have sufficient spatial resolution to understand the nanoscale distribution of receptor force. A technique capable of linking receptor forces to the ultrastructure of the cytoskeleton is required. Tackling these two

problems, measuring the 3D orientation of pN receptor forces and enabling super-resolved measurement of the nanoscale distribution of receptor forces, are the topic of this dissertation.

## 2.2 A Brief History of Mechanobiology

Mechanobiology is the study of how physical forces and mechanical properties affect biological functions. Early approaches to biology were concerned with the influence of forces on biological function. For example, the German surgeon Julius Wolff wrote a book in 1892 entitled "Das Gesetz der Transformation der Knochen" (The Law of Bone Transformation) that described Wolff's law, which holds that bone remodels and adapts to the loads that it experiences[26, 27]. The biologist D'Arcy Wentworth Thompson wrote a book "On Growth and Form" in 1917 that treated biology, ranging from childhood growth to cell division and the trabeculae in bone in terms of basic mathematics and physical forces[28]. Despite this early recognition of the importance of mechanics, the technology of the time was insufficient to quantify biological forces, especially at the cellular and molecular levels. Accordingly, over the next 50 years most progress in biology focused on a chemical, not physical perspective, a trend that the advent of molecular biology further reinforced.

Within the past 50 years, mechanobiology slowly gained traction. Some early experiments focused on biological functions that were clearly mechanical in nature: hearing, gravity sensing, and touch. Investigators found that mechanical stimulus applied to cochlear hair cells produced electrical signals[29], an early demonstration that cells can respond to mechanical forces with chemical changes. Structures identified in gravity-sensing vestibular hair cells linked stereocilia to the microtubule cytoskeleton, providing a

structural mechanism for mechanosensation. These results also provided early evidence implicating the cytoskeleton as an active participant in mechanobiology[30, 31]. EM imaging of muscle stretch receptors in model organisms suggested that strain bourne by the extracellular matrix might be transmitted to neurons as a means of mechanosensation[32].

At the molecular level, evidence mounted that mechanical forces altered function. For example, twisting forces applied via magnetic beads coated in integrin ligand produced focal adhesion formation, suggesting that integrin receptors are mechanosensors[33]. It has been long appreciated that molecular forces could shorten receptor-ligand bond lifetimes[34]. Mathematical frameworks[35] and later empirical evidence demonstrated that pN forces could not only shorten receptor-ligand bond lifetimes (slip bonds), but also could increase bond lifetimes[36-40] (catch bond behavior). An increase or decrease in the duration of receptor-ligand interactions provides a potential mechanism for mechanical forces to alter biochemical signaling.

Force transmitted via receptors not only alters bond lifetime, but can also directly alter the conformation of the receptor itself (Figure 1). Single molecule measurements have demonstrated conformational shifts in force-bearing receptors, including integrins[41]. Optical tweezer measurements suggested that the TCR may undergo a force-induced extension and that this conformational switch may facilitate antigen recognition[42]. The platelet glycoprotein Gp1b-IX binds to von Willebrand factor and is thought to have a mechanosensitive domain that unfolds under force (e.g. fluid shear), contributing to platelet mechanosensing[43]. Thus, force altering receptor confirmation is another potential mechanism of mechanosensing.

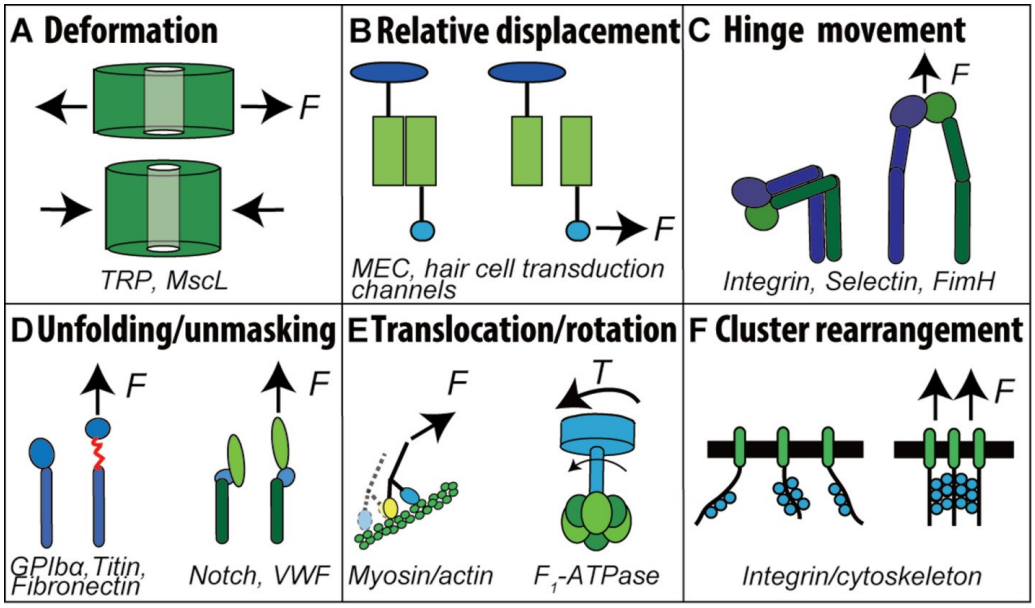


**Figure 1: Effects of Receptor Force on Proteins**

Receptors forces can have many direct effects on protein conformation that lead to cellular signaling. Figure from Chen, Y., et al *Molecular Biology of the Cell* 2017. Reprinted with permission, Copyright (2017) American Society for Cell Biology

### 2.3 Receptor Forces May Enhance the Fidelity of Biological Signaling

It is now well-appreciated that cell mechanics and substrate stiffness are linked to genetic or signal transduction programs. For example, mechanical forces regulate development[15], differentiation[14], and malignant behavior[13].

However, the advantage molecular forces confer in many processes is not clear. In the case of adhesion receptors, molecular forces are a logical consequence of those receptor's role in mediating cell attachment and locomotion. However, many recognition and signaling receptors are also mechanically active. For example, recent molecular tension probe measurements revealed that the TCR transmits defined piconewton forces to the pMHC, and that these forces facilitate TCR antigen discrimination [9, 44]. The B cell

receptor (BCR) also uses mechanical force to internalize antigen, a process that may ensure that only multivalent, high-affinity antigens which collectively withstand the cellular force are internalized[45]. This raises a critical question, why would cells expend energy to exert force on the critical, but tenuous bonds that mediate signaling events. In a recent review article, we posited that cells exert pN receptor forces on receptor-ligand interactions, deliberately increasing the energy cost of signaling processes in exchange for increased signaling specificity[1]. We termed this idea "mechanical proofreading," akin to more well-known kinetic proofreading[46, 47].

Three basic modes of mechanical proofread likely operate in mechanobiology: force-induced alterations in bond lifetime, a mechanical "stress" test, and a mechanical "strain" test (Figure 2).

The role of alterations in bond lifetime in mechanical proofreading is conceptually easy to understand. If a signaling process produces secondary messengers during the lifetime of a a receptor-ligand interaction, increasing the lifetime of that interaction will increase signaling. AFM measurements provided the first direct evidence for a catch bond between P-selectin and P-selectin glycoprotein ligand-1[40]The TCR-pMHC bond is believed to be a catch bond[8]. A catch bond has also been demonstrated in the bond between lymphocyte function-associated antigen-1 (LFA-1) and intercellular adhesion molecule 1 (ICAM-1)[48]. Combined with the observation that dendritic cells (DC) immobilize ICAM-1 on their surface in response to inflammatory signals[49], these results raise the possibility that that the LFA-1-ICAM-1 catch bond may help T cells recognize stimulated DCs. In non-lymphocyte systems, the platelet glycoprotein GPIbα exhibits catch bond behavior when interacting with Von Willebrand factor[50]. Bacterial adhesion under flow is regulated

by a catch bond between FimH and mannose[37]. It is likely that catch bonds are a bioloigally general mechanism for mechanical proofreading, ensuring that biological processes occur only at specific, desirable interfaces via extremely specific mechanically stable receptor-ligand bonds (Figure 2).

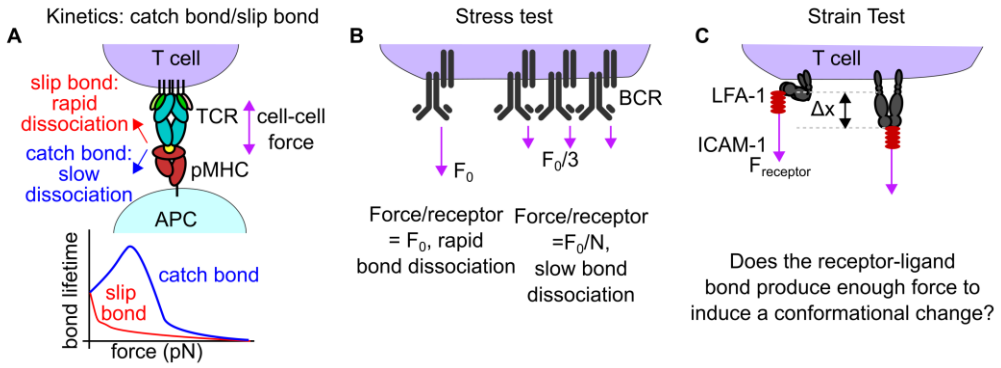


**Figure 2: Mechanical Proofreading**

(**a**) Forces borne by receptor-ligand interaction can reduce the off rate of that interaction which may facilitate mechanical proofreading (a catch bond). The TCR-pMHC bond is a catch bond. (**b**) Mechanical proofreading "stress" test wherein single bonds are insufficient to withstand the applied cellular force. Only when the force is spread across many bonds will the entire force-bearing structure survive to produce biological signaling. This mode of mechanical proofreading may occur in BCR-antigen internalization. (**c**) Mechanical proofreading "strain" test in which pN forces produce a conformational shift in a receptor only if the strength of the receptor-ligand bond is sufficient. This mode may operate in integrin signaling, e.g. LFA-1:ICAM bond. (CC BY 4.0) from Brockman, J., & Salaita, K. *Frontiers in Physics* 2019.

Qualitatively, catch bonds provide a means to spend mechanical energy (from cyotoskeletal and motor protein forces) in exchange for specificity. Most molecular bonds exhibit slip bond behavior; therefore, if a cell expends mechanical energy via the application of cytoskeletal or motor protein applying force to a receptor-ligand bond, and bond lifetime increases, the interaction is verly likely to be "correct." Catch bonds thus

complement the kinetic proofreading model and offer a potent means for mechanical proofreading.

What about non-catch-bond receptor-ligand interactions? Even for slip-bonds, mechanical proofreading can still occur via a "stress test." Receptor clustering is crucial to many biological signaling pathways and may also provide a mechanical advantage to force-bearing receptors. When force-bearing receptors cluster together, the stress (defined as force per unit area) applied at a cell-cell junction may be reduced because the force is distributed over many bonds. Receptor clustering therefore offers an opportunity for a mechanical proofreading "stress test," which selects for cellular structures composed of many force-bearing proteins. Collectively, clustered proteins may withstand forces that would rupture any single bond. Note that for the stress test mechanism to function, the cellular force-generating machinery must be connected to groups of receptors (e.g. one actin stress fiber transmitting force to many integrins).

Consider a cluster of N receptors withstanding a total force F at a cell-cell junction. Force balance dictates that each receptor is bearing a force of approximately F/N. Clustering leads to an N fold decrease in the force experienced per ligand-receptor pair. Based on the Bell model[34], the reduction in force on each receptor-ligand pair will lead to a significant enhancement in the bond lifetime relative to the case where receptors bear F individually, increasing the probability that the cellular structure will survive long enough to initiate biochemical signaling. To achieve the desired specificity and sensitivity, biological systems can alter both F and N. Increasing F produces shortened bond lifetime, decreasing sensitivity. Conversely, increasing N reduces the per-receptor force, facilitating signalling under force, potentially decreasing specificity. High F and high N may achieve

both high sensitivity and specificity by enabling only highly multivalent interations to initiate biochemical signalling.

B cell receptor (BCR) antigen internalization is an example of a mechanical proofreading stress test. BCR signaling is intricately related to the B cell cytoskeleton[51]. Clusters of BCRs are thought to use mechanical force to internalize antigen. Natkanski et al. demonstrated that B cells internalize plasma membrane sheet bound antigen in a myosin IIa dependent manner, and that clathrin-coated structures seem to be associated with antigen internalization[45]. Interestingly, BCR microclusters were observed to resist contractile forces for 20-30 seconds; however, AFM measurements demonstrated that single BCR-antigen bonds do not endure long enough for the observed membrane invagination to occur[45]. The authors hypothesize that forces exerted by B cells shorten the BCR-antigen bond lifetime, ensuring that only multivalent, high-affinity antigens which collectively withstand the cellular force are internalized (Figure 2)[45]. These findings are supported by the observation that B cells exert measurable traction forces through the B cell receptor, and that the magnitude of traction force scales with the number of clustered BCRs involved in force transmission[52]. Additionally, DNA-based molecular tension sensor measurements demonstrated that the BCR utilizes molecular forces to extract antigen from follicular dendritic cells, and that stiff follicular dendritic cells produce stronger BCR forces and more stringent antigen affinity discrimination[53]. Collectively, this evidence points towards a mechanical stress test facilitating BCR selection for high-affinity antigen.

A mechanical stress test may also be important to TCR signalling. The TCR is known to exert pN forces on the TCR-pMHC bond[9], but the importance of nanoclusters in TCR force transmission is not known. Super-resolution imaging has suggested that TCRs

form nanoclusters, and that clustered TCRs are more likley to be phosphorylated and to participate in downstream signalling[54]. TCRs are known to cluster at the surface of microvilli on the T cell surface[55] and TCR-bearing microvilli selectively stabilized at the T cell-antigen presenting cell interface[56]. Collectively, this evidence raises the possibility that TCR nanoclusters, and potentially microvilli, may facilitate a mechanical stress test.

Mechanical stress within other supramolecular complexes may also be important. For example, the focal adhesion has been proposed to behave like a molecular clutch, with mechanical unfolding of adaptor proteins serving to recruit more integrins to the adhesion site to share the applied load[57]. Thus focal adhesions may sense and respond to substrate stiffness via a mechancial proofreading stress test, where specific combinations of force and adhesion site density produce focal adhesion growth and maturation.

Finally, forces on receptors can alter the conformation of a receptor. The many forms this alteration can take have been excellently reviewed elsewhere (Figure 1)[58]. The force-induced conformational change in receptor shape can be considered a mechanical proofreading “strain test” (Figure 2). Conformational shifts may expose cryptic binding sites, leading to protein recruitment or to phosphorylation of a previously inaccessible site. Force-reconfigurable proteins therefore offer a third potential mode of mechanical proofreading. In the mechanical proofreading strain test, a receptor-ligand bond must withstand a threshold force to produce a conformational shift before eliciting biochemical signaling. Note that for the strain test to function, a large energy threshold must prevent the receptor from spontaneously experiencing the conformational shift in the absence of a large input of mechanical work by a cell.

Integrins are well-studied examples of the mechanical proofreading strain test. They exhibit profound conformational shifts, existing in a low-affinity, bent conformation at rest, but are able to adopt a high affinity extended state[59]. Integrins may be an ultrasensitive molecular switch, able to extend in response to pN forces[60].

In the context of lymphocytes, the integrin $\alpha_L\beta_2$, also known as LFA-1, binds to ICAM, and is important to immune cell-cell adhesion and to T cell function[61]. LFA-1 undergoes outside-in activation in response to surface bound, but not soluble ICAM[62], and molecular forces increase the rate of LFA-1 extension and slow the rate of LFA-1 bending (Figure 2)[41]. It is believed that actin forces transmitted through LFA-1 to immobilized ICAM-1 induce extension of LFA-1 and that actin is critical to the formation and maintenance of the immunological synapse[63]. Additionally, recent interference photoactivation localization microscopy (iPALM) measurements, which resolve the location of fluorophores along the microscope optical axis with ~10 nm resolution, have measured the extension of LFA-1 at a T cell-surface interface[64].

The T cell receptor (TCR) may also utilize a mechanical strain test during T cell antigen recognition. Optical tweezer measurements demonstrated a force dependent extension in the FG loop of the TCR[42]. The FG loop extends 8-15nm under the influence of pN forces. Deleting the FG loop of the TCR removed the force-dependent extension behavior and reduced the ability of T cells to respond to antigen as assessed by IL-2 production[42]. The FG loop extension of the TCR therefore presents another example of a potential mechanical proofreading strain test. Because TCR forces are between 12 and 19 pN[9], and because the FG loop extension is known[42], the height of the mechanical proofreading energy barrier that TCR forces must surmount has been calculated as ~37 $k_BT$

(assuming 10nm displacement and 15pN forces), or almost twice the energy of one ATP hydrolysis. This energy of discrimination could explain the remarkable specificity of T cell antigen recognition[65]. The mechanical proofreading strain test is therefore capable of extreme specificity.

A mechanical strain test may also operate to regulate platlet activation. Platelets must be tightly regulated to prevent erroneous clot formation. Data from our lab suggests that the platelet integrin $\alpha_{IIb}\beta_3$ is anisotropcially mechanosensitive, requiring lateral forces to undergo outside in activation to enable platelet spreading and activation on a surface[66, 67] which may explain why platelets ignore soluble fibrinogen in the blood, only binding to fibrinogen attached to other activated platelets. Additionally, the platelet glycoprotein complex GPIb-IX-V, has a mechanosensitive domain that extends several nanometers under force[43], making it another likely candidate for a strain test for mechanical proofreading.

In conclusion, receptor forces can alter proteins in a variety of ways, and may be able to influence or proofread cell functions (Figure 1, Figure 2). Mechanical forces act at all levels of biology, from bone remodeling in response to macroscale forces[26], to force-induced conformational changes at the molecular level[41]. Measuring receptor forces represents a significant challenge. Next, we will discuss techniques for quantifyting biological forces at the cellular and molecular levels.

## 2.4 Techniques for Measuring Biological Forces

As discussed in the previous section, mechanical forces are intricately intertwined with biological function at all length scales, from tissue-level changes and remodeling

down to the single-receptor level; moreover, these forces have significant ramifications for biological signaling. Quantifying the forces exerted at the cellular level required significant technological developments that will be discussed in this section. These technologies have been excellently reviewed elsewhere[20, 68], and will only be discussed briefly here.

### *2.4.1 Traction Force Microscopy*

In 1980, Harris, Wild, and Stopak noted that when cells are cultured on silicone rubber, the cells deform and wrinkle the rubber, indicating that the cells transmit stresses to their substrate (Figure 3)[69]. This method provided early evidence that cells exert forces on their surroundings; however, quantifying these forces was challenging. A decade after this initial report, a series of papers[19, 70, 71] established traction force microscopy (TFM) as a technique for quantifying cell traction forces (Figure 4). In TFM cells apply stress to a mechanically well-characterized substrate, producing deformations that are tracked by the motion of fluorescent beads or other markers within the gel. By quantifying the displacement field induced by cellular stresses, it is possible to calculate the stress field that produced the observed strain (Figure 4).

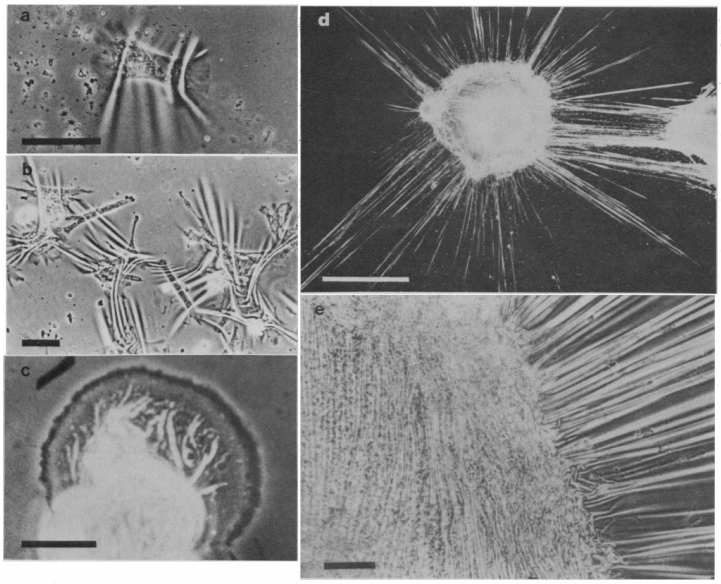


**Figure 3: Cells Transmit Forces to Their Substrate**

In an early precursor to TFM, cells were cultured on a sheet of polymerized silicone rubber floating on a thin film of oil. Cells cultured on this film wrinkled the film, providing some of the first direct evidence for cell traction forces (**a**) Single chick heart fibroblast (50 μm scale bar), and (**b**) an aggregate of chick heart fibroblasts (100 μm scale bar). (**c**) PTK-1 cell (20 μm scale bar) beginning to spread on the substrate and generating ruffling patters (thick dark band). (**d**) Low magnification dark field and (**e**) high magnification phase contrast image of the same chick heart explant. Scalebar in **d** is 1mm and 100 μm in **e**. This figure is reprinted with permission from Harris, Stopak, and Wild, *Science* 1980. Copyright (1980) The American Association for the Advancement of Science.

TFM has since become the gold standard for measuring traction forces. TFM indirectly samples traction forces by measuring the strain cellular forces produced on the substrate. Importantly, TFM can only detect stresses large enough to produce strains detectable via fluorescence microscopy, a requirement that generally limits the force sensitivity of TFM to the nanonewton range[20]. Additionally, most optical microscopy techniques offer worse spatial resolution along the optical axis (*z*) of the microscope

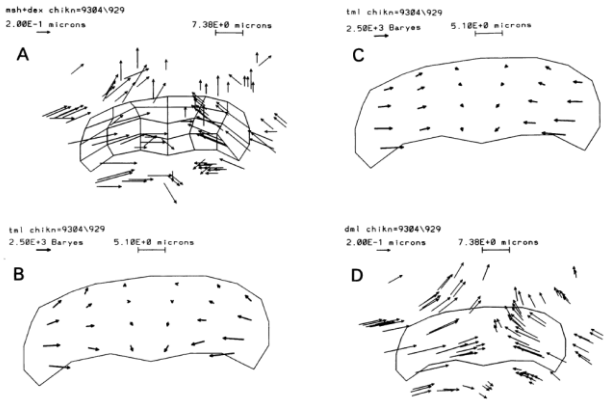


**Figure 4: Early Traction Force Microscopy Measurements**

(**a**) Bead displacements and mesh for a migrating fish epidermal keratocyte. (**b, c**) Two independent traction force reconstructions with slightly different assumptions for this cell produce similar results. (**d**) Theoretical reconstruction of expected bead displacements given the estimated traction field in **b**. Figure reprinted with permission from Dembo, M., et al *Biophysical Journal* 1996. Copyright (1996) Biophysical Journal.

relative to the axes perpendicular to the optical axis (*xy*). TFM is generally less sensitive to normal forces, where bead displacements must be measured along the optical axis.

In practice TFM generally is capable of quantifying nanonewton (nN) forces with micrometer (μm) spatial resolution[20]. In comparison, single receptor forces are pN scale, while force-bearing proteins such as integrins commonly measure nanometers (nm) in length. TFM is only sensitive to forces three orders of magnitude greater than individual

pN receptor forces. Additionally, it lacks the spatial resolution to provide molecular details of cell-surface contacts. Ongoing efforts have focused on improving the spatial resolution of TFM. For example, improvements in the mathematical reconstruction of traction stresses, and the use of two spectrally separable beads enabled ~1 μm spatial resolution in TFM measurements[72]. Super-resolution microscopy techniques including Stimulated Emission Depletion (STED), Structured-illumination microscopy (SIM), and fluorophore fluctuation analysis enabled higher-resolution bead tracking in TFM measurements, also enabling 1 μm resolution using single-color beads[73-75].

TFM has also recently been combined with spinning disc confocal microscopy to measure 3D traction stresses generated by cells embedded in hydrogel matrices[76] and to measure the 3D stresses exerted by cells on 2D substrates[77]. Another recent report utilized 3D SIM to produce high spatial resolution images of cellular traction stresses, including forces normal to the substrate[73]. While these advances establish the ability of TFM to measure 3D traction stresses, the computational difficulty of executing these techniques has precluded their widespread adoption, and the resulting measurements are still limited to nN force sensitivity and μm spatial resolution.

Techniques conceptually similar to TFM are also available to measure cellular forces. Traction forces have also been measured via the displacement of flexible microneedle arrays, but these measurements suffer from the same resolution limits as TFM[78].

### *2.4.2 Single-Molecule Approaches*

In contrast to TFM and microneedle arrays, single molecule techniques such as optical traps, atomic force microscopy, and biomembrane force probes offer the ability to measure piconewton forces at the expense of losing information about whole cell behavior[79]. Optical traps use a highly focused laser to hold a bead in place and provide a restoring force to oppose forces that move the bead away from the center of the laser trap[80]. By moving the bead, it is possible to apply defined pN scale forces to biomolecules and cells, or to measure forces that cells apply to the beads. Optical traps have enabled measurement of single motor molecule forces, and of the retraction forces of cellular structures such as filopodia[81, 82]. Optical trap measurements also revealed the mechanosensitive domain in the platelet glycoprotein Gp1b-IX[43], and an extension of the FG domain of the TCR under pN force[42]. Biomembrane force probes (BFP), another single-molecule technique, use the predictable deformation and mechanical characteristics of a red blood cell membrane to measure piconewton forces applied to biomolecules or cells[70]. BFP has been used to measure force-induced conformational changes in single integrins[41] and to probe the catch bond of the TCR-pMHC bond[8].

Despite their power to interrogate the mechanical behavior of individual receptors under force, single-molecule approaches have several drawbacks. Many single-molecule experiments require that the investigator apply forces to the biomolecule of interest. Whether the receptor itself exerts forces under physiological conditions is therefore unknown. Additionally, information is only gained about a single protein at a time, thus single molecule approaches do not provide the maps of receptor forces provided by TFM or micropillar arrays.

### *2.4.3 Molecular Tension Sensing Approaches*

A recent and powerful approach to directly measure pN receptor forces is to engineer molecular probes to serve as tension sensors[68]. Generally, these probes deform under the influence of pN forces, and report this tension as an increase in fluorescence intensity or fluorophore fluorescence lifetime. Several classes of these probes exist.

Early approaches in molecular tension sensing engineered genetically encoded molecules to perform tension sensing[24]. These probes operate via Förster Resonance Energy Transfer (FRET). In FRET, energy is non-radiatively transferred from a donor fluorophore that has been excited by a photon to an acceptor fluorophore, resulting in a decrease in fluorescence from the donor and an increase in fluorescence from the acceptor. FRET relies upon dipole interactions between the electronic fields of the fluorophores and only occurs when fluorophores are separated by less than a few nanometres. Importantly, FRET efficiency decreases rapidly with distance, enabling FRET to act as a "molecular ruler" that reports the distance between the FRET donor and acceptor molecules. Grashoff et al. incorporated a genetically encoded tension sensor (TSMod) comprised of a fluorescent protein FRET pair, mTFP1 and venus (A206K), linked by a force-extensible $(GPGGA)_8$ sequence within the focal adhesion protein vinculin[24]. Forces transmitted through vinculin to the TSMod construct extended the linker, physically separating the mTFP1 and venus FRET pair, reporting pN forces via changes in FRET index and fluorescence lifetime of the donor fluorophore. This class of genetically encoded tension probes has since been extended to enable multiplexed measurement of different force levels, and to measure forces borne by cadherins, talin, and within the wing muscles of developing *Drosophila* embryos[83-85]. Although genetically encoded tension probes are

powerful, they suffer from several limitations. First, they operate on a FRET principle and thus sometimes offer a low signal-to-noise ratio (SNR). Second, these sensors measure decreases in the FRET efficiency when the probe is experiencing mechanical strain. However, the resting state (zero force) FRET efficiency is low, limiting the dynamic range of these sensors, as measuring further FRET reductions in the mechanically strained state is challenging. Third, these tension-sensing molecules must be incorporated into a force-bearing protein and likely perturb the biological activity of that protein. Finally, genetically encoded tension sensors are excellent for measuring intracellular forces, but do not report pN forces transmitted from a cell to the extracellular environment.

To quantify receptor-generated forces transmitted by the cell to its environment, several approaches are available. The Salaita lab has pioneered Molecular Tension Fluorescence Microscopy (MTFM)[21], a library of techniques that utilize molecular tension probes to transduce pN forces into fluorescence detectable via a fluorescence microscope[21, 22]. The general principle of MTFM is depicted in Figure 5.

In MTFM, tension probes are comprised of force-extensible polymers adhered to a microscope coverslip and presenting an adhesion ligand. The force-extensible polymer domain is flanked by a fluorophore and quencher. When receptor forces extend the tension probe, the fluorophore is separated from the quencher, producing up to a 100-fold increase in fluorescence that is readily detected by fluorescence microscopy (Figure 5)[9]. Additionally, because these probes measure extracellular forces, they can be chemically synthesized with extremely bright synthetic fluorophores, and can employ synthetic quenchers or quenching processes such as nanometal surface energy transfer, enabling

MTFM probes to have a much higher SNR than FRET-based genetically encoded tension probes[22, 86].

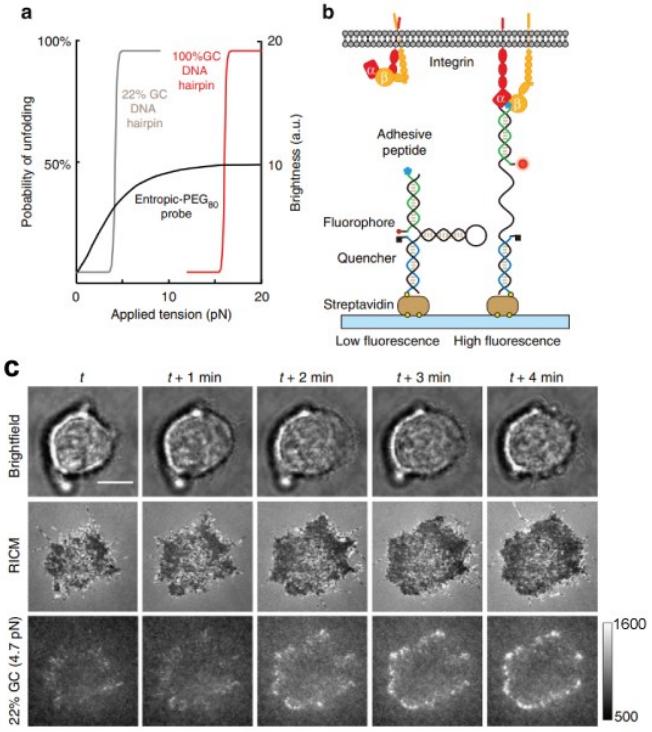


**Figure 5: Principle of DNA-Based Molecular Tension Probes:**

(**a**) Theoretical plot of the relationship between force and fluorescence in DNA tension probes. DNA tension probes are characterized by an $F_{1/2}$, which is the equilibrium force that leads to a 50% chance of probe unfolding. The slope of the probability of unfolding as a function is very steep at the $F_{1/2}$, thus these exhibit a nearly digital transition between open and closed states as receptor force exceeds the $F_{1/2}$. (**b**) Schematic depiction of DNA-based tension probes, which are comprised of a surface anchored strand (blue), a hairpin strand (black), and a ligand strand (green) that presents a cell adhesion ligand, commonly the integrin ligand cyclo-Arg-Gly-Asp (cRGD). The hairpin unfolds when receptor force exceeds the probe $F_{1/2}$, which separates a fluorophore from a quencher, producing an increase in fluorescence that is measurable via a microscope. (**c**) Brightfield, cell-surface contact area measured via reflection interference contrast microscopy (RICM), and tension signal fluorescence for a HCC1143 cell plated on cRGD-modified DNA-based tension probes. This figure is modified with permission from Zhang, Y., et al. *Nature Communications* 2014. Copyright (2014) Springer Nature.

To date, tension probes have utilized polyethylene glycol (PEG)[21, 86], protein domains such as titin Ig domains[87], and DNA hairpins[9, 22, 88] as force-extensible domains and have demonstrated the ability to quantify forces in the range of 2.5-100 pN. The most sensitive and versatile MTFM probes to date are comprised of DNA[9, 22], thus these probes will form the basis of this thesis work.

Other groups are developing molecular tension sensor technology similar to MTFM. Alexander Dunn uses FRET-based probes for single-molecule sensitivity pN tension detection[89, 90]. Mingxu You has recently adapted DNA-haripin based tension probes for visualizing tension at cell-cell junctions by adhering the tension probe to the cell membrane via cholesterol-tagged DNA[91, 92]. Finally, Pavel Tolar has developed a series of probes to demonstrate that B cells use molecular-force, not proteolysis to internalize antigen presented at the B-cell dendritic cell interface[53].

Another important molecular tension probe technology is the Tension Gauge Tether (TGT)[25]. TGTs are DNA-based probes that present a cellular adhesion ligand and are immobilized onto a substrate. Importantly, the TGT ruptures irreversibly when receptor force exceeds the programmed tension tolerance ($T_{tol}$), defined as the force that leads to TGT rupture within 2 seconds. Because TGTs rupture irreversibly when receptor force exceeds the $T_{tol}$, TGTs offer a means to place a limit on the allowable force a cell can transmit to a substrate. TGTs therefore both offer a means to report and control receptor-generated forces. Variants of the TGT technology that resist nuclease degradation, serially connected TGTs for accurate force-quantification, and constructs that report molecular tension with a turn-on fluorescence signal have also been recently reported, rendering this technology even more versatile[6, 93-95].

## 2.5 Current Limitations of Molecular Tension Probes

In general, molecular tension sensing approaches offer a marked improvement in force sensitivity and spatial resolution over TFM and microneedle arrays. While TFM and microneedle arrays generally offer nN force sensitivity and ~μm spatial resolution, molecular tension sensors offer the ability to detect pN molecular forces with diffraction-limited (~250 nm) spatial resolution [20]. Nevertheless, several important limitations restrict the capabilities of molecular tension sensors. Molecular tension probes do not resolve the orientation of cellular forces while TFM and micropillars are capable of reporting force orientation. The orientation of molecular forces is believed to be an important parameter in cellular signalling. Additionally, force-bearing structures exhibit nanoscale organization, but the diffraction-limited spatial resolution of molecular tension probes is insufficient to resolve the nanoscale distribution of pN receptor forces. These two challenges, measuring the 3D orientation and nanoscale distribution of pN receptor forces, are the focus of this thesis work.

## 2.6 Biological Importance of Receptor Force Orientation

Mounting evidence suggests that the orientation of pN receptor forces may influence signaling. In a seminal optical trap study, Reinherz and colleagues mechanically stimulated T cells with several stimulatory antibodies on a bead held within an optical trap. Their measurements suggested that shearing forces preferentially trigger T cells, as measured by calcium flux[16] (Figure 6). Follow up experiments conducted by the same group have replicated the finding, suggesting that shear forces may increase the sensitivity

of the T cell to cognate antigen[96]. However, the molecular details of this interaction, including membrane topology and the angles of interactions of the biomolecules at the bead-cell interface are not known values in these optical trap experiments, thus the evidence supporting the hypothesis that the TCR is an anisotropic mechanosensor remains incomplete.

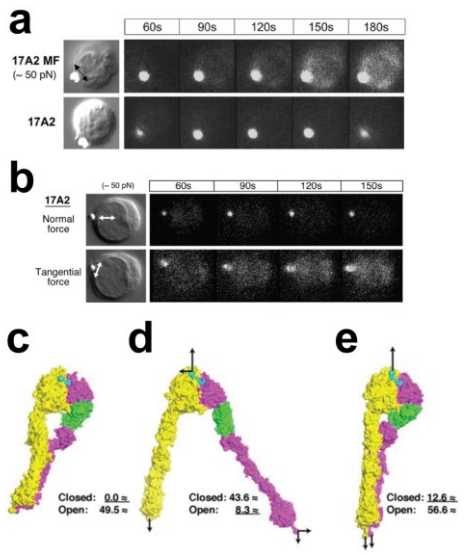


**Figure 6: Importance of Receptor Force Orientation.**

(**a**) T cells activate, as measured by calcium flux, when the anti-TCR antibody 17A2 exerts shearing forces relative to the cell surface. 17A2 is not activating in the absence of force. (**b**) Shearing forces activate T ce3lls, but normal forces do not, suggesting that the T cell receptor maybe an anisotropic mechanosensor. Figures from Kim, S., et al. *Journal of Biological* Chemistry 2009, reproduced with permission from the American Society for Biochemistry and Molecular Biology. (**c**) Structure of an integrin $\alpha_{IIb}\beta_3$ integrin in the extended closed state. Steered molecular dynamics simulations were used to simulate (**d**) shearing forces and (**e**) normal forces. The closed an open numbers representd the distance of C terminal residue 433 from the closed or open state, while the underlined state is the shape most compatible with the integrin conformation after forces. The model sugge3sts that shearing forces (**d**) bias the integrin to the extended open state while normal forces (**e**) bias the integrin to the extended closed state. Figure modified from Zhu, J., et al *Molecular Cell* 2009, reprinted with permission from Elsevier.

The orientation of integrin-mediated receptor forces may also alter biological outcomes. Steered molecular dynamics simulations based on the crystal structure of the integrin ectodomain suggest that lateral forces exerted on the integrin $\alpha_{IIb}\beta_3$ facilitate a conformational shift from the bent and extended-closed state to the extended-open state while normal forces bias the integrin towards the extended-closed state[17] (Figure 6). Integrin extension is thought to regulate ligand binding[97, 98], thus it is possible that lateral or shearing forces transmitted through integrins could be important to outside-in integrin activation. Evidence from our lab revealed that human platelets fail to spread and activate on RGD-coated supported lipid bilayers (SLB) where the RGD ligand is laterally mobile; however, platelets will spread and activate readily on chemically identical but laterally immobile RGD attached to a glass coverslip. These experiments suggest that platelets may be anisotropic mechanosensors, utilizing shearing forces to test whether a ligand is immobilized[6]. This result may explain why platelets ignore soluble fibrinogen in the blood, only binding to fibrinogen attached to other activated platelets.

To address the need for a technique to measure the 3D orientation of pN receptor forces, this thesis presents an integration of fluorescence polarization (FP) techniques with DNA-based molecular tension probes to enable Molecular Force Microscopy (MFM)[67]. MFM generates the highest resolution maps of pN traction force orientations to date.

## 2.7 Nanoscale Organization of Force-Bearing Cellular Structures

Recent advances in fluorescence microscopy have enabled "super-resolution," allowing optical microscopy to reveal features of biological structures that are smaller than the canonical ~250 nm "diffraction limit" of optical microscopy. Super-resolution

microscopy has been extensively reviewed[99], and will only be treated briefly here. One class of super-resolution microscopy techniques leverages single molecule localization microscopy (SMLM). SMLM fits the center of the point spread function (PSF) of single fluorescent emitters and integrates many events to build a "map" of the location of those emitters.

Several stochastic super-resolution techniques that leverage SMLM exist. Stochastic Optical Reconstruction Microscopy (STORM) and Photoactivation Localization Microscopy (PALM) leverage chemical/photophysical blinking of small molecule fluorophores and photoactivatable fluorescent proteins, respectively, to produce the single-molecule fluorescence required for SMLM[100, 101]. A recently developed stochastic super-resolution microscopy technique DNA-based Point Accumulation for Imaging in Nanoscale Topography (DNA-PAINT) leverages transient binding of fluorophore-tagged "imager" strands to complementary DNA "docking" sequences to produce fluorescence blinking events amenable to single-molecule localization[102]. DNA-PAINT is of particular interest in this work because it leverages DNA-DNA association to produce single-molecule fluorescence signal and thus may be compatible with DNA tension probes.

Super-resolution imaging has revealed the ultrastructure of several force-bearing biological systems. For example, STORM measurements of the actin and spectrin cytoskeleton have revealed periodic alternating actin and spectrin rings within the axon of neurons[103]. Nanoscale structure is also present within focal adhesions, organelles that mediate cell adhesion to surfaces. Interference-based PALM measurements have revealed organized layers of proteins normal to the substrate within focal adhesions (Figure 7)[104]. Likewise, live cell PALM measurements revealed fibrillar actin and paxillin structures within focal adhesions[105]. Finally, structured-illumination microscopy (SIM)

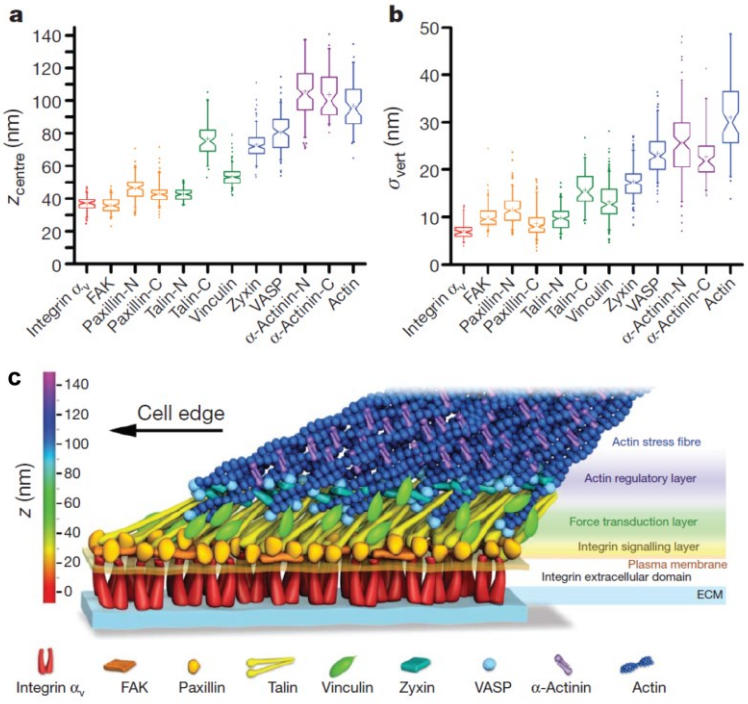


**Figure 7: Nanoscale Organization of the Focal Adhesion**

(a) Z-position and (b) spread of focal adhesion proteins imaged via iPALM, which combines PALM with interferometry to localize the 3D position of photoactivatable proteins with nm resolution. Focal adhesion proteins seem to exist in defined strata. (**c**) Schematic depiction of the axial organization of focal adhesion proteins. This figure is adapted from Kanchanawong, P., et al *Nature* 2010 and used with permission. Copyright (2010) Springer Nature.

measurements and stimulated emission depletion (STED) measurements have both suggested that focal adhesions are comprised of linear protein units[106, 107].

Cytoskeletal and force-bearing cellular structures clearly exhibit impressive nanoscale organization. These ordered cellular structures likely transmit organized forces to their surroundings, yet no technique is currently able to measure the nanoscale distribution of receptor tension. An imaging modality capable of super-resolved measurement of the distribution of piconewton receptor forces, and of linking those forces to the protein structures that produce them, is required to advance understanding of the role of molecular forces in mechanobiology. To address this technological gap, this thesis describes the combination of DNA-PAINT with DNA based tension probes to enable tension-Point Accumulation for Imaging in Nanoscale Topography (tPAINT). tPAINT provides super-resolved maps of pN receptor-generated tension with up to ~25nm spatial resolution.

# CHAPTER 3. FLUORESCENCE POLARIZATION MEASUREMENTS OF RECEPTOR FORCE ORIENTATION

This section contains text and data reported in a previous publication, Brockman, J., et al *Nature Methods* 2018, reprinted with permission from reference [67].

## 3.1 Abstract

To address the need for a tool capable of measuring the magnitude and orientation of pN molecular forces, we hypothesized that piconewton receptor forces exerted on molecular tension probes would reorient those probes, enabling measurement of molecular force orientation via fluorescence polarization microscopy techniques. The resulting technique, Molecular Force Microscopy (MFM) enables mapping of the 3D orientation of pN traction forces produced by cells. We demonstrated the power of this technique by measuring the forces transmitted by human platelets and mouse fibroblasts with diffraction limited spatial resolution[67].

## 3.2 Introduction

Fluorophores are molecules that absorb visible light and then emit red-shifted light (fluorescence). When a fluorophore is excited by a photon, an electron is excited from the highest occupied molecular orbital (HOMO) to the lowest unoccupied molecular orbital (LUMO). The movement of electric charge during this transition defines the excitation transition dipole moment (TDM) of the fluorophore. This dipole behaviour of fluorophores provides them with several extremely useful characteristics. For example, fluorophores are preferentially excited by light that is polarized parallel to their excitation transition dipole

moment (TDM). Additionally, the movement of charge during the fluorescence emission process (from LUMO to HOMO) also results in an emission TDM, thus fluorophores emit light polarized along the axis of their emission TDM. The excitation and emission TDMs of fluorophores are often, but not always, similar in orientation. Fluorescence polarization (FP) techniques utilize the polarized excitation and emission fluorophores to probe biomolecule properties, including mobility and molecular orientation[108]. Fluorescence polarization microscopy (FPM) has been used to reveal the orientation of nuclear pore proteins[109, 110], yeast septin during budding[111], the orientation of cell membranes[112-114], and the orientation and nanoscale order of biomolecules and single molecules[115, 116].

This work utilizes two different FP techniques, excitation and emission resolved fluorescence polarization microscopy. In emission resolved FPM, a linearly polarized light source excites fluorophores while a polarizing beamsplitter splits the fluorescence emission into components parallel and perpendicular to the excitation light source. In this work, the optical setup depicted in Figure 8a was utilized for excitation resolved FPM experiments. Fluorophores were excited with a linearly polarized 561 nm light source and the resulting polarized fluorescence emission was split into components parallel and perpendicular to the excitation polarization via a polarizing beamsplitter.

An alternate FP experiment, excitation resolved FPM, measures fluorophore brightness as a function of variation in the polarization state of a linearly polarized light source. When the excitation light source is perpendicular to the fluorophore's TDM, very little fluorescence is observed. Conversely, when the excitation light source is parallel to the fluorophore's TDM, the fluorophores produce stronger fluorescence. The optical path for the excitation resolved FPM experiments conducted in this work are also given in

Figure 8b. In the excitation resolved FPM experiments presented in this chapter, we varied the polarization state of a linearly polarized light source with a motorized, rotatable half-wave plate that allowed us to freely vary the polarization state of the excitation light in the XY plane.

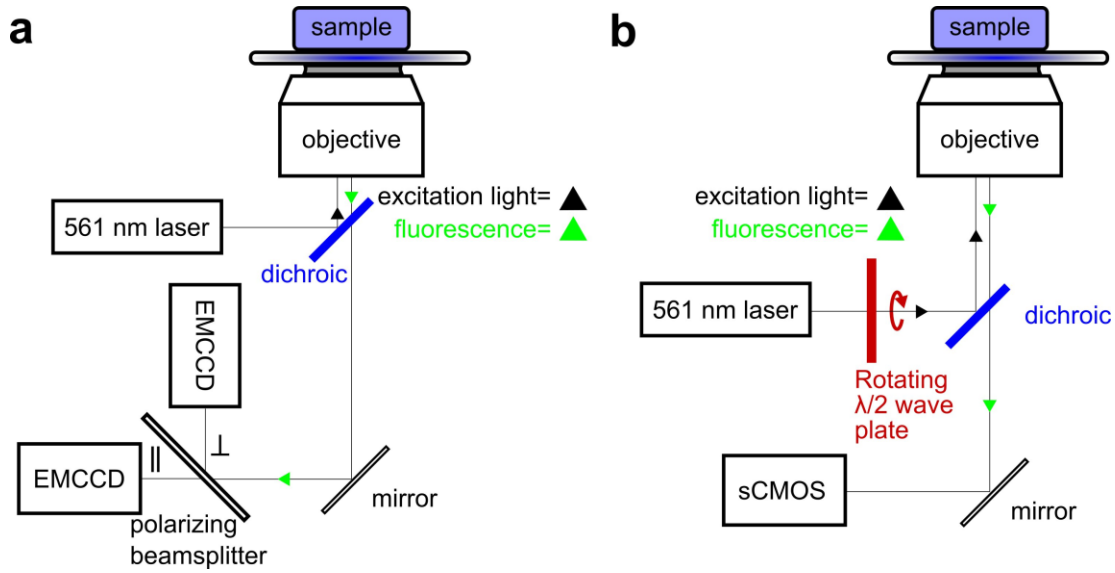


**Figure 8: Light Paths Used in This Work**

(**a**) Emission resolved and (b) Excitation resolved fluorescence polarization microscopy optical paths. For both optical lines, the laser was operated in widefield mode with the laser focused at the back focal plane of the microscope.

## 3.3 Results

### *3.3.1 Receptor Forces Confine the Mobility of DNA-based Molecular Tension Probes*

We hypothesized that DNA-based molecular tension probes would align with the orientation of the applied receptor forces. To test this hypothesis, we generated a mathematical model based on the worm-like-chain (WLC) force-extension behaviour of DNA to determine the degree to which DNA hairpins will be confined to an orientation

parallel to the applied receptor force. The probe DNA hairpin (Figure 5) unfolds when the applied force exceeds the $F_{1/2}$, the equilibrium force that produces a 50% chance of hairpin unfolding. Probe extension under force ruptures the hairpin secondary structure, which becomes extended single-stranded DNA (ssDNA). The Cy3B-BHQ1 fluorophore quencher pair is highly quenched, thus Cy3B effectively only contributes to the measured fluorescence signal upon force-induced hairpin unfolding. We have termed this mechanism "mechano-selection," as only probes experiencing forces equal to or exceeding the $F_{1/2}$ contribute to MFM fluorescence. Accordingly, we only consider the conformational flexibility of mechanically strained probes. Note that the values in Table 1 were used for all subsequent WLC calculations.

**Table 1: Parameters for WLC Calculation**

| Parameter | Definition | Value |
|---|---|---|
| T | temperature | 298 K (25°C) |
| $F_{WLC}$ | applied force | pN (user specified and varied within the model) |
| x | extension | nm (depends on the user specified force) |
| N | number of ssDNA bases | 31 |
| $L_c$ | contour length | 20.95 nm |
| b | length per base | 0.676 nm [ref [117]] |
| $l_p$ | persistence length ssDNA | 2 nm [ref [118]] |

The double stranded DNA (dsDNA) arms of the probe are rigid because these are 21 bp in length (7.14 nm), significantly smaller than the ~53 nm persistence length of dsDNA[119]. The unfolded hairpin is comprised of a 31 bp segment of ssDNA with restricted

conformational flexibility due to the applied force. To define the flexibility of the strained ssDNA segment, we first employed the worm-like chain (WLC) model. We used a recently-published extension-force dependence model[120], given in Equation 1.

$$x(F_{WLC}) = L_c\left[\frac{4}{3} - \frac{4}{3\sqrt{f+1}} - \frac{10e^{\sqrt[4]{\frac{900}{f}}}}{\sqrt{f}\left(e^{\sqrt[4]{\frac{900}{f}}} - 1\right)^2} + \frac{f^{1.62}}{3.55 + 3.8f^{2.2}}\right], \quad (1)$$

$$f = \frac{F_{WLC}l_p}{k_BT}$$

With this formula, we find that when $F_{WLC} = F_{1/2} = 4.7$ pN, the ssDNA hairpin is extended to 66% of its contour length ($L_c$). Because the ssDNA is force-bearing, it adopts, on average, an orientation aligned with the direction of the applied cellular force (Figure 9). To reach this conclusion, we assume a constant applied force by a fixed cell receptor. The upper dsDNA handle of the tension probe may freely pivot around rotatable bonds attaching the cRGD ligand to the DNA probe. Since the dsDNA handle is also linked to the ssDNA segment, rotation of the dsDNA handle (angle β, Figure 9b) away from an orientation parallel to the applied force leads to extension of the ssDNA hairpin from its equilibrium extension. Extending entropic springs, such as ssDNA, beyond their equilibrium mean end-to-end distance is energetically unfavorable. We assume that the end of the ssDNA that is not attached to the dsDNA handle is also fixed in place. In the full model geometry, receptor force specifies $\Phi_{force}$ and $\theta_{force}$, while thermal energy may produce misalignment between the upper dsDNA rod and the axis of receptor force. The full geometry is shown in Figure 9c.

The force, $F_{WLC}$, required to extend the ssDNA a given distance ($x$) is calculated as depicted in Equation 2 [ref [119]].

$$F_{WLC}(x) = \frac{k_B T}{l_p}\left[\frac{1}{4}\left(1 - \frac{x}{L_c}\right)^{-2} - \frac{1}{4} + \frac{x}{L_c} - 0.8\left(\frac{x}{L_c}\right)^{2.15}\right] \quad (2)$$

The integral of the force-extension curve provides the energy required to extend the polymer to any position beyond its equilibrium length (Equation 3).

$$E_{WLC}(x) = \int_0^x F_{WLC}(x)dx \quad (3)$$

The minimal force experienced by probes that contribute to the observed fluorescence is 4.7 pN, which enables calculation of the initial equilibrium extension ($x^0$) using Equation 1. Thermal energy allows the ssDNA chain to explore additional conformations (extension *x'*, red, Figure 9b). To estimate tension probe flexibility, we first estimate the energy required to extend the ssDNA away from its equilibrium position. The cellular force extends the ssDNA segment to length $x^0$. Further extension (stretching the ssDNA to length *x'*, red line, Figure 9b) requires thermal energy as described by Equation 4.

$$Work_{thermal}(x') = \int_{x^0}^{x'} F_{WLC}(x)dx \quad (4)$$

To construct a Boltzmann distribution, we define a partition function, $Z$, which is determined by integrating all possible extensions ($x'$) of the ssDNA. We also introduce a factor of sin(β) to account for the rotational restriction of the dsDNA handle due to the cellular force. The partition function is given in Equation 5.

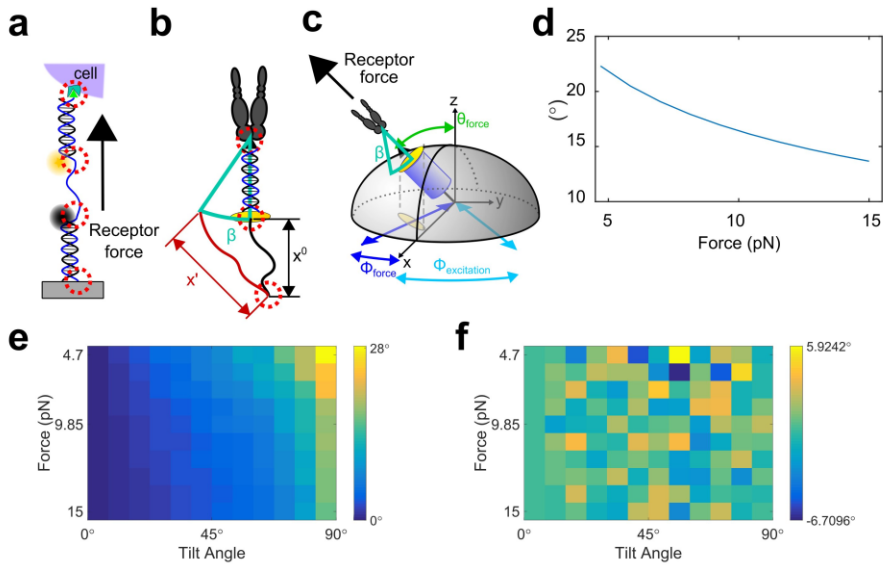


**Figure 9: Force-Induced Confinement of DNA Tension Probes**

(a) The DNA tension probe is composed of 2 dsDNA segments, (length 7 nm << $l_{p,\ dsDNA}$ = 53 nm) which we treat as rigid rods. Flexible ssDNA links these rods. Rotatable bonds are indicated by red dashed circles. (b) The dsDNA rod may rotate though angle β about its anchorage to the integrin via the link between the cRGD ligand and the DNA probe (arc of motion is indicated by the black arc). The cyanine fluorophore (ensemble average orientation depicted as a yellow disc) can theoretically adopt any plane tangential to the arc. The motion of the dsDNA rod along this arc is constrained by its attachment to the ssDNA entropic spring. Receptor force is sufficient to produce an extension, $x^0$, of the ssDNA spring (black curvy line), but extending the hairpin further, to an extension x' (red curvy line) requires additional energy input. This energy must come from the thermal energy of the system. (c) The gray hemisphere represents all possible orientations of the DNA tension probe; the turquoise arc demonstrates the constrained motion of the probe that is possible under applied receptor force. For clarity, the entire DNA tension probe (two dsDNA rods and the ssDNA hairpin) is represented as a single blue cylinder. The black arc illustrates the flexibility of the full DNA tension probe. (d) Average angle between the dsDNA helix and the axis of cellular force (β) as a function of applied cellular force. (e) Deviation of $\theta_{force}$ and (f) $\Phi_{force}$ due to the flexibility of the ssDNA portion of the DNA tension probe. For e and f, β angles were randomly chosen by binning 100 random numbers on the interval 0-1 into the cumulative distribution function for β. Each pixel in e and f represents the average error of 100 β angles. This stochastic simulation was repeated 3 times with similar results.

$$Z = \int_{x^0}^{L_c} \sin\left(\beta(x')\right) \exp\left(-\frac{1}{k_B T} \int_{x^0}^{x'} F_{WLC}(x)dx\right) dx' \quad (5)$$

Finally, with Equations 4 and 5, we can construct a Boltzmann distribution to describe the probability of ssDNA adopting a stretched conformation , *x'*, as written in Equation 6

$$P(x') = \frac{\sin\left(\beta(x')\right) Work_{thermal}(x')}{Z}$$
$$= \frac{\sin(\beta(x'))\exp\left(-\frac{1}{k_B T}\int_{x^0}^{x'} F_{WLC}(x)dx\right)}{\int_{x^0}^{L_c} \sin\left(\beta(x')\right) \exp\left(-\frac{1}{k_B T}\int_{x^0}^{x'} F_{WLC}(x)dx\right) dx'} \quad (6)$$

The average extension can be calculated as the weighted average of the ssDNA extension (Equation 7). The average extension, $x^0$, varies as a function of the applied cellular force because the force required to extend a worm-like chain increases with increasing extension.

$$x_{average} = \int_{x^0}^{L_c} P(x)x\, dx \quad (7)$$

From the Pythagorean theorem, we can create an expression (Equation 8) for the end-to-end extension as a function of the angle, β (green arc, Figure 9b), between the orientation of the dsDNA handle that is rigidly ligated to the cyanine dye, and the axis of cellular force. $r_{helix}$ is 7.14 nm, the length of the upper dsDNA handle.

$$x'^2 = \left(x^0 + r_{helix}(1 - cos\beta)\right)^2 + (r_{helix} sin\beta)^2 \quad (8)$$

From this expression, we used a symbolic equation solver to derive the following expression (Equation 9) for β as a function of $x^0$, $x'$, and $r_{helix}$.

$$\beta(x^0, x', r_{helix}) = \tan^{-1}\left(\frac{\frac{\sqrt{-x'^4 + 2x'^2x^{0^2} + 4x'^2x^{0^2}r_{helix} - x^{0^4} - 4x^{0^3}r_{helix} - 4x^{0^2}r_{helix}^2}}{2\sqrt{x^{0^2}r_{helix}^2 + 2x^0 r_{helix}^3 + r_{helix}^4}}}{\frac{-x'^2 + x^{0^2} + 2x^0 r_{helix} + 2r_{helix}^2}{2r_{helix}(x_0 + r_{helix})}}\right) \quad (9)$$

Using Equations 6 and 9, we calculated the average angular deviation of the dsDNA handle from the axis of applied force via Equation 10.

$$\beta_{average} = \int_{x^0}^{L_c} P(x)\beta(x)\, dx \quad (10)$$

Figure 9d plots the predicted mean probe misalignment from the orientation of the applied force (β) as a function of applied force. The model reveals that β varies from 22.3° (0.86 nm average extension, defined as x'-$x^0$) at the $F_{1/2}$ to 13.6° (0.32 nm average extension) at 15 pN. In line with expectations, the applied force confines the flexibility of the probe, with an average of 22.3° variability from the axis of the applied force for the weakest detectable integrin force signals.

Finally, we sought to determine how the variation in β alters MFM measurements. We constructed a cumulative distribution function (CDF) from the probability distribution for β and used this CDF to randomly select the phase of 100 sinusoids. To model the greatest possible error, we assume that the angular variation in β exists as rotations exclusively in the image (XY) plane. These sinusoids represent the fluorescence intensity that would be produced by a range of fluorophores with average angular excursion β as $\Phi_{excitation}$ is varied. To mimic an MFM measurement, we summed the sinusoids and curve fit the resulting summed fluorescence signals. We performed this simulation for receptor forces ranging from 4.7 pN to 15 pN, and for tilt angle ($\theta_{force}$) values ranging from 0° to 90°. The results of this simulation are presented in Figure 9e-f. MFM underestimates very high values of $\theta_{force}$ by up to 28° when receptor force is low and when $\theta_{force}$ is near 90°. However, for most combinations of receptor force magnitude and $\theta_{force}$, MFM underestimates $\theta_{force}$ by less than ~10° due to a thermal energy misaligning DNA tension probes with the orientation of the applied receptor force.

### *3.3.2 Emission Resolved Fluorescence Polarization MTFM*

Having confirmed *in silico* that pN receptor forces should induce DNA tension probes to align parallel to receptor forces, we next sought to empirically test this phenomenon. We first turned to emission resolved fluorescence polarization experiments. Emission resolved FP leverages the polarized fluorescence emission of fluorophores to gain information about fluorophore orientation. Fluorophores are preferentially excited when their excitation TDM is aligned parallel to the polarization of a light source. The probability of exciting a fluorophore depends on the square of the projection of the fluorophore excitation TDM onto the excitation light source polarization.

For MFM, we chose to use DNA-based molecular tension probes[22] that utilize the cyanine fluorophore Cyanine 3B (Cy3B) as a fluorescent reporter of tension, and the molecular quencher Black Hole Quencher 1 (BHQ1). When the receptor force transmitted to the molecular tension probe exceeds the probe $F_{1/2}$, the hairpin unfolds and the Cy3B dye separates from the BHQ1 quencher, producing a significant enhancement in fluorescence (Figure 5). The bonds that anchor the probe to the coverslip and to the integrin receptor are rotatable, thus the DNA tension probe aligns parallel to the orientation of the pN force (Figure 9). Importantly, NMR and FRET studies have demonstrated that cyanine fluorophores stack with dsDNA nucleobases perpendicular to the long axis of the DNA helix, in the manner of additional bases[121-123]. Therefore, we hypothesized that receptor forces should control both the orientation of the DNA tension probe and the orientation of the Cy3B fluorophore linked to that probe.

#### 3.3.2.1 MTMF Fluorescence Anisotropy Computational Model

To test this hypothesis, we developed a mathematical model to describe force-induced rearrangement of fluorophore orientation. The geometry of the probe and fluorophore are given in Figure 10. Receptor forces are specified by the angle $\Phi_{force}$, which describes rotations in the *xy* plane, and $\theta_{force}$, which describes a tilt of the force away from the *z*-axis. $\Phi_{force}$ and $\theta_{force}$ describe the reference frame of the Cy3B fluorophore after probe reorientation due to receptor force. The "tilted" reference frame for Cy3B is described by the coordinate system *pqr*. Note that the DNA probe can freely rotate about its long axis (defined by the orientation of *r*), thus the Cy3B fluorophore may explore all $\psi$ angles in reference frame *pqr*.

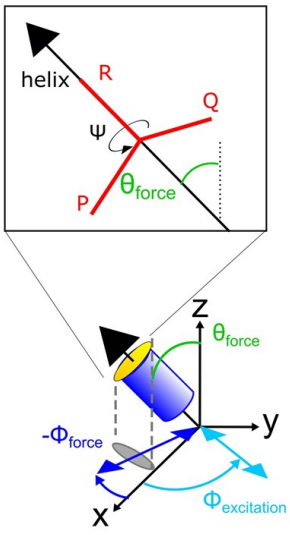


**Figure 10: Coordinate System for Force-Induced Reorientation of DNA Tension Probes**

Receptor forces reorient molecular tension probes. The cyanine fluorophore is depicted as a yellow disc because the probe can freely rotate along its long axis (rotation denoted by ψ in the inset). A receptor force specified by $\Phi_{force}$ and $\theta_{force}$ reorients the tension probe. The orientation of the fluorophore in its tilted reference frame (*pqr*) can be expressed in the microscope reference frame (*xyz*) by a series of rotations. Note that rotations in $\Phi_{force} = 0$ at the x axis a follow the right-hand rule, thus this figure depicts a negative $\Phi_{force}$ orientation (negative sign added to figure for clarity).

We express the orientation of the fluorophore (yellow disc, Figure 10) as a series of three rotations, given in equations 11, 12, and 13.

$$rotation\ 1 = \begin{bmatrix} \cos\phi_{force} & sin\phi_{force} & 0 \\ -sin\phi_{force} & cos\phi_{force} & 0 \\ 0 & 0 & 1 \end{bmatrix} \tag{11}$$

$$rotation\ 2 = \begin{bmatrix} \cos\theta_{force} & 0 & -sin\theta_{force} \\ 0 & 1 & 0 \\ sin\theta_{force} & 0 & cos\theta_{force} \end{bmatrix} \tag{12}$$

$$rotation\ 3 = \begin{bmatrix} \cos\psi & sin\psi & 0 \\ -sin\psi & cos\psi & 0 \\ 0 & 0 & 1 \end{bmatrix} \quad (13)$$

We will define the fluorophore TDM by the vector $\boldsymbol{\mu}$. To express the orientation of fluorophores in reference frame *pqr* ($\boldsymbol{\mu_{PQR}}$) in the microscope reference frame ($\boldsymbol{\mu_{XYZ}}$), one multiplies $\boldsymbol{\mu_{PQR}}$ with the transpose of these rotations as in Equation 14.

$$\boldsymbol{\mu_{XYZ}} = rotation\ 1' \times rotation\ 2' \times rotation\ 3' \times \boldsymbol{\mu_{PQR}} \quad (14)$$

In reference frame *pqr*, Cy3B has the excitation transition dipole moment given by Equation 15. Note that the principal component of Cy3B's excitation TDM within the *pq* plane was computed to reduce the computational complexity of the mode.

$$\boldsymbol{\mu_{PQR}} = a\,\hat{\boldsymbol{p}} + b\hat{\boldsymbol{q}} + c\hat{\boldsymbol{r}}, = \sqrt{12.25^2 + 2.56^2} = 12.51, b = 0, c = 0.08 \quad (15)$$

The values of the projection of Cy3B's TDM onto reference frame *pqr* (a, b, and c from Equation 15) were computed using Time-Dependent Density Functional Theory. The orbitals and excitation/emission dipoles of Cy3B are displayed in Figure 11. Notably, both excitation and emission TDMs are within the plane of the fluorophore. Because cyanine fluorophores stack with DNA in the manner of additional nucleobases[121-123], the TDM of Cy3B will always occupy a plane orthogonal to the orientation of applied receptor forces. This fixed relationship, where Cy3B is perpendicular to applied receptor forces, enables us to infer force orientation by determining the orientation of Cy3B fluorophores.

With Equations 14 and 15, we can compute the orientation of the Cy3B fluorophore disk in the *xyz* coordinate system given a specific set of $\theta_{force}$ and $\Phi_{force}$ using Equations 16, 17, and 18.

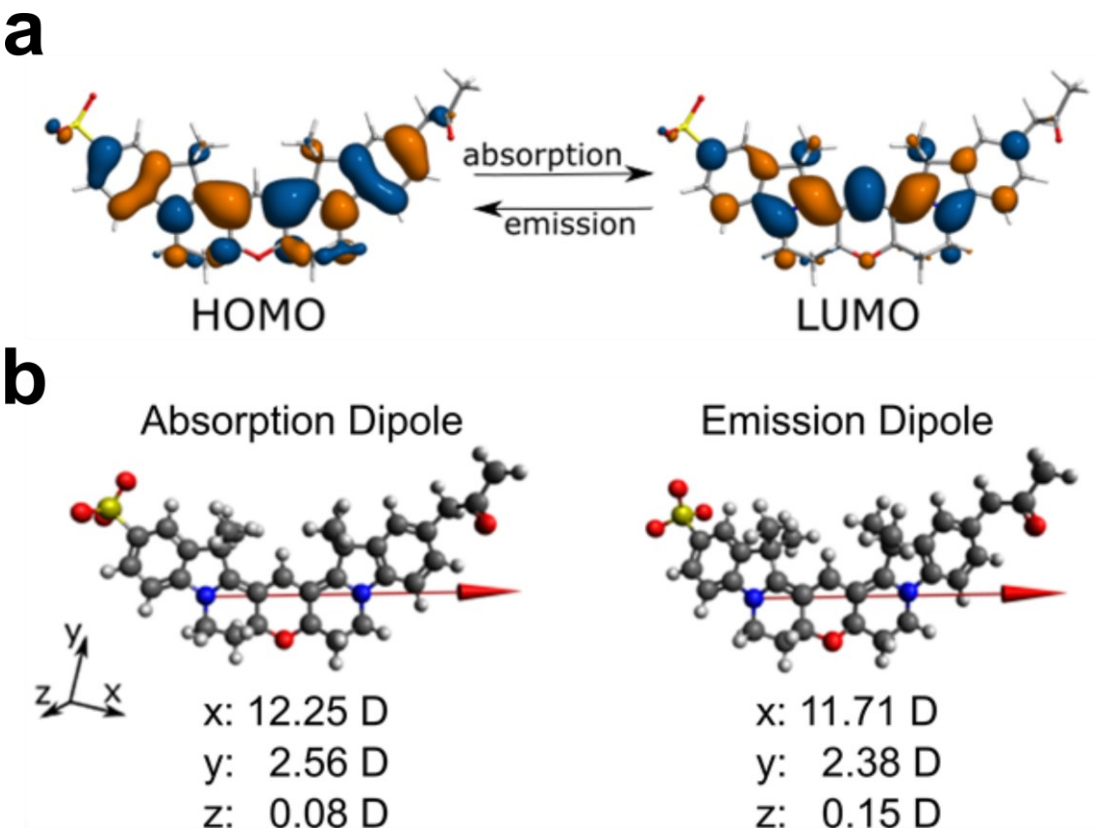


**Figure 11: Cy3B Transition Dipole Moment**

(**a**) We computed the molecular orbitals involved in the first absorption and emission excitation in Cy3B calculated using Time-Dependent Density Functional Theory (TDDFT) at the B3LYP/6-31G* level of theory. Orbitals are plotted using Visual Molecular Dynamics software package (VMD, version 1.9.1) with an isosurface contour value of 0.05. The ground state geometry of Cy3B optimized in water using the conductor-like-screening solvation model (COSMO) model in the ORCA software package (left) and the optimized excited state geometry of Cy3B (right) are both shown. (**b**) Optimized ground state geometry (left, $S_0$; Absorption Dipole) and excited state geometry (right, $S_1$; Emission Dipole, shown on the right) overlaid with the calculated absorption and emission dipoles (red arrows). The red arrows represent the TDM for absorption (left) and emission (right) respectively. Note that the absorption and emission dipoles are essentially parallel and that both lie in the plane of the cyanine fluorophore.

$$\begin{aligned}\mu_x = \; & csin\theta_{force}cos\phi_{force} \\ & - b\cos\psi sin\phi_{force} - bcos\theta_{force}cos\phi_{force}sin\psi \\ & - a\sin\psi sin\phi_{force} + acos\theta_{force}cos\psi cos\phi_{force}\end{aligned} \tag{16}$$

$$\begin{aligned}\mu_y = {} & acos\phi_{force}sin\psi + acos\theta_{force}cos\psi sin\phi_{force} + bcos\psi cos\phi_{force} \\ & - bcos\theta_{force}sin\psi sin\phi_{force} + csin\theta_{force}sin\phi_{force}\end{aligned} \tag{17}$$

$$\mu_z = ccos\theta_{force} - acos\psi sin\theta_{force} + bsin\theta_{force}sin\psi \tag{18}$$

Where a, b, and c are defined in Equation 15.

In emission resolved polarization experiments (light path depicted in Figure 8a) we will employ linearly polarized light (polarized along the x-axis). Therefore, the electric field vector describing the polarization of the excitation light ($\boldsymbol{E}$) is:

$$\boldsymbol{E} = 1\,\hat{\boldsymbol{x}} + 0\,\hat{\boldsymbol{y}} + 0\hat{\boldsymbol{z}} \tag{19}$$

The probability of exciting a fluorophore is defined as the square of the projection of the fluorophore vector onto the electric field vector. In this case, the excitation probability is:

$$P_{excitation} = (\mu_x)^2 \tag{20}$$

The probability of detecting a fluorophore is proportional to its squared projection along the detection axis multiplied by the excitation probability. In the calculation of these

probabilities, we rely on 3 assumptions: 1) each pixel contains multiple DNA force probes, 2) cyanine dyes conjugated to the end of dsDNA are known to stack perpendicular to the long axis of the dsDNA[121-123], and 3) our experimental exposure times are sufficiently long to allow rotational freedom of the force probe around the long axis of the probe. The fluorophores will therefore sample all Ψ in reference frame PQR, thus we integrate and average over all Ψ. The expected fluorescence intensities in the parallel ($I_x$) and perpendicular ($I_y$, $I_z$) channels are therefore:

$$I_x = \frac{1}{2\pi}\int_0^{2\pi} (\mu_X)^4 d\psi \tag{21}$$

$$I_y = \frac{1}{2\pi}\int_0^{2\pi} (\mu_x)^2 (\mu_y)^2 d\psi \tag{22}$$

$$I_z = \frac{1}{2\pi}\int_0^{2\pi} (\mu_x)^2 (\mu_z)^2 d\psi \tag{23}$$

With this mathematical framework in place, it is now possible to conduct and interpret emission resolved fluorescence polarization microscopy experiments.

### *3.3.3 Fluorescence Anisotropy Measurement of pN Force Orientation*

Fluorescence anisotropy (r) is defined as a phenomenon where light emitted by a fluorophore is not emitted equally along all axes. Anisotropy is defined as the difference between the fluorescence detected parallel and perpendicular to a light source, divided by the total observed fluorescence intensity. For excitation light polarized along the *x*-axis and

polarized excitation measured along the *x* and *y* axes, anisotropy is defined by Equation 24.

$$r = \frac{I_x - I_y}{I_x + I_y + I_z} \tag{24}$$

Fluorescence anisotropy generally measures the ratio of a fluorophore's fluorescence lifetime relative to its rotational correlation time ($\tau_c$). The rotational correlation time is the time required for a molecule to rotate 1 radian from its original orientation. One can relate fluorescence anisotropy to the rotational correlation time via the Perrin equation (Equation 25), where $r_0$ is the fluorophore's intrinsic anisotropy and $\tau$ is the fluorophore's fluorescence lifetime.

$$r(\tau) = \frac{r_0}{1 + \frac{\tau}{\tau_c}} \tag{25}$$

The rotational correlation time, $\tau_c$, can be computed from the Stokes-Einstein relationship (Equation 26), where $\eta$ is the solvent viscosity, $R_h$ is the hydrodynamic radius of the fluorophore, T is temperature, and k is boltzmann's constant.

$$\tau_c = \frac{\eta \frac{4}{3} \pi R_h^3}{kT} \tag{26}$$

The limiting anisotropy, $r_{0,}$ has a theoretical maximum of 0.4 if the excitation and emission TDMs are parallel. A fluorescence lifetime of 2.8 ns has been reported for Cy3B[124] and its rotational correlation time is likely on the order of 0.4-0.6 ns, similar to

that of Cy3[108]. With these assumptions, the anisotropy of free Cy3B in solution is expected to be ~0.05. We measured the anisotropy of Cy3B in solution as 0.057 (Figure 12a). Upon conjugation with a tension probe, the fluorescence anisotropy of Cy3B increased to 0.257, indicating that the rotation of Cy3B was restricted by associating with the much larger DNA helix (designated 0T probe in Figure 12). Importantly, increasing the rigidity of the linker via the addition of two additional thymine nucleobases between the terminus of the dsDNA helix and the Cy3B (2T probe) reduces the measured anisotropy to 0.191 (Figure 12a). This is counter-intuitive because increasing the molecular weight of the DNA via the addition of the two thymines would be expected to increase the rotational correlation time of the fluorophore-DNA conjugate, increasing the anisotropy. Instead the anisotropy decreased with the addition of two thymines. This decrease in anisotropy likely means that the 2T linker attenuated base stacking, decreasing the time the Cy3B spends stacked with the DNA duplex, resulting in a decrease in anisotropy. These data provide evidence that Cy3B, like Cy3 and Cy5, stacks with DNA helix.

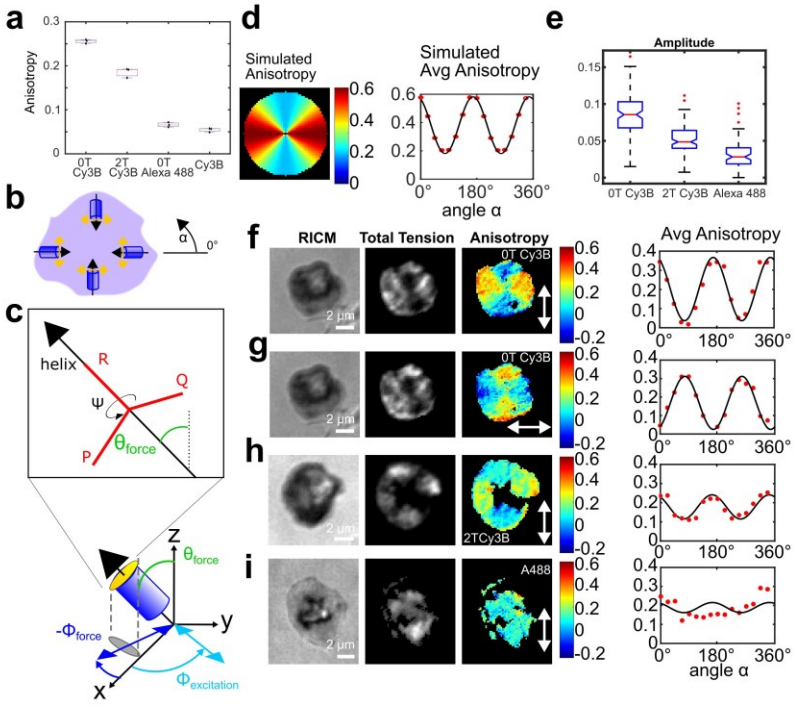


**Figure 12: Excitation Resolved Fluorescence Polarization Microscopy Measurements of DNA Tension Probes**

(**a**) Cy3B linked to the MFM probe via a 6-carbon linker (0T) exhibited increased fluorescence anisotropy (median 0.257) compared to soluble Cy3B (median 0.057). Adding 2 additional thymines (2T) to the linker reduced the anisotropy (median 0.191), despite the increased mass. Alexa 488, a hydrophilic dye not expected to stack with DNA, had low fluorescence anisotropy when linked to the MFM probe (median 0.066). All differences are statistically significant (2 tailed 2 sample t-test, $p< 0.05$). The red line indicates the median, black dots represent the sample means, 25/75% quartiles are indicated by the blue box, whiskers extend to 1.5 times the interquartile range. (**b**) Platelets are expected to be roughly contractile, orienting MFM probes centripetally. (**c**) Geometry of the anisotropy model (**d**) Modeling predicts a $\cos^2$ α pattern of anisotropy. (**e**) Measurements of platelets and the 0T Cy3B probe revealed an anisotropy pattern resembling a bowtie. Splitting the anisotropy into wedges (0° indicated in panel **b**) revealed the expected $\cos^2\alpha$ distribution. We measured the amplitude of the fitted $\cos^2$ angular anisotropy distributions for many platelets. The amplitude was attenuated for 2T and Alexa 488 tension probes compared to the 0T probe (0T, median 0.086, 107 platelets, $n$=4 independent experiments; 2T, median 0.049, 116 platelets, $n$=4 experiments; Alexa 488, median 0.028, 71 platelets, $n$=3 independent experiments). All differences are statistically significant (2 tailed 2 sample t-test allowing unequal variance on the amplitudes of individual platelets, $p<0.05$). Representative images of RICM, tension, and anisotropy for a platelet on (**f**) a 0T Cy3B DNA probe modified surface, (**g**) a 0T surface when the excitation polarization is

**Figure 12, continued:** rotated 90°, (**h**) 2T tension probe, and (**i**) Alexa 488 tension probes. White arrows indicates the excitation polarization and the plots depict the average anisotropy within 16 evenly spaced wedges rotating α degrees around the center of each of the 4 indicated platelets. All experiments were performed with the 4.7 pN hairpin.

#### 3.3.3.1 Anisotropy Experiments Confirm that Cellular Forces Reorient Tension Probes

We next sought to test our hypothesis that molecular forces would reorient DNA-based molecular tension probes. Using the mathematical framework established earlier, we modeled the expected anisotropy of an ensemble of tension probes that have been re-oriented by pN receptor forces. For fluorophores free in solution, fluorescence anisotropy is a measure of fluorophore mobility relative to its fluorescence lifetime; however, anisotropy may also be used to understand the orientation of confined fluorophores. If a fluorophore is physically constrained by association with a biomolecule, polarized excitation and fluorescence detection can provide information about biomolecule structure. For example, fluorescence anisotropy has been used to study the orientation of fluorophores embedded in cell membranes[113], GFP-tagged protein in the nuclear pore complex[109, 110], and septin during yeast budding[125, 126]. In the case of Cy3B conjugated to DNA tension probes, the Cy3B stacks with the DNA perpendicular to the long axis of the DNA. When receptor forces reorient the tension probe, the orientation of the Cy3B DNA is likewise changed (Figure 12c).

We therefore modeled the expected results of fluorescence anisotropy experiments conducted with molecular tension probes on a model contractile system. We chose to work initially with human platelets. Platelets are mechanosensitive and highly mechanically

active[5-7], additionally, the small size of platelets (2-5μm) makes them challenging targets for conventional force mapping techniques such as traction force microscopy and micropillar arrays. Finally, TFM and micropillar array measurements of platelet-generated force determined that platelets are generally contractile[3, 127], providing an excellent testbed for *in silico* modeling. We modeled platelet contraction *in silico* by computing the expected anisotropy for a circular array of tension probes, specifying that all forces are oriented towards the center of the cell (Figure 12b). We integrated equations 21, 22, and 23 in MATLAB for a simulated, inwardly contractile platelet with all possible values of $\theta_{force}$ (the *z*-orientation of receptor forces). For the image shown, $\theta_{force}$ was set to 40° (Figure 12d). These calculations enabled computation of the expected fluorescence intensities $I_x$, $I_y$, and $I_z$ for excitation light polarized along the *x* axis. We corrected for the effects of our high numerical aperture objective (1.49 NA, oil immersion objective, immersion oil refractive index n=1.515 and sample refractive index n=1.37) as previously described[113]. Following this high numerical aperture correction, anisotropy can be calculated as:

$$r = \frac{I_{x,calculated} - I_{y,calculated}}{I_{x,calculated} + 2I_{y,calculated}} \tag{27}$$

Note that only $I_x$ and $I_y$ are experimentally observed, so we make the assumption that fluorophore emission perpendicular to the excitation polarization is equal in *y* and *z* (i.e. $I_z = Iy$). The modeling predicted a "bowtie" shape of fluorescence anisotropy, where the anisotropy is high on the right and left side of the cell but low at the top and bottom of the cell (Figure 12d). To quantify the angular distribution of anisotropy, we divided the computed anisotropy into 16 evenly-spaced 22.5° wedges and plotted the average anisotropy as a function of angle, α, around the platelet. This analysis revealed that

anisotropy is predicted to vary spatially, taking the shape of $\cos^2\alpha$ (Figure 12d, $\alpha = 0°$ and angle of rotation indicated in Figure 12a).

Finally, we sought to experimentally validate the predictions of the fluorescence anisotropy model. Human platelets were seeded on a surface presenting cRGD-labeled DNA tension probes with a Cy3B fluorescence reporter. For the 0T tension probe with no nucleobases separating the Cy3B from the terminus of the top arm of the DNA tension probe (designated 0T in Figure 12), the platelet exhibits the expected bowtie pattern of fluorescence anisotropy (Figure 12f). Rotating the orientation of the excitation polarization by 90° rotates the observed fluorescence anisotropy pattern, confirming that the observed anisotropy pattern is dependent on the orientation of the excitation light (Figure 12g). When Cy3B-DNA stacking is reduced via the 2T tension probe, the anisotropy pattern is present, but the amplitude of the $\cos^2\alpha$ function is reduced, consistent with poor Cy3B-DNA stacking (Figure 12f). Finally, the anisotropy of Alexa488 conjugated DNA tension probes did not exhibit the bowtie pattern. Alexa488 is hydrophilic and not expected to stack with DNA. The amplitude of the $\cos^2\alpha$ "bowtie" pattern for many platelets was computed, revealing that the amplitude is consistently highest for the 0T probe. Together, these results support the hypothesis that DNA tension probes are reoriented by pN molecular forces, and that fluorescence polarization techniques provide a means to measure this force-induced DNA tension probe reorientation.

### 3.3.4 *Conceptual Framework for Quantifying Receptor Force Orientation Via Excitation Resolved FPM*

Fluorescence anisotropy measurements confirm the central hypothesis that pN receptor forces reorient tension probes. However, fluorescence anisotropy measurements provided only a whole-cell approximation of pN force orientations. To understand the role of pN force orientation in biological signaling, a technique to resolve the orientation of pN receptor forces with high spatial resolution is required.

Excitation resolved fluorescence polarization microscopy offers a route to determining the orientation of fluorophores. In excitation resolved FP, fluorescence is

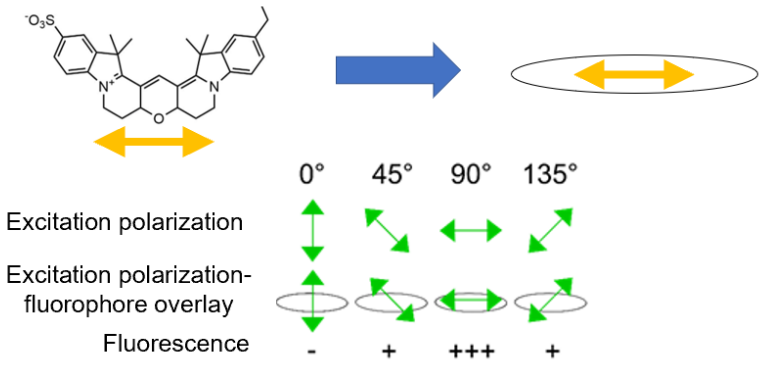


**Figure 13: Schematic Depiction of the Principal of Excitation Resolved FPM**

Fluorophores are excited preferentially by light polarized parallel to their excitation transition dipole moment (TDM). The fluorophore Cy3B is shown, with its excitation TDM schematically depicted as a double-headed yellow arrow. In later figures, we will consider an ensemble of fluorophores with an elliptical projection along the optical axis. The ensemble of fluorophore TDMs is represented here as an ellipse. When the excitation polarization of light is varied, the measured fluorescence varies. To determine the average orientation of the fluorophores (the long axis of the ellipse) one must simply find the excitation polarization that produces the greatest fluorescence.

quantified as a function of excitation polarization ($\Phi_{excitation}$). The concept of excitation resolved FPM is illustrated schematically in (Figure 13).

Excitation resolved FPM requires the addition of a rotatable half-wave plate into the path of a polarized excitation source. The light path used in the excitation resolved FPM experiments is depicted in Figure 8b. Excitation resolved FPM is able to measure fluorophore orientation because the probability of exciting a fluorophore depends on the alignment between the fluorophore orientation and $\Phi_{excitation}$ (Figure 13, Equation 28), where $p_{excitation}$ is the probability of exciting the fluorophore, A is a proportionality constant, and $\alpha$ is the angle between the excitation TDM of the fluorophore, $\boldsymbol{\mu}$, and the excitation polarization orientation, $\Phi_{excitation}$.

$$p_{excitation} = \mathrm{A}\cos^2(\alpha) \tag{28}$$

Conceptually, equation 28 means that the observed fluorescence will be high when $\Phi_{excitation}$ is well-aligned with $\boldsymbol{\mu}$, while very little fluorescence will be observed when $\Phi_{excitation}$ is perpendicular to $\boldsymbol{\mu}$.

### *3.3.5 Excitation Resolved FPM Measurements of Known Fluorophore Ensembles*

To confirm our ability to perform excitation resolved FPM, we measured the orientation of a known ensemble of fluorophores. The cyanine fluorophore 1, 1'-dioctadecyl-3, 3, 3', 3'-tetramethylindocarbocyanine (DiI) contains two, 18-carbon chains that insert into lipid bilayers, causing the fluorophore, and its TDM, to orient parallel to the lipid bilayer surface.

To produce a known ensemble of highly oriented DiI molecules, supported lipid bilayers (SLB) were coated onto 5 μm silica beads. Briefly, small unilamellar vesicles (SUV) with an average diameter of 100 nm were prepared by lipid extrusion. In brief, 4 mg $mL^{-1}$ of DOPC lipid was diluted in ~1mL chloroform in a round bottom flask and the chloroform was removed by rotary evaporation to form a thin lipid film. The lipid film was further dried under a stream of $N_2$ and then hydrated with 2 mL of 18MΩ nanopure water. To dissolve the lipid film, three freeze-thaw cycles were performed. The lipid solution was then repeatedly extruded (~10 times) through a 100 nm polycarbonate filter until the solution became clear. The extruded SUVs are stored at 4°C and used within 4-6 weeks. 100 μL of 1 mg $mL^{-1}$ 5 μm silica beads were mixed with 100 μl of 2 mg $mL^{-1}$ DOPC vesicles and equilibrated on a rocker for 15 min at room temperature. This procedure created a supported lipid bilayer (SLB) coating the bead surface. These beads were purified by 3 successive 5 min spins at 2000 RPM. After each spin, the supernatant was removed and replaced with 1 mL of 1x PBS. The SLB beads were incubated with 5 μM DiI for 15 minutes. The DiI loaded SLB beads were separated from free DiI via 3 successive 5 min spins at 2000 RPM. Once again, the supernatant was removed in between each spin and replaced with 1 mL of 1x PBS. Finally, SLB beads were placed in clean wells of a coverslip-bottom 96-well plate in 1x PBS. Because DiI orients parallel to the supported lipid bilayer, DiI-doped SLBs on silica beads produce an ensemble of DiI that are parallel to the surface of the 5 μm bead surface (Figure 14a).

We conducted emission resolved FP anisotropy experiments on the DiI-beads and observed a “bowtie” pattern of anisotropy (Figure 14b), which is consistent with

fluorophores that are arranged parallel to the surface of the bead (compare to Figure 12b, d).

Next, we performed excitation resolved FP experiments on the DiI beads using the optical path depicted in Figure 8b. Briefly, experiments were conducted on a Nikon Eclipse Ti microscope, operated by Nikon Elements software, with a Chroma quad cube and an RICM cube. A 150 mW OBIS 561 nm laser was used to illuminate the sample, operating at 3% power. The polarization of the laser was rotated via a 400-800 nm SM1-threaded mounted 1-inch achromatic half wave plate (Thorlabs) rotated via a motorized precision rotation stage (Thorlabs, PRM1Z8) and a k-cube brushed DC servo motor controller (Thorlabs, KDC101) to control the excitation polarization. The rotator was operated by the Kinesis software. Images were taken on a Hamamatsu ORCA-Flash4.0 v2 Digital CMOS (Product code: C11440-22CU). Images were collected with a 100x 1.49 NA CFI Apochromat TIRF series oil-immersion objective (Nikon Instruments). The exposure time for all imaging experiments was 50 ms. Nikon Elements "Fast Acquisition" was used to maximize the acquisition speed and eliminate any delay between frames. The lasers were operated in widefield mode, focused on the back focal plane and travelling along the optical axis. Prior to image acquisition, the half wave plate was set in motion. After the rotator reached its maximum velocity of 25°/s (corresponding to 50°/s of excitation polarization rotation), 73 fluorescence images were acquired continuously with a 50 ms exposure time. The entire image sequence required 3.6 seconds to complete. Each image corresponded to a change in excitation polarization of 2.5° of arc, centered around the target excitation angle (e.g. the polarizer rotated through an arc from -1.25°-1.25° during the 50 ms acquisition for the "0°" image.

Using this experimental design, the DiI Beads were illuminated with light with $\Phi_{excitation}$ ranging from 0° to 180°. Representative images of the fluorescence collected from the bead at $\Phi_{excitation}$ 0°, 45°, 90°, and 135° reveal notable changes in fluorescence intensity, where the edges of the beads that are parallel to $\Phi_{excitation}$ have the greatest fluorescence intensity (Figure 14c). Plotting the fluorescence intensity reveals a $\cos^2(\Phi_{excitation})$ dependence of intensity as a function of $\Phi_{excitation.}$ (Figure 14d) in accordance with the predictions of equation 28. The orientation of the ensemble of fluorophores within each pixel can be calculated by determining the value of $\Phi_{excitation}$ that produces the maximum fluorescence intensity, hereafter known as the azimuth (Figure 14d). When the azimuths for every pixel of this bead are plotted, the calculated fluorophore orientations are parallel to the bead's surface (Figure 14e) confirming our ability to measure known fluorophore ensembles with excitation resolved FPM.

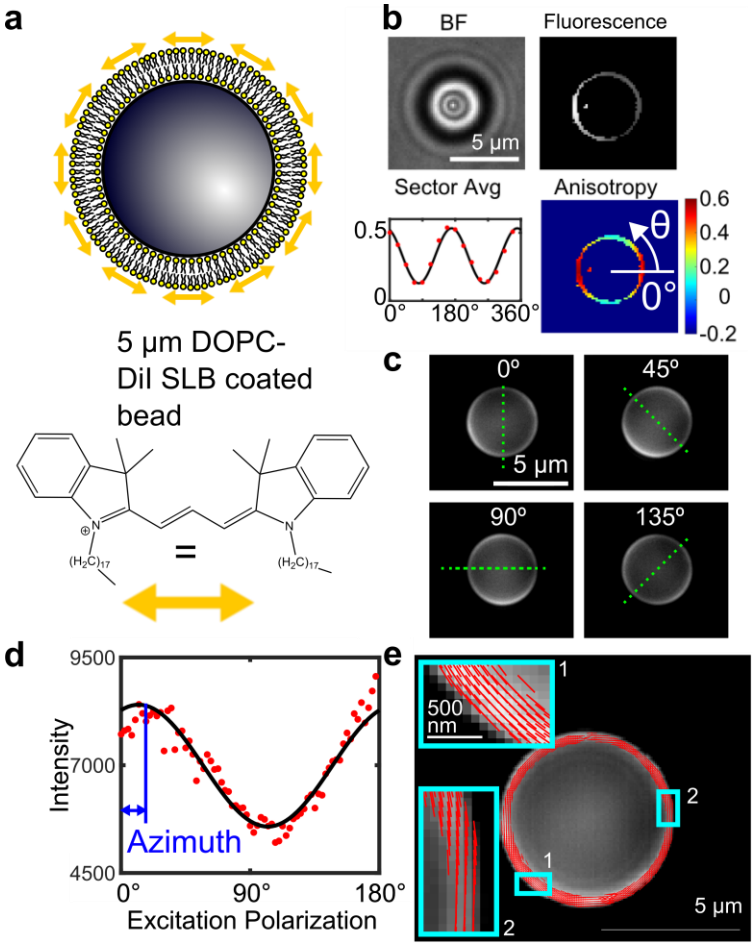


**Figure 14: Fluorescence Polarization Measurements of DiI Coated Beads**

(**a**) 5 µm silica beads were coated with 100% DOPC supported lipid bilayers (SLB) doped with DiI, a dye that inserts carbon tails into lipid membranes. The TDM of DiI is therefore parallel to the SLB/bead surface. (**b**) Fluorescence anisotropy measurements reveal a $\cos^2$ distribution consistent with TDMs aligned parallel to the bead surface. The anisotropy pattern is representative of 42 beads (from $n$=3 independent experiments). (**c**) Rotating the excitation polarization (green dashed line) results in observable fluorescence intensity changes. The DiI fluorescence is most intense on the edges of the bead that are parallel to the excitation polarization. (**d**) Plotting the fluorescence intensity of a pixel as a function of excitation polarization reveals a $\cos^2\theta$ distribution. The excitation polarization angle of the peak fluorescence, the azimuth, corresponds to the fluorophore TDM orientation in that pixel. (**e**) DiI azimuths are tangential to the surface of the bead as expected, demonstrating the accuracy of our optical system in measuring the orientation of fluorophores via excitation-resolved fluorescence polarization. The data shown is representative of 70 beads ($n$=3 independent experiments, 2 experiments were performed with the 73-image acquisition, one with a previously reported 4-point acquisition method).

### *3.3.6 Mathematical Framework for Measuring Molecular Force Orientation with Excitation Resolved FPM*

By taking a series of images of a sample with varying polarization angle ($\Phi_{excitation}$), we demonstrated the ability of excitation resolved FPM to measure the *xy* projection of fluorophore ensembles. How do we relate fluorophore orientation to force orientation? In the case of Cy3B coupled to DNA tension probes, Cy3B stacks perpendicular to the DNA long axis[121-123]. We define a unit helix vector, $\boldsymbol{h}$, which is the orientation of the long axis of the DNA helix, and parallel to the applied pN receptor force. The vector $\boldsymbol{h}$ is characterized by the azimuthal angle $\Phi_{force}$ and tilt angle $\theta_{force}$. The TDM of Cy3B, $\boldsymbol{\mu}$, is defined by its cone angle γ) relative to $\boldsymbol{h}$. The excitation probability of each fluorophore ($p_{exc}$) is dependent on the angle (α) between the excitation electric field vector $\boldsymbol{E}$ (which is specified by $\Phi_{excitation}$) and the transition dipole moment of the fluorophore, $\boldsymbol{\mu}$ (equation 28). We will only utilize Cy3B, and will employ a constant laser power for all experiments so we will define $\boldsymbol{E}$ and $\boldsymbol{\mu}$ as unit vectors. The probability of exciting a given Cy3B fluorophore is given as:

$$p_{exc,i} = \mathrm{A}\,(\boldsymbol{E}\cdot\boldsymbol{\mu_i})^2 \tag{29}$$

As discussed previously, the following analysis relies on three principles: 1) each pixel contains multiple open DNA force probes, 2) cyanine dyes conjugated to the end of dsDNA are known to stack perpendicular to the long axis of the dsDNA[121-123], and 3) our experimental exposure times are sufficiently long to allow rotational freedom of the force probe around the long axis of the probe. We therefore assume that observed intensity values are reflective of an ensemble average of all possible fluorophore orientations constituting

a disk perpendicular to DNA helix. Therefore, the intensity values will be related to the average $p_{exc}$ of all possible orientations. We call this average the proportion of successful excitation events ($P_{exc}$). We numerically approximated this value by simulating many (~100) fluorophores evenly distributed around the helix vector, **h.** These fluorophore dipoles ($\boldsymbol{\mu}_i$) were created using the rotations described in equations 11, 12, and 13, where Ψ varies to produce the distribution of dipoles. From this set of *n* fluorophore dipoles, $P_{exc}$ is approximated as the average:

$$P_{exc} = \frac{1}{n}\sum_{i=1}^{n} p_{exc,i} \tag{30}$$

Therefore, $P_{exc}$ varies with $\boldsymbol{h}$ and $\boldsymbol{E}$. Experimentally, we use plane polarized light propagating along the optical axis (*z* axis). $P_{exc}$ therefore depends on the interaction between the helix vector **h** and **E**. We assume that this interaction is fully characterized by the cone angle, γ (e.g. the angle between **μ** and **h**). We computed the TDM of Cy3B (Figure 11) and determined that both the absorption and emission TDM's lie in the plane of the molecule. Based on NMR and FRET evidence, cyanine dyes stack with DNA[6,7], thus the angle γ between the Cy3B transition dipole and the DNA helix long axis is expected to be 90°. The interaction is also characterized by the percentage of time the fluorophore is unstacked from the DNA force probe (c), which we estimate as 10% based on literature precedent[7]. Therefore:

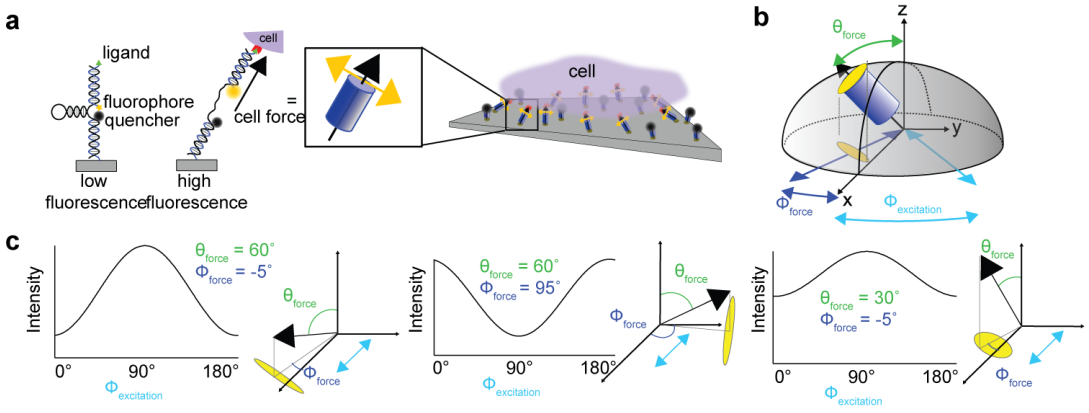


**Figure 15: Principle of Excitation Resolved FPM Measurement of Receptor Forces**

(**a**) Principle of molecular tension probes. Yellow arrows, fluorophore transition dipole moments; green triangles, RGD ligands; red polygon, integrin receptors. (**b**) Receptor forces dictate DNA probe orientation (gray hemisphere, possible orientations), fluorophore orientation, and the *XY* projection of Cy3B (yellow ellipse in the *XY* plane). (**c**) Hypothetical plots of the measured fluorescence intensity as a function of $\Phi_{excitation}$ for three force orientations. Maximum intensity occurs when $\Phi_{excitation}$ and the fluorophore *XY* projection (gray ellipse) align. Force *xy* orientation ($\Phi_{force}$) controls the phase of the observed sinusoid (compare $\Phi_{force} = -5°$ to $\Phi_{force} = 95°$), while force tilt angle ($\theta_{force}$) alters the amplitude of the sinusoid (compare $\theta_{force} = 60°$ to $\theta_{force} = 30°$). The cyan arrows depict $\Phi_{excitation} = 0°$.

$$P_{exc} = P_{exc}(\theta_{\text{force}}, \phi_{\text{force}}, \phi_{\text{excitation}}, \gamma = 90°, c) \tag{31}$$

Finally, we assume that $P_{exc}$ is linearly proportional to the observed intensity, meaning:

$$I = a\, P_{exc} \tag{32}$$

Where $I$ is the observed fluorescence intensity and $a$ is a proportionality constant. All subsequent measurements will rely on ratios between observed fluorescence intensities

(*I*), therefore we will disregard the proportionality constants *a* and *A* in equations 29 and 32.

Cy3B stacks with the DNA tension probe perpendicular to the helix axis, ***h*** (Figure 15a, b). Due to the rotatable bonds that anchor the DNA tension probe to the surface, the Cy3B TDM samples a disc of orientations (yellow disc, Figure 15b). The *xy* projection of the disc of Cy3B TDMs is an ellipse. When $\Phi_{force}$ changes, the ellipse rotates such that the long axis of this ellipse is perpendicular to the orientation of the receptor force (Figure 15c). Conversely, variations in $\theta_{force}$ change the ratio of the major and minor axes of the ellipse (Figure 15c). In the limiting case where $\theta_{force} = 0°$ (*z*-axis oriented forces), the *xy* projection of the fluorophores becomes a circle. Thus when $\theta_{force} = 0°$ the fluorophore is equally likely to be excited for all $\Phi_{excitation}$ values. In contrast, for a high aspect ratio ellipse (forces with large *xy* projections and $\theta_{force}$ ~90°) the probability of exciting the fluorophore is highly dependent on $\Phi_{excitation}$. As shown in Figure 15c, the excitation probability, and thus the intensity is minimized when $\Phi_{excitation} = \Phi_{force}$.

$$P_{exc,min} = P_{exc}(\theta_{\text{force}}, \phi_{\text{force}}, \phi_{\text{excitation}} = \phi_{\text{force}}, \gamma = 90°, c) \quad (33)$$

In contrast, the observed intensity is maximized when $\Phi_{excitation} = \Phi_{force} \pm 90°$.

$$P_{exc,max} = P_{exc}(\theta_{\text{force}}, \phi_{\text{force}}, \phi_{\text{excitation}} = \phi_{\text{force}} \pm 90°, \gamma = 90°, c) \quad (34)$$

Simulation of DNA force probes with $\Phi_{force}$=0°, $\gamma = 90°$, c=0.1, and varying $\theta_{force}$ confirms that $P_{exc,min}$ is dependent on $\theta_{force}$ while $P_{exc,max}$ is independent of $\theta_{force}$ (Figure 16d, e). Conceptually, this relationship can be understood by considering the elliptical *xy*

projection of the fluorophore TDM. When the $\theta_{force}$ is high the fluorophore TDM *xy* projection is highly elliptical thus the projection of the fluorophore TDM varies as a function of $\Phi_{excitation}$; in contrast, when $\theta_{force}$ is close to zero (*z*-oriented forces), the TDM *xy* projection is nearly circular, thus $P_{exc}$ is not very dependent on $\Phi_{excitation}$.

With this framework in place, it is relatively easy to determine the *xy* orientation of pN receptor forces. The *xy* orientation of receptor forces transmitted to the DNA tension

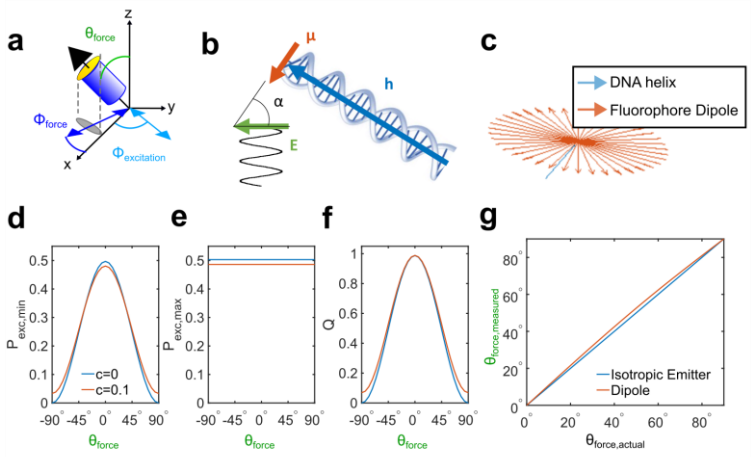


**Figure 16: Computing $\theta_{force}$ from Excitation Resolved Fluorescence Polarization Experiments**

(**a**) Coordinate system and (**b**) diagram of fluorescence excitation event. All vectors are given a magnitude of 1. The orange vector represents the transition dipole moment of the fluorophore. The green vector represents the electric field vector **E** of plane-polarized light used to excite the fluorophore. The blue vector represents the DNA helix vector **h**, which is equivalent to the force vector (shown in panel **a**) and is specified by $\theta_{force}$ and $\Phi_{force}$. (**c**) We generated a discrete approximation set of permissible fluorophore orientations when **μ** is stacked orthogonally to **h**. (**d**) We generated the minimum and maximum $P_{exc}$ value as a function of $\theta_{force}$ while holding $\Phi_{force}$ and $\Phi_{excitation}$ constant. The minimum excitation probability ($P_{exc,min}$) varies as a function of $\theta_{force}$. (**e**) The maximum excitation probability ($P_{exc,max}$) does not vary as a function of $\theta_{force}$. (**f**) The ratio Q ($P_{exc,max}$/ $P_{exc,min}$) is readily measured experimentally and varies as a function of tilt angle. (**g**) The assumption that fluorophores are isotropic emitters introduces no more than 2.5° error in the measured tilt angle ($\theta_{force,measured}$, elsewhere denoted as $\theta_{force}$).

probe ($\Phi_{force}$) can be found by measuring fluorescence intensity, I, as a function of $\Phi_{excitation}$ and fitting $\Phi_{force}$ in the expression:

$$I_{observed}(\phi_{excitation}) = amplitude * \cos^2(\phi_{excitation} - \phi_{force} + 90°) \quad (35)$$

Note that because the Cy3B TDM lies perpendicular to $\boldsymbol{h}$, $\Phi_{force}$ is offset 90° from the $\Phi_{excitation}$ that produces the maximum fluorescence. This relationship is depicted visually in Figure 15.

In order to determine the $z$ component of pN receptor forces transmitted to DNA tension probes, we derived a quantitative relationship between $\theta_{force}$, the ratio of $P_{exc,min}$, and $P_{exc,max}$. We define Q as the ratio between $I_{min}$ and $I_{max}$ observed for a specific pixel.

$$Q = \frac{I_{min}}{I_{max}} = \frac{a \cdot P_{exc,min}}{a \cdot P_{exc,max}} = \frac{P_{exc,min}}{P_{exc,max}} \quad (36)$$

Therefore, we can use the relationship described in equation 36 to fit experimental data into this model by taking the ratio of minimum and maximum intensity values from the fit sinusoid (equation 35). Plotting Q as a function of $\theta_{force}$ reveals that the relationship between $P_{exc,min}$ and $P_{exc,max}$ takes the form:

$$Q = (1 - b)\cos^2 \theta_{force} + b \quad (37)$$

where b is a ratio offset parameter, which accounts for the percentage of time that the dye spends stacked with the DNA. The ratio offset parameter b is the minimum possible value of Q, and varies with c and $\gamma$. The effect of $\gamma$ on $P_{exc}$ can be approximated numerically

by allowing the fluorophores to wobble off of the *pq* plane in fluorophore reference frame *pqr*. The effect of c is described by the following formula:

$$P_{exc} = P_{exc}^{0}(1 - c) + \frac{1}{3}c \tag{38}$$

where 1/3 is the excitation probability for a randomly oriented ensemble of fluorophores and $P_{exc}^{0}$ corresponds to the case where c=0.

$$P_{exc}^{0} = P_{exc}(\theta_{\text{force}}, \phi_{\text{force}}, \phi_{\text{excitation}}, \gamma, 0) \tag{39}$$

Using the above equation, b can be calculated by using an estimated value for c, $\theta_{force}$=90°, $\Phi_{force}$=0° and $\Phi_{excitation}$=[0°,90°].

$$b = \frac{P_{exc,min}}{P_{exc,max}} = \frac{P_{exc}(90°, 0°, 0°, \gamma, c)}{P_{exc}(90°, 0°, 90°, \gamma, c)} \tag{40}$$

When c is set to .10, γ=90°, we find that b=.069. This estimated value for the ratio offset parameter (b) was used in all subsequent measurements.

The ratio of the minimum to maximum fluorescence for a given pixel on a detector can be experimentally measured as $\Phi_{excitation}$ is varied. From Q, it is possible to calculate $\theta_{force}$. When equation 37 is solved for $\theta_{force}$, we derive the following relationship.

$$\theta_{\text{force}} = \cos^{-1}\sqrt{\frac{Q - b}{1 - b}} \tag{41}$$

Equation 41 allows us to experimentally estimate the average tilt angle of DNA force probes within each pixel. Note that this analysis restricts $\theta_{force}$ to a range of 0° to 90°, introducing a degeneracy into the calculation of $\theta_{force}$. However, the DNA probes are surface-immobilized, thus only tilt angles above the surface are experimentally relevant. Regardless, force measurements are still degenerate along the *xy* force axis. Excitation resolved FPM does not differentiate between "up and to the left" and "up and to the right," hence we will display forces as dipoles, not vectors in all subsequent analyses.

Finally, we make the simplifying assumption that fluorophores emit isotropically rather than as dipoles with $I \propto \cos^2(\delta)$ where δ is the angle between the emission direction and $\boldsymbol{\mu}$. To examine the consequences of this assumption, we simulated the expected intensity values where the collection efficiency varies as a function of tilt angle, and then used those intensity values with the above method to estimate the error that arises as a result of the simplifying assumption. Variations arise from: 1) the anisotropic emission pattern, in which different amounts of light emit towards the detector depending on the tilt angle of the fluorophore, and 2) the direction and polarization dependent reflection of emission light (calculated using the Fresnel equations) of a glass-water interface separating the fluorophore from the detector. The measured value of $\theta_{force}$ changes by a maximum of 2.5° due to the simplifying assumption (Figure 16g). Taken together, these results indicate that the isotropic emitter assumption is negligible for measuring $\theta_{force}$.

In summary, we have derived a means of measuring $\Phi_{force}$, the *xy* orientation of receptor forces, and $\theta_{force}$, the *z* orientation of receptor forces. Next, we will use this mathematical framework to measure the 3D orientation of receptor forces.

### *3.3.7 Molecular Force Microscopy Measurement of pN Receptor Force Orientation*

We first tested our ability to measure the orientation of traction forces generated by integrin $\alpha_{IIb}\beta_3$ in human platelets because their activation and clotting functions are mediated by mechanical forces[5-7]. Human platelets were seeded on a coverslip presenting the cRGD peptide (cyclo-Arg-Gly-Asp). The platelets produced robust tension signal within 10-15 minutes of seeding on the surface (Figure 17d). As with beads experiments, $\Phi_{excitation}$ was varied by rotating a $\lambda/2$-waveplate at 25°/s (corresponding to 50°/s rotation in $\Phi_{excitation}$) through 180° of arc. Fluorescence images were captured on a Hamamatsu Orca-Flash4.0 v2 Digital sCMOS with a 50ms exposure time. Platelet tension signal was imaged for $\Phi_{excitation}$ varying from 0° to 180°. Overlaying images of platelet tension signal captured with $\Phi_{excitation}$=0° and $\Phi_{excitation}$=90° reveal spatial differences in intensity due to force-induced reorientation of DNA tension probes. The intensity differences become particularly apparent in the green-magenta overlay, where green corresponds to the $\Phi_{excitation}$=0° image and magenta corresponds to the $\Phi_{excitation}$=90° image (Figure 17d). Extracting the raw intensity values from a single pixel (indicated by green arrow in Figure 17d), reveals the expected sinusoidal variation in tension signal fluorescence as $\Phi_{excitation}$ is varied (Figure 17e). The intensities were fit to a sinusoid (equation 35) in MATLAB via nonlinear curve fitting. The phase of this sinusoid specifies $\Phi_{force}$, while the amplitude of the sinusoid specifies $\theta_{force}$ (via equation 41). When this analysis is extended to every pixel with measurable tension signal on the detector, it is possible to calculate the *xy* and *z* orientation of pN receptor forces transmitted by the cell to the substrate. This data was rendered as an MFM map (Figure 17f).

In an MFM map (Figure 17f), 3D pN force orientation is rendered as colored bars. Forces are rendered as dipoles because excitation resolved FPM measures the axis of a fluorophore's excitation TDM, introducing degeneracy into the measurement of force orientation. The *xy* orientation of each dipole indicates the *xy* axis of receptor forces in

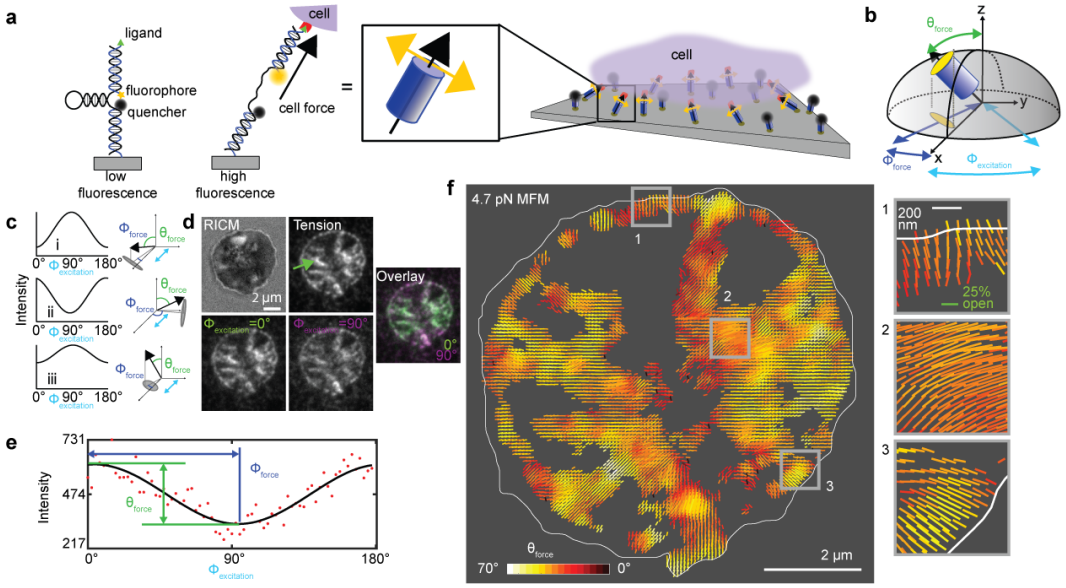


**Figure 17: Molecular Force Microscopy Map of Platelet pN Receptor Forces**

(**a**) Principle of molecular tension probes. Yellow arrows, fluorophore transition dipole moments; green triangles, RGD ligands; red polygon, integrin receptors. (**b**) Receptor forces dictate DNA probe orientation (gray hemisphere, possible orientations), fluorophore orientation, and the *xy* projection of Cy3B (yellow ellipse in the *xy* plane). (**c**) Hypothetical plots of fluorescence intensity as a function of $\Phi_{excitation}$ for three force orientations. Maximum intensity occurs when $\Phi_{excitation}$ and the fluorophore *xy* projection (gray ellipse) align. Force *xy* orientation controls the phase (i,ii), while tilt angle alters amplitude (i,iii). Cyan arrows indicate the orientation of $\Phi_{excitation} = 0°$. (**d**) Platelet RICM, 4.7-pN total tension, tension at $\Phi_{excitation} = 0°$ (green) and Φexcitation = 90° (magenta), and overlay. (**f**) Fluorescence intensity as a function of $\Phi_{excitation}$ (red dots) for a single pixel (green arrow in (**d**) and sinusoidal fit (solid line). The 3D force is described by the phase ($\theta_{force}$) and the amplitude ($\Phi_{force}$). (**f**) MFM map of platelet integrin forces. Dipole orientation corresponds to $\Phi_{force}$; color indicates $\theta_{force}$; length indicates percentage of open tension probes within each pixel. Gray background represents intensity below a threshold of signal-to-noise ratio <5. Representative of 79 MFM maps of platelets from $n = 5$ independent experiments.

that pixel on the detector, denoted $\Phi_{force}$ in this work. The color of each dipole indicates the *z* component of the pN receptor force, denoted $\theta_{force}$ in this work. Black and red dipoles indicate forces that are mostly out of the plane (*z* oriented forces, $\theta_{force}$ close to 0°), while yellow and white dipoles indicate forces with a significant *xy* component (Figure 17f). Finally, the length of the dipole represents the percentage of tension probes that are open within that pixel on the detector, with longer dipoles representing a larger number of tension probes experiencing $F>F_{1/2}$ within that pixel. We measured the probe density as 694±32 molecules/$\mu m^2$ (mean ± SEM), with an average of 3.4 probes/pixel (Table 4). $\theta_{force}$ and $\Phi_{force}$ thus represent the average receptor force orientation of the forces transmitted to many probes within each diffraction-limited area.

### *3.3.8 Quantifying the Accuracy of MFM*

We sought to determine the accuracy limitations of the MFM measurement via *in silico* modeling. We generated ensembles of fluorophores using the rotations defined in equations 11, 12, and 13 for every possible combination of $\Phi_{force}$ and $\Phi_{force}$. Photon noise and background signal arising from incompletely quenched tension probes were added to the calculated signal. The noise-added intensity values were subjected to the same curvefitting employed in experimental MFM analysis. The calculated force orientations were then compared to the ground truth. The average errors in $\Phi_{force}$ and $\theta_{force}$ measurements are displayed in Figure 18 for a Monte Carlo simulation of MFM force

recovery for noise-added data. This *in silico* modeling showed that the accuracy of MFM depends on the signal brightness and on $\theta_{force}$. Higher signal to noise ratio (increased

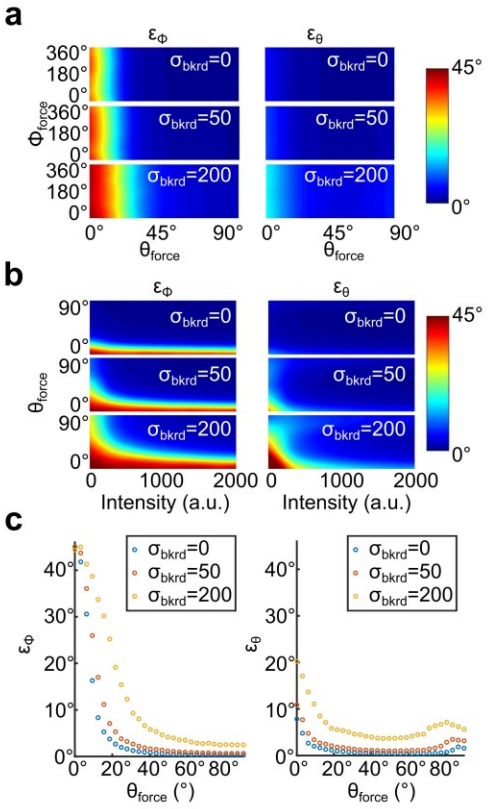


**Figure 18: *In Silico* Modeling of MFM Accuracy**

Error due to noise was estimated using a Monte Carlo method. Expected intensity values for 72 evenly spaced $\Phi_{excitation}$ values between 0 and 180° for a given helix orientation were generated. Normally distributed background noise and photon noise $\sigma_{pho}=\sqrt{I}$ were added to each measurement. $\theta_{force}$ and $\Phi_{force}$ were estimated using the noise-added intensity values and the method described in this work. The errors in $\theta_{force}$ and $\Phi_{force}$, denoted $\varepsilon_\theta$ and $\varepsilon_\Phi$, respectively, were calculated as the absolute difference between the true values and the calculated values of $\theta_{force}$ and $\Phi_{force}$. When calculating photon noise, we assumed that one photon produced one count on the detector. This process was repeated 100 times for a given orientation, and the average error was calculated. $\varepsilon_\theta$ and $\varepsilon_\Phi$ are displayed as heat maps. (**a**) Error depends on $\theta_{force}$, but not on $\Phi_{force}$ for all three levels of background noise tested. (**b**) $\varepsilon_\Phi$ is high for small tilt angles and poor signal to noise ratios. $\theta_{force}$ is overestimated for poor signal to noise ratios and low values of $\theta_{force}$. (**c**) Cross sections across the heatmaps in **b** at a simulated intensity of 1000 a.u. enable easy visualization of the dependence of $\varepsilon_\theta$ and $\varepsilon_\Phi$ on $\theta_{force}$ and signal to noise ratio.

signal fluorescence intensity) and high $\theta_{force}$ (lateral forces) lead to more accurate force recovery. This trend makes intuitive sense. MFM relies on fitting the phase and amplitude of fluorescence intensity as a function of $\Phi_{excitation}$. Noisy signal decreases the ability of MFM to accurately fit forces. Similarly, as $\theta_{force}$ approaches 0° (*z*-oriented forces) the amplitude of the sinusoidal variation in fluorescence is dampened and becomes harder to detect. As a side effect of this decreased amplitude in fluorescence variation, accurate $\Phi_{force}$ measurement becomes difficult for forces mostly oriented along the *z*-axis. Figure 18c depicts the dependence of accurate $\Phi_{force}$ recovery as a function of $\theta_{force}$. In general, we report force orientations with an error <15° for $\theta_{force}$ and <10° for $\Phi_{force,}$ except for vertical forces ($\theta_{force}$<10°), where MFM less accurately measures $\Phi_{force}$.

The measurement of the parameters $\theta_{force}$ and $\Phi_{force}$ is affected by ensemble averaging of the fluorescence of many fluorophores within each diffraction limited region. It is possible that there may be some variability in the pN receptor forces transmitted to probes within a pixel on the detector. It does not seem likely that these probe-to-probe variations will be large, because spatially adjacent probes are likely coupled to similarly oriented cytoskeletal elements. When the $\theta_{force}$ for two probes within a diffraction-limited area varies, MFM will report an intermediate value near the average of the two $\theta_{force}$ values without affecting the reported $\Phi_{force}$ (Figure 19a). Mathematically, this result occurs because varying $\theta_{force}$ leads to the summation of two sinusoids with identical phase but differing amplitude. However, if the $\Phi_{force}$ for two probes within a diffraction-limited area varies, then MFM will accurately report the average $\Phi_{force}$ but will underestimate the value of $\theta_{force}$ (Figure 19). This underestimation is due to the summation of two sinusoids with differing phase but identical amplitudes. Therefore,

ensemble averaging will tend to lead to underestimation of $\theta_{force}$. Given the spatial resolution of MFM, large variations in $\theta_{force}$ and $\Phi_{force}$ are unlikely since colocalized receptors are likely coupled to the same actomyosin force generating machinery.

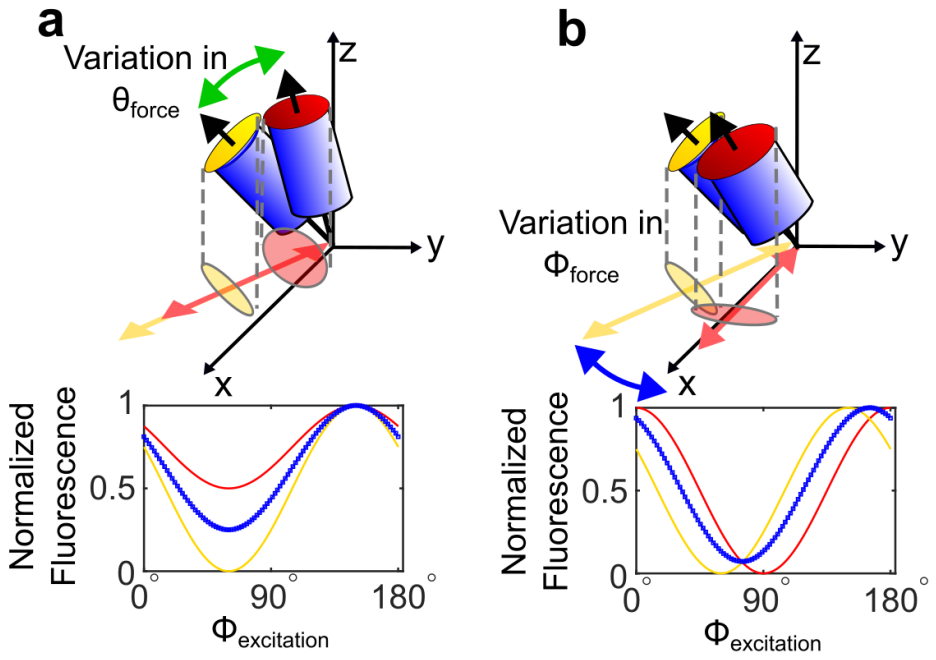


**Figure 19: Qualitative Effects of Probe Orientation Variability**

(**a**) Schematic representation of two hairpins that differ in the Z component of the cellular force (indicated by the green double-headed arrow). Fluorophore orientations are rendered as colored discs while the XY projection of each disk is rendered as a translucent ellipse in the XY plane. The red and yellow hairpins produce the red and yellow fluorescence intensity curves as a function of $\Phi_{excitation}$. Adding the fluorescence intensity curves and renormalizing to the new maximum intensity reveals the resultant sinusoid (blue boxes). For the case where the red and yellow hairpins differ in the force Z-component, the measurement of $\Phi_{force}$ is not altered; however, ensemble averaging does produce an intermediate amplitude sinusoid (blue boxes). (**e**) Schematic representation of two hairpins that differ in the XY orientation of applied receptor force (indicated by the blue double-headed arrow). Adding these curves produces a new sinusoid with phase ($\Phi_{force}$) that is the average of the phases of the component sinusoids. The amplitude of the resultant sinusoid is also reduced, causing underestimation of the tilt angle ($\theta_{force}$)

### *3.3.9 Detection of a Force Axis in Human Platelet Traction Forces*

Having empirically demonstrated the ability of MFM to accurately measure the orientation of pN receptor forces, we sought to understand the receptor forces of two biological testbeds: human platelets and fibroblasts.

Previous TFM measurements of platelet integrin forces suggested that platelets, unlike many cell types, contract isotropically[127]. Upon close inspection of the platelet MFM

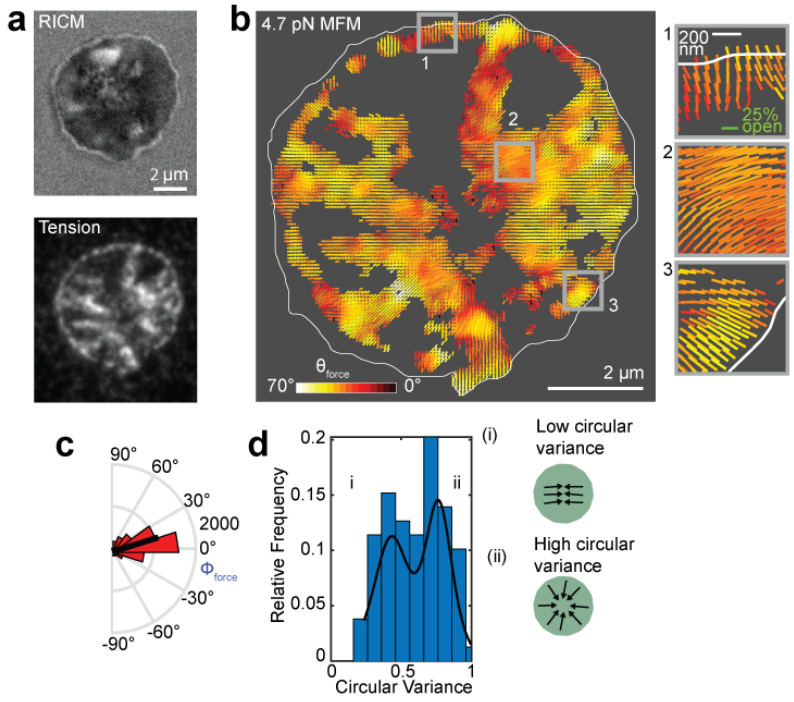


**Figure 20: A Subset of Platelets Contract Along an Axis**

(**a**) Platelet-surface contact area (RICM), 4.7pN tension signal, and (**b**) MFM map of platelet integrin forces. (**c**) Radial histogram (rose plot) of the *xy* orientation of all forces in each pixel from the MFM map in panel **b**. This platelet exhibits contraction along the left-right axis. The thick black bar indicates the intensity-weighted average orientation of platelets, indicating that this platelet is exerting forces primarily along an axis oriented at ~15°. (**d**) Histogram of the circular variance of 79 platelets from *n* = 3 independent experiments reveal two populations, a low circular variance population (contraction along an axis), and a high circular variance population (isotropic contraction).

map, platelet forces seemed to be preferentially aligned along an axis. We produced a radial histogram (rose plot) of the orientation of platelet *xy* forces and found that this platelet


**Figure 21: Platelet *xy* Force Distributions Indicate Two Patterns of Platelet Traction Forces**

Sample radial histograms of platelet XY force axes (a random subset of the 79 analyzed platelets from *n*=5 independent experiments) reveal two populations. We quantify these populations by calculating the circular variance of platelet XY forces. (**a**) In low circular variance platelets (variance < 0.65 based on the bimodal distribution from Figure 20 XY forces are concentrated in a few bins within the rose plots. (**b**) In high circular variance platelets (variance > 0.65), XY forces appear more uniformly distributed.

contracts along an axis (Figure 20c). We extended this analysis to 79 platelets, and identified a subset of platelets that exhibit contraction along a force axis (Figure 21).

To quantify this distribution of platelet integrin forces, we calculated the circular variance (a method of quantifying the variability of data sets in polar coordinates) for 79 platelets from 5 independent experiments. High circular variance corresponds to forces that are relatively uniformly distributed radially (Figure 20d-ii), while low circular variance corresponds to platelets that exhibit anisotropic contraction along an axis (Figure 20d-i). We fit the distribution of platelet circular variance to a bimodal distribution (Figure 20d). Based on this bimodal distribution, we defined a circular variance cutoff of 0.65 to differentiate isotropic contraction from anisotropic contraction. Examples of rose plots from isotropically contractile and anisotropically contractile platelets are provided in Figure 21.

Further inspection of the MFM map suggested that the anisotropic contraction may be due to the tension near the middle of the cell. The forces measured at the lamellipodial edge of the cell appeared to be oriented towards the cell center. To test this hypothesis, we produced a binary mask of the platelet based on applying a Chan-Vese edge finding algorithm[128] to the platelet RICM footprint. A binary mask was generated based on the identified edges of the platelet (Figure 22a-c). The platelet was then segmented into the set of all pixels within 7 pixels of the edge, and the central region (Figure 22d, e).

The force orientations within the “ring” region and “center” region were then compared to a field of dipoles oriented toward the centroid of the platelet. The deviation of the ring and center regions for this platelet are shown in Figure 22f. The ring region median deviation was 10.7°, compared to 16.25° for the central region for the platelet shown in this figure. This analysis was extended to 79 platelets, and the median ring deviation was shown to be 16° relative to a median deviation of 21.3° for the center. The data were

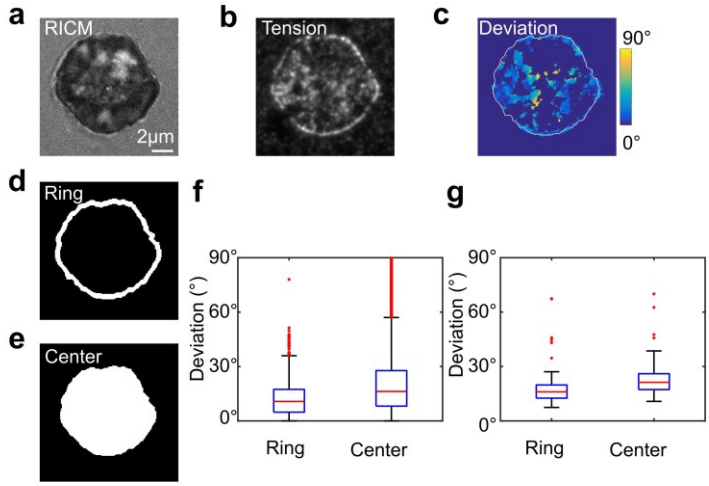


**Figure 22: Identification of Two Spatially Distinct Regions of Platelet Forces**

(**a**) RICM and (**b**) 4.7 pN tension signal for a representative human platelet. (**c**) The angle between the measured force orientation and a vector oriented towards the cell's centroid was computed and displayed as a heatmap. To quantify the behavior of the contractile ring compared to the interior tension signal, masks were generated from the RICM image via a Chan-Vese edge finding algorithm. (**d**) Masks were generated of the outermost 7 pixels, the "Ring" and (**e**) the "Center" regions of each platelet. (**f**) The deviation from isotropic force alignment within the center and ring of the platelet shown above were quantified. The ring median deviation is 10.7° deviation with 1057 pixels analyzed. Center median deviation is 16.25° with 3035 pixels analyzed. The red line indicates the median, quartiles are indicated by the blue box, whiskers extend to 1.5 times the interquartile range, and the red dots indicate outliers. Note that adjacent pixels are not independent measurements, thus statistical tests were not employed here. (**g**) The average deviation from isotropic force alignment was quantified for all platelets, revealing that platelet traction force alignment is different in the center compared to the exterior ring (the average center and ring deviation from isotropic force alignment of 79 platelets from $n$=5 experiments were pooled for a paired t-test, $p=2.2\times10^{-8}$, 95% confidence interval -6.6° to -3.4°). Ring median deviation is 16.0°. Center median deviation is 21.3°. The red line indicates the median, quartiles are indicated by the blue box, whiskers extend to 1.5 times the interquartile range, and the red dots indicate outliers.

subjected to a paired t-test and found to be statistically significantly different. This analysis supports the hypothesis that the tension at the lamellipodial edge is more centripetally oriented than the tension within the platelet center.

We sought a biological context for this observation. To understand the platelet cytoskeleton responsible for this force pattern, we stained for F-actin with Alexa 647-labeled phalloidin, and stained for microtubules with an Alexa 488-labeled anti-α-tubulin antibody. We observed a peripheral rim of actin, along with an inner mass of cortical actin (Figure 23). We also observed a coiled tubulin architecture (Figure 23). Integrin tension seems to be colocalized primarily with the actin cytoskeleton of the platelet.

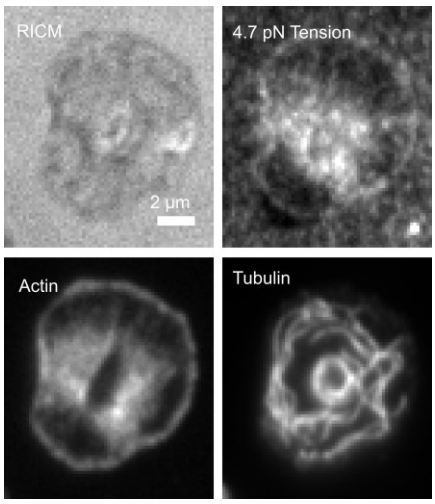


**Figure 23: Platelet Actin and Tubulin Immunostaining**

Platelets were fixed and stained for actin and tubulin. Tension (measured before fixation) colocalized with actin and anti-localized with tubulin. Platelet tension was imaged in conjunction with actin in *n*=2 independent experiments. Platelet actin and tubulin were co-stained in *n*=3 independent experiments. Platelet tension, actin, and tubulin (shown here) were simultaneously imaged in 52 platelets (from one experiment).

### *3.3.10 MFM Measurement of Platelet Aggregate Forces*

Many biological processes require mechanical coordination between cells, including collective cell migration[129], cancer invasion[130], and clot retraction[2, 4]. Because TFM relies on measuring substrate deformation to measure cellular forces, it is challenging for TFM to resolve traction forces exerted by multicellular aggregates[131]. In dense cellular aggregates, it becomes difficult to assign specific traction stresses to specific cells because all cells are jointly deforming the gel. In MFM, however, all tension probes independently report receptor forces, enabling measurement of receptor forces with diffraction-limited resolution. To demonstrate this capability, small platelet aggregates were created by suspending platelets in 1x Tyrodes buffer (pH 7.4) supplemented with 0.1% BSA w/v, Hank's Balanced Salt Solution, 2 mM $MgCl_2$, 1 mM $CaCl_2$, 1 unit/μL thrombin, and 10 μg/μL fibrinogen immediately prior to imaging. This mixture was inverted 3 times and immediately pipetted into one well of a microchannel formed from an Ibidi μ-slide VI$^{0.4}$

and a 25 mm x 75 mm glass coverslip. Platelet aggregates were observed on the surface within 5-10 min. The platelet aggregates were subjected to MFM analysis (Figure 24).

We determined that the average force axes of the constituent platelets did not appear to be ordered across platelet aggregates (6 aggregates with >5 cells from *n*=3 independent experiments). Additionally, force orientations were not aligned in 38% (12/31) of platelet-platelet boundaries, further indicating that platelet forces are not necessarily coordinated within a clot. These findings, combined with the observation that platelet contraction increases with microenvironment stiffness[5], could contribute to understanding the characteristic anisotropy and spatial heterogeneity of clot structure and mechanics[132].

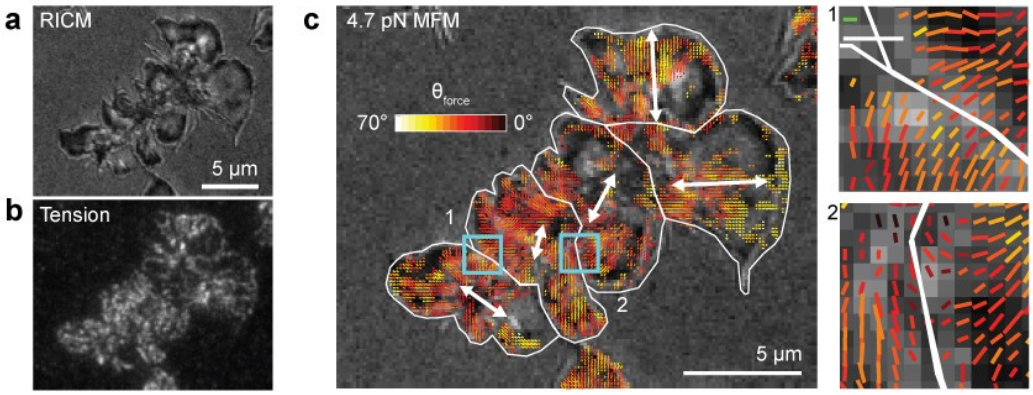


**Figure 24: Multicellular MFM of Platelet Aggregates**

(**a**) RICM, (**b**) 4.7 pN tension, and (**c**) MFM image of a platelet aggregate comprised of five cells. The MFM image was overlaid onto the RICM, and white dipoles indicate average force orientation of individual platelets within the aggregate. The average force axes (white arrows) appear disordered (z=0.225, p=0.813, Rayleigh test for uniformity). ROI 1 and 2 (represented on full MFM map by cyan boxes) show zoom-ins at the boundaries between platelets in the aggregate (green scale bar 10% open; white scale bar 500 nm). In total, 6 platelet aggregate MFM maps were produced from *n* = 3 independent experiments.

### *3.3.11 Mapping Fibroblast Focal Adhesion Forces with MFM*

To demonstrate that MFM is biologically general, we mapped the orientation of integrin forces in NIH-3T3 fibroblasts. Fibroblasts adhere through integrin-based focal adhesions (FAs), which physically bridge the cytoskeleton with the extracellular matrix. Fibroblasts stably expressing GFP-paxillin were plated on the tension probes and imaged, generating an MFM map (Figure 25a-c).

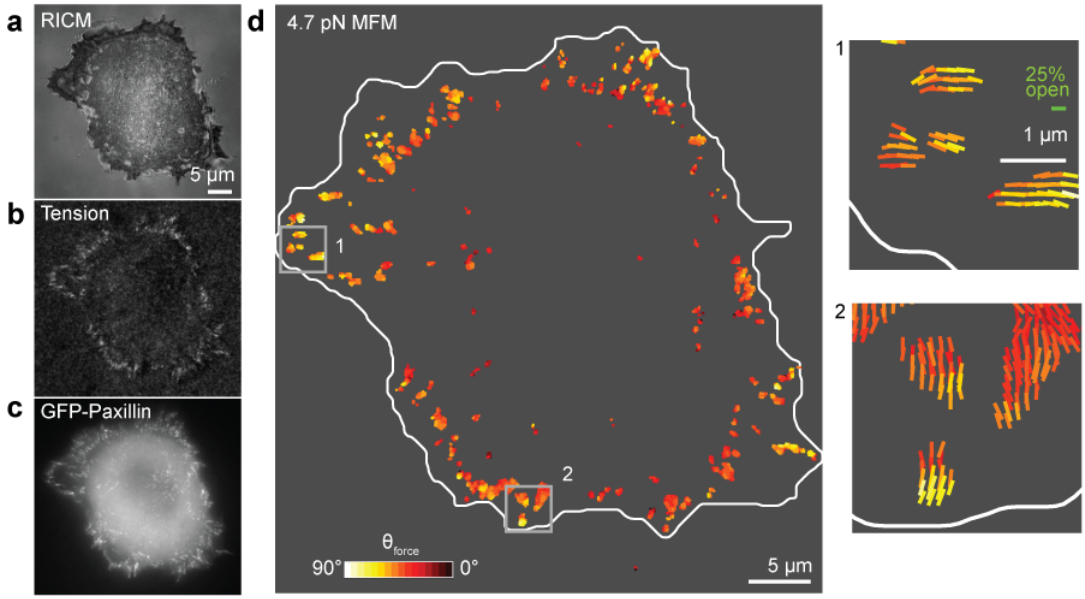


**Figure 25: Fibroblast MFM Map**

(**a**) RICM, (**b**) 4.7 pN tension, (**c**) GFP-Paxillin, and (**g**) MFM map of fibroblast seeded on a tension probe substrate for 30 min. The grey background in the MFM image represents pixels below an intensity threshold where the signal-noise ratio < 5. ROI 1 and 2 show zoom-in to highlight the organization of integrin forces with FAs. 37 fibroblast MFM maps from *n*=3 independent experiments.

To more deeply understand focal adhesion forces, we manually selected 494 focal adhesions from 15 cells (sourced from 3 experiments). At this early stage of fibroblast spreading, focal adhesion forces were generally aligned towards the centroid of the cell

(Figure 26a). Additionally, we calculated the circular variance of the $\Phi_{force}$ values within focal adhesions, and found little variation within each focal adhesion. There was also only 1.5° of variation in average $\theta_{force}$ values between the proximal and distal halves of these focal adhesions. Taken together, these data suggest that integrin forces within focal adhesions are very coherent and highly aligned both in plane, and normal to the substrate (Figure 26).

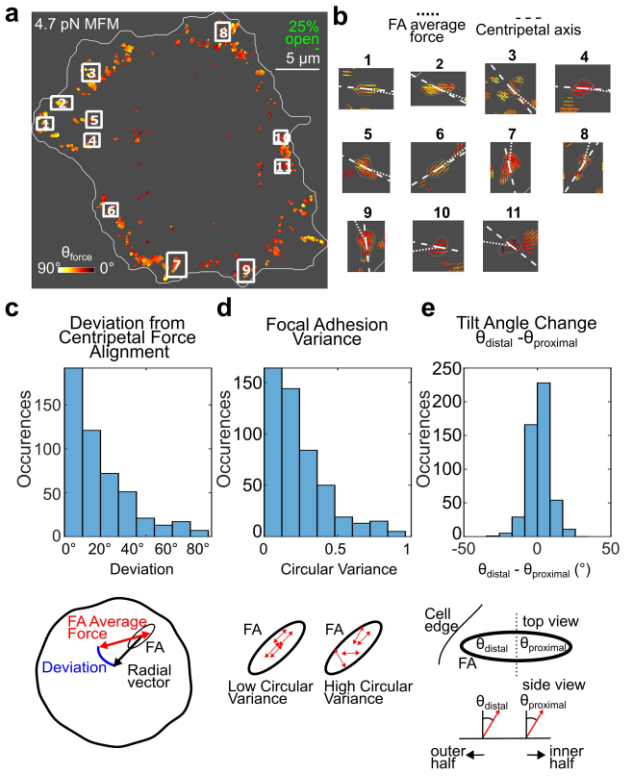


**Figure 26: Detailed Focal Adhesion Force Analysis**

(**a**) We identified focal adhesions (FA) by segmenting the 3T3 cell tension images. 494 focal adhesions were identified from 15 single fibroblasts entirely contained within the image frame (*n*=3 experiments). (**b**) For each FA, we measured the average force axis and calculated an axis oriented from the FA centroid to the centroid of the cell (the centripetal axis). (**c**) For individual FAs, the deviation between the average FA force axis and the centripetal axis was only 21.3° and the distribution was heavily biased towards 0° deviation, indicating general force alignment along axes oriented towards the cell center. (**d**) The circular variance for individual FA's was low (average circular variance of 0.236), indicating coherent force alignment. (**e**) We measured the difference between the distal and proximal halves of FAs and found this difference was small (1.5°), suggesting that integrin forces FA forces are tightly organized.

Finally, we compared integrin MFM maps for platelets and fibroblasts. We found that the average $\theta_{force}$ value was similar at 40° ± 2° for platelets and 39 ° ± 4° for fibroblasts (Figure 27a, data quoted as mean ± s.d.). However, fibroblast forces are more spatially variant, exhibiting more *z*-oriented forces near the cell center (median central $\theta_{force}$ of 30°) but become more lateral near the cell periphery (median peripheral $\theta_{force}$ of 42°). In contrast,

platelets exhibit less variation in $\theta_{force}$ values, with a median central $\theta_{force}$ of 35° and median peripheral $\theta_{force}$ of 40° (Figure 27b).

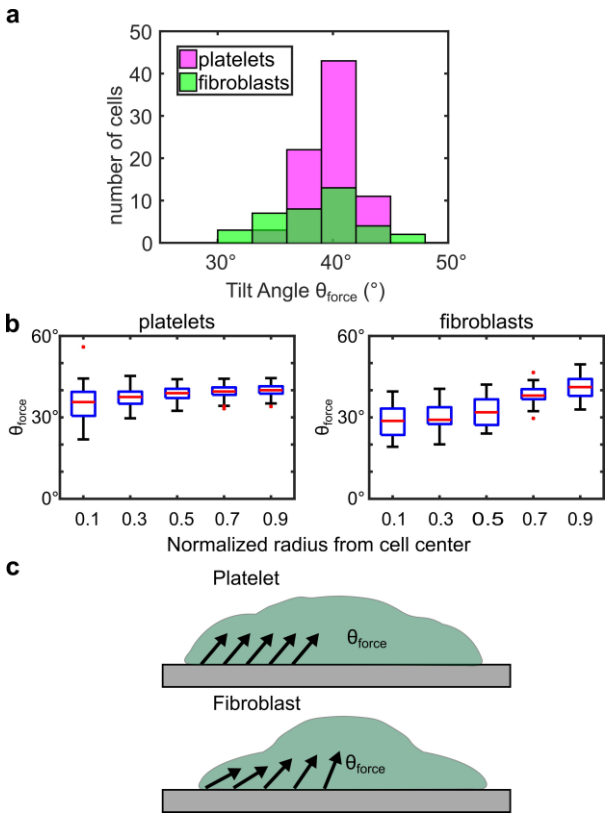


**Figure 27: Comparison of Fibroblast and Platelet Normal Forces**

(**a**) Histograms of pixel-by-pixel tilt angles observed in platelets and fibroblasts reveal similar whole cell mean tilt angles: platelets, 40°±2°; fibroblasts, 39°±4° (mean ± standard deviation). The means are not significantly different (2 tailed 2 sample t-test allowing unequal variance, p=0.09, 79 platelets from *n*=5 experiments; 37 fibroblasts from *n*=3 experiments). (**b**) Box plot displaying the average tilt angle of all pixels within the specified radius from the cell center for fibroblasts and platelets. Platelet tilt angle varies little from the cell center (median 34.7°) to the cell edge (median 39.9°) while fibroblast tilt angles increase from the cell center (median 28.7°) compared to at the cell edge (median 41.3°). A one-way ANOVA was used to test the significance in the variation of $\theta_{force}$ as a function of normalized radius. Both platelet and fibroblast $\theta_{force}$ variation are significant (platelet, $p=5x10^{-19}$, F=25.86; fibroblast, $p=3.2x10^{-7}$, F=12.25) (**c**) Scheme depicting the tilt angle trends.

## 3.4 Discussion

Molecular tension probes enable measurement of pN receptor forces with up to 250 nm spatial resolution[22]. This resolution compares favorably with the nN force sensitivity and ~1 μm spatial resolution of TFM[133, 134]; however, TFM is capable of measuring the orientation of traction forces while molecular tension sensors report only tension magnitude[20]. With MFM, this limitation of molecular tension probes has been removed[67]. MFM may still have room to improve. Unlike TFM, the current implementation of MFM only resolves the axis of receptor forces. Our lab recently published a FP technique, Variable Incidence Angle Linear Dichroism (VALiD), that is capable of measuring the orientation of fluorophores without degeneracy[135]. Combining VALiD with MFM could provide the means to uniquely identify force orientation, not the force axes reported via MFM. This advancement could be exciting, as it is possible that there may be small outward forces at the edge of spreading cells, forces that could be masked by larger contractile forces in TFM measurements.

The observation of an axis of anisotropic contraction in platelets is an excellent demonstration of the power of MFM to make biological measurements. Platelet integrin forces have been previously measured via TFM; however, with the lower spatial resolution of TFM platelets appeared to be isotropically contractile[127]. MFM reveals a more nuanced phenotype, the "ring" of tension at the platelet edge exhibits more-or-less isotropic forces, but the forces at the center of the cell are anisotropic in about half of the platelets measured. In this work, we categorized platelets as isotropically contractile or anisotropically contractile based on the circular variance of the observed *xy* force orientations. At this point, it is unclear whether these two populations are due to platelet heterogeneity or due

to the dynamics of platelet force evolution during activation and spreading. Timelapse imaging of platelet forces during spreading could clarify this issue in the future.

Physiologically, platelets adhere to sites of injury and must withstand the shear stress exerted by the flow of blood. The experiments conducted in this work were conducted under static conditions. Accordingly, the platelet forces observed here may not necessarily be representative of platelet forces *in vivo*. Future work could incorporate fluid flow into MFM experiments to determine how flow affects platelet force generation. It may be necessary to modify the experimental setup to include von Willebrand Factor to enable platelets to adhere under flow[136]. A recent TFM study of platelet forces under flow suggested that platelets may primarily contract in the direction perpendicular to the flow[137]. The authors modelled the total stress transmitted by the platelets to the surface. They believe that the stress of the flow is primarily transmitted to the face of the platelet directly facing the flow. If the platelet contracted parallel to the flow, stress from both contractile forces and fluid flow would be concentrated at the front of the platelet, potentially leading to a failure of the platelet adhesive machinery within this high-stress zone. By contracting along the axis perpendicular to the applied shear, platelets may spread out the stress more evenly[137]. This force organization in response to shear stress suggests that the anisotropic contraction reported via MFM may be advantageous.

The biological origins of the force axis revealed by MFM are not currently known. In resting platelets, discoid shape is likely maintained by a circular microtubule marginal band. A recent report suggested that during activation, dynein slides microtubules in the platelet marginal band apart, producing expansion of the marginal band. This band then appears to buckle, thrusting portions of the band above the plane and driving the remainder

below the plane. This process may be aided by actomyosin contractility, and seems to be important to platelet activation[138]. We observed this marginal band coiling in our immunostaining experiments. Additionally, this process of coiling leads to the formation of a symmetry axis, which may explain the anisotropic contraction we observe in human platelets.

Fibroblast MFM dovetails well with other measurements of focal adhesion forces and structure. The average $\theta_{force}$ angle of 40° for fibroblast integrin forces matches structural data from other investigators. In particular, Valerie Weaver and colleagues used scanning angle interference microscopy to interrogate the orientation of the focal adhesion protein talin by expressing a talin fusion protein with fluorescent proteins. This group measured the orientation of N-terminal mCherry and C-terminal mEmerald, finding that the C-terminus was on average 37nm higher than the N-terminus. Given the 60 nm length of talin, the authors predict that the talin adopts a 51° orientation relative to the *z*-axis[139]. Waterman and colleagues recently employed fluorescence polarization measurements of GFP conjugated $\alpha_V\beta_3$ to demonstrate that integrins adopt a coaligned, tilted orientation within focal adhesions and are oriented via coupling to talin and the actin cytoskeleton[140]. These measurements agree with MFM measurement of a 40° tilt angle for integrin forces within focal adhesions, and with the measurement of highly coherent forces within focal adhesions.

The current implementation of MFM requires the addition of a rotatable λ/2 waveplate into the optical path. Although this modification is well within the capability of fluorescence imaging labs, it may deter some among the biological community who are interested in implementing MFM. Enabling MFM to be used by the broader scientific

community is of significant interest. Importantly, commercially available Structured Illumination Microscopes are likely capable of performing MFM. Structured Illumination Microscopy (SIM) is a super-resolution technique that illuminates samples with linearly polarized light that self-interferes to produce a structured illumination profile. By phase shifting and rotating this pattern, it is possible to reconstruct a super-resolved image. However, as a by-product of this process, samples are illuminated with three different excitation polarizations. A recent report successfully leveraged SIM imaging to measure the orientation of fluorophores via excitation resolved FPM[141]. Accordingly, commercially available SIM microscopes should be capable of MFM imaging without modification. Work is currently underway in the Salaita lab to perform SIM-MFM, making this technique significantly more accessible.

Finally, MFM is currently the only technique capable of measuring the 3D orientation of pN molecular forces. Most implementations of TFM are not able to measure *z*-oriented forces. There are several reports of TFM measurements that do resolve 3D traction stresses. Christopher Chen's group reported measuring the 3D traction stresses of a cell embedded within a polymer matrix[76]. Another report from his lab measured 3D traction forces transmitted by cells to a 2D polymer gel (2.5D-TFM)[77]. However, the computational difficulty of these methods has largely prevented their widespread adoption. Additionally, TFM is less sensitive to forces along the optical axis (*z*-oriented forces) due to the poor resolution of optical microscopy along the optical axis. A recent report utilized 3D SIM to measure the 3D orientation of traction stresses, but was only able to do so with ~1μm spatial resolution. MFM clearly offers a less computationally intensive, and much higher spatial resolution technique than TFM. One other method, Elastic Resonator

Interference Stress Microscopy (ERISM) does allow measurement of pN forces in the *z*-direction by using a thin, deformable substrate and interference measurements of substrate deformation. ERISM offers ~1.6 μm spatial resolution, and is only sensitive to forces of ~300 pN in the *xy* direction[142]. These techniques do provide one significant benefit over MFM. MFM is performed on an extremely stiff glass substrate, while TFM and ERISM can be performed on compliant gels that match the stiffness of native tissue. Adapting tension probes for use with compliant gels is of significant future interest.

In summary, MFM is currently the only technique capable of measuring the 3D orientation of pN molecular forces. We hope that this unique capability will provide significant insight into molecular forces, and provide a means to test longstanding hypotheses that the orientation of molecular forces can alter signaling outcomes.

## 3.5 Materials and Methods

This section will describe the protocols used in the synthesis of DNA tension probes, the surface chemistry employed to conjugate these probes to glass coverslips, and the characterization of these surfaces.

### *3.5.1 Materials*

N-hydroxyl succinimide azide (NHS-azide,88902), DiI (CN-1006) and NHS-Biotin (20217) were purchased from Thermo Fischer Scientific (Waltham, MA). Cy3B-NHS ester (PA63101) was acquired from GE Healthcare Life Sciences (Pittsburgh, PA). DNA was custom synthesized by Integrated DNA Technologies (Coralville, IA). Cyclo[Arg-Gly-Asp-d-Phe-Lys(PEG-PEG)] (PCI-3696-PI), elsewhere abbreviated as

cRGD, was acquired from Peptides International (Louisville, KY). #1.5 25mm glass coverslips (Product code: 7225-01) were purchased from Electron Microscopy Sciences (Hatfield, PA). Streptavidin (S000-01) was obtained from Rockland-Inc(Pottstown, PA). μ-Slide $VI^{0.4}$ 6 channel slides (80606) and 25 mm x 75 mm glass coverslips (10812) were purchased from Ibidi (Verona, WI). 96-well glass bottom plates (655892) were obtained from Greiner (Kremsmünster, Austria). 5-μm silica beads (SS06N) were acquired from Bang Laboratories (Fishers, IN). Lipoic acid-PEG-NHS (Mw=3400, PG2-LANS-3k) and mPEG-NHS (Mw=2000, PG1-TH-2k) were purchased from Nanocs (New York, NY). 1,2-dioleoyl-sn-glycero-3-phosphocholine (DOPC) lipid was purchased from Avanti Polar Lipids Inc. (Alabaster, AL). Gold nanoparticles were acquired from Nanocomposix (San Diego, CA). TEM performed by Nanocomposix indicated an average gold nanoparticle diameter of 8.6±0.6 nm. All other reagents and materials were purchased from Sigma-Aldrich and used without purification. All buffers were prepared with 18.2 MΩ nanopure water.

### *3.5.2 DNA Tension-Probe Synthesis and Characterization*

DNA MFM probes were synthesized as previously described[22]. The sequences of all strands are provided in Table 2.

**Table 2: MFM Tension Probe Sequences**

| **Name** | **Sequence** |
|---|---|
| Anchor strand with BHQ-1 | 5'-/BHQ 1/-CGC ATC TGT GCG GTA TTT CAC TTT-/3Bio/-3' |
| Anchor strand without BHQ-1 | 5'-CGC ATC TGT GCG GTA TTT CAC TTT-/3Bio/-3' |

| Table 2, continued | |
|---|---|
| 0T-Ligand Strand | 5'-/5Hexynyl/-TTT GCT GGG CTA CGT GGC GCT CTT-/3AmMO/-3' |
| 2T-Ligand Strand | 5'-/5Hexynyl/-TTT GCT GGG CTA CGT GGC GCT CTT **TT**-/3AmMO/-3' |
| Ligand Strand- Alexa 488 | 5'-/5Hexynyl/-TTT GCT GGG CTA CGT GGC GCT CTT-/3AlexF488N/-3' |
| 22% GC 4.6 pN hairpin | 5'-GTG AAA TAC CGC ACA GAT GCG TTT GTA TAA ATG TTT TTT TCA TTT ATA C TTT AAG AGC GCC ACG TAG CCC AGC-3' |
| AuNP anchor strand | /5ThiolMC6-D/-TTT GCT GGG CTA CGT GGC GCT CTT-/3BHQ_2/-3' |
| AuNP ligand strand | /5AmMC6/-CGC ATC TGT GCG GTA TTT CAC TTT-/3Bio/-3' |
| AuNP hairpin | 5'-GTG AAA TAC CGC ACA GAT GCG TTT CAT ATT TCA TTT TTT TGT AAA TAT GTT TAG AAT CTA GAT GTT AAC CCT TTA AGA GCG CCA CGT AGC CCA GC-3' |

The synthesis of DNA-based tension probes has been previously described[22]. Briefly, 100 nmoles of c(RGDfK(PEG-PEG)) was reacted with approximately 150 nmoles of NHS-azide in DMF overnight to produce Product 1 (Figure 28). Product 1 was purified via reverse phase HPLC with a Grace Alltech C18 column (1 mL/min flow rate; Solvent A: 0.1M TEAA + 0.05% TFA, Solvent B: acetonitrile + 0.05% TFA; starting condition: 90% A + 10 % B, 1%/min gradient B) and its identity was verified with MALDI-TOF (Figure 28, Table 3).

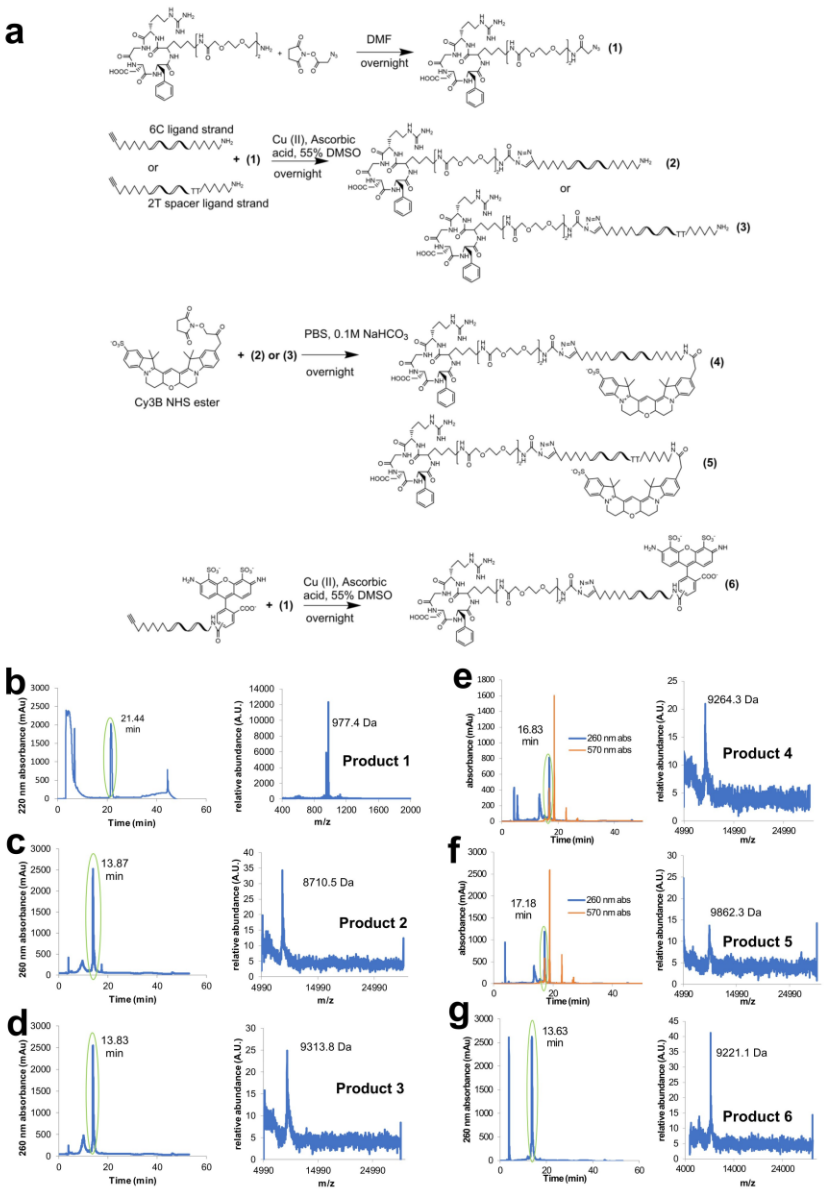


,

**Figure 28: HPLC and MALDI-TOF Characterization of MFM probes**

(**a**) Synthesis scheme for MFM probes. HPLC chromatogram and MALDI-TOF spectra for (**b**) Product 1, (**c**) Product 2, (**d**) Product 3, (**e**) Product 4, (**f**) Product 5, and (**g**) Product 6.

Product 1 was ligated to the tension probe ligand strand via 1,3-dipolar cycloaddition reaction (Figure 28). Briefly, 5 nmoles of alkyne ligand strand was reacted overnight with ~75 nanomoles of product 1 in the presence of 0.5M ascorbic acid, 0.5M Cu-TBTA, and 50% DMSO to form product 2/3 (Figure 28). Products were purified with a P2 size exclusion column and reverse phase HPLC with an Agilent Advanced oligo column (0.5 mL/min flow rate; Solvent A: 0.1M TEAA, Solvent B: acetonitrile; starting condition: 90% A + 10 % B, 1%/min gradient B) and the product's identity was verified via MALDI-TOF (Figure 28**,** Table 3). Following the above procedure, products 2, 3, and 6 were produced by varying the identity of the alkyne-conjugated ligand strand (Figure 28).

**Table 3: MALDI-TOF Mass Measurement**

| **Product** | **Expected MW (Da)** | **Measured MW (Da)** |
|---|---|---|
| c(RGDfK(PEG-PEG))-azide | 977.1 | 977.4 |
| c(RGDfK(PEG-PEG))-0T ligand strand | 8706.1 | 8710.5 |
| c(RGDfK(PEG-PEG))-2T ligand strand | 9314.5 | 9313.8 |
| c(RGDfK(PEG-PEG))-0T ligand strand-Cy3B | 9249.4 | 9264.3 |
| c(RGDfK(PEG-PEG))-2T ligand strand-Cy3B | 9856.8 | 9862.3 |
| c(RGDfK(PEG-PEG))-0T ligand strand-Alexa488 | 9222.6 | 9221.1 |

Products 2 and 3 were dried and reacted overnight with a 15x excess of Cy3B-NHS or Alexa-488-NHS dissolved in 1 μL DMSO to produce products 4, 5, and 6 (Figure 28). The total reaction volume was 10 μL, composed of 1x PBS supplemented with 0.1M $NaHCO_3$. The reaction pot was purified by a P2 size exclusion gel to remove unreacted dye followed by HPLC purification (0.5 mL/min flow rate; Solvent A: 0.1M TEAA, Solvent B: acetonitrile; starting condition: 90% A + 10 % B, 1%/min gradient B) to purify products 4 and 5. The identities of products 4 and 5 were confirmed via MALDI-TOF (Figure 28**,** Table 3).

Please note that the DNA probes immobilized using AuNP have been previously characterized[9] and are not described here.

### *3.5.3 Surface Preparation and Characterization*

Surface for streptavidin-based tension surfaces were prepared based on our published protocols[9, 22]. Briefly, glass coverslips were successively sonicated (~5 min) in nanopure (18.2 MΩ) water followed by sonication in ethanol. Coverslips were dried at 90° C for 15 minutes and then cleaned in piranha solution, a 3:1 mixture of concentrated sulfuric acid and 30% hydrogen peroxide (caution, piranha acid is extremely corrosive and may explode if exposed to organic materials), washed 6 times in nanopure water and then immersed in 4 successive beakers of ethanol. The piranha-cleaned surfaces were reacted with ~2.5% 3-(Aminopropyl)triethoxysilane (APTES) v/v in ethanol in a fume hood for 1 h. The coverslips were then washed 3 times with ethanol and dried under a stream of ultra-high purity $N_2$. Immediately following drying, the surfaces were cured in an oven at 90°C for 30 min. After cooling, the surfaces were incubated overnight with NHS-Biotin (2-3 mg

$ml^{-1}$) in DMSO. The surfaces were then washed with ethanol, dried under ultra-high purity $N_2$, mounted in Attofluor Chambers (Life Technologies), and washed with 10 mL of 1x PBS. Surfaces were blocked with 0.1% BSA (w/v) for 30 min and then washed with 1x PBS. The surfaces were then incubated in 1 mg $mL^{-1}$ streptavidin in 1x PBS for 45 min. The surfaces were then washed with 10 mL of 1x PBS. Finally, the surfaces were incubated with 10 nM DNA tension probes for 1 h and then washed with 10 mL 1x PBS prior to beginning cell experiments.

To calibrate the density of DNA tension probes on streptavidin surfaces, a fluorescent lipid bilayer calibration curve was constructed based on a previously reported protocol[143]. Small unilamellar vesicles (DOPC and increasing amounts (0-0.075 mol%) of Lissamine Rhodamine B-DHPE) were prepared and deposited on base etched, glass bottom 96 well plates for 15 min to form SLBs. Fluorescence intensity was measured using a Nikon Ti-E microscope. The density of fluorophores per unit area was determined from the footprint of DOPC (0.72 $nm^2$) within supported lipid membranes[144]. Therefore, the number of DOPC molecules per $\mu m^2$ of supported lipid bilayer is ~2.787 x $10^6/\mu m^2$. We constructed a supported lipid bilayer calibration curve to relate the known Lissamine Rhodamine B-DHPE density to fluorescence intensity. To use this calibration curve to calculate Cy3B-DNA density, a scaling factor (*F* factor) is introduced to account for the difference in brightness between Cy3B and Rhodamine B. We prepared varying concentrations (50, 100, and 200 nM) of Cy3B-DNA and Lissamine Rhodamine B-DHPE molecules and compared their intensities at the same concentration to obtain the *F* factor, defined as:

$$F = \frac{I_{solution}(Cy3B\ DNA)}{I_{solution}(Rhodamine\ B - DHPE)} \quad (42)$$

where $I_{\text{solution}}$ (Cy3B-DNA) and $I_{\text{solution}}$ (Rhodamine B-DHPE) are the intensity of the Cy3B-DNA or the Rhodamine B-DHPE in solution at identical concentrations, measured on a fluorescence microscope by focusing into the solution (~10 μm above the coverslip). We obtained an average *F* factor of ~12.47.

We measured the average intensity (from 30 ROIs) of an "unquenched" Cy3B-DNA tension probe surface as 10356±329 A.U. (mean ± s.e.m.). We then converted this intensity into the equivalent Lissamine Rhodamine B-DHPE intensity. Finally, we used our Lissamine Rhodamine B-DHPE calibration curve to estimate the Cy3B-DNA tension probe density as 694.6±32.7 probes per μm$^2$ (mean ± s.e.m.) as specified in a previous report[143]. Table 4 below describes the steps of this calculation.

**Table 4: Streptavidin Surface Probe Density Calculation**

| | |
|---|---|
| Average intensity of an unquenched tension probe surface | 10356±329 |
| "Corrected" average intensity | 830.5±26.4 |
| Linear equation of the fluorescent lipid calibration curve relating observed fluorescence to probe density | y = 0.808x + 269.2 |
| Number of tension probes per μm$^2$ | **694.6±32.7** |

For platelet aggregate experiments, gold nanoparticle-based tension probes were prepared following our previous work[9, 86]. Briefly, rectangular glass coverslips (25 x 75 mm) were cleaned using piranha solution as described above. Slides were then washed in 6 successive beakers of nanopure water and then etched in a beaker of KOH (0.5 M) for 1 hour in an ice-filled sonicator. The coverslips were washed in 6 successive beakers of nanopure water, followed by 3 successive beakers of ethanol. In a fourth beaker of ethanol, slides were reacted with 3% APTES v/v for 1 h. Coverslips were washed 2x with acetone, 3-6 times with nanopure water, dried under a stream of $N_2$ gas, and firmly attached to Ibidi channels (μ-Slide $VI^{0.4}$). The silanized slides were reacted with 1% w/v lipoic acid polyethylene glycol (MW = 3400) and 10% w/v 2000 molecular weight polyethylene glycol ($PEG_{2000}$) in 0.1 M NaHCO3 (pH 9) for 30 min. Slides were washed 3x with nanopure water and dried under a stream of ultra-high purity $N_2$. Slides were reacted for 30 min with 1% NHS-acetate in 0.1M $NaHCO_3$ (pH 9) to consume any unreacted amines on the surface. 50 μL of 8.8nm gold nanoparticles (AuNPs), concentration 20 nM, were added to each well and allowed to incubate for 30 min. Unbound AuNPs were removed by washing the channels 3 times with 1 mL of nanopure water. Finally, 45 μL of 300 nM DNA tension probes and 2.7 μM passivating ssDNA (AuNP anchor strand were added to each channel and each channel was sealed firmly with parafilm. Slides were incubated with the DNA overnight at 4°C in a petri dish. A water soaked kimwipe was also placed in the petri dish to maintain humidity during this reaction. Just prior to imaging, channels were washed with a cell imaging media and cells were added.

### *3.5.4 Image Processing*

We performed all image processing in MATLAB 2016a (MathWorks). The bioformats toolbox enabled direct transfer of Nikon Elements image files (.nd2) into the MATLAB environment. To save computational time, we analyzed user-identified ROIs containing cells. Edge finding was accomplished through Chan-Vese edge finding (available on MathWorks File Exchange)[23].

#### 3.5.4.1 Correcting for Microscope Polarization Bias and Laser Illumination Profile

Images of an autofluorescent plastic slide (Chroma: 92001) under conditions identical to cell imaging conditions enabled correction for the microscope's polarization bias and the uneven illumination of the laser. The autofluorescence of the Chroma slide is not ordered, thus any changes in intensity as a function of polarization must be due to the bias introduced by the microscope. We normalized the set of 73 images to the maximum intensity according to the following equation:

$$Bias_i = \frac{Bias\ Image_i - background_{detector}}{\max(Bias)}, i = 1, 2, \ldots 73 \quad (43)$$

where max(Bias) is the detector background subtracted maximum intensity within the image sequence.

We normalized cell images to this set of normalized illumination correction images as follows to correcting for both for the uneven illumination profile of the laser and for the polarization bias of the microscope

$$Cell\ Image_i = \frac{Raw\ Image_i - background_{detector}}{Bias_i} \quad (44)$$

3.5.4.2 Background Subtraction and Signal to Noise Ratio (SNR)

We next determined the local background ($background_{surface}$) and subtracted this value from the cellular tension signal. $Background_{surface}$ corresponds to the fluorescence of the quenched, randomly oriented fluorophores attached to DNA probes not experiencing cellular force.

$$Cell\ Image_{i,background\ subtracted} = Cell\ Image_i - background_{surface} \quad (45)$$

User-defined ROIs were used to determine the local background intensity. When single cells could be isolated with rectangular ROIs, we defined a background ROI as a "frame" consisting of all pixels within 3 pixels of the edge of the ROI. When the border of the ROI contained fluorescence intensity from a second cell, a user-identified square served in place of the "frame". We then defined $Background_{surface}$ as the mean intensity and the noise as the standard deviation of the intensity within the background ROI. Only pixels with a SNR of >5 were accepted for analysis.

3.5.4.3 Photobleaching Correction

To correct for the loss of fluorescence intensity due to photobleaching, we employed previously described method[12]. Briefly, we defined an average whole cell bleaching exponent by taking the mean value of the bleach exponents for each pixel of the cell. The bleach exponents for each pixel were calculated as:

$$Bleach\ Exp = \ln\left(\frac{I_{0^\circ}}{I_{180^\circ}}\right)/72 \tag{46}$$

In this expression, $I_{0^\circ}$ is the image corresponding to $\Phi_{excitation}=0°$ and $I_{180^\circ}$ is the image and corresponding to $\Phi_{excitation}=180°$, or Cell $Image_{1,background\ subtracted}$ for $I_{0^\circ}$ and Cell $Image_{73,background\ subtracted}$ for $I_{180^\circ}$ in equation 3. Pixels where fluorescence increased from $I_{0^\circ}$to $I_{180^\circ}$ were excluded as this increase must be due to biological changes or to random noise, not photobleaching. To correct for bleaching, we applied the following formula:

$$\begin{aligned} Cell\ Image^{Bleach\ Corrected}_{i,background\ subtracted} \\ = Cell\ Image_i \\ * \exp(mean(Bleach\ Exp) * (i-1)), \qquad i = 1,2,\dots 73 \end{aligned} \tag{47}$$

3.5.4.4 Curve fitting

We thresholded the bleach corrected images by the signal-noise ratio. Because intensity changes as a function of polarization reflect fluorophore orientation, pixel fluorescence intensity will vary from very high to very low as a function of $\Phi_{excitation}$. We therefore applied the SNR threshold pixel-by-pixel to the maximum fluorescence intensity in each pixel fluorescence polarization series ($\max(Cell\ Image_i^{Bleach\ Corrected})$). We performed nonlinear curve fitting in MATLAB pixel-by-pixel by fitting fluorescence intensity as a function of $\Phi_{excitation}$ to the function:

$$Intensity = amplitude * \cos(2(\phi_{excitation} - azimuth)) + average \tag{48}$$

The fitted azimuth gives the average fluorophore orientation, described as the azimuth within a pixel, while the amplitude and average provide the tilt angle of the cellular force. To speed computation, we employed a dynamic initial guess for each pixel: the initial amplitude was set as 1.35*(Imax-average), the average was initially set as the average intensity within each pixel, and the phase was initially specified as the azimuth, defined by:

$$azimuth\ guess = \frac{1}{2}\arctan\left(\frac{I_{45^\circ} - I_{135^\circ}}{I_{0^\circ} - I_{90^\circ}}\right) \tag{49}$$

# CHAPTER 4. MAPPING THE NANOSCALE DISTRIBUTION OF PICONEWTON FORCES WITH TENSION-PAINT

## 4.1 Abstract

Despite the vital role of mechanical forces in biology, no technique has been reported to image receptor forces with sub-100 nm resolution. Here, we present tension-PAINT (tPAINT), leveraging molecular tension probes with DNA-PAINT to map pN mechanical events with ~25 nm resolution. We applied tPAINT to integrin receptors in live human platelets and mouse embryonic fibroblasts using probes engineered to map tension in real time or to integrate force history over time. Finally, tPAINT reveals a link between platelet forces at the leading edge of cells and the actin-rich ring nucleated by the Arp2/3 complex.

## 4.2 Introduction

Mechanical forces are vital to biology, regulating diverse processes including early development, platelet activation, and immune function[7, 9, 15]. Force magnitude, orientation, and dynamics influence cellular signaling outcomes. Interestingly, force-transducing structures, such as filopodia, focal adhesions, and the cellular cytoskeleton, are organized at the nanoscale[85, 117] and therefore may apply dynamic forces with nanoscale organization[104, 107]. To better understand how mechanical forces are coupled to biochemical signaling pathways, methods are needed to map the nanoscale distribution of forces in living cells. However, to our knowledge, no technique is currently capable of mapping the dynamics of pN-scale forces with sub-100 nanometer resolution.

The most sensitive tension probes to map the pN forces applied by cells are comprised of a DNA stem-loop hairpin flanked by a fluorophore-quencher pair[22]. These probes act as force-triggered switches, and are generally comprised of a force-extensible element (e.g. a polymer/protein chain, or a DNA stem-loop structure) flanked by a fluorophore-quencher pair[21, 22, 87, 145]. When receptor forces are transmitted to the molecular tension probe, the force-extensible element extends, separating the fluorophore from the quencher and producing an up to 100x increase in fluorescence[9]. Most implementations of molecular tension probe measurements to date provide diffraction-limited (~250 nm) spatial resolution.

Recent advances in fluorescence microscopy have enabled "super-resolution," allowing optical microscopy to reveal features of biological structures that are smaller than the canonical ~250 nm "diffraction limit" of optical microscopy. Super-resolution microscopy has been extensively reviewed[99], and will only be treated briefly here.

One class of super-resolution microscopy techniques leverages single molecule localization microscopy (SMLM). The basic workflow of SMLM is depicted in Figure 29. Fluorophores are stochastically switched between the ON (bright) and OFF (dark) states thus only a small subset of fluorophores are ON during each imaging "frame." The position of fluorophores that are ON within each frame is precisely determined by fitting a point spread function to the observed single-molecule fluorescence. By combining data from thousands of cycles, it is possible to produce a super-resolved image. Effectively, SMLM

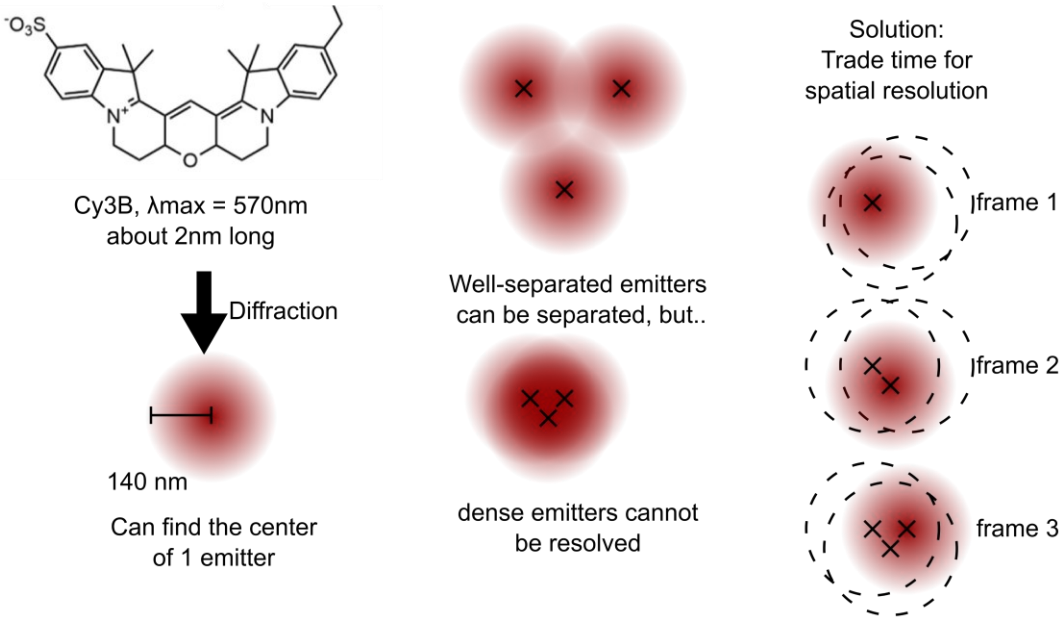


**Figure 29: Principle of Single Molecule Localization Microscopy (SMLM):**

Diffraction causes single fluorescent emitters to appear as larger, diffraction-limited points on a detector with a radius defined by their wavelength. For green fluorophores such as Cy3B, diffraction will cause a single fluorophore, which measures only 2nm in length, to appear as a 140nm radius spot on a detector such as a CCD or sCMOS cameral. Via non-linear curve fitting, it is possible to computationally determine the position of the fluorophore; however, curvefitting is only possible for well-separated fluorophores. SMLM-based techniques such as STORM, PALM, and DNA-PAINT rely on localizing the subpopulation of emitters that are ON within each image frame. By combining data from many frames, it is possible to build a super-resolved "map" of the locations of all of the fluorophores that were localized during each imaging frame.

techniques temporally separate single fluorophores that are spatially close. One effect of this approach is that events must be integrated over time to produce a super-resolved map of fluorophore locations, effectively exchanging temporal resolution for spatial resolution.

Commonly used SMLM-based techniques include stochastic optical reconstruction microscopy (STORM) and photoactivation localization microscopy (PALM), which work by chemically/photochemically forcing all but a small subset of fluorophores into a

transient dark state, enabling single molecule localization of fluorescent probes within each frame[100, 146]. These super-resolution techniques have produced images of biological structures with ~20 nm resolution, a feat previously only attainable via electron microscopy.

DNA-PAINT (DNA-based Point Accumulation for Imaging in Nanoscale Topography) is a recently-developed super-resolution technique that produces single molecule fluorescence via a different principle. Single-molecule fluorescence is achieved by localizing fluorophores attached to short (~9nt) fluorophore-tagged imager strands that transiently bind to complementary docking strands[102, 147-149]. These docking strands can be ligated to the biomolecule of interest, enabling super-resolved measurement of cellular structures with even greater precision than is possible with STORM or PALM[150]. DNA-PAINT has achieved both high spatial and temporal resolution super-resolution imaging[151-153].

In principle, one could directly image fluorophore-labeled "turn-on" molecular tension probes using super-resolved imaging techniques such as STORM, PALM, STED, or SIM, which routinely generate sub-diffraction images of biological structures[99]. However, many challenges complicate the use of turn-on tension probes for sub 100-nm super resolved imaging of receptor mechanics. FRET-based tension probes are challenging to integrate with stochastic super resolution microscopy techniques such as STORM. In fact, to our knowledge, FRET indexes have never been successfully calculated for fluorophores via stochastic super-resolution imaging techniques because both the donor and acceptor would have to simultaneously be in the excitable (ON) state. Attempts to integrate single-molecule FRET with STED are ongoing[154, 155]; however, STED requires

specialized optics, and the most sensitive molecular tension probes utilize dark quenchers (e.g. BHQ2), not fluorescent donor-acceptor FRET pairs[9, 22].

The "turn-on" tension probes commonly employed by the Salaita lab utilize fluorophore-quencher pairs; however, these probes are also likely to be challenging to adapt for use with many super-resolution imaging modalities. For example, quenching Cy5 with BHQ2 can produce photoswitching with high excitation intensities[156]. In the context of tension probes where fluorescence intensity reports receptor tension, photoswitching of the fluorophore would produce spurious, non-mechanical single molecule localizations. Additionally, both the fluorophore and quencher may photobleach[157], leading to a failure to report pN forces or to spurious, non-mechancial fluorescence, respectively. Finally, in dSTORM, a small subset of fluorophores are activated within each cycle. These fluorophores may not coincide with the subpopulation of tension probes experiencing mechanical force, leading to low localization density. In summary, it is unlikely that techniques such as dSTORM could be applied to measure pN receptor forces via turn-on tension probes. STED may offer a route to rapid, turn-on tension measurement, but requires specialized optics and is subject to photobleaching.

To adapt DNA tension probes for super-resolved imaging of receptor mechanics, we leveraged the technique DNA-based Point Accumulation for Imaging in Nanoscale Topography (DNA-PAINT). DNA-PAINT relies on the transient binding of fluorophore-tagged "imager" strands to ssDNA "docking" sequences decorating the biomolecule of interest[147, 149]. DNA-PAINT offers a potential route to super-resolved measurement of pN receptor forces by circumventing issues like probe photobleaching and photoswitching. It is robust to photobleaching because fluorophores are drawn from the nearly inexhaustible

supply of imagers present in solution. Moreover, DNA-PAINT requires only one fluorophore, avoiding the challenges associated with FRET and quencher-induced photoswitching.

We reasoned that when pN receptor forces open the stem structure of DNA-based molecular tension probes, this stem opening exposes ssDNA to solution that was previously concealed. Therefore, if a DNA-PAINT docking site is concealed within the dsDNA stem of a tension probe, imagers will only bind to the probe when it is currently experiencing receptor force. DNA-based molecular tension probes should function as force-triggered switches that only permits imager binding when the probe is experiencing pN receptor forces exceeding the probe $F_{1/2}$.

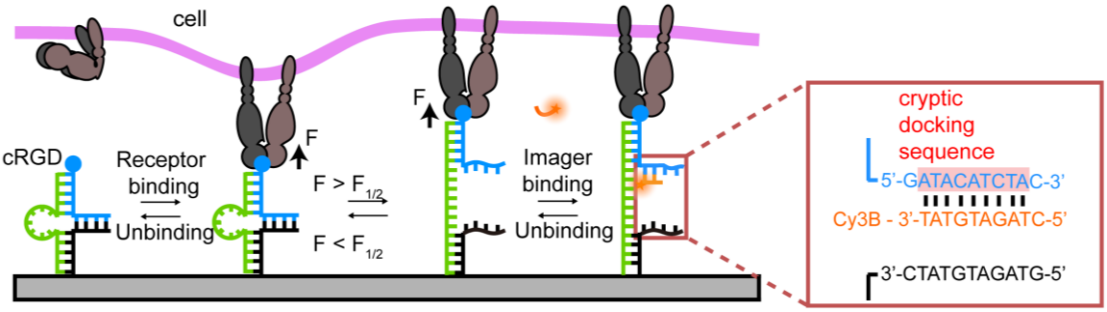


**Figure 30: Concept of tPAINT**

To make DNA-based tension probes amenable to use with DNA-PAINT, a cryptic docking site was encoded within a tension probe. The docking site is hidden within a dsDNA duplex when the tension probe is not under force, or when the receptor forces transmitted to the probe are less than the probe's $F_{1/2}$. When receptor force exceeds the probe $F_{1/2}$, the stem opens and reveals the cryptic docking site, allowing fluorophore-tagged imager strands to bind to mechanically opened probes. This process is reversible, thus when receptor force falls below the $F_{1/2}$, the cryptic docking site is concealed again. Imagers only bind probes that are currently experiencing receptor forces in excess of the probe $F_{1/2}$.

This chapter will describe the design and implementation of tension-Point Accumulation for Imaging in Nanoscale Topography (tPAINT), which is capable of imaging the nanoscale distribution of pN receptor forces.

## 4.3 Results

### *4.3.1 tPAINT Requires a Mechanically Unstrained Docking Site*

Adapting DNA based tension probes for use with DNA-PAINT requires careful design and consideration of the biophysical effects of mechanical force on DNA. Mechanical forces exerted on ssDNA increase the end-to-end length of that DNA beyond its zero-force length[158]. Mechanical force also affects dsDNA. For example, force exerted on DNA duplexes can cause that duplex to rupture[25, 159-161]. Intriguingly, force can also alter the rate of DNA-DNA association. A dual optical trap study by Chemla and colleagues found that low forces transmitted to ssDNA linearize the DNA. Because the transition state for DNA-DNA binding is thought to be a short region of DNA arranged linearly in preparation for DNA-DNA association, pN force transmitted to ssDNA can increase the $k_{on}$ for DNA-DNA binding. However, pN forces also increase the $k_{off}$ of the DNA duplex. Hence low levels of force (~5pN) can actually increase DNA-DNA binding[162]. However, for forces exceeding 5pN, stretching can reduce the $k_{on}$ of DNA hybridization to a mechanically strained sequence.

In published DNA-based molecular tension probes, a stem-loop DNA hairpin structure opens reversibly when receptor force exceeds the hairpin $F_{1/2}$, defined as the equilibrium force that leads to a 50% change of hairpin unfolding. Conceptually, a cryptic DNA docking site could be encoded within the stem-loop, enabling imager binding only

when the DNA probe is experiencing receptor tension. Previous studies from several groups have demonstrated that integrin forces in many cell types exceed 10pN, and may be as large as 20-50pN in magnitude[22, 23, 25, 68, 86, 87, 163]. It is possible that these forces could produce a reduced imager binding rate to conventional DNA tension probes in which the cryptic docking site is encoded in the mechanically strained stem-loop structure (Figure 31).

We designed a strain-free tPAINT (sf-tPAINT) probe to circumvent this difficulty (Figure 30, Figure 31). This probe funnels mechanical force away from the docking site after probe opening. In this new design, the sf-tPAINT sensor functions as a force-triggered switch. The cryptic docking sequence is strained before receptor force, $F$, exceeds the probe $F_{1/2}$. However, after $F$ exceeds the probe $F_{1/2}$, the stem opens and the mechanical force is borne by an unstructured, polyT loop (green strand in sf-tPAINT probe, Figure 31).

### *4.3.2 Mathematical Modelling of Imager Hybridization to tPAINT Probes*

When tension ($F$) is applied to single stranded DNA, larger magnitudes of $F$ ($F > 10$ pN for our probes) impose a kinetic barrier to hybridization to its complement (e.g. the imager)[162]. Similarly, $F$ applied to a duplex will increase its dissociation rate[162]. Accordingly, receptor tension that acts to unfold a DNA stem-loop tension probe (strained-tPAINT) will impede imager hybridization to the cryptic docking site. The barrier to hybridization will also increase as a function of the magnitude of applied $F$. The strain-free tPAINT (sf-tPAINT) probe described in this work is designed to avoid this issue. The sf-tPAINT probe presents a non-mechanically strained docking site which is available for imager binding in a force-independent manner. To develop a quantitative understanding

for the force-dependence of imager binding to the two probe constructs (conventional[22] strained-tension probe compared to the sf-tPAINT probe), we adapt the force-dependent hybridization kinetics and dehybridization models from Woodside & Block *et. al.*[164], and Whitley, Comstock, & Chemla[162]. Specifically, we use these models to estimate the barrier for imager binding as a function of applied $F$. This is a critical parameter as it dictates the frequency of localizations and the temporal resolution of live-cell tPAINT.

We define three discrete chemical states of a tension probe, as shown in Figure 31: closed, opened, and imager-bound (hereafter simply called "bound"). These three states are considered for the conventional strained tension probes as well as the sf-tPAINT probes. For both types of probes, the transition between the closed and opened states (step **1** in Figure 31) is force-dependent. However, the two probes diverge in the force-dependence of imager binding (step **2** versus step **3** in Figure 31). To consider the force-dependence of each probe, we constructed a model of the tPAINT-imager system. We first considered the kinetics for the transition between the closed and open states. Then we incorporated the imager binding kinetics as a function of force. These kinetic equations are then used to infer the equilibrium distribution of tPAINT probes in the three states.

To calculate the force-dependent equilibrium distribution of these states, we first calculated the kinetic rate constants of each of the four possible transitions as a function of $F$ ($k_{open}$, $k_{close}$, $k_{off}$, and $k_{on}$ – see Figure 31). We modeled the first three constants as zero-order rate constants that strictly depend on $F$ (for given imager and hairpin sequences), while $k_{on}$ is a pseudo-first-order rate constant such that imager binding also depends on the concentration of the imager, $\mathrm{C}$.

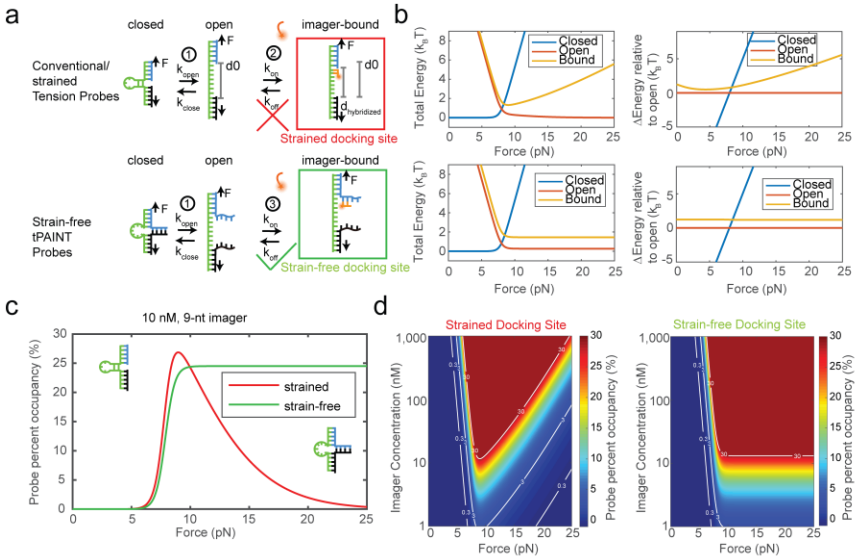


**Figure 31: Kinetic Modeling Predicts Impeded Imager Binding for Mechanically Strained Docking Sites**

(**a**) tPAINT relies upon imager binding to ssDNA that is exposed when forces open a DNA-based molecular tension probe (1). With previously published DNA-based tension probes, the exposed ssDNA is stretched (length $d_0$) and load-bearing due to the applied *F*. When applying *F* to this type of tPAINT probe, the imager transiently binds to a mechanically stretched docking site. Thus, the stretched docking site must shorten to adopt the structure of B-form DNA (to length $d_{hybridized}$), against the applied load. This hybridization process requires mechanical work equal to $F\Delta x$, where $\Delta x = d_0 - d_{hybridized}$ (2). Additionally, overstretching of DNA produces a kinetic barrier to imager hybridization. Modeling and experiments further quantify this prediction. To address this barrier to imager binding, we created strain-free tPAINT (sf-tPAINT) probes. Upon mechanical exposure of the docking site in sf-tPAINT probes, mechanical force is funneled to the backbone strand (green) and thus the docking site is no longer strained (3). (**b**) Kinetic model-based plots showing the total energy as a function of the applied *F* for strained/strain-free and closed (blue), open (orange), and imager bound (yellow) probes. The two plots to the right show the difference in energy compared to the open (non-bound) probe as a function of *F*. Note that the bound state of the strained probe is destabilized with increasing *F*, which is in contrast to the sf-tPAINT probe which is independent of *F*. (**c**) Plot of applied *F* versus the imager occupancy for strained (red line) strain-free tPAINT probes (green line). Note that for low forces ($F < 10$pN) imager binding to the strained probe may be enhanced but for large forces, such as fibroblast integrin or platelet forces, imager binding is impeded. (**d**) 3D plots showing the relationship between *F*, imager concentration and docking site occupancy for the strained and strain free tPAINT probes. As expected, increasing imager concentration enhances docking site occupancy. *F* hinders imager binding for the strained tPAINT probes, but this is not the case for the sf-tPAINT design.

The zeroth-order rate constant for hairpin opening, $k_{open}$, can be approximated using the Bell model[34] as discussed in Woodside *et al.*[164] according to equation 50.

$$k_{open}(F) = k_{open}(0)\exp\left(\frac{F\Delta x_f^{\ddagger}}{\mathrm{k_B T}}\right) \tag{50}$$

In equation 50, $k_B T = 4.114$ pN nm (the Boltzmann constant at room temperature), $k_{open}(0)$ is the zero-force opening rate, and $\Delta x_f^{\ddagger}$ is the force-independent extension from the folded state to the transition state. We used $\Delta x_f^{\ddagger} = 5.1\,nm$ and $k_{open}(0) = 0.017 s^{-1}$ based on experimentally-measured parameters for the "10R50/T4" hairpin studied in Woodside *et al.*, which had a 10 base pair (bp) stem of 50% GC content (similar to the strained tPAINT probe in this work) and a 4 nucleotide (nt) loop (values presented in figure 3 and table 1 of ref. [164]). While the 4 nt loop in the 10R50/T4 hairpin is smaller than the 7 nt loop used in our strained tPAINT probe, the same study showed that $\Delta x_f^{\ddagger}$ and $k_{open}(0)$ do not depend meaningfully on loop size[164]. Also note that these values were determined in 50 mM MOPS and 200 mM KCl buffer at room temperature which is slightly different than the buffers used in this work.

The zeroth-order rate constant for hairpin closing, $\mathrm{k_{close}}$, can be approximated using a similar form to the force-dependent opening rate.

$$k_{close}(F) = k_{close}(0)\exp\left(-\frac{F\Delta x_u^{\ddagger}}{k_B T}\right) \tag{51}$$

where $\Delta x_u^{\ddagger}$ is the force-independent change in distance between the unfolded state and the transition state for hairpin closing and $k_{close}(0)$ is the zero-force hairpin closing rate. The $\Delta x_u^{\ddagger}$ reported for the 10R50/T4 hairpin by Woodside *et. al* was 4.0 nm, but that study found that $\Delta x_u^{\ddagger}$ depends strongly on loop and stem length. While a construct with a 10 bp stem and a 7 nt loop was not studied, hairpins with 15 bp stems with loops ranging in length from 3 nt to 20 nt were studied, and a linear trend between loop length and $\Delta x_u^{\ddagger}$ was observed. We found through curve fitting that the slope of that trend was 0.4 nm/nt, and so we adjusted their reported $\Delta x_u^{\ddagger}$ value to obtain $\Delta x_u^{\ddagger} = 4.0\,nm + (3\,nt)(0.4\,nm/nt) = 5.2\,nm$. We solved for $k_{close}(0)$ by setting $F_{1/2} = 8$ pN and setting $k_{open}(F_{1/2}) = k_{close}(F_{1/2})$ to arrive at the following expressions which yields an estimated value of $8.3\text{x}10^6$ $s^{-1}$ for $k_{close}(0)$.

$$k_{close}(0)\exp\left(-\frac{8\,pN\;5.2\,nm}{4.114\,pN\,nm}\right) = k_{open}(0)\exp\left(\frac{8\,pN\;5.1\,nm}{4.114\,pN\,nm}\right)\#(4) \qquad (52)$$

$$k_{close}(0) = k_{open}(0)\exp\left(\frac{8\,pN}{4.114\,pN\,nm}(5.1\,nm + 5.2\,nm)\right) \qquad (53)$$

Before considering the kinetics of imager hybridization, we first validated that the $F$-dependence of hairpin opening could be accurately reconstructed from the mathematical relationships presented above. We constructed a Markov matrix (M) to represent state transitions and solved for the steady state fraction of probes in an open state ($\chi_o$) and a closed state ($\chi_c$) at a given force magnitude with the assumption that all probes were initially in a closed state.

$$\begin{bmatrix}\chi_c\\ \chi_o\end{bmatrix} = \mathrm{M}^{\mathrm{p}}\begin{bmatrix}1\\0\end{bmatrix} = \begin{bmatrix}1-\Delta t k_{open} & \Delta t k_{close}\\ \Delta t k_{open} & 1-\Delta t k_{close}\end{bmatrix}^{\mathrm{p}}\begin{bmatrix}1\\0\end{bmatrix} \quad (54)$$

In this matrix $\Delta\mathrm{t}$ is the duration of the simulation timestep and $\mathrm{p}$ is a positive integer representing the number of simulation timesteps. In order to ensure stability of the dynamic system, we selected a small timestep ($\Delta\mathrm{t} = 10^{-9}$ s). To best approximate equilibrium conditions, we also simulated a very large number of timesteps ($\mathrm{p} = 10^{10}$), yielding an equilibration time of 10 s, which is an order of magnitude larger than the timescale of imager binding. We found that in the absence of imager we had a typical $\chi_o$ vs. $F$ profile (not shown), wherein $\chi_o$ increases from ~0 to ~1 over a range of forces that spans 4 pN that is centered on the 8 pN $F_{1/2}$.

We next considered the kinetics of imager binding and unbinding. For unbinding, $k_{off}$ is described using an adaptation of the Bell Model developed by Whitley, Comstock, and Chemla[162].

$$\begin{aligned} k_{off}(F) &= k_1 \exp\left(-\frac{\Delta G^{\ddagger}(F)}{k_B T}\right) \\ &= k_1 \exp\left(-\frac{\Delta G^{\ddagger}(0) - \int_0^F \left(x^{\ddagger}(f) - x_b(f)\right) df}{k_B T}\right) \end{aligned} \quad (55)$$

$k_1$ is the unbinding attempt rate, $\Delta G^{\ddagger}(0)$ is the zero-force activation energy barrier height, f is an integration variable, and $x^{\ddagger}$(f) and $x_b$(f) are the force-dependent extensions of the transition state and bound state, respectively. Here, we use $k_1 = 10^7\ s^{-1}$ according to literature precedent[165], and approximated $G^{\ddagger}(0)$ by the relation $\Delta G^{\ddagger}(0) = 0.45 +$

$(1.65 \times Duplex\ length)$ (in units of $k_BT$) for duplexes 8-10 bp in length, thus yielding $\Delta G^{\ddagger}(0) = 15.3\ k_BT$. This value yields $k_{off}(0) = 0.23\ s^{-1}$, which is within an order of magnitude of the imager unbinding rate measured in our work despite the differing buffer conditions. Both $x^{\ddagger}$(f) and $x_b$(f) can be calculated using the worm-like-chain (WLC) model, which describes the relationship between the entropic tensile force of a polymer chain and the chain's end-to-end extension. This relationship can be accurately approximated using the numerical approximation developed by Petrosyan[120]:

$$x_{WLC} = bN\left(\frac{4}{3} + \frac{4}{3\sqrt{\frac{FP}{k_BT}+1}} - \frac{10\exp\left(\sqrt[4]{900\frac{k_BT}{FP}}\right)}{\sqrt{\frac{FP}{k_BT}}\left(\exp\left(\sqrt[4]{900\frac{k_BT}{FP}}\right)-1\right)^2} + \frac{\left(\frac{FP}{k_BT}\right)^{1.62}}{3.55+3.8\left(\frac{FP}{k_BT}\right)^{2.2}}\right) \quad (56)$$

where $b$ is the polymer's length per monomer (in nm), $N$ is the number of monomers in the segment (for nucleic acids, segment length is measured in basepairs or nucleotides) and $P$ is the persistence length of the polymer. For the calculation of $x_b$(f) we used $b = 0.34$ nm and $P = 53\ nm$, as was used by Chemla and colleagues[162]. For the calculation of $x^{\ddagger}$(f) we used $b = 0.54\ nm$ and $P = 2.6\ nm$, as calculated by Whitley *et al.*[165] For both we used $N = 9$ nt, which corresponds to the length of the imager. Finally, we can write an equation to calculate $k_{on}$ as a function of *F:*

$$k_{on}(F) = k_1 \exp\left(-\frac{\left(\Delta G^{\ddagger}(F) - \Delta G^{o}(0) + \int_0^F \left(x_u(f) - x_b(f)\right)df\right)}{k_B T}\right) \quad (57)$$

$\Delta G^o$ is the free energy of hybridization and $x_u(f)$ is the force-dependent extension of the unbound imager docking site and can be calculated from equation 56 with $P = 53\,nm$ and $b = 0.34\,nm$. As with our estimate of $\Delta G^{\ddagger}(0)$, we estimated $\Delta G^o(0)$ by analyzing supplemental figure 7 from Whitley *et al.*[162], yielding $\Delta G^o(0) \approx 17.3\,k_B T$. With this value, we calculate that $k_{on}(0) = 7.4 * 10^6\ M^{-1}\ s^{-1}$. This value of $k_{on}$ is consistent with reports for the hybridization rate of DNA-PAINT imagers[151], and with our own measurements (Figure 43).

Using these parameters, we constructed a new Markov-matrix equation to simulate the steady state dynamics in the presence of an imager, wherein probes can also reversibly transition from an open state to a bound state denoted by $\chi_b$.

$$\begin{bmatrix}\chi_c \\ \chi_o \\ \chi_b\end{bmatrix} = \begin{bmatrix}1 - \Delta t k_{open} & \Delta t k_{close} & 0 \\ \Delta t k_{open} & 1 - \Delta t(k_{close} + k_{on}C) & \Delta t k_{off} \\ 0 & \Delta t k_{on} C & 1 - \Delta t k_{off}\end{bmatrix}^{\mathrm{p}} \begin{bmatrix}1 \\ 0 \\ 0\end{bmatrix} \quad (58)$$

We also note that the relationships for $k_{on}$ and $k_{off}$ are only relevant to conventional DNA hairpin tension probes, wherein the imager binding site is stressed. However, our new design has an unstressed imager binding site. As such, for our new design $k_{on}$ and $k_{off}$ are both force-independent constants. In other words, $k_{on}(F) = k_{on}(0)$ and $k_{off}(F) = k_{off}(0)$ for all $F$. For both cases, we can also measure the overall

free energy of each of the three states. The free energy of each state will be proportional to the number of probes that populate that state.

$$\begin{bmatrix} E_c \\ E_o \\ E_b \end{bmatrix} = (\exp(\chi_c) + \exp(\chi_o) + \exp(\chi_b))^{-1} \begin{bmatrix} exp(\chi_c) \\ exp(\chi_o) \\ exp(\chi_b) \end{bmatrix} \quad (59)$$

Applying equation 58 with the parameters described above, we were able to calculate the steady-state fractional probe occupancy of the bound ($\chi_b$), open ($\chi_o$), and closed ($\chi_c$) states for a variety of $F$ and C values. For the conventional/strained DNA hairpin probe with an imager concentration of $C = 10$ nM, $\chi_b$ (the proportion of imager-bound tension probes) increases sharply as $F$ approaches $F_{1/2}$, peaks at a value of ~27%, and then steadily decreases to zero as increasing $F$ poses an increasing kinetic barrier to imager hybridization. These results are summarized in Figure 31c. Integrin forces have been reported to range from 1-100pN[22, 87, 90]. At $F = 18$ pN, $\chi_b$ is 10-fold lower than its maximum value and equal to ~2.7%. In contrast, for the unstressed probe, $\chi_b$ increases monotonically as $F$ increases above $F_{1/2}$ and then asymptotes to a value of 24.5%. The model predicts that the sf-tPAINT probe outperforms the strained probe for receptor forces in excess of ~10pN (Figure 31). To summarize, imager binding to the strained/conventional tPAINT probe is highly force-dependent within a physiologically-relevant force range, while binding to the new sf-tPAINT probe is not. Interestingly, $\chi_b$ for the strained-tPAINT probe peaks at a higher value than the $\chi_b$ asymptote for the sf-tPAINT probe (Figure 31c) This counter-intuitive finding results from the fact that small magnitudes of force (<10 pN) actually increase the on-rate because this level of force helps to align the duplex in a linear manner which is thought to facilitate binding[165].

Note that at the 10nM imager concentration, $\chi_b$ increases to a surprisingly high value of ~25%. This finding suggests that a large fraction of opened tension probes are bound at any given time. This observation is also illustrated by plots of $E_o$, $E_c$, and $E_b$ as calculated with equation 12 (Figure 31c, d). However, this observation may not be borne out experimentally because: 1) fluorophores may bleach before the imagers dehybridize, reducing the fraction of opened probes that result in fluorescent signal, 2) model parameters were estimated from literature values that were obtained under different buffer conditions to our experiments, and utilized different stem-loop sequences, and 3) our model assumes free diffusion of imagers beneath the cell whereas in reality the effective association rate of the imager to the probe may be impeded by the confined environment of the surface and particularly beneath the cell.

### *4.3.3 Mechanical Strain-Free tPAINT Probes Outperform Strained Probes*

We next sought to experimentally verify the requirement for mechanical strain free tPAINT probes. We synthesized cRGD-based tension probes as previously described[22] (Figure 52). The sequences of the probes used in this chapter are provided in Table 6.

We synthesized Cy3B-BHQ2 labeled "turn-on" conventional and sf-tPAINT tension probes (Figure 32, Figure 52). Human platelets in 1x Tyrode's buffer were activated with ADP and seeded on the surface. Both the conventional and sf-tPAINT probe successfully report pN integrin forces with an increase in fluorescence (Figure 32a, b), confirming that both probes are capable of reporting pN receptor forces. To test the hypothesis that DNA docking sites that do not experience mechanical strain will outperform mechanically strained docking sites, we next synthesized tension probes

without the Cy3B-BHQ2 fluorophore-quencher pair (Figure 52). We performed paired experiments in which human platelets were seeded on surfaces where adjacent channels were functionalized with either the strained-tPAINT or sf-tPAINT tension probe. Both the strained-tPAINT and sf-tPAINT tension probes produced an increase in single-molecule localizations within the platelet-surface contact area; however, sf-tPAINT probes produced

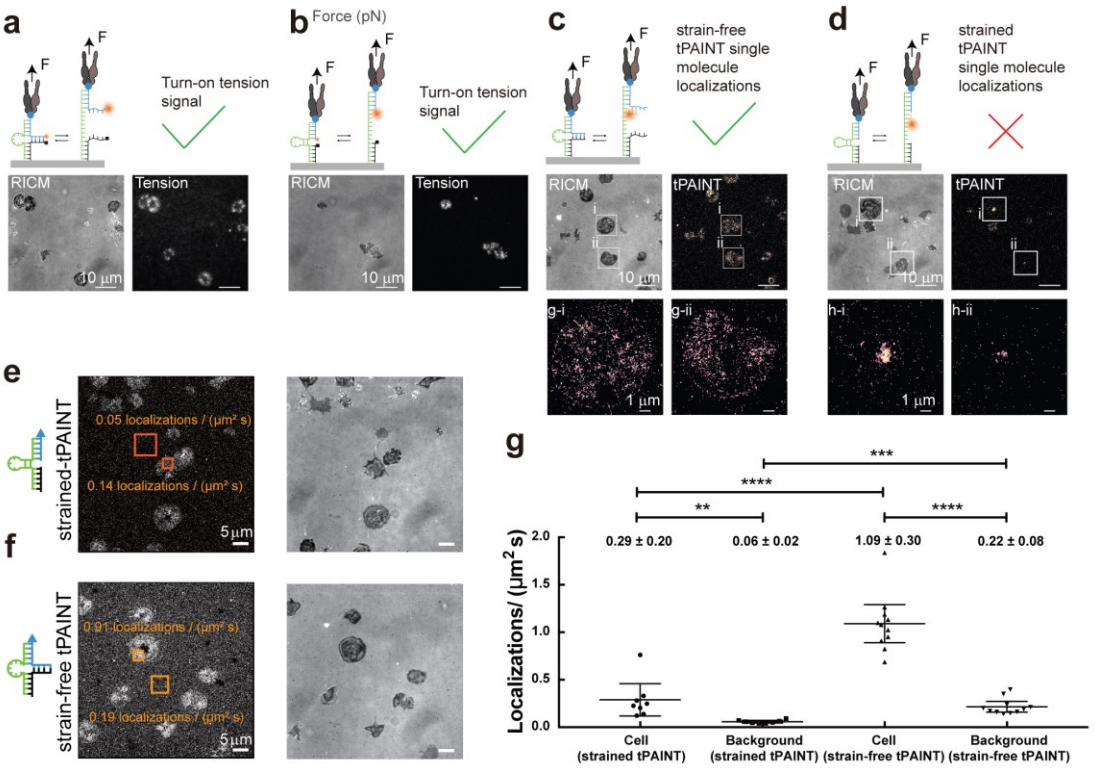


**Figure 32: sf-tPAINT Probes Outperform Strained Probes**

(**a-d**) Experimental validation of modeling predictions using traction forces generated by human platelets. (**a, b**) Probes were tagged with fluorophore-quencher pairs (turn-on probes) to confirm probe opening. Both probes generated similar turn-on signals. (**c, d)** Strained and sf-tPAINT probes were incubated with 10nM Cy3B-imager and imaged for 5000 frames. Strained tPAINT probes produced poor quality images and miss lamellipodial edge tension; in contrast, sf-tPAINT probes successfully images and reveal the lamellipodial edge tension. (**e-g**) Activated human platelets were added to each well and allowed to spread for 10-15 min before the addition of 10 nM Cy3B imager. 7500 frames were collected at 5Hz in TIRF excitation mode and single molecule localization was performed in the Picasso software suite.

**Figure 32, continued:** (**g**) Quantification of the number of single molecule localizations ($\mu m^{-2}$ $s^{-1}$) was quantified for 3 ROIs in the background and 3 ROIs underneath cells for both strained and sf-tPAINT probes. Each data point represents the mean of these 3 ROIs from a single PAINT data. Mean ± standard deviation is provided in the figure for each category. For both probes, more localizations were observed under cells than in the background. However, a greater number of localizations under the cell were observed for sf-tPAINT probes, demonstrating the importance of strain-free docking sites in tPAINT measurements. Results are representative of n = 4 independent strained tPAINT surfaces and n = 6 independent sf-tPAINT surfaces (11 images for strained tPAINT, 8 images for sf-tPAINT). Data is displayed as mean with 95% confidence interval. The data shown in (**e** and **f**) are from paired experiments using different channels on the same glass coverslip and using the same platelet donor. The results shown are representative of $n$ = 3 experiments. Turn-on tension probe data is representative of $n$ = 3 experiments for the strained-tPAINT probe and of $n$ = 6 experiments for the redesigned turn-on tPAINT tension.

significantly more localizations than strained-tPAINT probes (Figure 32c-g). It is important to note that it is not impossible to use the strained-tPAINT probe; however, the sf-tPAINT probes produce approximately four times more single molecule localizations $\mu m^{-2}s^{-1}$ than the strained probe. These results empirically demonstrate that the sf-tPAINT probe outperforms a probe with a mechanically strained docking site. Accordingly, all subsequent experiments were performed with the strain-free docking site probe (sf-tPAINT probe).

### *4.3.4 tPAINT Super-Resolved Imaging of pN Recptor Forces with Sub-100nm Resolution*

We next set out to image pN receptor forces with the optimized sf-tPAINT probe. In this new design, the sf-tPAINT sensor functions as a force-triggered switch, exposing an unstrained cryptic docking sequence when receptor force, $F$ exceeds the probe $F_{1/2}$, which is defined as the equilibrium $F$ that produces a 50% probability of unfolding. To test this design, we coated coverslips in cyclic-Arg-Gly-Asp (cRGD) sf-tPAINT probes and seeded human platelets onto these substrates. We used human platelets as a model

because of their small size (2-5 μm), and the intimate link between mechanical forces and their clotting functions[6, 67].

Platelets spread rapidly on the substrate, and upon addition of 10 nM Cy3B imager, single molecule fluorescence spots were observed under the cell-surface contact area. Platelets were imaged in TIRF excitation mode at 5 Hz for 12 min. Localization of single Cy3B molecules using the Picasso software suite[149] revealed super-resolved maps of platelet pN integrin forces (Figure 33a-d). Because sf-tPAINT probes only recruit imagers from solution when the probe is experiencing mechanical forces, we were able to visualize dynamics of platelet tension as these cells engaged with the cRGD tension probe surface. To confirm the biological generality of the sf-tPAINT probe, we also imaged integrin forces generated by mouse embryonic fibroblasts (MEF) cells expressing GFP-vinculin

and were able to measure single-molecule forces transmitted by focal adhesions, as determined by GFP-vinculin fluorescence (Figure 33e-g).

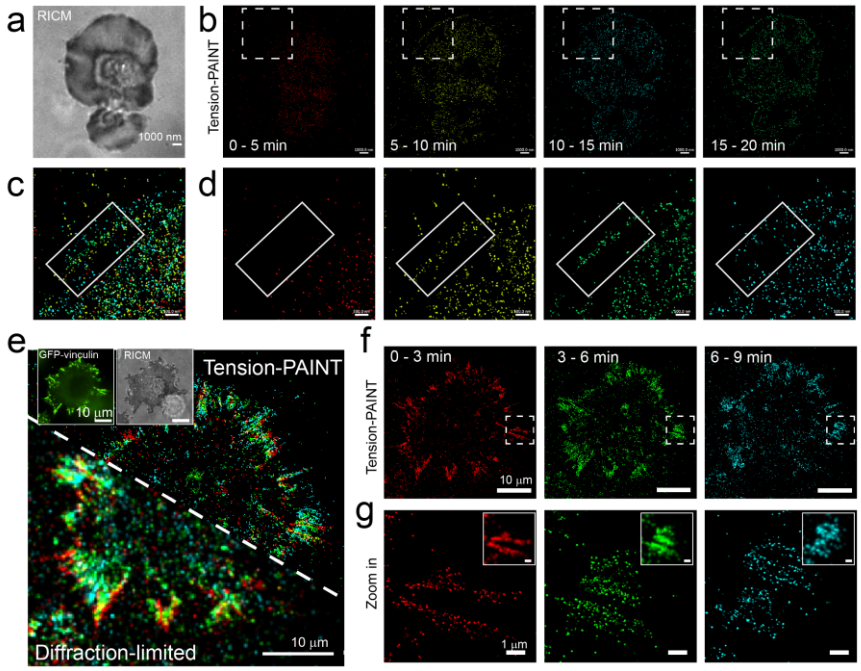


**Figure 33: tPAINT Imaging of pN Receptor Forces**

(**a**) RICM and (**b**) time resolved 8pN sf-tPAINT of human platelets performed in Tyrode's buffer using the strain-free tPAINT probe and 10nM Cy3B imager. (**c-d**) Zoom-in of dotted box in (**b**) focusing on platelet lamellipodial edge tension. The white box in (d) provides a frame of reference showing the movement of the edge tension. Note that significantly fewer single molecule localizations are observed in Tyrode's media compared to Tyrode's media supplemented with 37.5mM $Mg^{2+}$. (**e**) RICM, GFP-vinculin, and 8pN sf-tPAINT of MEF cell spreading in cell culture media (fluorobrite-DMEM, supplemented with 0.5-1% heat-inactivated fetal bovine serum). (**f**) Focal adhesion dynamics are visible in time-resolved sf-tPAINT. (**g**) Magnified view of the dotted box region in f. Insets depict the diffraction limited reconstruction of the super-resolved single molecule localizations in **g**. Data shown is representative of $n = 4$ platelet and $n = 3$ fibroblast experiments.

Although Figure 33 demonstrates single-molecule localization of pN receptor forces via sf-tPAINT, we were not satisfied with the quality of the tPAINT images produced. Many optical super-resolution microscopy measurements, including DNA-

PAINT, rely on stochastic "blinking" of single molecules to resolve the spatial location of multiple fluorophores within a diffraction limited spot[100, 102, 146, 147, 149, 166]. To produce a super-resolved image, the fluorophores localized within many consecutive imaging frames are combined to render a single super-resolved map. This integration over time presents a unique challenge to live-cell imaging because cell dynamics may "blur" the super-resolved image. In the case of tPAINT, individual tension probes are rigidly affixed to the coverslip, thus cellular motion is not an issue; however, temporal variations in the forces transmitted to tPAINT probes result in a failure of live-cell sf-tPAINT to report all receptor tension events. Specifically, in tPAINT, the sites of the probes are fixed, but each probe is transiently open and available for imager binding only as long as $F > F_{1/2}$. Integrin-ligand bond lifetimes are reported to be 0.1-20 seconds under force[39, 167]. In Figure 33, the imager on rate has been reported as $k_{on} = 1.2x10^6\ M^{-1}s^{-1}$, and this imager was used at 10nM concentration[147]. The expected influx rate of imager to an open cryptic docking site on a mechanically strained probe is $0.012\ s^{-1}$, meaning that, on average, an imager will visit an open sf-tPAINT probe once every 83.3 seconds. Because integrin-ligand bond lifetimes are significantly shorter than the 83 sec dark time in between imager binding events, sf-tPAINT underestimates the number of binding events that occur in Figure 33. In principal, one could increase the influx rate of imager to the cryptic docking site to decrease the dark time. To increase the influx rate, one could increase the concentration of imager; however this solution also increases the background fluorescence and presents problems associated with non-mechanical imager binding that will be discussed in depth later (Figure 37).

A more elegant solution is to increase the imager $k_{on}$. Recent work by Jungmann and colleagues demonstrated solutions to maximize imager $k_{on}$ for DNA-PAINT,

significantly increasing the speed of DNA-PAINT imaging[151]. Jungmann and colleagues achieve this increase in $k_{on}$ by utilizing high concentrations of $Mg^{2+}$ to charge-shield the imager, and by optimizing the sequence of the imager to reduce self-interaction[151].

We therefore seeded human platelets on a coverslip functionalized with cRGD-sf-tPAINT probes in 1x Tyrodes buffer supplemented with 37.5mM $Mg^{2+}$ to maximize the on-rate of imager sampling and better capture short-lived mechanical events. Upon addition of 10nM Cy3B-tagged imager, platelets were imaged at 5Hz in TIRF excitation mode. Single-molecule fluorescence signal was observed under the cell-surface contact area and subjected to single-molecule localization in Picasso[149].

Speed-optimized sf-tPAINT enabled us to produce high-quality super-resolved images of platelet integrin-mediated forces during platelet spreading (Figure 34). The rapid imager sampling of mechanically-opened tension probes, coupled with the fact that sf-tPAINT probes open reversibly and only report tension when an integrin is actively transmitting tension greater than the 8.5pN $F_{1/2}$ of the probe, allows sf-tPAINT to create a timelapse of platelet mechanics (Figure 34). Each frame in Figure 34a integrated 200 sec of single molecule localizations. sf-tPAINT revealed that platelets engage with the surface initially with amorphous tension and filopodial projections before forming a "ring" structure of tension at the platelet lamellipodial edge that spreads outwards over the course of the timelapse (Figure 34a, b). We quantified the width of the platelet lamellipodial edge via linescans, and found that this rim can be as thin as ~90nm, measured as the FWHM of a gaussian fit to the localization density (Figure 34c).

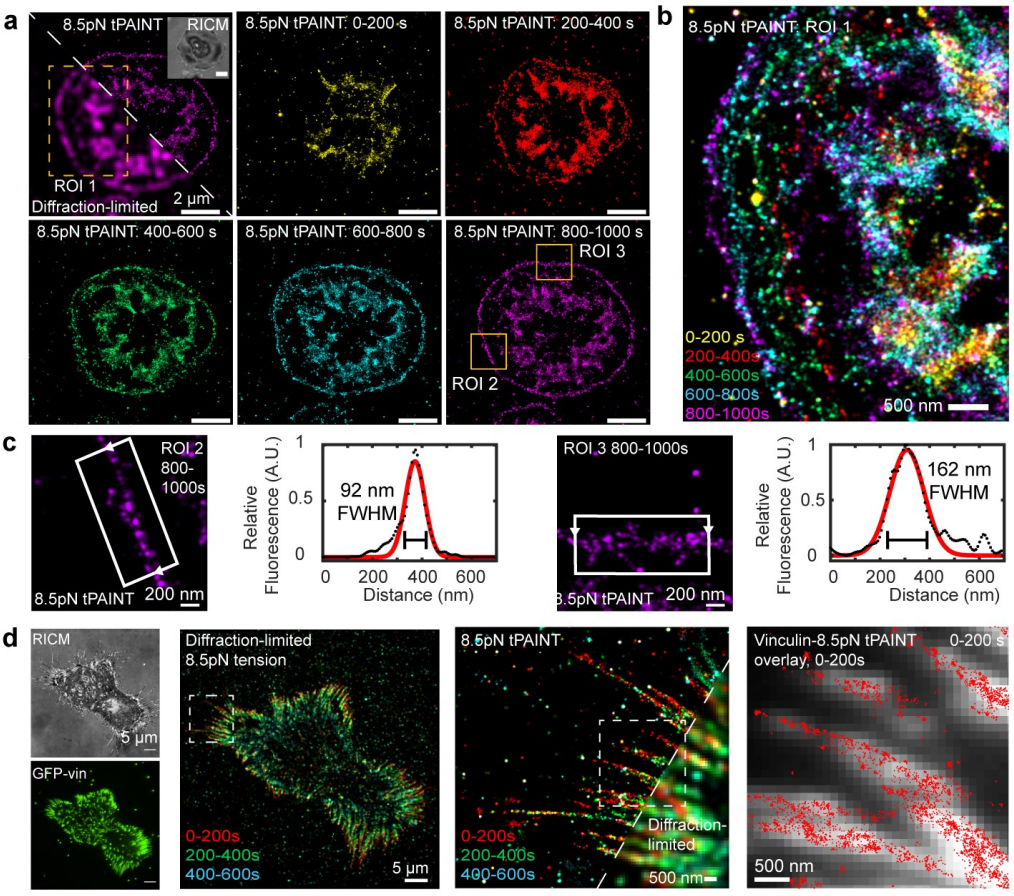


**Figure 34: Speed-Optimized sf-tPAINT of Platelet and Fibroblast Integrin Forces**

(**a**) Timeseries showing sf-tPAINT of 8.5 pN integrin forces during the process of platelet activation. Reflection interference contrast microscopy (RICM) is shown in the inset. The first frame shows a diffraction-limited/tPAINT overlay of the 800-1000s time bin. (**b**) Color-coded timeseries showing dynamics of lamellipodial tension during spreading (ROI 1 indicated by dotted box). (**c**) Representative zoom-ins of lamellipodial edge tension along with line scans reporting FWHM of a gaussian fit to a greyscale rendering of sf-tPAINT (800-1000 sec time bin). (**d**) sf-tPAINT image of the 8.5 pN MEF integrin tension. Image time bins are color-coded. GFP-vinculin fluorescence colocalizes with sf-tPAINT single molecule localizations. The data shown are representative of $n = 3$ independent platelet experiments from 3 different donors (8 images) and $n = 4$ fibroblast experiments (10 images).

To demonstrate the biological generality of tPAINT, we next imaged mouse embryonic fibroblasts stably expressing GFP-Vinculin (MEF-GFP-vinculin) via sf-

tPAINT. Fibroblasts spread and formed focal adhesions (Figure 34d). Following the addition of 10 nM Cy3B-imager in media supplemented with 75 mM $Mg^{2+}$, we imaged the cell in TIRF excitation mode at 5 Hz, and performed single molecule localization to produce super-resolved maps of integrin tension (Figure 34d). Integrin-generated tension was associated with focal adhesion area and generally extended slightly beyond the distal tip of the focal adhesion footprint (Figure 34d), a finding consistent with previous diffraction-limited molecular tension measurements[163], and with TFM measurements that found that the centroid of focal adhesion traction stresses was ~1μm closer to the cell edge than the centroid of the focal adhesion itself[133].

We wanted to confirm that sf-tPAINT localizations corresponded to physical structures or movements of platelets and fibroblasts. Accordingly, we superimposed sf-tPAINT localizations corresponding to 60 seconds of single-molecule forces with the cell-surface contact area (measured via RICM) for human platelets (Figure 35a, b). We found that sf-tPAINT single molecule localizations, which correspond to single integrin forces, colocalize to platelet filopodia and lamellipodia spreading.

For example, a platelet filopodia formed during this acquisition (yellow box, Figure 35a, filopodia indicated by a green arrow). An RICM contrast change in the filopodia occurred from minutes 1-2, indicating close contact between the filopodia and the surface. The contrast change in the filopodia footprint coincided with the onset of sf-tPAINT localizations around 2-3 minutes after the beginning of the acquisition (Figure 35b). The At later time points (5-7 min after the beginning of imaging), a ring of sf-tPAINT localizations occurred at the leading lamellipodial edge of the platelet lamellipodia. The platelet lamellipodia overtook the position of the filopodia by around 4-5 minutes into the

acquisition (Figure 35b). In Figure 35b for images taken from 1-10 min, the, the location of the platelet edge in the previous minute of acquisitions is given by the yellow dotted line. The platelet lamellipodial edge spreads during the 10 minute observation time. These overlays demonstrate that the sf-tPAINT single-molecule localizations at the platelet lamellipodial edge track the spreading of the platelet edge as measured via RICM (Figure 35b). Similarly, sf-tPAINT localizations are located primarily within focal adhesions as measured by GFP-vinculin fluorescence (Figure 35c-d).

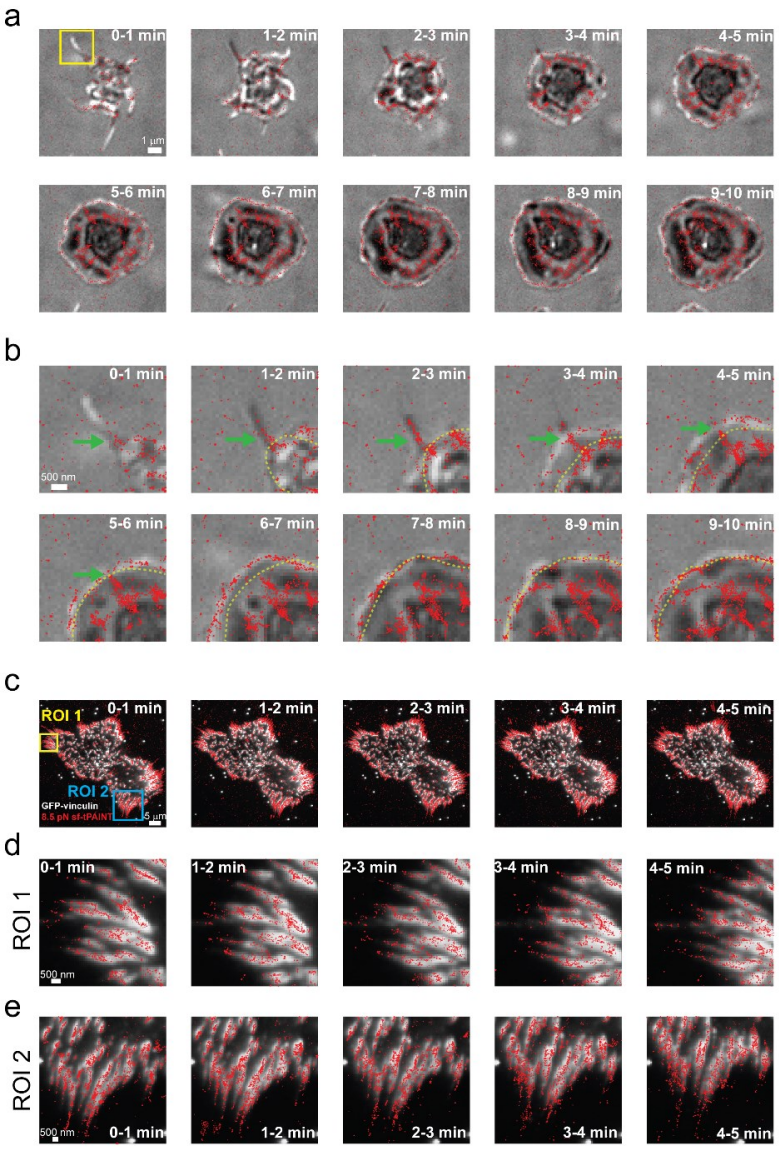


**Figure 35: sf-tPAINT Localizations Are Spatially Linked to Lamellipodial Spreading and Focal Adhesion Sliding**

(**a**) 8.5 pN tPAINT integrin forces (red points) and RICM (grey) were simultaneously imaged in a spreading human platelet. Each RICM image is collected at the beginning of the time window, while the 8.5pN sf-tPAINT data represents the accumulated signal in a 60 sec interval. (**b**) Zoom-in images of the region highlighted with yellow box in **a**. The green arrow denotes the formation of a filopodium and the force associated with extension of this structure. For frames corresponding to minutes 1-10, the cell edge in the previous frame is highlighted with a dashed yellow line. Note that the filopodial forces are still resolved even after lamellipodial spreading. (**c**) Full cell view of a mouse

**Figure 35, continued:** embryonic fibroblast (MEF); (**d**) and (**e**) show the zoom-ins of the regions highlighted with yellow and blue boxes, respectively. Note that the focal adhesion (as indicate by the vinculin-GFP data) is offset from the mechanical localizations. The tension signal extends beyond the tip of the focal adhesions away from the cell body, and this is clear both in the full view of the cell (**c**), as well as the zoom in panels (**d**) and (**e**). This could be consistent with previous reports by Waterman and colleagues which found that the centroid of focal adhesion traction stresses is consistently ~1μm distal to the focal adhesion centroid. This finding is also consistent with previous publications from our lab.

cellular dynamics. These dynamic changes produce a unique challenge for tPAINT. To produce a super-resolved tPAINT image it is necessary to integrate signal from many frames; however, rapid cellular dynamics may "blur" tension features if too many events are integrated to produce an image. To explore this tradeoff between integrating sufficient numbers of events to produce high-quality tPAINT images and blurring of tension features, we produced tPAINT images by integrating between 50s and 1000s of tPAINT localizations (Figure 36). The tradeoff between localization density and obscuring tension features is particularly apparent when considering the platelet tension ring. Integrating more events causes the apparent width of the ring to increase (Figure 36a, c), likely because the ring is spreading during the integration period convolving cellular dynamics with the true width of the ring.

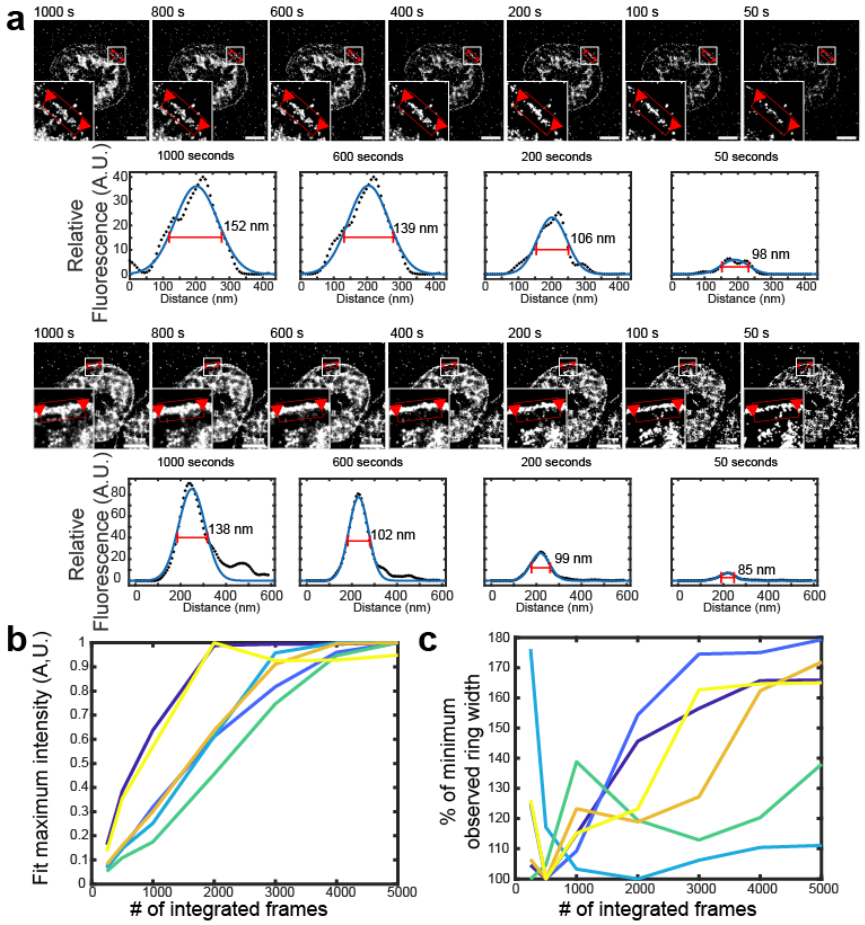


**Figure 36: Tension Feature Dimensions Depend on the Imaging Window in sf-tPAINT**

(**a**) Live-cell sf-tPAINT imaging of platelet tension displayed using different time windows (ranging from 50 sec to 1000 sec). The apparent length or width of cellular tension features depends on the number of frames that are integrated to produce a super-resolved image. To demonstrate this point, we rendered the lamellipodial edge of 3 human platelets (from $n = 3$ independent experiments, 2 platelets shown) and measured the apparent width of the lamellipodial edge tension ring as tPAINT data is integrated over various time windows. Super-resolved tPAINT images were rendered as greyscale images, and ring width was measured via linescan analysis (black dots). The data were fit to a gaussian via Matlab's curvefitting tool (blue line). The measured FWHM of the fitted gaussians depends on the number of frames integrated to produce the super-resolved tPAINT image. (**b**) Plot showing that the localization density generally increased with increasing the number of integrated frames. Each color shows a unique ROI. (**c**) Plot showing the relation between the FWHM of the tension ring and the number of integrated frames. The data shown are from 3 human platelets from $n = 3$ independent experiments (2 linescans per platelet). In principle,

**Figure 36, continued:** it is desirable to use the minimum number of frames possible to render an image in order to minimize feature blurring due to cellular dynamics during the imaging window; however, image quality decreases, with localizations becoming more punctate, when fewer frames are integrated. To produce high-quality tPAINT images, these considerations must both be balanced. All scale bars are 2 μm.

### *4.3.5 Characterizing the Signal-to-noise Ratio of tPAINT*

We noted that some single-molecule binding events occur within cell-free areas of the surface. This suggests that a portion of the single-molecule events we observe are not mediated by receptor forces opening tPAINT probes. To understand the origin of the single molecule fluorescence events that occur outside the cell-surface contact area, we synthesized imager complementary to the tPAINT tension probes, denoted the "specific imager strand," and imagers with a scrambled sequence that are not complementary to the tPAINT tension probes, denoted the "scrambled imager strand" (Figure 37a, b) We prepared cell-free tPAINT surfaces and added scrambled or specific imagers to the surface at 2.5, 5, and 10nM and collected 2000 frames at 5Hz in TIRF excitation. Representative tPAINT images for the accumulated-tPAINT probe (Figure 37c) and the sf-tPAINT probe (Figure 37d) are provided. We calculated a localization flux (localizations $\mu m^{-2}$ $s^{-1}$) for 3-5 regions of interest per surface for both specific and scrambled imager ($n$ = 3 independent experiments, Figure 37e). For both the accumulated-tPAINT probe and sf-tPAINT probe, the scrambled imager produced very low levels of single-molecule localizations, while the specific imager produced a significant increase in the localization flux for 10 nM relative to the scrambled imager (2-way ANOVA). Because the background localization flux is imager-sequence-specific, it is unlikely to be the result of non-specific imager binding to

the surface. Instead, it is probable that the background signal is due to imager binding to open tPAINT probes. tPAINT probes could have constitutively exposed docking sites due to synthesis defects. For sf-tPAINT probes, these defects could be present in the anchor strand (black strand, Figure 37b), causing the docking site to be constantly available for imager binding. Similarly, thermal energy will lead to probe "breathing," meaning

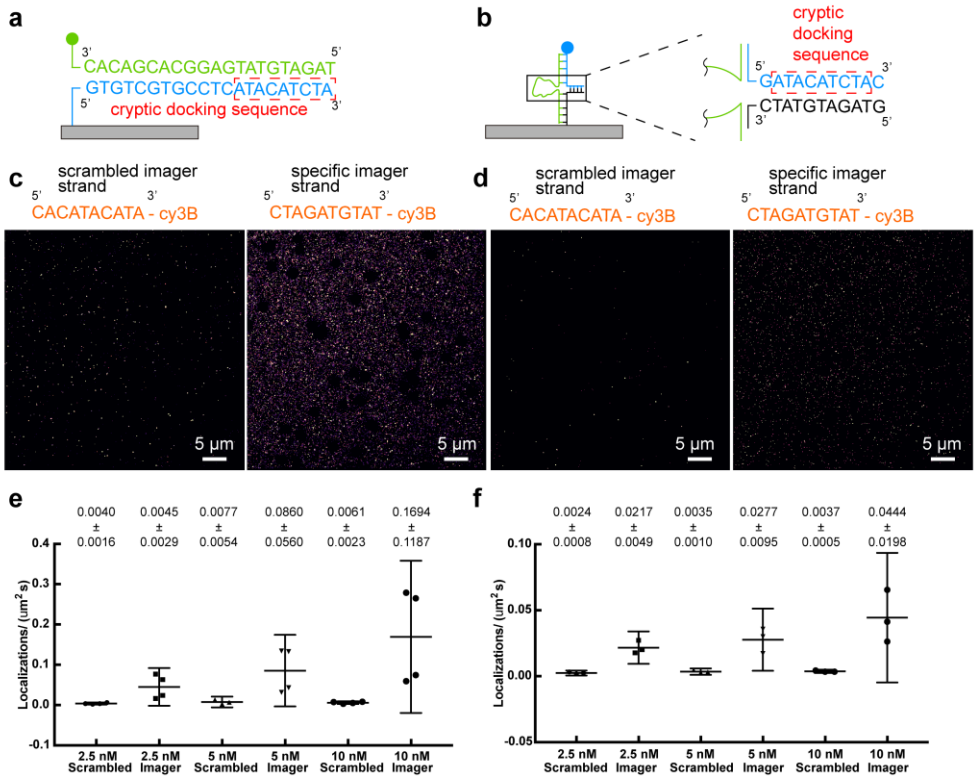


**Figure 37: tPAINT Background Single-Molecule Localizations Are Imager-Sequence-Specific**

(**a**) Surfaces presenting accumulated-tPAINT probes or (**b**) sf-tPAINT probes were incubated with scrambled-imager and imager. (**c**) Representative images compiled from 2000 frames of single molecule localization for accumulated-tPAINT surfaces and (**d**) sf-tPAINT probes incubated with 5 nM scrambled and specific imagers. Increased numbers of localizations occur for identical concentrations of specific imagers relative to scrambled controls. The average localizations/($\mu m^2 s$) were quantified at 2.5, 5, and 10 nM scrambled and specific imagers for (**e**) accumulated-tPAINT and (**f**) sf-tPAINT surfaces (4 independent experiments for each condition).

**Figure 37 continued:** For (**e**) and (**f**) the localization flux was computed for 5 regions per image to compute an average localization flux per surface (black points). Mean ± standard deviation is provided for each category in the figure. Error bars display a 95% CI. Mean ± standard deviation is provided in the figure for each category. Data were compared via a 2-way ANOVA. For localization on accumulated-tPAINT probe surface: 2.5 nM scramble is not statistically different than 2.5 specific (p=0.9968); 5 nM scramble is not statistically different than 5 nM specific (p=0.7527); 10 nM scramble is statistically different than 10 nM specific (p=0.0115). For localization on sf-tPAINT probe surface: 2.5 nM scramble is not statistically different than 2.5 specific (p=0.3153); 5 nM scramble is not statistically different than 5 nM specific (p=0.1051); 10 nM scramble is statistically different than 10 nM specific (p=0.0023).

that at equilibrium a small proportion of tension probes will be transiently open and thus available for imager binding. For the accumulated-tPAINT probe, the ligand strand (green strand, Figure 37a) has a slow off rate that will cause an increase in the number of open accumulated-tPAINT probes as a function of time. Similarly, any improperly assembled accumulated-tPAINT probes will also present constitutively available binding sites on the surface.

Given that some background signal is present in tPAINT experiments, we sought to characterize the signal-to-noise ratio. We calculated the localization flux (localizations $\mu m^{-2}$ $s^{-1}$) for platelet-surface contact areas and for cell-free regions (Figure 38). The accumulated-tPAINT probe offers a signal-to-noise ratio of up to 17, while the sf-tPAINT probe with 37.5mM $Mg^{2+}$ produces a signal-to-noise ratio of up to 10. The source of contrast in tPAINT experiments is "mechanoselection," meaning that the majority of the observed signal comes from mechanical strain exposing the docking site of probes that experience receptor forces exceeding the probe $F_{1/2}$.

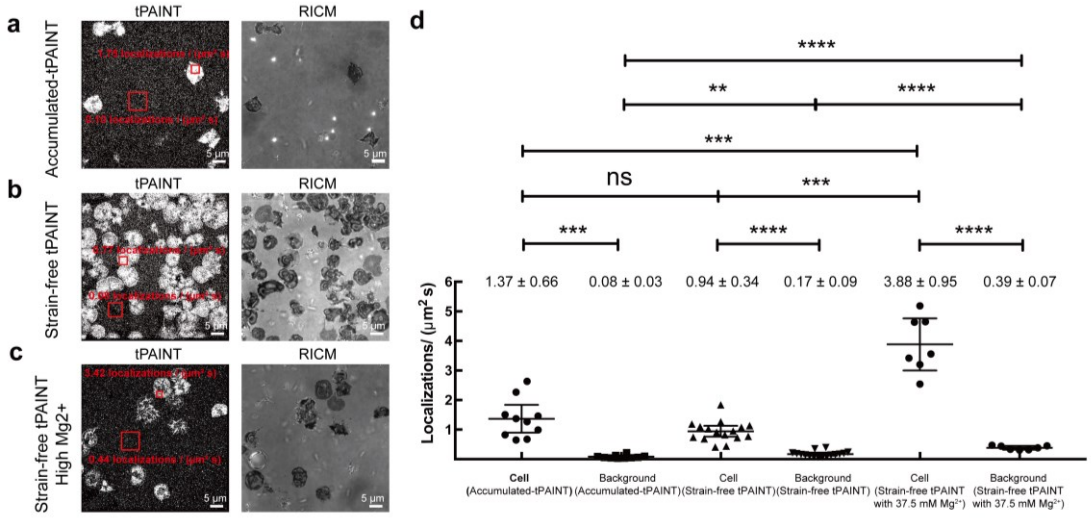


**Figure 38: Mechanoselection Produces a Signal-to-Noise Ratio of Up to 17 for tPAINT**

Human platelets were seeded on surfaces presenting cRGD-modified (**a**) 12pN $T_{tol}$ accumulated-tPAINT probes at low [$Mg^{2+}$], (**b**) strain-free tPAINT at low [$Mg^{2+}$], and (**c**) strain-free tPAINT with 37.5 mM $Mg^{2+}$. Note that the $F_{1/2}$ of the sf-tPAINT probe is somewhat dependent on ionic strength; therefore, the $F_{1/2}$ of the sf-tPAINT probe is 8 pN in mM $Mg^{2+}$and 8.5 pN in 37.5 mM $Mg^{2+}$. However, because higher $F_{1/2}$ probes should be opened by receptors less frequently than low $F_{1/2}$ probes (assuming that low forces are more common), this change in $F_{1/2}$ cannot account for the trends observed in this figure. Also, note that the images displayed are raw-unfiltered single molecule localizations of tPAINT images with the contrast adjusted to emphasize the background localizations. (**d**) The average, per image localizations/($\mu m^2$s) for both the background and for the mechanical footprint of platelets (3 ROIs per image) were computed for 9 images from 5 independent experiments. The number of single molecule localizations were significantly enhanced under the cell. Results are representative of $n$ = 4 independent accumulated-tPAINT surfaces, $n$ = 8 sf-tPAINT surfaces and $n$ = 3 high [$Mg^{2+}$] sf-tPAINT surfaces (10 images for accumulated-tPAINT, 16 images for strain-free, 7 images for high [$Mg^{2+}$] strain-free). Mean ± standard deviation is provided in the figure for each category. Data is displayed as mean with 95% confidence interval. ** $p<0.01$, *** $p<0.001$, **** $p<0.0001$.

### *4.3.6 Further Enhancing the Sampling Rate of tPAINT*

Supplementing imaging media with high concentrations of Magnesium works well to increase imager on rates[151] and increase the quality of tPAINT images (compare Figure

33 to Figure 34). However, divalent cations may alter biological function. The ability to perform tPAINT without high concentrations of $Mg^{2+}$ is therefore of significant interest.

#### 4.3.6.1 Potential Biological Effects of Elevated $Mg^{2+}$

The use of elevated $Mg^{2+}$ likely modulates biological function in tPAINT experiments. For example, the platelet integrin $\alpha_{IIb}\beta_3$ interacts with a c-terminal γ-chain sequence (KQAGDV) of fibrinogen[168, 169] and also recognizes the Arg-Gly-Asp (RGD) sequence used in this work and in previous molecular tension probe experiments[6, 67]. The $\alpha_{IIb}$ subunit is made up of a small cytoplasmic region, TM domain, 2 "calf" domains, a "thigh" domain, and a C-terminal 7-bladed β-propeller. $\beta_3$ contains a larger cytoplasmic tail, TM domain, 4 EGF domains, a PSI domain, hybrid domain, and a β-I domain. According to structural models, integrins take on 3 main conformations with relation to ligand binding: a low affinity "bent" conformation, an intermediate affinity extended-closed conformation, and a ligand-bound high affinity state (extended with open headpiece)[170]. Integrins, including $\alpha_{IIb}\beta_3$, possess several metal ion binding sites that coordinate divalent cations (generally $Ca^{2+}$ or $Mg^{2+}$) and that are important to integrin function. Formation of the dimeric integrin structure itself requires μM divalent cations, and both $Ca^{2+}$ and $Mg^{2+}$ can substitute for each other in some of the metal ion binding pockets.[171] The $\beta_3$ A-domain contains a metal ion dependent adhesion site (MIDAS), adjacent MIDAS (ADMIDAS), and synergistic metal binding site (SyMBS), where $Mg^{2+}$ occupies the MIDAS and $Ca^{2+}$ occupies the ADMIDAS and SyMBS.[172] The $Mg^{2+}$ cation is even critical for ligand binding, as the he MIDAS $Mg^{2+}$ coordinates the aspartate in the RGD. In crystal structures of $\beta_3$ the MIDAS is partially occupied at 1 mM $Mg^{2+}$ and fully

occupied at 5 mM $Mg^{2+}$ concentration[172]. Undoubtably, the use of 37.5mM $Mg^{2+}$ during sf-tPAINT platelet experiments will alter integrins behavior in these experiments[172].

Beyond altering integrins, $Mg^{2+}$ may also affect platelet function. In the early 1990s, it was observed that low mM doses of $Mg^{2+}$ prolonged bleeding time, and inhibited platelet fibrinogen binding and aggregation[173], with aggregation being abolished in the 1-4 mM range[174]. Additionally, $Mg^{2+}$ inhibits other markers of platelet activation, such as P-selectin exposure[175, 176]. It is not immediately clear how to interpret the $Mg^{2+}$ reliance of platelet integrins with the platelet inhibitory effect of similar concentrations of $Mg^{2+}$. $\beta_3$ contains two types of binding sites for metal ions, ligand competent (LC) sites which promote ligand binding, and inhibitory (I) sites which inhibit ligand binding by increasing the dissociation rate of RGD[177]. Initially the latter sites seem like likely candidates for the effect of $Mg^{2+}$, but this hypothesis is weakened by these sites' $Ca^{2+}$ specificity[178]. Nevertheless, it is possible that $Mg^{2+}$ can "substitute" for $Ca^{2+}$ here, especially at higher concentrations.

The effect of divalent cations is not limited to platelets. For example, $Ca^{2+}$ and $Mn^{2+}$ directly alter $\alpha_v\beta_3$ conformation[179]. Cations have been shown to alter the organization and formation of $\alpha_v\beta_3$ and $\alpha_v\beta_5$ focal adhesions[180]. It is reasonable to suspect that the 75 mM $Mg^{2+}$concentration employed in fibroblast experiments may also alter their biology.

#### 4.3.6.2 Tuning Imager Sequence to Increase the Rate of Imager Sampling

Due to the potential of elevated $Mg^{2+}$ to alter biological function, it is desirable to have alternative means to increase the $k_{on}$ of the imager. Jungmann and colleagues[151] provided two means to increase imager $k_{on}$, charge shielding DNA with high concentrations

of divalent cations (e.g. $Mg^{2+}$ as was done in Figure 34), or tuning the sequence of the imager to avoid transient self-interactions between nucleobases in the imager. The imager used in Figure 34 has the sequence CTAGATGTAT. The imager contains all 4 nucleobases, and these bases may transiently interact at room temperature. Transient interactions will cause the imager to spend a significant proportion of its time in bent conformations. Recent optical trap measurements suggest that the transition state for DNA-DNA binding is visited before the strands form base pairs, and that the rate limiting step in hybridization may be aligning the strands before base pairs form[162]. Self-associations that cause the imager to spend a significant amount of time in bent conformations will decrease the imager $k_{on.}$ Accordingly, Jugnmann and colleagues used an imager with the sequence TCCTCCC and found that its $k_{on}$ is $7.1x10^6$ $M^{-1}s^{-1}$ compared to $1.25$ $x10^6$ $M^{-1}s^{-1}$ for the CTAGATGTAT imager.

We sought to adapt our sf-tPAINT probes to work with the speed optimized TCCTCCC imager. We synthesized four different variants of this speed optimized sf-tPAINT probe (Table 6). We performed tPAINT imaging with MEF-GFP-vinculin cells using probes that differed slightly in their thermal stability (and therefore $F_{1/2}$) to identify a probe that suppressed background signal and produced rapid binding kinetics (Figure 39). We found that the signal-to-background ratio was further enhanced by adding two additional T bases to either ends of the stem structure of the sf-tPAINT probe (Figure 39), perhaps due to decreasing the steric hindrance posed by the tension probe as the imager approaches the docking site.

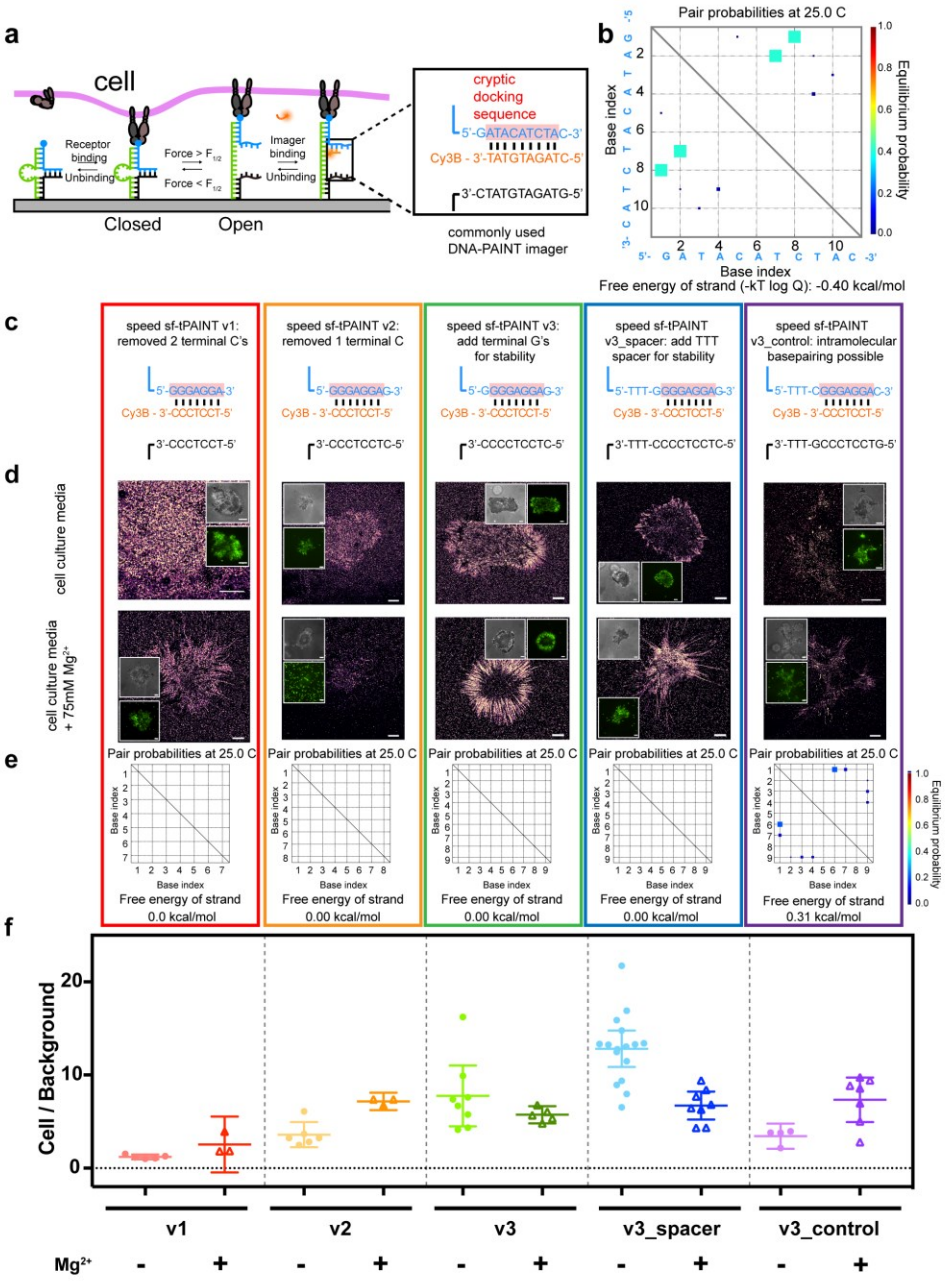


**Figure 39: Sequence Optimized sf-tPAINT Probes**

(**a**) Schematic that shows how strain-free tPAINT probes function and the sequences for the imager and cryptic docking site. (**b**) NUPACK modeling of the docking site reveals internal base-pairing, producing a kinetic barrier that impedes imager binding, reducing the on rate. (**c**) Sequence and design of speed-optimized sf-tPAINT docking sites (blue) that were modeled and tested. The highlighted pink sequence represents the imager binding domain (**d**) Representative speed sf-tPAINT images of MEF GFP-

**Figure 39, continued:** vinculin cells that were imaged in cell culture media (~0.8 mM $Mg^{2+}$) and in 75 mM $Mg^{2+}$ supplemented media. (**e**) NUPACK modeling of the speed sf-tPAINT probes showing that the docking site lacks internal base pairing. (**f**) Plot showing the ratio between tPAINT localizations under the cell normalized to the number of localizations in the background. v1, v2, and v3 use the same imager, but the docking site differs in its thermodynamic stability. v1, v2, and v3 are progressively more stable with the addition of flanking G-C base pairs. Hence, v1 and v2 showed greater levels of thermal breathing and background localizations at low $Mg^{2+}$ conditions. v3 produces improved signal/noise signal compared to the v1 and v2. The signal/background ratio was further improved by incorporating a TTT spacer in between the arm of the sf-tPAINT probe and the docking site, likely by increasing the accessibility of the docking site. The v3_control is predicted to form internal base-pairs, and accordingly it shows lower S/N compared to v3. This result underscores the importance of preventing intramolecular base-pairing, even when the speed-optimized sequence is used. The images and data displayed are from $n$ = 3 independent experiments for v1-v3, and $n$ = 4 independent experiments for v3_spacer and v3_control. All scale bars are 5 μm. Data were compared via a 2-way ANOVA. v3_spacer (in the no added $Mg^{2+}$ case) is statistically different from v1 ($p < 0.0001$), v2 ($p<0.0001$), v3 ($p = 0.0022$), and v3_control ($p<0.0001$). The v3_spacer exhibits the greatest S/N among the sequences tested; this is the superior speed-optimized sf-tPAINT design. Data in **f** is displayed as mean with 95% confidence interval.

Importantly, the speed-optimized sf-tPAINT probe enables high quality super-resolved imaging of pN receptor forces without the use of divalent cations that might perturb the biological system. However, using a high concentration of $Mg^{2+}$ provides an even higher $k_{on}$ rate, providing a means to image very dynamic processes. A subset of MEF-GFP vinculin cells produced significant filopodia upon contact with the surface. These cells were imaged with 75mM $Mg^{2+}$ and 10nM of the speed-optimized v3_spacer probe. Due to the high imager $k_{on}$, we were able to measure filopodia forces with up to 1 minute temporal resolution (Figure 40a-c). We overlaid the sf-tPAINT single-molecule localizations with the RICM footprint of the cell and confirmed that the observed single-molecule signal coincides with filopodia (Figure 40b). We were also able to visualize filopodia retraction and lateral filopodial motions of as little as 100nm (Figure 40d-g).

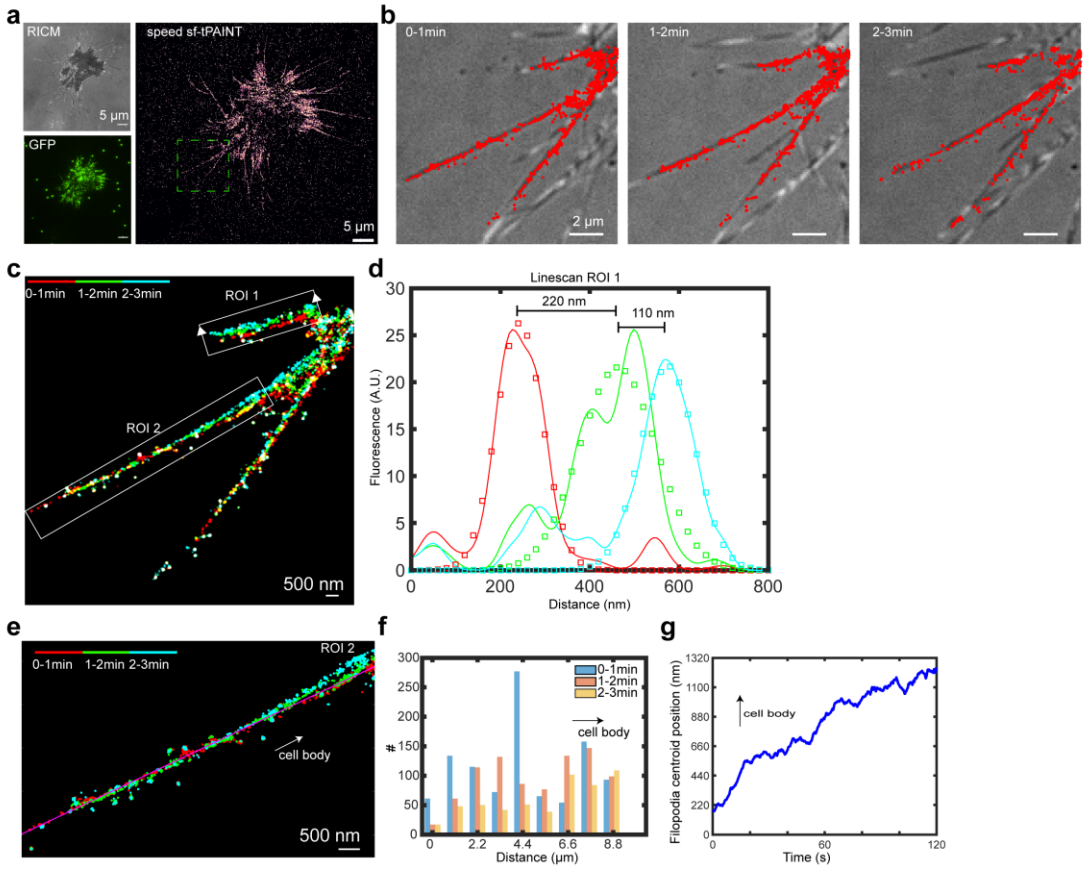


**Figure 40: Speed-Optimized sf-tPAINT Measurements of Filopodial Tension**

(**a**) A subset of MEF GFP-vinculin cells produced filopodia after they spread on cRGD-presenting 9.1 pN tPAINT surfaces. Integrating 900 frames (collected at 5 Hz; 3 min total time imaging interval) revealed integrin-generated tension exerted by the fibroblast. (**b**) Filopodia were identified using RICM. Time-resolved single-molecule tension localizations were manually masked according to the contact area of individual filopodia. The region shown in (**b**) corresponds to the green box from (**a**). Note that only the localizations within the region of interest are displayed and analyzed in in **b-g**. (**c**) Overlay of sf-tPAINT filopodial tension dynamics. Color indicates the time bin during which the localizations were observed. (**d**) Linescans from the region indicated in the white box from **c** reveal lateral filopodial "scanning". Data points (squares) are derived from a Gaussian fit of the raw data which is represented by solid lines. (**e**) Zoom-in of middle filopodia from (**c**) where color indicates the time bin. The magenta line represents a best fit calculated using linear regression. (**f**) Histogram of single molecule localizations projected onto the magenta line from **e**. (**g**) Filopodial centroid position inferred from the average projection of single-molecule localizations onto the magenta line within a 1 min sliding window reveals the dynamics of filopodial retraction.

### *4.3.7 Accumulated-tPAINT: Super-Resolved Receptor Force History*

Even when utilizing speed-optimized PAINT (elevated $Mg^{2+}$ and sequence optimized probes), tPAINT will not fully record all receptor-mediated mechanical events. To eliminate undersampling of mechanically opened probes, we employed DNA tension probes that rupture irreversibly under force. These probes are inspired by the tension gauge tether (TGT) originally developed by Wang and Ha[25]. In contrast to the $F_{1/2}$ that characterizes reversible DNA-based molecular tension probes such as the sf-tPAINT probes, TGTs are characterized by a tension tolerance ($T_{tol}$). The $T_{tol}$ is defined as the force that will lead to DNA duplex rupture within two seconds[25] and is based on magnetic tweezer measurements and the de Gennes model of DNA rupture[159, 160]. These probes rupture irreversibly when receptor force, $F$, exceeds the $T_{tol}$, potentially enabling a tPAINT technique that reports the force-history of cells (Figure 41a). We termed this technique accumulated-tPAINT.

To adapt the TGT to enable these probes for accumulated-tPAINT, a cryptic DNA-PAINT docking site was encoded withing the surface-anchored strand of the TGT. This docking site is left anchored to the surface after probe rupture (Figure 41a). Because these duplexes rupture irreversibly, imagers repeatedly sample the exposed cryptic binding sites, generating accumulated-tPAINT images of the force "history" of mechanical events where $F > T_{tol}$. We synthesized accumulated-tPAINT probes (Table 6, Table 7, Figure 52) comprised of a DNA duplex with one oligonucleotide anchored to the substrate while the other is modified with cRGD (Figure 41a). Conceptually, accumulated-tPAINT is amenable to long term imaging of receptor forces, and higher resolution/precision is possible simply by imaging receptor forces for a longer time.

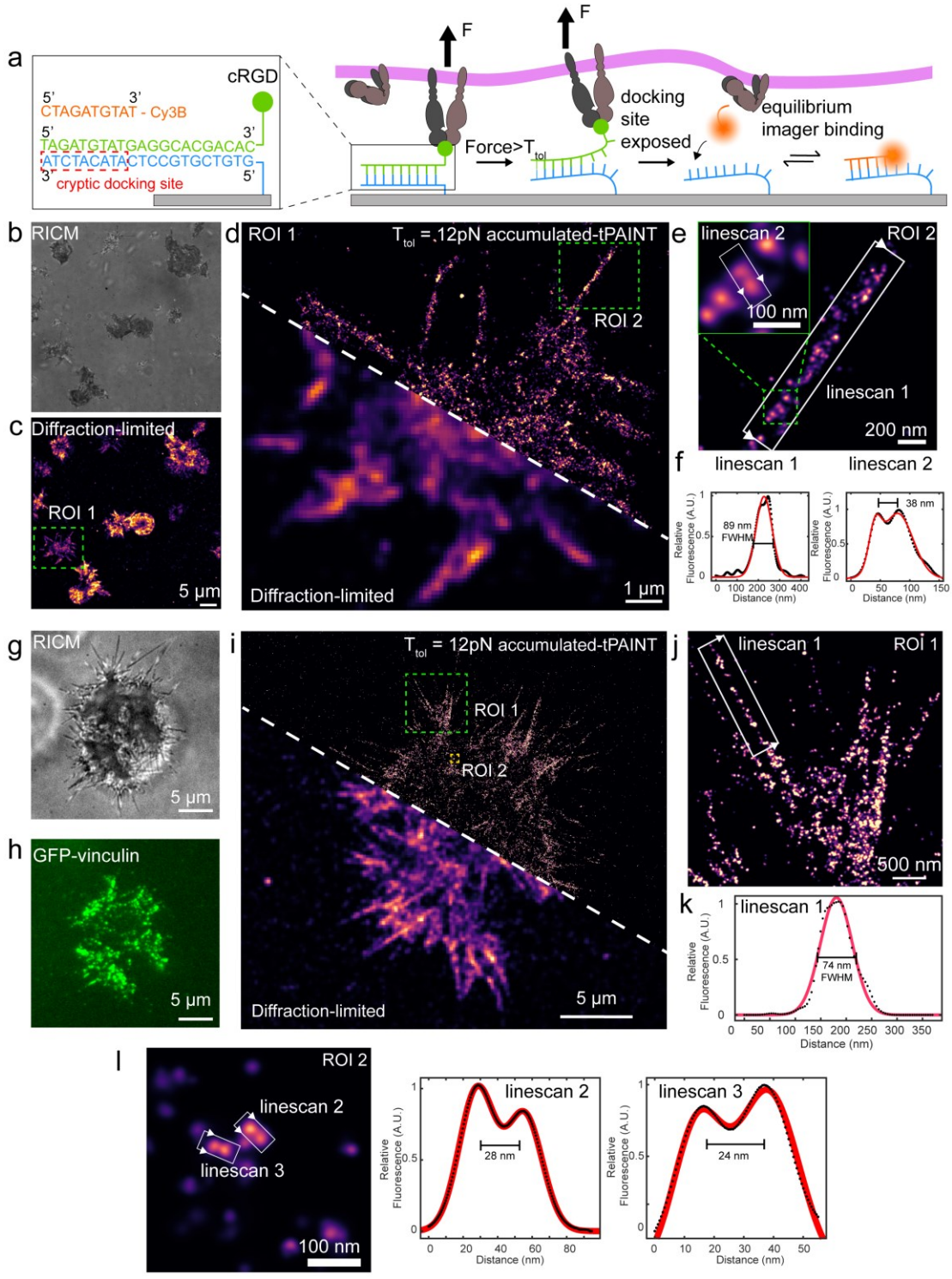


**Figure 41: Accumulated-tPAINT Measurement of Platelet and MEF Receptor Force History**

**Figure 41, continued:** (**a**) Schematic showing mechanism of accumulated-tPAINT. When integrin $F > T_{tol}$, the probe ruptures, exposing a cryptic docking site. Cy3B imager strands transiently bind to this exposed site to report the cellular traction force footprint. (**b**) and (**c**) show RICM and diffraction-limited 12 pN tension map of platelets seeded on the surface for 25 min. Color indicates the localization density. (**d**) Overlay of accumulated tPAINT image with the diffraction-limited reconstruction. (**e**) Zoom-in of the green ROI noted in **d**. (**f**) Linescans of structures noted as **i** and **ii**. The direction of the linescan is depicted using white arrows. Red fit is based on a Gaussian with FWHM shown on plots. (**g**) RICM and (**h**) GFP vinculin images of MEF cells on an *accumulated*-tPAINT surface for ~25 min. (**i**) 12 pN *accumulated*-tPAINT and diffraction-limited overlay. (**j**) Zoom-in of ROI indicated by the green rectangle in **i**. (**k**) Linescan across the filopodial tension indicated by ROI in **j**. (**l**) 12 pN tension hot spots that are separated by 24 and 28 nm. The platelet data shown is representative of $n = 8$ replicates (22 images) while the fibroblasts data is representative of $n = 9$ replicates (24 images).

We seeded human platelets on the $T_{tol}$ = 12 pN accumulated-tPAINT surface and, after ~10 min, performed accumulated-tPAINT (Figure 41b). Platelets were imaged in TIRF excitation mode at 5 Hz over a duration of 25 min with 2.5 nM Cy3B imager. As expected, single molecule Cy3B imager localizations were enhanced at the platelet-surface contact area, providing an average signal-to-noise ratio of 17 (Figure 38). Overlaying the diffraction-limited reconstruction (Figure 41c) with the accumulated-tPAINT image demonstrates the improved resolution (Figure 41d). Specifically, we identified the tension footprint of a platelet filopodium measuring 89 nm in width (Figure 41e, f). The platelet data shown in Figure 41 was collected with ~10 nm precision (0.09 pixel) determined by nearest neighbor analysis[181] (Figure 42), matching the typical precision metrics for DNA-PAINT[148].

We also produced accumulated-tPAINT maps of MEF traction forces (Figure 41g-l), showing filopodial-generated tension ~74 nm in width (Figure 41j, k). In our hands, we

were able to resolve ruptured probes separated by ~25 nm within the MEF tension footprint (Figure 41l).

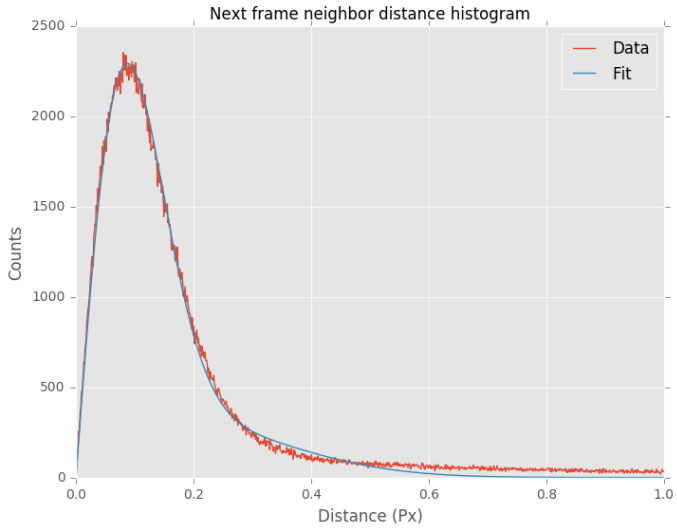


**Figure 42: Precision of tPAINT Measurement**

The nearest-neighbor localizations in temporally adjacent frames were calculated in Picasso to determine the localization precision as previously described. For the single molecule localizations that produced the image in Figure 41b-f, the nearest neighbor distance was calculated as 0.09 pixels, corresponding to a precision of ~10 nm.

Finally, we wanted to determine the spatial resolution limit of tPAINT. We suspected that the resolution of tPAINT is limited not by the localization precision, but by the spatial distribution of tPAINT probes on the substrate. We performed two different measurements to assess the surface density of probes. The first measurement was to directly image the density of probes on the surface via DNA-PAINT. Surfaces were coated in a layer of docking sites and imaged with 250 pM Cy3B imager for up to 11 hours to produce images of the surface density of docking sites (Figure 43a, c, g). We performed intensity-based peak finding and density-based spatial clustering (DBSCAN) to identify the spacing between clusters of docking sites on the substrate. These analyses suggested

that on average clusters of tPAINT probes were spaced 43 nm (intensity based peakfinding, Figure 43a, b) or 55 nm (DBSCAN, Figure 43c, d) apart. We noted that the localization density for the clusters on the surface was not uniform (Figure 43g), indicating that many docking sites were densely spaced within these clusters on the surface. We performed quantitative-PAINT (qPAINT)[182] which uses the predictable binding kinetics of imagers to docking sites to count the number of biomolecules in dense structures. We calibrated our imager binding $k_{on}$ as $1.2x10^{-6}$ $M^{-1}s^{-1}$ by measuring the influx rate of imagers to DNA origami bearing individual DNA docking sites at varying imager concentrations (2.5, 5, and 10nM, Figure 43e-f). We applied the calibrated $k_{on}$ rate to clusters on the docking site surface, and found that dense clusters of docks on the surface may contain as many as 15 docks within 110nm.

As an orthogonal measurement to quantify the density of tension probes on the surface, we performed quantitative fluorescence measurements by using SLBs with known densities of fluorophore-labeled lipids as reported in previous publications[143]. We measured the density of tension probes on the surface as 2420 +/- 249 per square micron (Figure 43i-l), which would suggest a dock is present on the surface approximately every 20nm. Taken together, these data demonstrate that tPAINT probes form a dense layer on the surface; however, the resolution of tPAINT is spatially heterogeneous due to the distribution of probes on the surface. The spatial resolution of tPAINT is likely limited by the surface density of tPAINT probes.

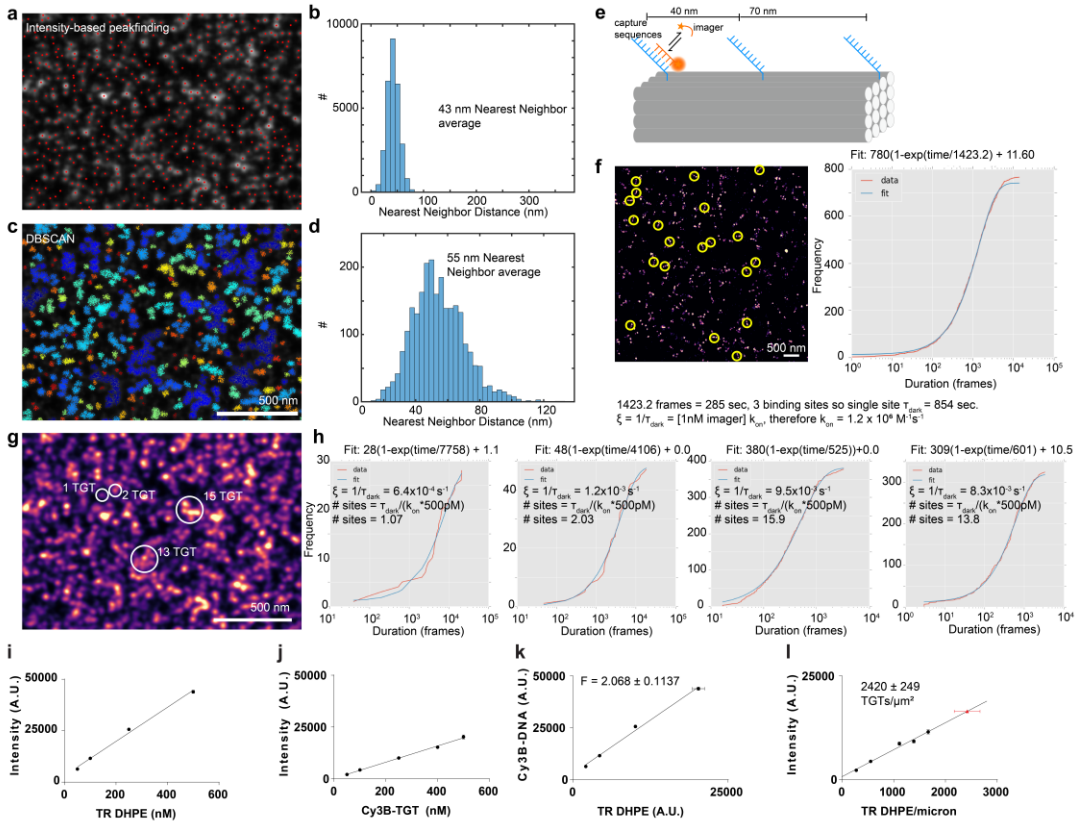


**Figure 43: Measuring the Surface Density of tPAINT Probes**

(**a**) Surfaces coated in docking sites were imaged using DNA PAINT with 500 pM Cy3B-imager and 200,000 frames were collected at 5 Hz. Intensity-based peakfinding (red dots) on the resulting DNA PAINT images revealed clusters of localizations. (**b**) Histogram of the nearest neighbor distances of all localizations identified by intensity-based peakfinding (only a small region of the whole image is shown in **a**). The average nearest-neighbor distance is 43 nm. (**c**) An alternate, DBSCAN-based clustering algorithm (20 localization minimum, 0.05 pixel search radius) was applied to the localizations contained within the ROI displayed in **a** and **c**. DBSCAN identified clusters of localizations. Each cluster is displayed with a unique color. (**d**) Histogram of the nearest neighbors of the centroids of the clusters identified by DBSCAN in **c**. Note that because DBSCAN is computationally intensive, it was applied to smaller ROIs than the intensity-based peakfinding. By this DBSCAN analysis, the average nearest neighbor distance between clusters was 55 nm for this ROI. Both algorithms identified clusters of varying size, shape, and localization number, suggesting that the current peakfinding/DBSCAN efforts have not identified individual docking sites on the surface. Accordingly, we elected to perform quantitative-PAINT (qPAINT) to directly count the docking sites on the surface. (**e**) To calibrate the influx rate, we

**Figure 43, continued:** performed DNA PAINT on DNA origami with 3 docking sites spaced by 40 and 70 nm. (**f**) DNA PAINT imaging was performed with 1, 2.5, and 5 nM Cy3B imager for $n = 3$ independent surfaces. The influx rate/$k_{on}$ were calculated by measuring the average influx rate of many origami (yellow circles in **f**). The plot to the right shows the cumulative distribution function of dark times between imager binding events (red) as well as an exponential fit (blue). As noted below the plot, the $k_{on}$ rate was calculated as $1.2 \times 10^6$ $M^{-1}s^{-1}$. (**g**) qPAINT was applied to a DNA PAINT image of the same region on the surface as (**a)** and (**c)**. (**h**) qPAINT analysis of the clusters indicated with white circles revealed that the dimmest peaks on the surface are single docking sites, while majority of the spots on the surface show 2 or more docking sites. Additionally, dense clusters (e.g. 13-15 docking sites) are often present on the surface. (**i-l**) Plots of quantitative surface density measurements used to determine the average density of probes on the surface. (**i,j**) Plots of fluorescence calibration curves for vesicles tagged with Texas-red phospholipid and soluble DNA oligos. (**k**) Plot showing the F factor calibration which is the ratio of the fluorescence of Texas red to Cy3B, calculated by measuring the fluorescence intensity of identical concentrations of Cy3B-labeled DNA and Texas red doped small unilamellar vesicles. (**l**) Using the F factor, we determined the average number of tPAINT probes on the substrate as 2420+/-249 probes per square micron. If distributed uniformly, we would expect to have one tension probe every 20 nm. In reality, the probes are non-uniformly distributed (**g**), thus the spatial resolution of tPAINT is spatially heterogeneous, ranging from 20-50nm depending on the local density of probes on the surface. The images in **a** and **c** are representative of $n = 3$ independent experiments.

### *4.3.8 sf-tPAINT Measurements Reveal that Platelet Lamellipodial Edge Tension is Arp2/3 Mediated*

We next sought to demonstrate the power of tPAINT to answer biological questions. We chose to focus on the ring of tension at the platelet lamellipodial edge (Figure 34). Several previous publications have utilized fibrinogen-coated TFM gels to measure platelet traction forces[127, 137]; however, these previous reports did not reveal the ring of forces at the platelet edge. Micropillar measurements have also revealed that platelets transmit forces to von Willebrand Factor via GP1b-IX-V[3]. To our knowledge, micropillar measurements have not been extended to single-platelet integrin forces but given the 2μm

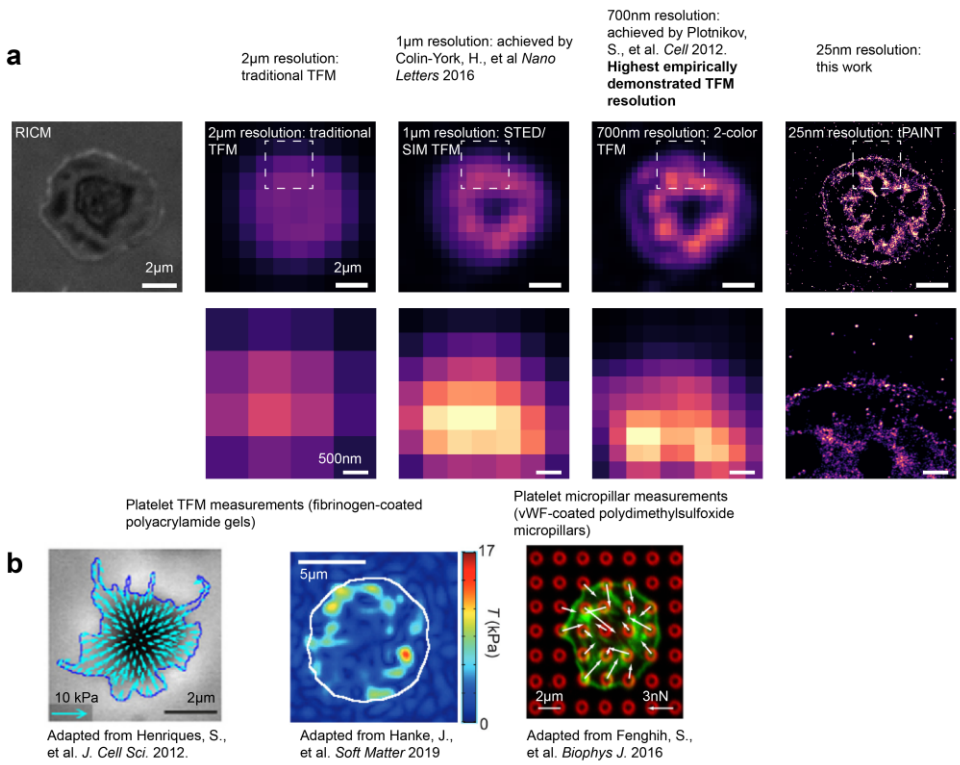


**Figure 44: Platelet Lamellipodial Edge Tension Requires High-Resolution Force Measurement**

(**a**) 8.5 pN sf-tPAINT images of platelet rendered at 2 m, 1 m, 0.7 m, and 25 nm resolution. The 0.7 m resolution represents the highest demonstrated resolution for TFM using two-color confocal imaging. Importantly, the edge tension of human platelets is only clearly resolved using sf-tPAINT. (**b**) Literature examples of human platelet TFM and micropillar data showing that many of the structural features of platelet mechanics cannot be resolved by TFM or micropillars. Note that the TFM data reports integrin-mediated forces on fibrinogen coated gels, while the micropillar data reports GP1b-IX-V forces transmitted to vWF coated pillars. Figure from Henriques, S. et al. *Journal of Cell* Science 2012 – adapted with permission from *Journal of Cell Science* (DOI of original article: 10.1242/jcs.108126). Figure from Hanke, J., et al *Soft Matter* 2019 – Published by the Royal Society of Chemistry and reused with permission under a Creative Commons Attribution-NonCommercial 3.0 Unported License. Figure from Fenghih, S., et al *Biophysical Journal* 2016 adapted with permission, Copyright Elsevier Science & Technology Journals.

spatial resolution of previous measurements[3], it seems unlikely that micropillars would be capable of resolving this ring of tension. Previous platelet mechanics measurements using DNA tension probes were able to report this ring[6, 67], but the ring appeared to be smaller than the diffraction-limited resolution of these previous widefield measurements.

#### 4.3.8.1 Quantifying the Dynamics and Size of the Platelet Lamellipodial Ring Tension

We observed that the ring of lamellipodial tension can be as thin as 90-160nm (Figure 34) and that this ring of tension appears to spread as the platelet lamellipodia edge advances (Figure 35). We wanted to quantify the spreading and width of this ring.

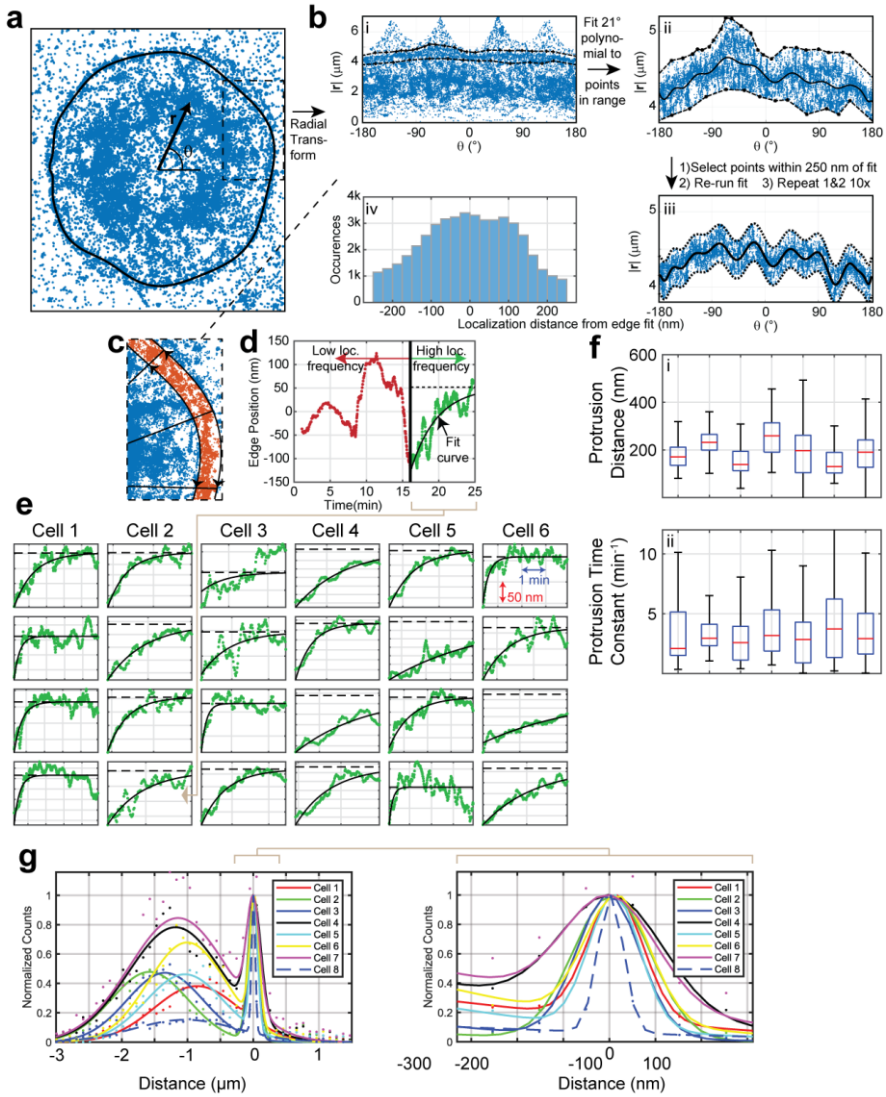


**Figure 45: Quantifying the Dynamics and Width of the Platelet Lamellipodial Edge Tension Ring**

**Figure 45, continued:** (**a**) Scatter plot of 8.5pN sf-tPAINT 20-30 min after seeding the cells. A radial coordinate system was established from the cell centroid (vector **r** and angle θ). The black contour denotes the approximate lamellipodial edge position calculated using an interactive algorithm. (**b**) To calculate edge position: i) data was transformed to a radial coordinate system and a polygon was manually drawn around the edge of the cell, ii) A 21$^{st}$-order polynomial was fit to the localizations within this polygon (shown as solid black line). iii) all localizations within 250 nm of the polynomial were selected and a new 21$^{st}$-order polynomial was fit to the localizations. This process was iterated 10 times. The final polynomial was taken as the cell boundary as shown in (**a**). iv) The distances of all localizations within 250 nm of the final contour was constructed. (**c**) Wedge-shaped regions of interest with 45°-wide slices were created and rotated around the origin in 1° increments to bin localizations within 250 nm of the boundary into angular slices. (**d**) Edge position of lamellipodial tension for each wedge was quantified as a function of time **b**-iv. The data shown corresponds to the 45° slice centered on θ=21° for cell 2 shown in (**c**). To identify the onset of platelet spreading, we identified the time quantified localization frequency. For the cell shown, localization frequency was ~2 $s^{-1}$, but increased to a sustained rate of ~8 $s^{-1}$ within the platelet footprint at ~15 min which was taken as the onset of lamellipodial edge tension and spreading. Prior to edge-formation, the measured edge position was random but followed a clear spreading trend after edge formation. The dynamics of lamellipodial outward edge migration were quantified by fitting edge position (R) vs. time (t) data to a decaying exponential function: position = $c-a*\exp[(t-t_0)/\tau]$, where τ, a, and c (which correspond to the protrusion time constant, the protrusion distance, and the final edge position, respectively) are all free fit parameters and $t_0$ (the time of edge formation) is obtained by finding the time point at which edge position is minimized. In (**d**), $t_0$ is denoted using a thick black line, and the fit curve is shown with a black curve. The best-fit c value is denoted using a dashed line. (**e**) For each of the six cells, calculated edge position data and fit curves are shown for $t > t_0$ for four non-overlapping 45° slices. (**f**) 343, 270, 213, 302, 318, and 308 slices, respectively, were analyzed using the fully-automated process described in **d** & **e**. Boxplots showing the populations of best-fit i) a values and ii) τ values are shown for each of the six cells. Median protrusion values (red horizontal line) ranged from 130 nm to 260 nm, with the compiled dataset having a median of 190 nm. Median τ values ranged from 2.1 min to 3.7 min, with the compiled dataset having a median of 2.9 min. (**g**) To calculate the width of the platelet lamellipodial edge, the localizations of a set of spread, static platelets corresponding to the single-molecule sf-tPAINT data from 1000 frames (collected at 5Hz) were fit to a 21$^{st}$ order polynomial as in (**a**). The distance of all localizations from this 21$^{st}$ order polynomial was calculated and plotted in a histogram (**g**). Zero in (**g**) represents the location of the 21$^{st}$ order polynomial, negative distances are towards the center of the platelet, while positive distances are towards the edge of the platelet. This analysis reveals a bimodal distribution of single-molecule localizations, a peak near the center of the platelet and a peak at the cell edge. The full width half maximum (FWHM) of 8 platelets ($n$ = 3 independent experiments) was calculated in this way. The average FWHM is 150 +/- 80 nm (mean +/- standard deviation).

We iteratively fit a polynomial to the single-molecule localizations of 6 platelets ($n$ = 3 independent experiments) and tracked the spreading of the lamellipodial edge tension ring. The mechanical ring was highly dynamic, translocating 185 +/- 75 nm over ~2-5 min (Figure 45). We applied a similar analysis to 8 well spread, static human platelets ($n$ = 3 independent experiments) and plotted a histogram of the distance of single-molecule localizations to the polynomial fit to the rim. We quantified the full-width-half-maximum of this distribution as 150 +/- 80 nm (Figure 45).

#### 4.3.8.2 The Platelet Lamellipodial Ring is Associated with an F-actin Ring

A technique capable of super-resolving both protein structures and the forces they generate could significantly advance the field of mechanobiology. Techniques such as TFM and micropillar arrays must use thick substrates such as a polymer gel or micropillar array[20]. These thick substrates are not amenable to single molecule localization. Accordingly, we are unable to find any reports of simultaneous traction force measurement with super-resolution measurement of protein structures. A technique capable of sub-100 nm mapping of both traction forces and protein assemblies generating those forces would be valuable to cell biology, enabling investigators to link receptor force generation with the protein structures that produce them.

A benefit of DNA-PAINT is that is enables facile multiplexing via exchange-PAINT[102]. In exchange-PAINT, biomolecule targets are labeled with orthogonal docking sites and sequentially imaged with orthogonal dye-labeled imager strands. In principle, tPAINT should be amenable to Exchange-PAINT, providing a means to super-resolve pN receptor forces and protein targets (exchange-tPAINT, Figure 46).

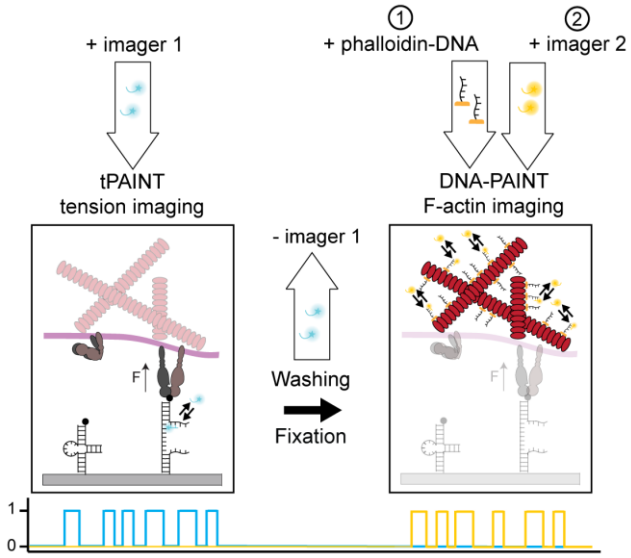


**Figure 46: Exchange-tPAINT Scheme**

Exchange-tPAINT enables super-resolved DNA-PAINT imaging of receptor mechanics by sequentially imaging live-cell receptor tension and protein targets within fixed cells.

The "ring"-like mechanical pattern of platelet integrin forces was consistent with the dimensions of high-density actin bundles that accumulate at the cell edge as observed by electron microscopy and fluorescence microscopy[183-186]. We therefore hypothesized that the peripheral ring of platelet tension might be associated with these actin bundles. We synthesized a phalloidin-DNA conjugate to enable PAINT imaging of F-actin structure[187].

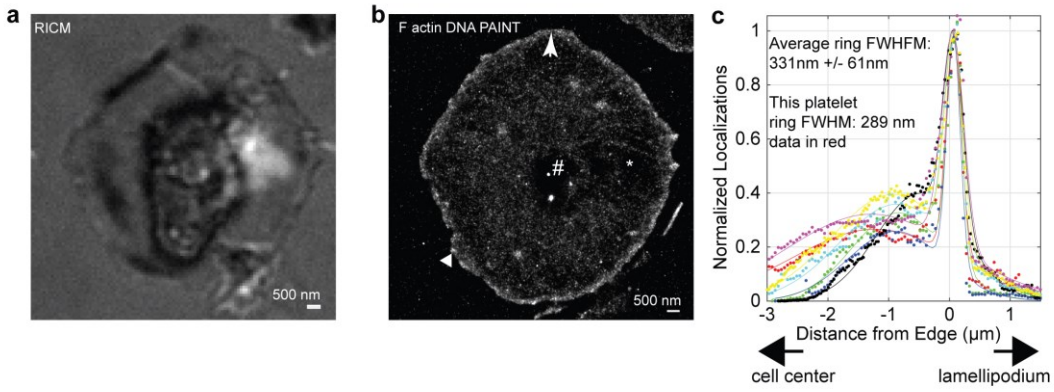


**Figure 47: DNA-PAINT Imaging of Platelet Actin Architecture**

(**a**) Human platelets RICM image and (**b**) F-actin DNA-PAINT image. (**c**) The full-width-half-maximum of the F-actin lamellipodial web was calculated using the procedure described in Figure 45 for 7 cells from 2 donors. The average actin web width is 330 +/- 60nm (mean +/- standard deviation).

tPAINT was used to image 14 pN platelet integrin tension exerted on cRGD-sf-tPAINT probes for 12 minutes at 5Hz in TIRF excitation. Immediately following tPAINT imaging, platelets were fixed with 4% formaldehyde for 10 minutes, permeabilized for 10 minutes with 0.1% triton, blocked with 3% BSA, and finally stained with 1μM DNA-conjugated phalloidin for 30 minutes. After staining, cells were imaged with 1nM Cy3B-tagged imager for 60 min at 5Hz. The images revealed a thin (330 +/- 60nm) ring of dense F-actin at the lamellipodial edge (Figure 47, 7 platelets $n = 2$ donors).

We next sought to determine whether the F-actin web was spatially associated with platelet lamellipodial tension. Overlaying time-resolved images of 14pN sf-tPAINT images with the F-actin images revealed that the platelet tension ring was spatially associated with the F-actin lamellipodial edge structure (Figure 48). Because pN tension was imaged in live cells just before fixation, we expect to see the closest spatial association

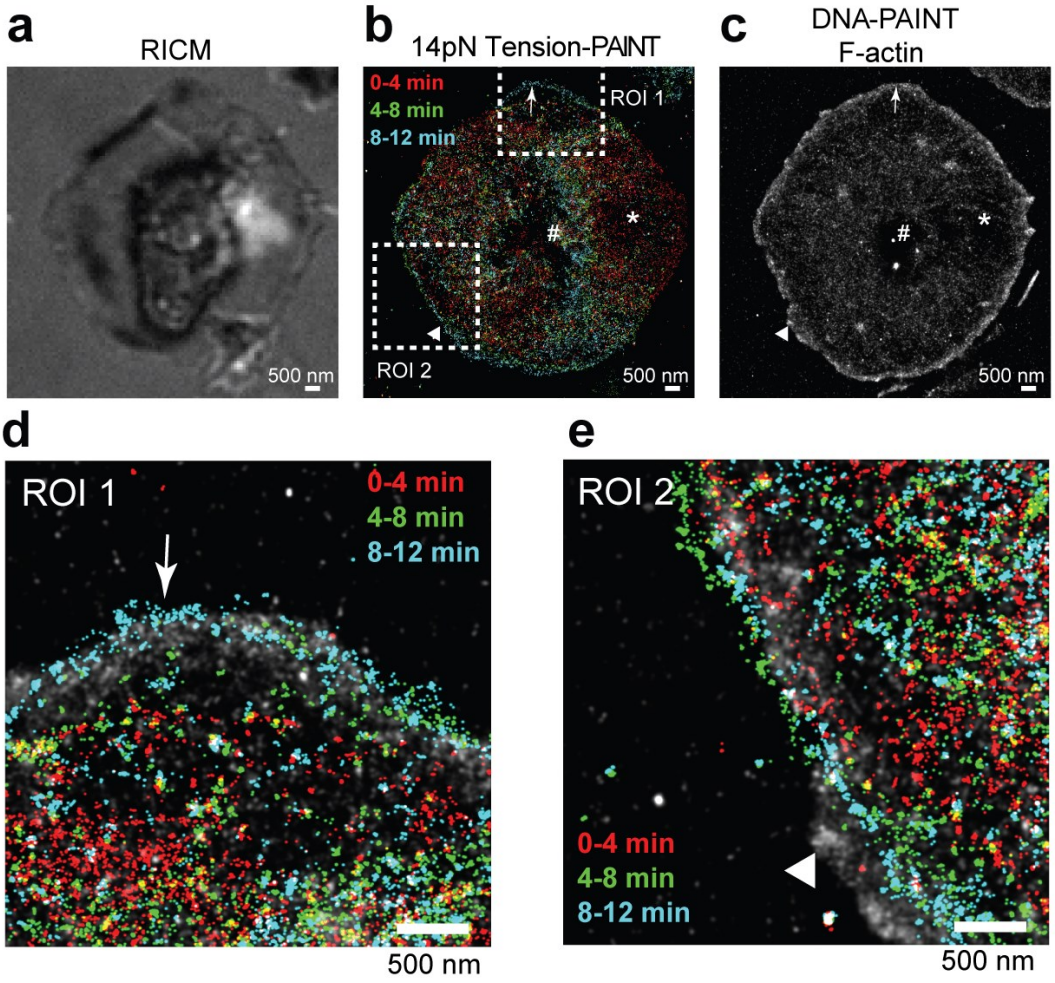


**Figure 48: Platelet Ring Tension Is Spatially Associated with the F-actin Ring**

Platelet 14 pN integrin tension was imaged before fixation, staining, and Exchange-PAINT to super-resolve the platelet actin cytoskeleton. (**b**) RICM, (**c**) time-resolved 14pN tension-PAINT, and (**d**) F-actin stained with DNA-tagged phalloidin images for one representative platelet. (**e-f**) Zoom in of tension at the lamellipodial edge reveals close association between tension and actin (arrow). In some regions, actin polymerization extends beyond tension (triangle). Note that an area of depleted actin (*) corresponds to an area where tension receded after 4 min. The # indicates a fiducial marker. Actin-tension data is representative of 7 platelets from $n$ = 2 independent experiments.

between late tension time points (8-12 min, cyan points in Figure 48b, d, e) and F-actin structure. Indeed, we observed that tension at the leading cell edge was often highly coupled with this F-actin rim (Figure 48b, d, white arrow). However, in some regions the

tension lags behind the F-actin edge (Figure 48b, e, indicated by the white triangle). We noted that in some regions, the platelet ring tension advanced rapidly during the observation window (compare 0-4 min red points with 8-12 min cyan points in Figure 48d, indicated by the white arrow). It is possible that regions where the tension ring lags behind the actin rim are areas of rapid actin polymerization in which the tension has not yet advanced to the ring edge (Figure 48e, white triangle). Also note that this platelet exhibited tension on the right side of the cell at 0-4 min but that the tension receded from the right side after that time (red points, Figure 48b, area of receding tension marked by an *). We noted that this area of receding tension was associated with a disrupted actin architecture within the interior of the platelet (Figure 48c, marked with *). Collectively, the close spatial association between platelet ring tension and the platelet lamellipodial edge actin architecture suggested a link between the actin structure and the integrin tension.

We next sought to understand the molecular origins of the platelet lamellipodial rim tension. We posited that the cell edge tension could be driven by Arp2/3-mediated branching actin polymerization. In previous studies, loss of Arp2/3 mediated branching polymerization caused platelets to lose lamellipodia and adopt a "spiky" morphology[188]. Additionally, Arp2/3 localizes to the lamellipodial edge of spreading platelets[189]. The role of Arp2/3 in lamellipodia is not limited to platelets because Arp2/3 deficient fibroblast cell lines do not exhibit lamellipodial spreading, instead relying on filopodia for protrusion and motility[190].

We therefore sought to pharmacologically inhibit Arp2/3-mediated branching actin polymerization in platelets. The Arp2/3 complex binds to the side of preexisting actin filaments and nucleates the formation of a new filament off the side of the old filament, so-

called branching actin polymerization. The small molecule CK666 binds to Arp2/3, blocking a conformational change required for its activity[191]. Additionally, CK666 has been previously used to inhibit Arp2/3 in platelets[188]. We therefore seeded platelets on sf-tPAINT surfaces and imaged control platelets (DMSO vehicle) and platelets treated with 50 μM CK666 after spreading. CK666 treatment abolished platelet lamellipodial rim tension in 2 platelets, while 7 other platelets failed to develop lamellipodial ring tension (9 platelets from $n = 2$ experiments, Figure 49). Pretreating platelets with 50 μM CK666 for 30 min prior to seeding slowed platelet spreading, prevented the formation of the rim tension, and often produced platelets with filopodia (Figure 49). Additional examples of

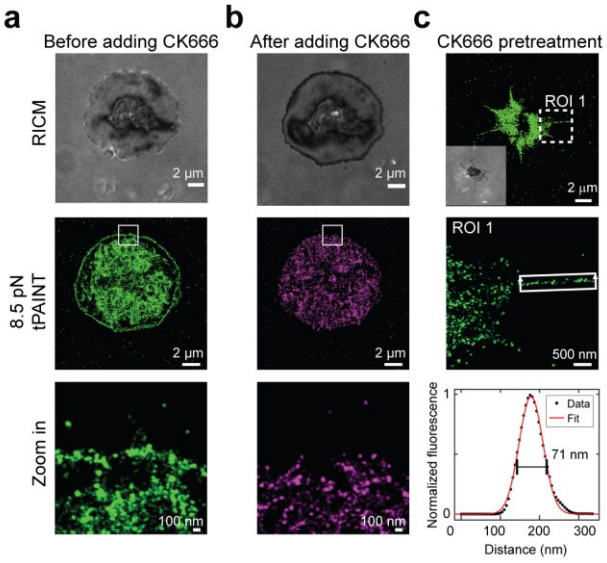


**Figure 49: Platelet Ring Tension Is Mediated by Arp2/3**

(**a**) Platelet contact area (RICM) and tPAINT signal before, and (**b**) after treatment with the Arp2/3 inhibitor CK666. CK666 removed platelet lamellipodial edge tension (2 platelets) or prevents lamellipodial edge tension (7 platelets) (9 platelets total from $n = 2$ independent experiments) (**c**) Platelets pretreated with 50 μM CK666 spread slowly, utilize filopodia to engage with the cRGD substrate, and do not exhibit lamellipodial edge tension

CK666 treated platelets are available in Figure 50. These data support the hypothesis that the platelet ring tension is Arp2/3 mediated.

Finally, previous work from our lab demonstrated that treating platelets with the myosin light chain kinase (MLCK) inhibitor ML-7 led to a global decrease in platelet tension[6]. We therefore seeded platelets on tPAINT surfaces and treated them with DMSO (vehicle control) or 10μM ML-7 and observed the expected decrease in 8.5 pN mechanical

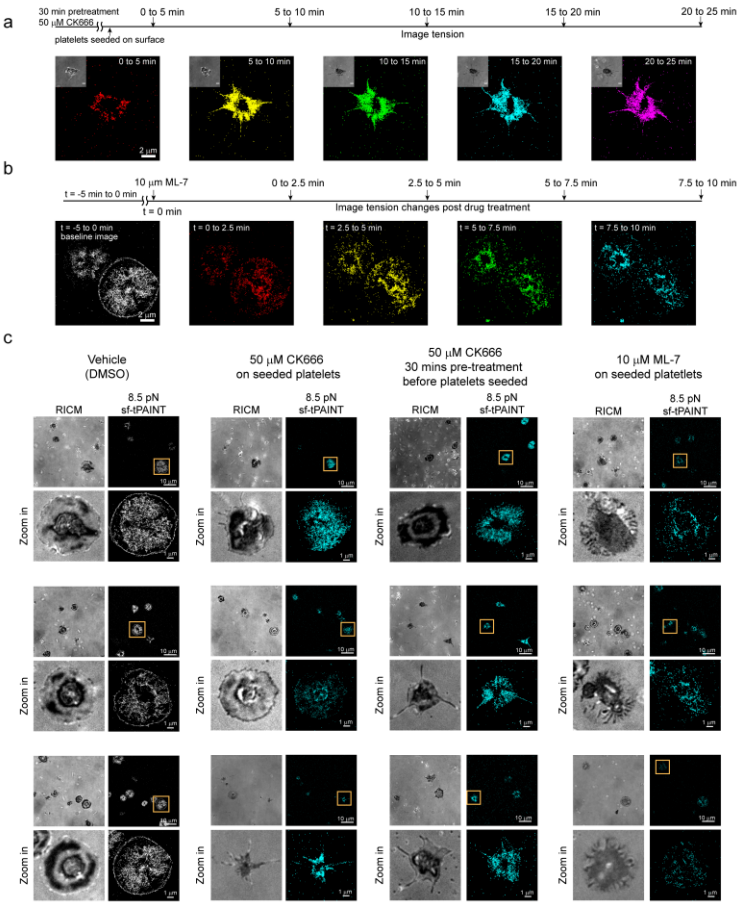


**Figure 50: Collage of Drug-treated Platelet tPAINT Signal**

(**a**) Time-resolved 8.5 pN tPAINT of platelets pre-treated with 50 μM CK666 for 30 min before being seeded on sf-tPAINT probes. (**b**) Time-resolved 8.5 pN tPAINT image of platelet before and after treatment with 10μM ML-7 (MLCK inhibitor).

**Figure 50, continued:** (**c**). Representative examples of images for cells treated with inhibitors displayed with a 5x density filter and kinetic filter. Human platelets treated with vehicle (DMSO) as control ($n$ = 3 independent experiments), human platelets treated with CK666 (50μM) after being seeded on the surface ($n$ = 2 independent experiments), human platelets pretreated with CK666 (50 μM) for 30 min before being seeded on the surface ($n$ = 3 independent experiments), human platelets treated with ML-7 (MLCK inhibitor, 10 μM) after being seeded on the surface ($n$ = 3 independent experiments). Three examples are shown for each condition. Note the absence of the thin lamellipodial edge tension upon inhibition of Arp2/3 (CK666 treatment).

events across the entire cell footprint, including in the cell center (Figure 50). ML-7 experiments also serve as a biological validation that the single molecule fluorescence events that we observe are due to receptor forces opening tPAINT probes.

Finally, we sought to determine the magnitude of the platelet lamellipodial ring forces. The $F_{1/2}$ of DNA-based molecular tension probes can be controlled by increasing the length of the stem that unfolds under force. We synthesized sf-tPAINT probes with $F_{1/2}$'s of 14 and 21pN (Table 6). We performed force-multiplexed tPAINT by conjugating cRGD-modified 8.5 pN and 14 pN or 8.5 pN and 21 pN probes on the same surface (Figure 51). The cryptic docking sites for the 8.5pN probe differed in sequence from the 14 pN and 21 pN probes. We synthesized two imagers with different fluorophores, targeting an Atto 488 conjugated imager to the 8.5pN sf-tPAINT probe and a Cy3B conjugated imager to the 14 pN and 21 pN tension probes. Human platelets were seeded on the force-multiplexed tPAINT surfaces with 7.5nM of both the Cy3B and Atto 488 conjugated orthogonal imagers. Platelets were simultaneously imaged with 488nm and 561nm TIRF excitation and imaged at 5Hz. Fluorescence emission was split by wavelength and captured simultaneously on two EMCCD cameras, enabling simultaneous force-multiplexed detection. 8.5 pN and 14 pN forces were both detected within the platelet lamellipodial

rim, but 21 pN forces were generally excluded from the lamellipodial ring tension (Figure 51). Receptor forces within the central region of platelets exceed 21 pN (Figure 51). These data are consistent with previous DNA-based tension probe measurements of platelet integrin forces[6].

Collectively, this data demonstrates that the platelet ring tension is likely Arp2/3 mediated, while the tension exerted within the center of the platelet is not (Figure 49, Figure 50). The tension rim is also spatially associated with the peripheral F-actin ring that has been described in previous publications[183, 184]. The low magnitude of lamellipodial forces similarly distinguishes the platelet edge tension from the interior tension (Figure 51). Interestingly, the polymerization force of F-actin has been quantified as 1-2pN[192], thus each integrin bound to sf-tPAINT probes must be connected to a network of polymerizing actin filaments to generate sufficient force to open the tPAINT probes.

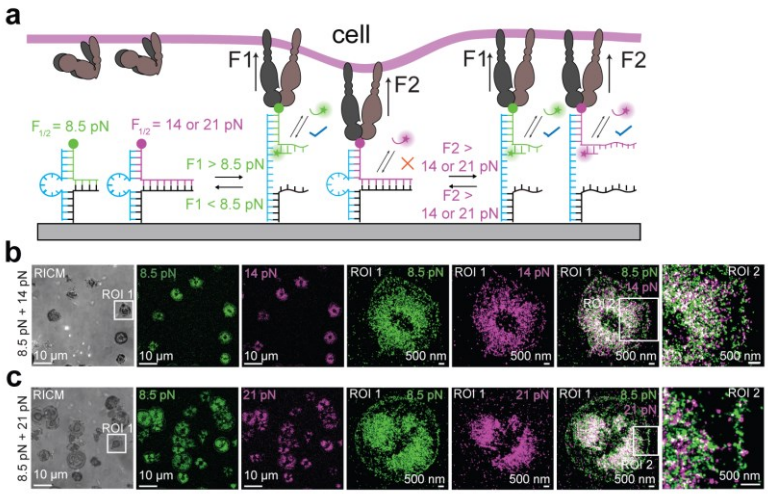


**Figure 51: Force-Multiplexed tPAINT Reveals Platelet Ring Forces Are Less Than 21pN**

(**a**) Force-multiplexed tPAINT is possible by coating surfaces in two probes with $F_{1/2}$ of 8.5 and 14 or 21pN. (**b**) Integrin forces within the ring are visible for probes with $F_{1/2}$ 8.5pN and 14pN. (**c**) Forces within the platelet ring rarely exceed 21pN. Force in the platelet center exceed 21pN.

## 4.4 Discussion

The current gold-standard technique for quantifying cell forces is Traction Force Microscopy (TFM), which calculates traction stresses transmitted to deformable polymer films with ~700 nm spatial resolution[20, 74, 193] (Table 5). Due to the need to resolve gel deformation in order to calculate traction stresses, TFM is generally only sensitive to nN forces[20]. tPAINT offers a complementary approach, mapping molecular (pN) mechanical events with up to 25 nm resolution.

**Table 5: Summary of Techniques for Quantifying Cellular Forces**

| Publication | Year | Spatial resolution | Required microscope | Notes |
|---|---|---|---|---|
| Sabass et al., *Biophysical Journal*[194] | 2008 | 1 μm | Confocal | Two color beads |
| Plotnikov, S., et al., *Cell*[133] | 2012 | 0.7 μm | Confocal | Two color beads |
| Colin-York et al. *Nano Letters*[74] | 2016 | 1-1.2 μm | STED, Confocal | Modeling suggests 500 nm is possible with 15 beads/$\mu m^2$, this resolution is not demonstrated |
| Polacheck, W., and Chen, C. *Nature Methods*[20] | 2016 | 2 μm for 2D<br>5 μm for 3D | Confocal microscope | Review article of the existing techniques |
| Colin-York et a. *Nano Letters*[73] | 2019 | 1 μm | SIM | Modeling suggests 500 nm is possible with 15 beads/$\mu m^2$, not demonstrated |
| Stubb, A., et al. *Nano Letters*[75] | 2020 | 1-2 μm | Spinning-disk confocal or widefield microscope | Beads tracking with 40 nm spatial resolution, no resolution indicated for traction forces |
| Zhang, Y., et al. *Nat Comm*[22] | 2014 | 250 nm | Widefield or TIRF microscope | First report of DNA tension probes |
| Morimatsu, M. et al. *Nano Letters*[89] | 2015 | 100 nm | TIRF with 3B analysis | Computational, 3B super-resolved analysis of pN receptor forces, |
| Zhao, Y., et al *Journal of the American Chemical Society*[195] | 2020 | 50 nm | TIRF, single molecule localization | Must photobleaching probes initially, therefore loses most tension information, poor temporal resolution and image quality |
| Tension PAINT (this study) | 2020 | 25 nm | TIRF microscope | |

In the context of molecular tension probes, a single report used 3B imaging for super-resolved mechanical measurements, but 3B is computationally intensive, susceptible to photobleaching, not suitable for long-term cellular imaging, and offers lower spatial resolution[89, 196]. Very recently, turn-on TGTs were used with SMLM to image the locations of pN receptor forces. Based on their localization precision, the authors claim that they can achieve ~50nm spatial resolution imaging of receptor force locations with this technique.

However, to achieve single molecule fluorescence required for super-resolution imaging of receptor forces, this group relies on photobleaching all of the signal that accumulated before the imaging period, thus this group eliminates most of the cell-generated signal before the experiment even begins. Additionally, each probe only reports a receptor force event once, hampering the ability of this technique to address receptor force dynamics[195]. Accordingly, this technique misses the majority of receptor-force events, and struggles with dynamic imaging. tPAINT solves both of these problems and offers superior spatial resolution.

Imager binding to mechanically triggered probes, or mechano-selection[67], is the contrast agent in tPAINT (Figure 38). Therefore, it is important that tPAINT probes are thermally stable enough to avoid excessive background signal due to (non-mechanical) probe breathing. The sf-tPAINT probes provide the first example of super-resolved dynamic measurements of cellular forces. This is a key feature, because the magnitude, spatial organization, timing, frequency, and history of forces influence signaling outcomes, as was recently shown in T cells[197] and in fibroblast adhesions[198]. The likelihood of capturing mechanical events in sf-tPAINT depends on bond lifetime and force lifetime in relation to the imager sampling rate, which may be up to ~0.3 $sec^{-1}$ in speed-optimized PAINT[151]. An additional consideration in sf-tPAINT is tuning the image time window to minimize blurring of dynamic features such as the tension generated by filopodia or the leading edge of spreading platelets (Figure 34**,** Figure 40).

Given that accumulated-tPAINT probes rupture irreversibly after experiencing pN receptor force (Figure 41), this probe offers high spatial resolution with potentially unlimited sampling of force-exposed docking sites. This improved resolution will be

important in imaging fixed samples, where temporal information is not needed and where Exchange-tPAINT is integrated in the workflow.

To demonstrate the capabilities of tPAINT we have mapped platelet and fibroblast integrin tension, revealing dynamic nanoscale features like the rim of tension at the spreading edge of platelets and scanning filopodia. We also demonstrate two types of multiplexed tPAINT; mapping two-thresholds of tension simultaneously or alternatively by performing Exchange-tPAINT to correlate integrin tension with the F-actin architecture driving it. Pharmacological studies confirm that platelet lamellipodial tension is driven by the Arp2/3 complex mediating actin branching. This ability to simultaneously super-resolve mechanical events and cytoskeletal structure is powerful, thus we anticipate that tPAINT will become a workhorse tool linking structural biology to mechanobiology. One limitation in tPAINT is the lack of orientation information, but this limitation will likely be resolved upon integration of recently developed polarization imaging to reveal 3D force vectors of DNA probes[67, 135]. Another limitation can be summarized as a trade-off between time and resolution (Figure 36Figure 36: Tension Feature Dimensions Depend on the Imaging Window in sf-tPAINT); real-time imaging with sf-tPAINT undersamples mechanical events but offers dynamical information in live cells, conversely accumulated tPAINT will sample all mechanical events at the cost of temporal resolution. Future speed optimizations in PAINT will alleviate this tradeoff enabling molecular force imaging combined with spatial mapping of the cell's machinery in real-time.

## 4.5 Materials and Methods

This section will detail the reagents, probe synthesis strategy, and image processing strategy involved in tPAINT.

### *4.5.1 Materials*

Cy3B-NHS ester (PA63101) was acquired from GE Healthcare Life Sciences (Pittsburgh, PA). DNA was custom synthesized by Integrated DNA Technologies (Coralville, IA). Cyclo[Arg-Gly-Asp-d-Phe-Lys(PEG-PEG)] (PCI-3696-PI), elsewhere abbreviated as cRGD, was acquired from Peptides International (Louisville, KY). Streptavidin (S000-01) was obtained from Rockland-Inc (Pottstown, PA). µ-Slide $VI^{0.4}$ 6-channel slides (80606) and 25 mm x 75 mm glass coverslips (10812) were purchased from Ibidi (Verona, WI). N-hydroxyl succinimide-5 kDa PEG-biotin (NHS-PEG-biotin, HE041024-5K) was purchased from Biochempeg (Watertown, MA). N-hydroxyl succinimide-5kDa mPEG (NHS-mPEG, PG1-SC-5k-1) was purchased from Nanocs (New York, NY). Sulfo-N-hydroxyl succinimide-acetate (sulfo-NHS-acetate26777) was purchased from Thermo-Fisher (Waltham, MA). (3-Aminopropyl)triethoxysilane (APTES, 440140, 99% purity) was purchased from Sigma-Aldrich. Tetraspek beads were purchased from Thermo-Fisher (T7279). All other reagents and materials (unless otherwise stated) were purchased from Sigma-Aldrich and used without purification. All buffers were prepared with 18.2 MΩ nanopure water.

### *4.5.2 Synthesis of tPAINT Probes and Key Reagents*

The sequences of the DNA sequences utilized in tPAINT probes are provided in Table 6.

**Table 6: tPAINT Tension Probe Sequences**

| **Name** | **Sequence (5' to 3')** |
|---|---|
| Imager | CTAGATGTAT/3AmMO/ |
| Imager with Cy3B | CTAGATGTAT/3Cy3B/ |
| Imager with Atto488 | CTAGATGTAT/3Atto488/ |
| Speed imager | TCCTCCC/3AmMO/ |
| Speed imager with Cy3B | TCCTCCC/3Cy3B/ |
| Imager-moderate/high | TAA TGA AGA/3AmMo/ |
| Imager-moderate/high with Cy3B | TAA TGA AGA/3Cy3B/ |
| Accumulated-tPAINT ligand BHQ2 | TAGATGTAT/iBHQ-2/GAGGCACGACAC/35OctdU/ |
| Accumulated-tPAINT anchor | /5Biosg/GTGTCGTGCCT/iUniAmM/CATACATCTA |
| Strain-free tPAINT backbone | GTGAAATACCGCACAGATGCGTTTTTTTTTTTT TTTTTTTTTTTTTTTTTTA AGAGCGCCACGTA GCCCAGC |
| Strain-free tPAINT anchor with BHQ2 | /5BHQ_2/GTAGATGTATCTTTCGCATCTGTGCG GTATTTCAC/3Bio/ |
| Strain-free tPAINT ligand | /55OctdU/GCTGGGCTACGTGGCGCTCTTTTTG ATACATCTAC/3AmMO/ |
| Strain-free tPAINT ligand with Cy3B | /55OctdU/GCTGGGCTACGTGGCGCTCTTTTTG ATACATCTAC/3Cy3B/ |
| Strain-free tPAINT ligand_moderate | /55OctdU/GCTGGGCTACGTGGCGCTCTTTTTG TCTTCATTAGTGCTC/3AmMo/ |
| Strain-free tPAINT anchor_moderate with BHQ2 | /5BHQ_2/GAGCACTAATGAAGACTTTCGCATCT GTGCGGTATTTCAC/3Bio/ |
| Strain-free tPAINT ligand_high | /55OctdU/GCTGGGCTACGTGGCGCTCTTTTTG TCTTCATTACTGTCGTGCCTC/3AmMO/ |
| Strain-free tPAINT anchor_high with BHQ2 | /5BHQ_2/GAGGCACGACAGTAATGAAGACTTT CGCATCTGTGCGGTATTTCAC/3Bio/ |
| | |

| **Table 6, continued** | |
|---|---|
| Strained-tPAINT backbone | GTGAAATACCGCACAGATGCGTTGTAGATGTA TTTTTTTTATACATCTACTTAAGAGCGCCACGTAGCCCAGC |
| Strained-tPAINT anchor | CGCATCTGTGCGGTATTTCAC/3Bio/ |
| Strained-tPAINT anchor with BHQ2 | /5BHQ_2/CGCATCTGTGCGGTATTTCAC/3Bio/ |
| Strained-tPAINT ligand | /55OctdU/GCTGGGCTACGTGGCGCTCTT/3AmMO/ |
| Strained-tPAINT ligand with Cy3B | /55OctdU/GCTGGGCTACGTGGCGCTCTT/3Cy3B/ |
| Speed tPAINT v1 ligand | /55OctdU/GCTGGGCTACGTGGCGCTCTTGGGAGGA |
| Speed tPAINT v1 anchor | TCCTCCCCGCATCTGTGCGGTATTTCAC/3Bio/ |
| Speed tPAINT v2 ligand | /55OctdU/GCTGGGCTACGTGGCGCTCTTGGGAGGAG |
| Speed tPAINT v2 anchor | CTCCTCCCCGCATCTGTGCGGTATTTCAC/3Bio/ |
| Speed tPAINT v3 ligand | /55OctdU/GCTGGGCTACGTGGCGCTCTTGGGGAGGAG |
| Speed tPAINT v3 anchor | CTCCTCCCCCGCATCTGTGCGGTATTTCAC /3Bio/ |
| Speed tPAINT v3_control ligand | /55OctdU/GCTGGGCTACGTGGCGCTCTTTTTCGGGAGGAC |
| Speed tPAINT v3_control anchor | GTCCTCCCGTTTCGCATCTGTGCGGTATTTCAC/3Bio/ |
| Speed tPAINT v3_spacer ligand | /55OctdU/GCTGGGCTACGTGGCGCTCTTTTTGGGGAGGAG |
| Speed tPAINT v3_spacer anchor | CTCCTCCCCTTTCGCATCTGTGCGGTATTTCAC/3Bio/ |

The synthesis strategy for tPAINT probes was based on a modification of previously published protocols[22, 67]. HPLC retention times of starting reagents versus products was used to characterize reagents (Figure 52). Retention times of all products and starting reagents are provided in Table 7.

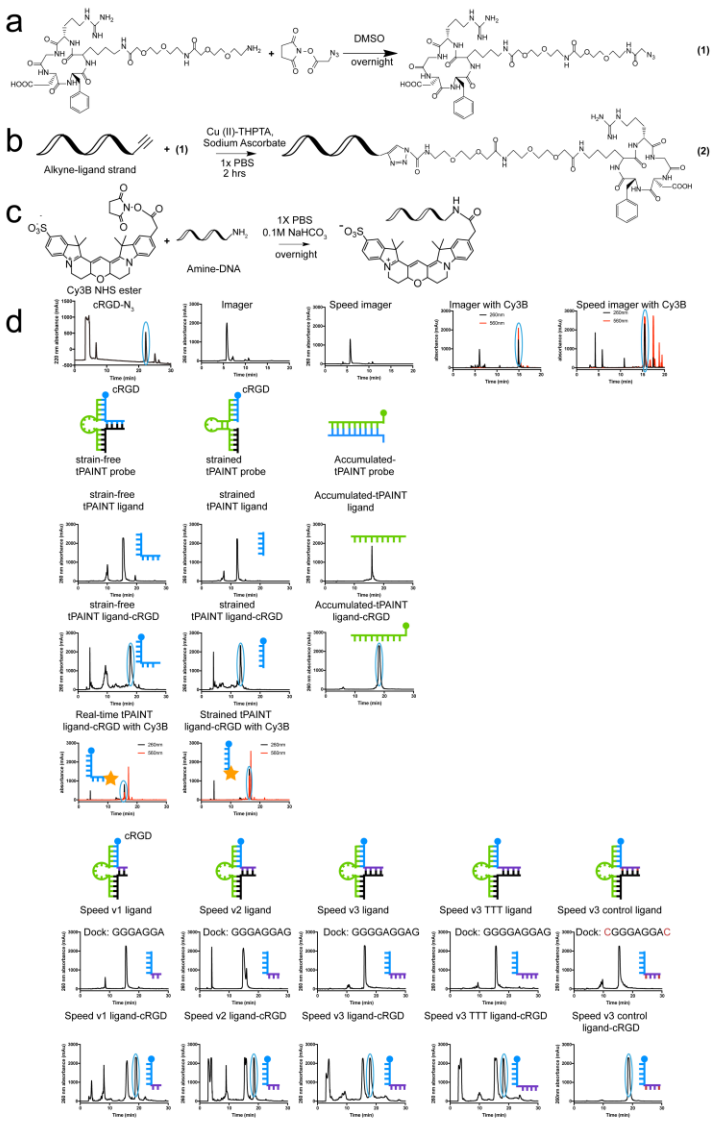


**Figure 52: Characterization of tPAINT Probes**

(**a**) Schematic showing the coupling between NHS-$N_3$ and cRGDfK-PEG-PEG-$NH_2$, (**b**) Alkyne-azide cycloaddition reaction to conjugate cRGD peptide to the DNA, and (**c**) coupling of Cy3b-NHS to DNA. (**d**) HPLC spectra of the all the starting material (cRGD and oligonucleotides) as well as the products generated in this work. Chromatograms of the starting materials were used to confirm the purity of the oligonucleotides custom synthesized by IDT. The products of the cRGD and dye coupling reactions were purified using HPLC and the peaks identified with the blue circles indicate the materials that was used for subsequent steps. The retention times of all starting reagents and products are listed in Table 7**.**

**Table 7: tPAINT Probe HPLC Retention Times**

| Product | Retention time (Minutes) |
|---|---|
| Imager | 5.8 |
| Imager with Cy3B | 14.9 |
| Speed imager | 5.8 |
| Speed imager with Cy3B | 15.5 |
| Accumulated-tPAINT ligand with BHQ2 | 15.9 |
| Accumulated-tPAINT ligand with BHQ2 - c(RGDfK(PEG-PEG)) | 18.3 |
| Strain-free tPAINT ligand | 15.3 |
| Strain-free tPAINT ligand - c(RGDfK(PEG-PEG)) | 17.8 |
| Strained-tPAINT ligand | 12.1 |
| Strained-tPAINT ligand - c(RGDfK(PEG-PEG)) | 15.7 |
| Speed tPAINT ligand v1 | 15.5 |
| Speed tPAINT ligand v1 - c(RGDfK(PEG-PEG)) | 18.9 |
| Speed tPAINT ligand v2 | 14.9 |
| Speed tPAINT ligand v2 - c(RGDfK(PEG-PEG)) | 18.5 |
| Speed tPAINT ligand v3 | 15.9 |
| Speed tPAINT ligand v3 - c(RGDfK(PEG-PEG)) | 17.9 |
| Speed tPAINT ligand v3_control | 15.4 |
| Speed tPAINT ligand v3_control - c(RGDfK(PEG-PEG)) | 18.6 |
| Speed tPAINT ligand v3_spacer | 16.0 |
| Speed tPAINT ligand v3_spacer - c(RGDfK(PEG-PEG)) | 18.2 |

To create the cyclo-Arg-Gly-Asp ligand, 100 nmoles of c(RGDfK(PEG-PEG)) was reacted with approximately 150 nmoles of NHS-azide in DMSO overnight to produce Product 1 (Figure 52a). Product 1 was purified via reverse phase HPLC with a Grace Alltech C18 column (1 mL/min flow rate; Solvent A: 0.1M TEAA + 0.05% TFA, Solvent B: acetonitrile + 0.05% TFA; starting condition: 90% A + 10 % B, 1%/min gradient B) (Figure 52d).

Product 1 was ligated to the tension probe ligand strand via 1,3-dipolar cycloaddition reaction (Figure 52b). Briefly, 5 nmoles of alkyne ligand strand was reacted overnight with ~75 nanomoles of product 1 in the presence of 0.1 M sodium ascorbate and

0.1 mM Cu-THPTA. The product was purified with a P2 size exclusion column, and then using reverse phase HPLC with an Agilent Advanced oligo column (0.5 mL/min flow rate; Solvent A: 0.1M TEAA, Solvent B: acetonitrile; starting condition: 90% A + 10 % B, 0.5%/min gradient B) (Figure 52d). Using the above procedure, any alkyne DNA could be conjugated to the cRGDfK peptide in a highly efficient manner.

Imager strands were dried and reacted overnight with a 15x excess of Cy3B-NHS dissolved in 1 μL DMSO to form product 3 (Cy3B labeled tension probes, Figure 52c). The total reaction volume was 10 μL, composed of 1x PBS supplemented with 0.1M $NaHCO_3$. The reaction pot was purified by a P2 size exclusion gel to remove unreacted dye followed by HPLC purification (0.5 mL/min flow rate; Solvent A: 0.1M TEAA, Solvent B: acetonitrile; starting condition: 90% A + 10 % B, 1%/min gradient B) to purify products 4 and 5 (Figure 52d).

To prepare the final tension probes, DNA oligonucleotides were hybridized at 200 nM or 1 μM in a 0.2 mL Thermowell Tube. DNA was heated to 90°C and then cooled at a rate of 1.3°C per min to 35°C.

To synthesize DNA docking site tagged phalloidin, excess TCO NHS ester was added to 20 nmol phalloidin amine in 20 μL DMSO containing 10% 10X PBS. The solution was vortexed briefly, then reacted at 50 °C for 1 hour. The product was purified by HPLC and identity was confirmed by ESI-MS. Tetrazine-PEG4-azide was then functionalized to alkyne functionalized DNA using copper(I)-catalyzed azide-alkyne cycloaddition. Briefly, 1 mg of tetrazine-PEG4-azide was dissolved in 20 μL 1:4 DMSO:H2O and warmed to 50 °C. The copper reaction mixture was prepared in a separate tube by combining, in the

following order, 1 eq. 20 mM CuSO4, 2 eq. 50 mM THPTA, and 5 eq. 50 mM ascorbic acid. The reaction mixture was then added to 15 nmol DNA in water and warmed to 50 °C. Once warmed, the solution was added to the tetrazine-PEG4-azide with dropwise addition of DMSO to maintain solubility. The reaction proceeded at 50 °C for 2 hours and the resulting product was purified using P-2 gel filtration. Finally, TCO phalloidin and tetrazine functionalized DNA were each dissolved in 10 μL 10X PBS and combined to make the final DNA docking site conjugated phalloidin. The reaction proceeded at room temperature overnight and the resulting product was purified by HPLC.

### *4.5.3 tPAINT Surface Preparation*

Tension-PAINT surface preparation was modified from previously published protocols[9]. Briefly, rectangular glass coverslips (25 x 75 mm) were cleaned using piranha solution. CAUTION: piranha can be explosive when mixed with organics. The piranha solution was prepared using a 1:3 mixture of $H_2O_2$ and $H_2SO_4$. Slides were then washed in 6 successive beakers of nanopure water and then etched in a beaker of KOH (0.5 M) for 1 hr in an ice-filled sonicator[199]. The coverslips were washed in 6 times using nanopure water, followed by 3 successive washes using ethanol. In a separate beaker of ethanol, slides were reacted with 3% v/v APTES for 1 h. Coverslips were then washed 3 times with ethanol and dried under a stream of $N_2$ gas. Slides were then reacted with cloud-point NHS-PEG-biotin (10% w/v) for 1 hr in 0.5 M $K_2SO4$ and 0.1M $NaHCO_3$ (pH 9). Next, slides were washed 3 times with nanopure water and reacted for 30 min with NHS-mPEG (5% w/v) and sulfo-NHS-acetate (1% w/v) in 0.5 M $K_2SO4$ and 0.1M $NaHCO_3$ (pH 9) to consume any unreacted amines on the surface. Slides were dried under $N_2$ gas, and then stored at -80°C for up to 2 weeks before use.

Before imaging, the μ-Slide VI$^{0.4}$ 6-channel slide was adhered on the 5kDa PEG-biotin surface. To further reduce non-specific DNA binding during the imaging, the micro-channels were passivated with 5% v/v Tween 20 in T50 buffer for 15-30 min[200, 201]. The channels were washed with 1XPBS and filled with 50μg/ml streptavidin for a 1-hour incubation. The channels were then washed with 1XPBS and incubated with 1 μM DNA probe solutions for 1 hr. For force-multiplexing experiments, the surfaces were incubated with two tension probes, each at 1 μM concentration. Finally, the channels were washed with cell imaging buffer before imaging. (FluoroBrite DMEM Media, A1896701, Thermo-Fisher)

### *4.5.4 Calculation of tPAINT Probe Surface Density*

We performed two different measurements to attempt to determine the surface density, and therefore the spatial resolution, of tPAINT measurements. The first was based on directly imaging a substrate coated in docking sites and the second was based on quantitatively determining the number of fluorophores attached to tension probes on the surface. To determine the number of fluorophores attached to the surface, we adapted a surface density quantification assay that was previously published[143]. This protocol requires the preparation of a supported lipid membrane because the bilayer structures provide a known molecular density on a glass slide surface that can be used to quantify DNA surface density.

Small unilamellar vesicles (SUV) were prepared by extrusion. 1,2-dioleoyl-sn-glycero-3-phosphocholine (DOPC) (850375C, Avanti Polar Lipids) and Texas Red 1,2-Dihexadecanoyl-*sn*-Glycero-3-Phosphoethanolamine, Triethylammonium Salt (TR

DHPE) were mixed in ~100 µL chloroform at 100 mol % DOPC or 99.5 mol% DOPC and 0.5 mol % TR DHPE. Chloroform was evaporated by rotary evaporation, and lipid cakes were dried under vacuum and under ultra-high purity nitrogen. Lipids were resuspended in water at 2 mg/mL and sonicated for 30 s prior to 3 freeze-thaw cycles. SUVs were extruded 10x in a 10 mL LIPEX Extruder (Transferra Nanosciences, Inc.) fit with a 0.08 µm polycarbonate filter (WHA110604, Whatman) and a drain disc (WHA230600, Whatman). The final concentration of TR in liposomes was measured on a Thermo Scientific Nanodrop 2000c spectrophotometer.

SLBs were formed in untreated glass-bottom 96-well plates (265300, Nunc). Glass was etched for 1 hour in 2.6 M sodium hydroxide and washed with 5 mL nanopure water and 5 mL 1x phosphate buffered saline (PBS). TR-labeled and unlabeled SUVs were added in known ratios for ~10 min to form SLBs containing 0.01 – 0.06 mol% TR-DHPE. SLBs were washed with 5 mL nanopure water and 2.5 mL 1x PBS. SLBs were imaged in nanopure water. When used for passivation, SLBs were prepared with 100 mol % DOPC.

The bulk probe density was determined by measuring the fluorescence intensity of single-stranded tension gauge tethers tagged with Cy3B and comparing this value to a fluorescence calibration curve generated by measuring the intensity of SLB standards containing Texas Red (TR)-labeled phospholipids. The number of TR DHPE per micron was estimated using the DOPC footprint in a membrane[144]. The Cy3B-DNA and TR fluorescence were equated by the F-Factor, $F$, which is defined as:

$$F = \frac{I_{Cy3B-DNA}}{I_{TR-DHPE}} \quad (60)$$

$F$ was determined by measuring the intensity of free dye-labeled DNA and TR-labeled (SUVs) in nanopure water at 50 – 500 nM fluorophore. To avoid surface adsorption, glass was passivated with a DOPC SLB prior to buffer exchanging with the sample. In-solution images were collected 5 μm above the surface.

### *4.5.5 DNA Origami Synthesis*

Single-stranded scaffold p7560 was prepared from M13 phage using a previously reported method. A 16HB rod was designed in caDNAno, based on a 4x4 square lattice cross-section. To synthesize 16HB, a 10-fold excess of staple strands were mixed with p7560 scaffold strand (10 nM) in folding buffer (5 mM Tris, 1 mM EDTA, 10 mM $MgCl_2$ with a total volume of 50 μL. The mixture was denatured at 85°C for 10 min, followed by a slow anneal from 60°C to 25°C over 18 hrs (-1°C/30 minutes). 16HB were purified from excess staples using agarose gel electrophoresis (0.67%) in 0.5×TBE+Mg buffer (45 mM Tris, 45 mM Boric acid, 1 mM EDTA, 10 mM $MgCl_2$). 16HB structures were characterized by agarose gel electrophoresis (1.5%) and negative stain TEM imaging (1% uranyl formate).

### *4.5.6 Imaging Conditions*

Imaging was accomplished on a Nikon Eclipse Ti microscope, operated by Nikon Elements software, a 1.49 NA CFI Apo 100x objective, perfect focus system, and a total internal reflection fluorescence (TIRF) laser launch with 75 mW 561 nm. A Chroma quad

cube (ET-405/488/561/640 nm Laser Quad Band) and reflection interference contrast microscopy (RICM) (Nikon: 97270) cube were used for imaging. Widefield epifluorescence illumination was provided by an X-Cite 120 lamp (Excelitas). An Andor iXon Ultra 897 electron multiplying charge coupled device was used for image acquisition. Lasers were operated in TIRF mode for all acquisitions.

Images were acquired using RAM capture via a Nikon Fast Timelapse acquisition. Cameras were operated at 17-MHz refresh rate with 300 EM gain and a 200 ms exposure time. A 1.5x lens introduced into the optical path allowed for imaging with a pixel size of 110 nm. For time-resolved measurements, Nikon JOBS was used to alternate between capturing 300 frames of single-molecule fluorescence signal and then one RICM image and one epifluorescence GFP image, enabling tracking of the cell position via widefield microscopy throughout the acquisition. The individual 300 frame single molecule image stacks were then stitched back together and analyzed in Picasso. 4-color tetraspek beads were used as fiducial markers.

For force-multiplexing experiments, orthogonal DNA imagers labeled with Atto 488 and Cy3B were employed. Single molecule localizations were collected simultaneously utilizing an Andor Tucam system with dual iXon Ultra 897 EMCCDs. Fluorophores were excited simultaneously with 488nm and 561nm TIRF illumination. All other imaging settings were identical to those described above.

### *4.5.7 tPAINT Data Processing*

Image processing was performed in MATLAB 2019a (MathWorks) and in Picasso[149], a software that is freely available via the Jungmann lab website. The bioformats

toolbox enabled direct transfer of Nikon Elements image files (.nd2) into the MATLAB environment. Drift correction was performed in Picasso by several consecutive rounds of redundant cross correlation.

Due to the presence of background, non-mechanical signal from sf-tPAINT probe "breathing" during experiments, it is necessary to filter the tPAINT single molecule localization data. Accordingly, we developed filtering algorithms to distinguish between force-mediated signal and background signal (Figure 53).

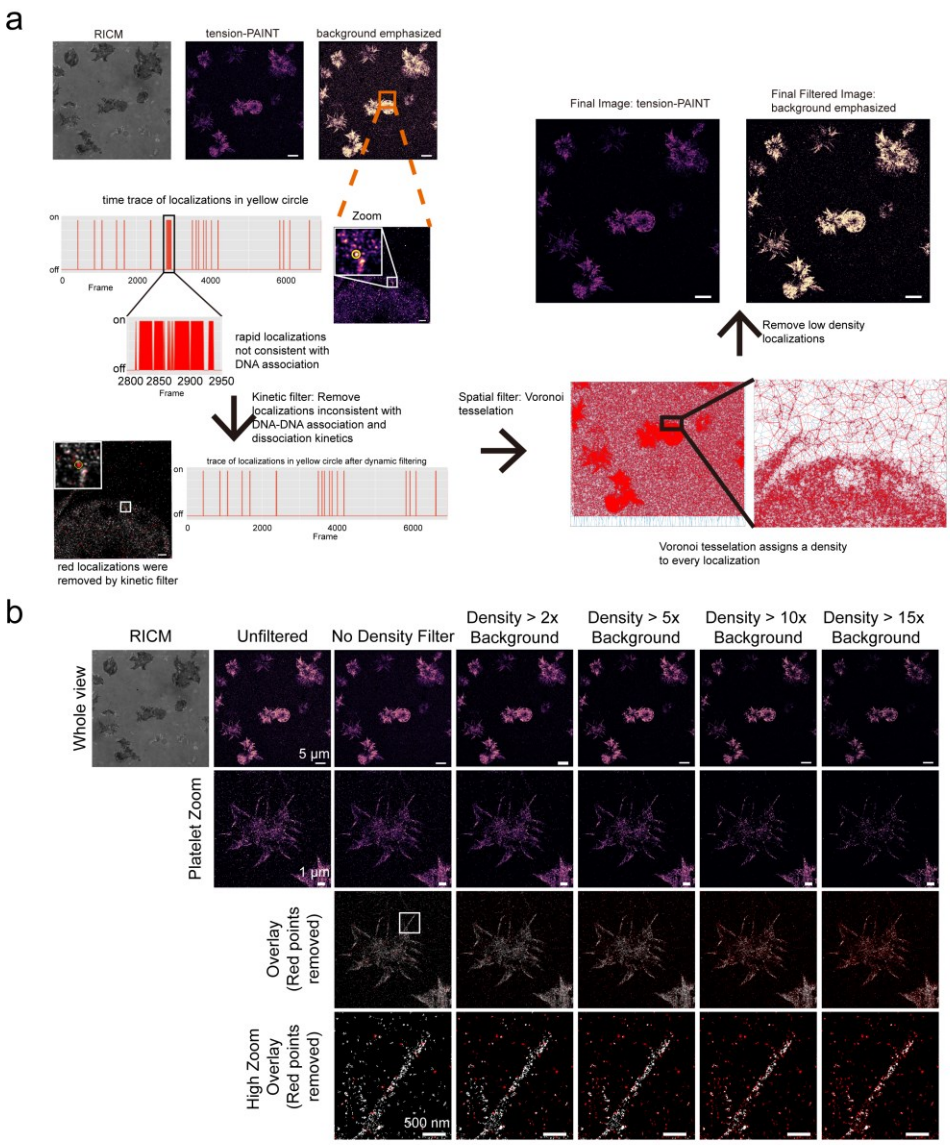


**Figure 53: tPAINT Image Processing Strategy**

(**a**) tPAINT data was subjected to kinetic and density-based filtering prior to analysis. Kinetic filtering was accomplished by sweeping a 25-frame moving window across the time trace of localizations within 35 nm oversampled pixels. If 14 events occurred within the 25-frame window (corresponding to 2.8 s of accumulated single molecule bond lifetime), all the component events were removed by this kinetic filter. Following the kinetic filter, a Voronoi-tessellation was computed for the data to objectively assign a local "density" to each localization. Data with density less than 3-5x the background density were removed. (**b**) To determine the effects of density-based filtering, single molecule localizations were subjected to an increasingly stringent density filter

**Figure 53, continued:** (2x, 5x, 10x, and 15x the background localization density). In the overlay, red points indicate localization density that has been removed by the density filter while white regions indicate localizations that passed the density threshold. The high zoom overlay displays the raw localizations as points, not gaussians. White points passed the filter while red points were removed. At the highest density-based filter settings, localizations on the edge of the filopodial extension are removed (high zoom overlay, 10x and 15x density filter). Scale bars: whole image view, 5 μm; platelet zoom view, 1 μm; high zoom view; 500 nm. background density (e.g. 2x, 5x, or 10x the background density) were removed to produce the final tPAINT image.

Briefly, we applied a kinetic filter to eliminate localizations associated with surface defects, dust or other contaminants on the surface. These localizations possess brief dark times (very high apparent $k_{on}$) or prolonged bright times (very low $k_{off}$). To remove these localizations the single molecule localizations were binned into 3x zoom oversampled pixels (3 oversampled pixels per 1 pixel on detector). Single localization events were identified as consecutive frames in which single molecule localizations occurred within each oversampled pixel, or within its 8 immediate neighbors. If more than 14 events occurred within 25 frames, all of the component events were removed from the data set. This treatment does not alter the single-molecule events that originate from DNA-DNA binding because the expected dark time between single molecule events is 100s for 10 nM imager concentration, thus multiple binding events within 5 seconds are unlikely. Additionally, the bond lifetime of the imager and the docking sites is too short to produce 14 consecutive bright frames. After the kinetic filter, we employed a Voronoi tessellation density filter to remove sparse localizations[202], reasoning that cell tension will produce denser localizations than the cell-free background (Figure 53). We then computed the Voronoi tessellation of the single molecule localization data set[202]. The Voronoi tessellation assigns a polygon to each localization such that each polygon contains the set

of all points that are closer to the localization than to any other localization. This procedure allows the objective assignment of the "area of influence" of each single molecule localization. With areas assigned to each localization, we further computed a first rank density to each localization, defined as the local density of a localization and its nearest neighbors (Figure 53). A background density was calculated as the average localization density within a user-defined cell-free region of the substrate. We the removed all single molecule localizations with a first rank density of less than 1-15x the background localization first rank density. This procedure may "erode" edge localizations, sharpening spatial features, thus it is important to use the lowest possible Voronoi density filter that produces high-quality images. The effects of different density filters are displayed in detail in Figure 53b.

For Tucam experiments, including simultaneous tPAINT-SRRF and force multiplexing, the single-molecule localization lists were registered after single molecule localization in Matlab. Localizations corresponding to tetraspek beads were manually identified and used as fiducial markers to apply a projective registration to the single-molecule dataset.

### *4.5.8 Calculation of Probe $F_{1/2}$*

To determine the $F_{1/2}$ of the sf-tPAINT probe, we utilized the worm-like chain model and previously published calculations[22]. Briefly, the $F_{1/2}$ is calculated as:

$$F_{1/2} = \frac{\Delta G_{fold} + \Delta G_{stretch}}{\Delta x} \tag{61}$$

The calculated probe F1/2 values for the tPAINT probes used in this thesis are displayed in Table 8.

**Table 8: tPAINT Probe $F_{1/2}$**

| | $\Delta G_{stretch}$ (kJ/mol) | $\Delta G_{fold}$ (kJ/mol) | $F_{1/2}$ (pN) |
|---|---|---|---|
| MTFM probe | 21.63 | 26.73 | 7.17 |
| Strained tPAINT probe | 21.63 | 32.34 | 8.00 |
| Strain-free tPAINT probe | 21.63 | 35.60 | 8.49 |
| Speed-optimized tPAINT probe v1 | 21.63 | 27.87 | 7.34 |
| Speed-optimized tPAINT probe v2 | 21.63 | 32.89 | 8.08 |
| Speed-optimized tPAINT probe v3 | 21.63 | 40.66 | 9.24 |
| Speed-optimized tPAINT probe v3_control | 21.63 | 43.30 | 9.63 |
| Speed-optimized tPAINT probe v3_spacer | 21.63 | 39.50 | 9.06 |
| Strain-free tPAINT probe_moderate | 21.63 | 74.68 | 14.28 |
| Strain-free tPAINT probe_high | 21.63 | 121.21 | 21.18 |

$\Delta G_{fold}$ is acquired from the IDT oligoanalyzer 3.1, which uses the UNAfold software package. $\Delta G_{fold}$ was calculated using 140 mM monovalent and 37.5 mM divalent salt at 25 °C and at a concentration of 250 nM oligonucleotide. $\Delta G_{stretch}$ is calculated using the following equation:

$$\Delta G_{stretch} = \frac{k_B T}{L_p} \frac{L_c}{4(1 - x/L_{c)}} [3\left(\frac{x}{L_c}\right)^2 - 2\left(\frac{x}{L_c}\right)^3] \quad (62)$$

The parameters used in the calculation of the probe $F_{1/2}$ using equation 62 are displayed in Table 9.

**Table 9: Parameters for $F_{1/2}$ Calculation**

| Parameter | Definition | Value |
|---|---|---|
| T | Temperature | 298 K (25°C) |
| $k_B$ | Boltzmann constant | 1.380648e-23 kJ/K |
| n | Number of nucleotides in loop | 31 |
| x | Loop extension | 0.44(n-1) nm |
| $\Delta x = x-2$ | Loop displacement | (0.44(n-1)-2) nm |
| $L_c$ | Contour length | 0.63 nm per nucleotide |
| $L_p$ | Persistence length ssDNA | 1.3 nm |

# CHAPTER 5. CONCLUSIONS

## 5.1 Summary of Advances

This thesis describes the invention of two new mechanoimaging modalities, Molecular Force Microscopy (MFM) and tension-Point Accumulation for Imaging in Nanoscale Topography (tPAINT).

MFM enables measurement of the 3D orientation of pN receptor forces[67]. We used MFM to measure the orientation of platelet integrin forces and discovered that human platelets exhibit an axis of anisotropic contraction that initial TFM measurements did not detect[127]. More recent TFM measurements have revealed that under shear stress, platelets contract primarily in the direction perpendicular to the shear stress. The authors calculate that platelet contraction perpendicular to the shear stress spreads out the platelet-surface stress distribution, avoiding a potentially catastrophic stress build up at the edge of the platelet facing the oncoming fluid flow[137]. It is possible that enabling platelet adhesion under the influence of shear stress is the biological purpose of the axis of anisotropic contraction revealed by MFM. We also measured focal adhesion 3D force orientations via MFM, which revealed that focal adhesion forces along the *x*, *y*, and *z* axes are all extremely coherent within individual focal adhesions. Interestingly, the average angle of focal-adhesion integrin forces from vertical ($\theta_{force}$) was 40° [67]. Previous interference-PALM measurements have measured the angle between the N and C terminus of the force transducing focal adhesion protein talin as ~51° [139], in good agreement with the $\theta_{force}$ value measured by MFM. This agreement makes sense, as actomyosin-generated forces are transmitted via talin to the integrins within focal adhesions.

tPAINT provides a means to image the nanoscale distribution of pN receptor forces with up to 25 nm spatial resolution. With exchange-tPAINT, it is possible to link pN receptor forces with the protein ultrastructure that produced them. Via tPAINT, we quantified the width and spreading dynamics of a peripheral ring of tension that develops at the platelet lamellipodial edge. This ring of tension was not visible in TFM maps of platelet traction forces[127, 137], but was visible in previous MTFM measurements[6, 67]. With exchange tPAINT, we were able to demonstrate that the platelet tension ring is spatially associated with a ring of actin at the platelet edge. This actin ring is likely the peripheral actin web that has been reported in previous super-resolution and EM imaging[183, 185]. To our knowledge, exchange-tPAINT is the first technique capable of resolving both the nanoscale distribution of receptor forces and the protein structures that generated them. This ring of tension could be inhibited by CK666 treatment, suggesting that the ring of tension is mediated by Arp2/3 branching actin polymerization. tPAINT is biologically general as it also enabled the measurement of integrin-mediated focal adhesion forces and filopodial forces, allowing us to resolve the dynamics of filopodia retraction and lateral scanning.

These two techniques offer the ability to probe receptor forces at nearly the molecular level. Accordingly, we believe that they will provide investigators with important tools to link biological forces to the protein structures that produce them.

## 5.2 Limitations of the Current Work

The techniques presented here represent a significant step forward in quantifying receptor forces; however, there are several important caveats to consider. First, there are

a number of factors that may limit the biological relevance of the measurements presented here. All of the experiments presented in this thesis were conducted with the model integrin ligand cyclo-Arg-Gly-Asp, not with the native protein ligands. It is worth remembering this caveat when considering the biological measurements presented here as cells may behave differently when presented with their native ligand. In principle, it is possible to generate tension probes with protein domain ligands[87], and DNA-based molecular tension probes have previously been used by our group to measure platelet forces transmitted to fibrinogen[6], thus future work could address this issue. Additionally, molecular tension probes, including those used in this thesis, are usually immobilized on glass coverslips which are extremely stiff. Substrate stiffness has significant impacts on cellular function[13, 198], thus the forces and cytoskeletal structures measured here are not necessarily representative of those present within tissue. For MFM this issue could be ameliorated by immobilizing tension probes on soft polymer gels, but has not yet been achieved by our group. It may never be possible to conduct tPAINT on soft gels as it requires single-molecule fluorescence for SMLM, complicating the use of the thick polymer gels typically used to achieve physiologically relevant substrate stiffness.

In MFM measurements, the orientation of many tension probes experiencing receptor forces exceeding the probe $F_{1/2}$ are reported. This ensemble averaging alters the measured force in non-trivial ways (Figure 19)[67]. Specifically, if probes within a diffraction-limited area experience forces with varying *z* orientation ($\theta_{force}$), then MFM will report close to the average $\theta_{force}$ value. However, if probes within a diffraction-limited area differ in the *xy* orientation of the force ($\Phi_{force}$), MFM will report the average $\Phi_{force}$, but will also under-report $\theta_{force}$ for that pixel (Figure 19). Accordingly, it is important to remember

that the $\theta_{force}$ values estimated by MFM provide a *lower bound* on the actual $\theta_{force}$ angle within a given diffraction-limited area. Future work could rectify this issue by combining single-molecule imaging with MFM.

With respect to the Exchange-tPAINT measurement presented in Chapter 4, the nature of the experiment warrants some caution. Receptor forces were measured in living cells but cytoskeletal imaging was performed after cells were fixed and stained on the microscope (Figure 46, Figure 48). Great care was taken not to disturb the sample; however fixation artifacts and the brief (10-30 second) delay between the cessation of tPAINT imaging and cell fixation may have produced small changes in the cell between tension imaging and cytoskeletal imaging. Work is already underway in the lab to image tension after fixation, an adjustment that would remove this issue.

One other critical limitation of tPAINT measurements is undersampling of receptor forces due to the stochastic binding of imagers to mechanically opened tPAINT probes. The $k_{on}$ for the imager used in the majority of the measurements in this thesis is $1.2x10^6$ $M^{-1}s^{-1}$, which, with the 10nM imager concentration typically used in tPAINT measurements, produces a dark time (the time between imager binding events) of approximately 83 seconds. The use of high concentrations of $Mg^{2+}$ can increase the $k_{on}$ to about $3.8x10^6$ $M^{-1}s^{-1}$, which significantly shortens the time between binding events[151], decreasing undersampling of mechanically-opened tension probes and improving image quality (compare Figure 33 to Figure 34). The speed-optimized imager with $Mg^{2+}$ increases imager $k_{on}$ to $13.6x10^6$ $M^{-1}s^{-1}$, providing an expected time of only 7 s between imager binding events[151]. Nevertheless, the stochastic nature of tPAINT imager binding means that short integrin forces may not be sampled. Additionally, the high $Mg^{2+}$ used to optimize

the imager $k_{on}$ can perturb cells or influence receptor conformation. For receptors or biological processes that are likely to be perturbed by the use of non-physiological $Mg^{2+}$ concentrations, dynamic tPAINT imaging may prove challenging. A recent preprint manuscript reports the use of fluorogenic imagers for DNA-PAINT, promising a 26 fold increase in imaging speed over traditional DNA-PAINT, potentially offering a route to live-cell tPAINT without the need for nonphysiological salt conditions[203]. At present, accumulated-tPAINT is the best option to image receptor forces without undersampling and without non-physiological salt concentrations at the cost of making interpretation of cellular force dynamics more challenging (Figure 41).

## 5.3 Future Directions

MFM and tPAINT provide new capabilities to the biological community, and may offer the opportunity to test several longstanding hypotheses.

One exciting hypothesis is that the TCR preferentially triggers T cell activation in response to shearing forces. This "anisotropic mechanosensing" hypothesis is supported by optical trap studies[16, 96]. These initial experiments are compelling, but the optical trap experiments that support the hypothesis report forces relative to the bulk cell surface. The orientation of the plasma membrane or the TCR in question are unknown. The orientation of individual TCR-pMHC forces has not been measured. MFM offers a route to directly test this hypothesis. However, the current implementation of MFM integrates 3.6s of data to produce one MFM map[67], making its temporal resolution insufficient to address TCR forces, which are very dynamic. To improve the temporal resolution of MFM, future iterations of this technique could utilize an electro-optic modulator to electronically control

the excitation polarization, or employ a recently reported emission-resolved FPM technique that splits fluorescence emission into components along four orientations to calculate fluorophore orientation with a single image[116, 204].

Another exciting hypothesis suggests that lateral forces induce an extended open integrin conformation, contributing to integrin activation[17]. This evidence is supported by results from our lab that demonstrated that platelets cannot spread and activate on laterally mobile RGD ligand, but will spread and activate on chemically-identical immobilized RGD[6]. Direct evidence linking the orientation of molecular forces with integrin conformation does not yet exist. Combining MFM with integrin conformation specific antibodies could provide empirical evidence to support this hypothesis[59].

tPAINT also offers an exciting new capability to localize receptor forces with near molecular resolution. Importantly, this work demonstrates Exchange-tPAINT, which uses orthogonal imagers to sequentially images pN receptor forces with tPAINT and then images other biomolecules (e.g. the cytoskeleton) with DNA-PAINT. Exchange-tPAINT offers a route to understand pN receptor forces, and to link these forces to the cytoskeletal or signaling protein that generated those forces. Many important biological questions could be answered by Exchange-tPAINT.

As an example of the potential of Exchange-tPAINT, integrin conformation specific antibodies could provide the means to link specific integrin conformations with mechanical forces[59, 167]. A recent report has linked an intermediate affinity and ectodomain integrin conformation of the platelet integrin $\alpha_{IIb}\beta_3$ with biomechanical platelet aggregation[167]. These experiments were conducted with multiple, conformation specific

antibodies that revealed the integrin configuration. tPAINT could determine whether these intermediate conformation integrins are force bearing. Similarly, a longstanding hypothesis put forward by Springer and colleagues suggests that integrins are extremely sensitive force-triggered molecules that trigger a conformation change upon the application of pN forces[17]. The relative abundance of different integrin conformations and the free energies required for integrin conformation changes have been measured via fluorescence anisotropy of FITC-tagged cRGD and Fabs that alter integrin conformation[59]. Mathematical modeling has suggested that both the binding of cytoskeletal adaptor proteins and pN cytoskeletal forces transmitted to the $\alpha_5\beta_1$ integrin are required to enable integrins to act as ultrasensitive switches, coordinating their conformation with cytoskeletal dynamics[60]. tPAINT could provide the means to directly probe the conformation of specific integrins while also measuring whether those integrins transmit forces to their surroundings. If Springer's hypothesis is correct, pN forces transmitted to tPAINT probes should correspond almost exclusively to extended-open integrins. Identifying force-bearing bent-closed integrins or extended closed integrins would be a surprising finding.

Additionally, tPAINT offers the ability to link receptor forces with larger cellular structures. For example, super-resolution measurements have suggested that the TCR is located at the tips of microvilli[55]. At the interface between T cells and antigen-presenting cells, microvilli constantly scan the antigen presenting cell surface. Upon antigen recognition, microvilli that bear TCR are stabilized within the immunological synapse, remaining in contact with antigen presenting cells for longer than microvilli that do not bear TCRs[56]. These findings point to a role for microvilli in TCR antigen recognition. Because the TCR is mechanically active[9] while TCRs are present at microvilli tips[55], it is

possible mechanically active TCRs are present primarily at the tips of microvilli. tPAINT provides the means to test this hypothesis, potentially linking microvilli with TCR-force generation. For example, Exchange-tPAINT could provide the means to probe TCR forces and to correlate them with microvilli, which could be identified by staining for molecules that localize to microvilli tips and base such as L-selectin and CD44, respectively[55].

tPAINT could also be used to understand whether TCR mechanics and nanoclusters are related. Some investigators believe that the TCR exists in nanoclusters on the T cell surface[54]. This claim is hotly debated, with recently reported FRET measurements failing to find a role for dimers or clusters of TCRs in antigen recognition[205]. Nonetheless, TCR nanoclusters are hypothesized to be important in several modes of TCR triggering, including serial-engagement[206, 207]. Whether TCR nanoclusters are important in TCR force generation is completely unknown. tPAINT is the only technique currently capable of determining whether mechanically-active TCRs are located in nanoclusters.

Finally, combining MFM with tPAINT (force-PAINT) would offer the ability to measure the 3D orientation of single-molecule forces, a capability that could be critical for determining how molecular force orientations contribute to cellular signaling. This capability could be particularly useful in testing the anisotropic mechanosensing hypothesis of T cell activation[16]. Preliminary experiments to develop this capability are already underway in our lab, and a single fibroblast imaged via force-PAINT is shown in Figure 54.

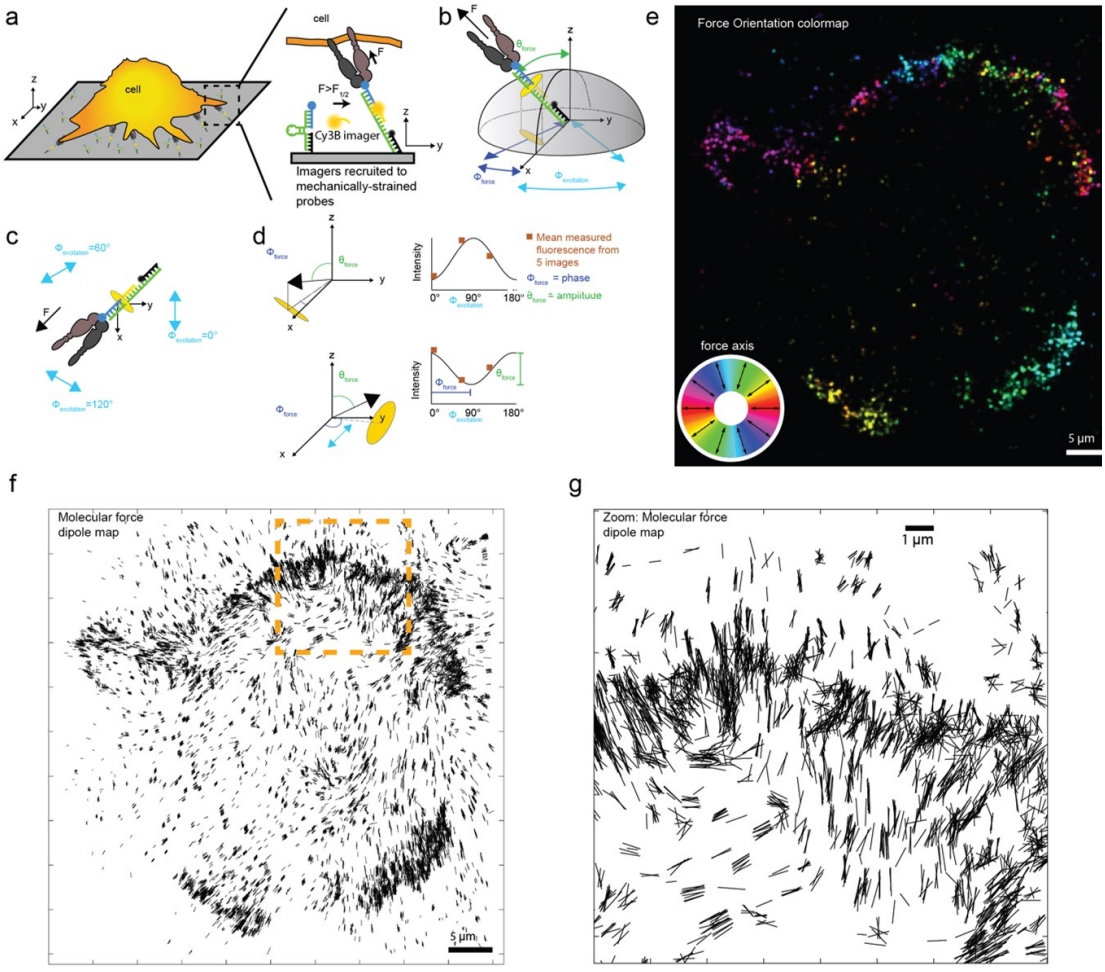


**Figure 54: Force-PAINT**

(**a**) Cells seeded on a substrate bearing DNA tension probes exert receptor forces on those probes. Molecular tension probes reorient parallel to the applied molecular forces. (**b**) DNA tension probes sample a hemisphere of conformations in the absence of forces (gray hemisphere); however, receptor forces dictate the DNA probe orientation. When imagers are recruited to the DNA tension probe, the fluorophore attached to the imager immediately stacks with the tension probe in the manner of another base. Therefore, fluorophore orientation, and the *xy* projection of the fluorophore (yellow ellipse in *xy* plane) are both dictated by applied receptor forces. Note that for ForcePAINT to work, a strained tPAINT probe must be used, which somewhat limits the number of localizations that are observed. (**c**) In ForcePAINT, the orientation tension probes are imaged by rapidly exciting fluorophores with 3 different excitation orientations ($\Phi_{excitation}$).

**Figure 54, continued.** (**d**) The fluorescence intensity measured for a given $\Phi_{excitation}$ depends on the orientation of the fluorophore with respect to $\Phi_{excitation}$ as it does in MFM. The fluorophore orientation is given by the phase of the sinusoid. (**e**) Preliminary forcePAINT map for a MEF cell exerting integrin forces on cRGD-tagged forcePAINT probes. Force orientations calculated for single molecule localizations are given by the color of the spots. The colorwheel maps color onto force orientation.

MFM and tPAINT have increased the resolution of molecular tension sensing to near the molecular level. These new technologies offer a means to test longstanding hypotheses, such as the importance of lateral forces in integrin and T cell activation. In conclusion MFM and tPAINT offer the mechanobiology community valuable new tools to link biological forces to protein structures and cellular signaling.

# APPENDIX A. PERMISSIONS

Copyright Clearance Center Marketplace™

## Order Confirmation

Thank you, your order has been placed. An email confirmation has been sent to you. Your order license details and printable licenses will be available within 24 hours. Please access Manage Account for final order details.

This is not an invoice. Please go to manage account to access your order history and invoices.

### CUSTOMER INFORMATION

Payment by invoice: You can cancel your order until the invoice is generated by contacting customer service.

**Billing Address**

Joshua Brockman
Emory University
General delivery
1515 Dickey Dr
ATLANTA, GA 30322
United States

9373670643
jmbrock@emory.edu

**Customer Location**

Joshua Brockman
Emory University
General Delivery
1515 Dickey Dr
ATLANTA, GA 30322
United States

**PO Number** (optional)

N/A

**Payment options**

Invoice

### PENDING ORDER CONFIRMATION

**Confirmation Number:** Pending

**Order Date:** 05-May-2020

**1. Molecular Biology of the Cell (Online)** 0.00 USD

| | | | |
|---|---|---|---|
| **Order license ID** | Pending | **Publisher** | American Society for Cell Biology |
| **ISSN** | 1939-4586 | **Portion** | Chart/graph/table/figure |
| **Type of Use** | Republish in a thesis/dissertation | | |

#### LICENSED CONTENT

5/5/2020 https://marketplace.copyright.com/rs-ui-web/mp/checkout/confirmation-details/45e9749b-bd10-471b-80f6-640e0c76dc15

| | | | |
|---|---|---|---|
| **Publication Title** | Molecular Biology of the Cell (Online) | **Country** | United States of America |
| **Author/Editor** | American Society for Cell Biology. | **Rightsholder** | American Society for Cell Biology |
| **Date** | 01/01/1992 | **Publication Type** | e-Journal |
| **Language** | English | | |

#### REQUEST DETAILS

| | | | |
|---|---|---|---|
| **Portion Type** | Chart/graph/table/figure | **Distribution** | Worldwide |
| **Number of charts / graphs / tables / figures requested** | 1 | **Translation** | Original language of publication |
| **Format (select all that apply)** | Print, Electronic | **Copies for the disabled?** | No |
| **Who will republish the content?** | Academic institution | **Minor editing privileges?** | No |
| **Duration of Use** | Life of current edition | **Incidental promotional use?** | No |
| **Lifetime Unit Quantity** | Up to 499 | **Currency** | USD |
| **Rights Requested** | Main product | | |

#### NEW WORK DETAILS

| | | | |
|---|---|---|---|
| **Title** | Mapping the 3D Orientation and Nanoscale Distribution of Piconewton Receptor Forces | **Institution name** | Emory University |
| | | **Expected presentation date** | 2020-05-29 |
| **Instructor name** | Joshua Brockman | | |

#### ADDITIONAL DETAILS

| | | | |
|---|---|---|---|
| **Order reference number** | N/A | **The requesting person / organization to appear on the license** | Joshua Brockman |

#### REUSE CONTENT DETAILS

| | | | |
|---|---|---|---|
| **Title, description or numeric reference of the portion(s)** | Figure 2 | **Title of the article/chapter the portion is from** | N/a |
| **Editor of portion(s)** | N/A | **Author of portion(s)** | American Society for Cell Biology. |
| **Volume of serial or monograph** | 28 | **Issue, if republishing an article from a serial** | N/A |
| **Page or page range of portion** | 3137 | **Publication date of portion** | 2017-11-07 |

**Total Items: 1** **Total Due: 0.00 USD**

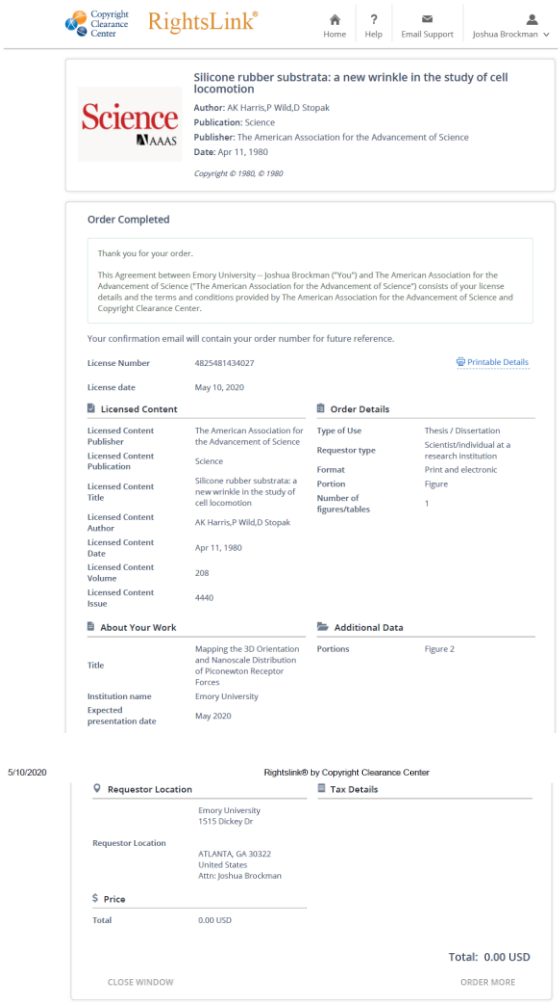
Copyright Clearance Center
RightsLink®
Home
Help
Email Support
Joshua Brockman
Science
AAAS
Silicone rubber substrata: a new wrinkle in the study of cell locomotion
Author: AK Harris,P Wild,D Stopak
Publication: Science
Publisher: The American Association for the Advancement of Science
Date: Apr 11, 1980
Copyright © 1980, © 1980
Order Completed
Thank you for your order.
This Agreement between Emory University -- Joshua Brockman ("You") and The American Association for the Advancement of Science ("The American Association for the Advancement of Science") consists of your license details and the terms and conditions provided by The American Association for the Advancement of Science and Copyright Clearance Center.
Your confirmation email will contain your order number for future reference.
Printable Details
License Number 4825481434027
License date May 10, 2020
Licensed Content
Licensed Content Publisher The American Association for the Advancement of Science
Licensed Content Publication Science
Licensed Content Title Silicone rubber substrata: a new wrinkle in the study of cell locomotion
Licensed Content Author AK Harris,P Wild,D Stopak
Licensed Content Date Apr 11, 1980
Licensed Content Volume 208
Licensed Content Issue 4440
Order Details
Type of Use Thesis / Dissertation
Requestor type Scientist/individual at a research institution
Format Print and electronic
Portion Figure
Number of figures/tables 1
About Your Work
Title Mapping the 3D Orientation and Nanoscale Distribution of Piconewton Receptor Forces
Institution name Emory University
Expected presentation date May 2020
Additional Data
Portions Figure 2


5/10/2020
Rightslink® by Copyright Clearance Center
Requestor Location
Emory University
1515 Dickey Dr
Requestor Location
ATLANTA, GA 30322
United States
Attn: Joshua Brockman
Tax Details
Price
Total 0.00 USD
Total: 0.00 USD
CLOSE WINDOW
ORDER MORE

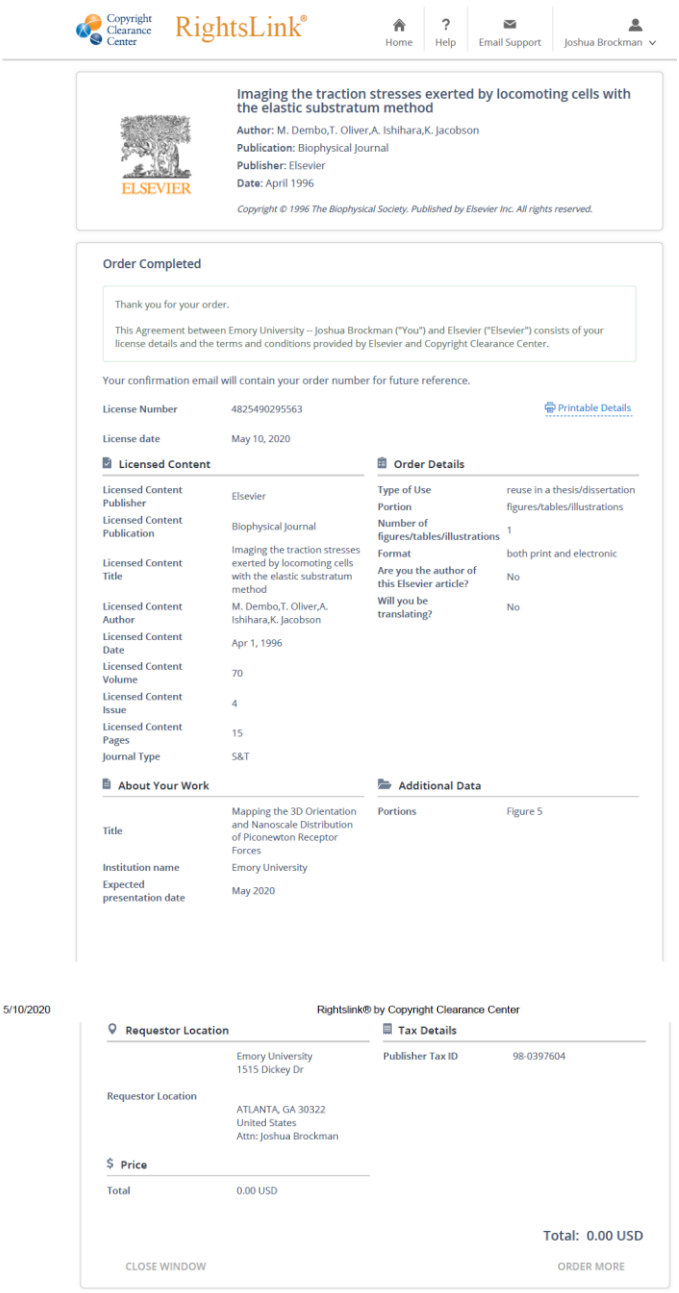

Copyright Clearance Center RightsLink®

Home | Help | Email Support | Joshua Brockman

ELSEVIER

**Imaging the traction stresses exerted by locomoting cells with the elastic substratum method**

**Author:** M. Dembo,T. Oliver,A. Ishihara,K. Jacobson
**Publication:** Biophysical Journal
**Publisher:** Elsevier
**Date:** April 1996

*Copyright © 1996 The Biophysical Society. Published by Elsevier Inc. All rights reserved.*

**Order Completed**

Thank you for your order.

This Agreement between Emory University -- Joshua Brockman ("You") and Elsevier ("Elsevier") consists of your license details and the terms and conditions provided by Elsevier and Copyright Clearance Center.

Your confirmation email will contain your order number for future reference.

Printable Details

| | |
|---|---|
| License Number | 4825490295563 |
| License date | May 10, 2020 |

**Licensed Content**

| | |
|---|---|
| Licensed Content Publisher | Elsevier |
| Licensed Content Publication | Biophysical Journal |
| Licensed Content Title | Imaging the traction stresses exerted by locomoting cells with the elastic substratum method |
| Licensed Content Author | M. Dembo,T. Oliver,A. Ishihara,K. Jacobson |
| Licensed Content Date | Apr 1, 1996 |
| Licensed Content Volume | 70 |
| Licensed Content Issue | 4 |
| Licensed Content Pages | 15 |
| Journal Type | S&T |

**Order Details**

| | |
|---|---|
| Type of Use | reuse in a thesis/dissertation |
| Portion | figures/tables/illustrations |
| Number of figures/tables/illustrations | 1 |
| Format | both print and electronic |
| Are you the author of this Elsevier article? | No |
| Will you be translating? | No |

**About Your Work**

| | |
|---|---|
| Title | Mapping the 3D Orientation and Nanoscale Distribution of Piconewton Receptor Forces |
| Institution name | Emory University |
| Expected presentation date | May 2020 |

**Additional Data**

| | |
|---|---|
| Portions | Figure 5 |

5/10/2020 Rightslink® by Copyright Clearance Center

**Requestor Location**

Emory University
1515 Dickey Dr

Requestor Location

ATLANTA, GA 30322
United States
Attn: Joshua Brockman

**Tax Details**

| | |
|---|---|
| Publisher Tax ID | 98-0397604 |

**Price**

| | |
|---|---|
| Total | 0.00 USD |

**Total: 0.00 USD**

CLOSE WINDOW ORDER MORE

Copyright Clearance Center RightsLink®

Home | Help | Email Support | Joshua Brockman

SPRINGER NATURE

**DNA-based digital tension probes reveal integrin forces during early cell adhesion**

**Author:** Yun Zhang et al
**Publication:** Nature Communications
**Publisher:** Springer Nature
**Date:** Oct 24, 2014



## Order Completed

Thank you for your order.

This Agreement between Emory University -- Joshua Brockman ("You") and Springer Nature ("Springer Nature") consists of your license details and the terms and conditions provided by Springer Nature and Copyright Clearance Center.

Your confirmation email will contain your order number for future reference.

Printable Details

| | |
|---|---|
| License Number | 4823200790086 |
| License date | May 06, 2020 |

### Licensed Content

| | |
|---|---|
| Licensed Content Publisher | Springer Nature |
| Licensed Content Publication | Nature Communications |
| Licensed Content Title | DNA-based digital tension probes reveal integrin forces during early cell adhesion |
| Licensed Content Author | Yun Zhang et al |
| Licensed Content Date | Oct 24, 2014 |

### Order Details

| | |
|---|---|
| Type of Use | Thesis/Dissertation |
| Requestor type | academic/university or research institute |
| Format | print and electronic |
| Portion | figures/tables/illustrations |
| Number of figures/tables/illustrations | 2 |
| High-res required | no |
| Will you be translating? | no |
| Circulation/distribution | 30 - 99 |
| Author of this Springer Nature content | no |

### About Your Work

| | |
|---|---|
| Title | Mapping the 3D Orientation and Nanoscale Distribution of Piconewton Receptor Forces |
| Institution name | Emory University |
| Expected presentation date | May 2020 |

### Additional Data

| | |
|---|---|
| Portions | Figure 1, Figure 2 |



### Requestor Location

Emory University
1515 Dickey Dr

Requestor Location

ATLANTA, GA 30322
United States
Attn: Khalid Salaita

### Tax Details

### $ Price

| | |
|---|---|
| Total | 0.00 USD |

Total: 0.00 USD

CLOSE WINDOW ORDER MORE

Copyright Clearance Center Marketplace™

# Order Confirmation

Thank you, your order has been placed. An email confirmation has been sent to you. Your order license details and printable licenses will be available within 24 hours. Please access Manage Account for final order details.

**This is not an invoice. Please go to manage account to access your order history and invoices.**

## CUSTOMER INFORMATION

Payment by invoice: You can cancel your order until the invoice is generated by contacting customer service.

**Billing Address**

**Mr. Joshua Brockman**
Emory University
General Delivery
1515 Dickey Dr
Atlanta, GA 30322
United States

+1 (937) 367-0643
jmbrock@emory.edu

**Customer Location**

**Mr. Joshua Brockman**
Emory University
General Delivery
1515 Dickey Dr
Atlanta, GA 30322
United States

**PO Number** (optional)

N/A

**Payment options**

Invoice

## PENDING ORDER CONFIRMATION

**Confirmation Number:** Pending

**Order Date:** 09-Jun-2020

### 1. Journal of biological chemistry

0.00 USD

| | | | |
|---|---|---|---|
| **Order license ID** | Pending | **Publisher** | AMERICAN SOCIETY FOR BIOCHEMISTRY AND MOLECULAR BI |
| **ISSN** | 1083-351X | | |
| **Type of Use** | Republish in a thesis/dissertation | **Portion** | Chart/graph/table/figure |

### LICENSED CONTENT

| | | | |
|---|---|---|---|
| **Publication Title** | Journal of biological chemistry | **Country** | United States of America |
| **Author/Editor** | AMERICAN SOCIETY FOR BIOCHEMISTRY & MOLECULAR BIOL | **Rightsholder** | American Soc for Biochemistry & Molecular Biology |
| | | **Publication Type** | e-Journal |
| **Date** | 01/01/1905 | **URL** | http://www.jbc.org/ |
| **Language** | English | | |

### REQUEST DETAILS

| | | | |
|---|---|---|---|
| **Portion Type** | Chart/graph/table/figure | **Distribution** | Worldwide |
| **Number of charts / graphs / tables / figures requested** | 2 | **Translation** | Original language of publication |
| | | **Copies for the disabled?** | No |
| **Format (select all that apply)** | Print, Electronic | **Minor editing privileges?** | No |
| **Who will republish the content?** | Academic institution | **Incidental promotional use?** | No |
| **Duration of Use** | Life of current edition | **Currency** | USD |
| **Lifetime Unit Quantity** | Up to 499 | | |
| **Rights Requested** | Main product | | |

### NEW WORK DETAILS

| | | | |
|---|---|---|---|
| **Title** | Mapping the 3D Orientation and Nanoscale Distribution of pN Receptor Forces | **Institution name** | Emory University |
| | | **Expected presentation date** | 2020-06-09 |
| **Instructor name** | Joshua Brockman | | |

### ADDITIONAL DETAILS

| | | | |
|---|---|---|---|
| **Order reference number** | N/A | **The requesting person / organization to appear on the license** | Joshua Brockman |

### REUSE CONTENT DETAILS

| | | | |
|---|---|---|---|
| **Title, description or numeric reference of the portion(s)** | Figure 4, Supplementary Figure 9 | **Title of the article/chapter the portion is from** | N/A |
| **Editor of portion(s)** | N/A | **Author of portion(s)** | AMERICAN SOCIETY FOR BIOCHEMISTRY & MOLECULAR BIOL |
| **Volume of serial or monograph** | 284 | | |
| **Page or page range of portion** | 31028-31037 | **Issue, if republishing an article from a serial** | N/A |
| | | **Publication date of portion** | 1905-01-01 |

Copyright Clearance Center RightsLink®

Home | Help | Email Support | Joshua Brockman

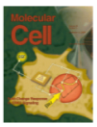

## Structure of a Complete Integrin Ectodomain in a Physiologic Resting State and Activation and Deactivation by Applied Forces

**Author:**
Jianghai Zhu,Bing-Hao Luo,Tsan Xiao,Chengzhong Zhang,Noritaka Nishida,Timothy A. Springer

**Publication:** Molecular Cell

**Publisher:** Elsevier

**Date:** 26 December 2008



### Order Completed

Thank you for your order.

This Agreement between Emory University -- Joshua Brockman ("You") and Elsevier ("Elsevier") consists of your license details and the terms and conditions provided by Elsevier and Copyright Clearance Center.

Your confirmation email will contain your order number for future reference.

| | |
|---|---|
| License Number | 4844941365766 |
| License date | Jun 09, 2020 |

Printable Details

### Licensed Content

| | |
|---|---|
| Licensed Content Publisher | Elsevier |
| Licensed Content Publication | Molecular Cell |
| Licensed Content Title | Structure of a Complete Integrin Ectodomain in a Physiologic Resting State and Activation and Deactivation by Applied Forces |
| Licensed Content Author | Jianghai Zhu,Bing-Hao Luo,Tsan Xiao,Chengzhong Zhang,Noritaka Nishida,Timothy A. Springer |
| Licensed Content Date | Dec 26, 2008 |
| Licensed Content Volume | 32 |
| Licensed Content Issue | 6 |
| Licensed Content Pages | 13 |
| Journal Type | S&T |

### Order Details

| | |
|---|---|
| Type of Use | reuse in a thesis/dissertation |
| Portion | figures/tables/illustrations |
| Number of figures/tables/illustrations | 1 |
| Format | both print and electronic |
| Are you the author of this Elsevier article? | No |
| Will you be translating? | No |

### About Your Work

| | |
|---|---|
| Title | Mapping the 3D Orientation and Nanoscale Distribution of Piconewton Receptor Forces |
| Institution name | Emory University |
| Expected presentation date | Jun 2020 |

### Additional Data

| | |
|---|---|
| Portions | Figure 4 |

### Requestor Location

| | |
|---|---|
| Requestor Location | Emory University<br>1515 Dickey Dr<br><br>ATLANTA, GA 30322<br>United States<br>Attn: Khalid Salaita |

### Tax Details

| | |
|---|---|
| Publisher Tax ID | 98-0397604 |

### $ Price

| | |
|---|---|
| Total | 0.00 USD |

**Total: 0.00 USD**

CLOSE WINDOW ORDER MORE

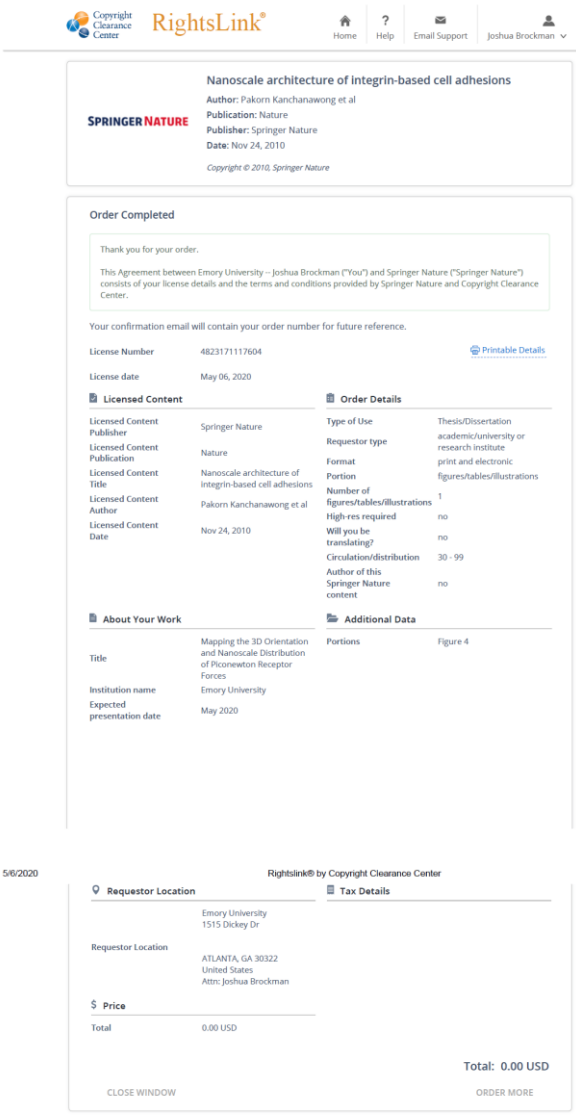

Copyright Clearance Center RightsLink®

Home | Help | Email Support | Joshua Brockman

SPRINGER NATURE

**Nanoscale architecture of integrin-based cell adhesions**

**Author:** Pakorn Kanchanawong et al
**Publication:** Nature
**Publisher:** Springer Nature
**Date:** Nov 24, 2010

*Copyright © 2010, Springer Nature*

**Order Completed**

Thank you for your order.

This Agreement between Emory University -- Joshua Brockman ("You") and Springer Nature ("Springer Nature") consists of your license details and the terms and conditions provided by Springer Nature and Copyright Clearance Center.

Your confirmation email will contain your order number for future reference.

Printable Details

| | |
|---|---|
| License Number | 4823171117604 |
| License date | May 06, 2020 |

**Licensed Content**

| | |
|---|---|
| Licensed Content Publisher | Springer Nature |
| Licensed Content Publication | Nature |
| Licensed Content Title | Nanoscale architecture of integrin-based cell adhesions |
| Licensed Content Author | Pakorn Kanchanawong et al |
| Licensed Content Date | Nov 24, 2010 |

**Order Details**

| | |
|---|---|
| Type of Use | Thesis/Dissertation |
| Requestor type | academic/university or research institute |
| Format | print and electronic |
| Portion | figures/tables/illustrations |
| Number of figures/tables/illustrations | 1 |
| High-res required | no |
| Will you be translating? | no |
| Circulation/distribution | 30 - 99 |
| Author of this Springer Nature content | no |

**About Your Work**

| | |
|---|---|
| Title | Mapping the 3D Orientation and Nanoscale Distribution of Piconewton Receptor Forces |
| Institution name | Emory University |
| Expected presentation date | May 2020 |

**Additional Data**

| | |
|---|---|
| Portions | Figure 4 |

5/6/2020 Rightslink® by Copyright Clearance Center

**Requestor Location**

Emory University
1515 Dickey Dr

Requestor Location

ATLANTA, GA 30322
United States
Attn: Joshua Brockman

**Tax Details**

**Price**

| | |
|---|---|
| Total | 0.00 USD |

Total: 0.00 USD

CLOSE WINDOW ORDER MORE

Copyright Clearance Center Marketplace™

# Order Confirmation

Thank you, your order has been placed. An email confirmation has been sent to you. Your order license details and printable licenses will be available within 24 hours. Please access Manage Account for final order details.

**This is not an invoice. Please go to manage account to access your order history and invoices.**

## CUSTOMER INFORMATION

Payment by invoice: You can cancel your order until the invoice is generated by contacting customer service.

| Billing Address | Customer Location |
|---|---|
| **Mr. Joshua Brockman**<br>Emory University<br>General Delivery<br>1515 Dickey Dr<br>Atlanta, GA 30322<br>United States<br>+1 (937) 367-0643<br>jmbrock@emory.edu | **Mr. Joshua Brockman**<br>Emory University<br>General Delivery<br>1515 Dickey Dr<br>Atlanta, GA 30322<br>United States |

| PO Number (optional) | Payment options |
|---|---|
| N/A | Invoice |

## PENDING ORDER CONFIRMATION

**Confirmation Number:** Pending

**Order Date:** 15-May-2020

### 1. Journal of cell science — 0.00 USD

| | | | |
|---|---|---|---|
| **Order license ID** | Pending | **Publisher** | COMPANY OF BIOLOGISTS LTD. |
| **ISSN** | 1477-9137 | | |
| **Type of Use** | Republish in a thesis/dissertation | **Portion** | Chart/graph/table/figure |

## REQUEST DETAILS

| | | | |
|---|---|---|---|
| **Portion Type** | Chart/graph/table/figure | **Distribution** | Worldwide |
| **Number of charts / graphs / tables / figures requested** | 1 | **Translation** | Original language of publication |
| **Format (select all that apply)** | Print, Electronic | **Copies for the disabled?** | No |
| **Who will republish the content?** | Academic institution | **Minor editing privileges?** | Yes |
| **Duration of Use** | Life of current edition | **Incidental promotional use?** | No |
| **Lifetime Unit Quantity** | Up to 499 | **Currency** | USD |
| **Rights Requested** | Main product | | |

## NEW WORK DETAILS

| | | | |
|---|---|---|---|
| **Title** | Mapping the 3D Orientation and Nanoscale Distribution of Piconewton Receptor Forces | **Institution name** | Emory University |
| | | **Expected presentation date** | 2020-05-29 |
| **Instructor name** | Joshua Brockman | | |

## ADDITIONAL DETAILS

| | | | |
|---|---|---|---|
| **Order reference number** | N/A | **The requesting person / organization to appear on the license** | Joshua Brockman |

## REUSE CONTENT DETAILS

| | | | |
|---|---|---|---|
| **Title, description or numeric reference of the portion(s)** | Figure 1 | **Title of the article/chapter the portion is from** | Force field evolution during human blood platelet activation |
| **Editor of portion(s)** | N/A | **Author of portion(s)** | Company of Biologists. |
| **Volume of serial or monograph** | 125 | **Issue, if republishing an article from a serial** | N/A |
| **Page or page range of portion** | 3914-3921 | **Publication date of portion** | 1966-01-01 |

## PUBLISHER TERMS AND CONDITIONS

The acknowledgement should state "Reproduced / adapted with permission" and give the source journal name. The acknowledgement should either provide full citation details or refer to the relevant citation in the article reference list. The full citation details should include authors, journal, year, volume, issue and page citation. Where appearing online or in other electronic media, a link should be provided to the original article (e.g. via DOI): Development: dev.biologists.org Disease Models & Mechanisms: dmm.biologists.org Journal of Cell Science: jcs.biologists.org The Journal of Experimental Biology: jeb.biologists.org

**Total Items: 1** — **Total Due: 0.00 USD**

Accepted: All Publisher and CCC Terms and Conditions

## Glycoprotein Ib-IX-V Complex Transmits Cytoskeletal Forces That Enhance Platelet Adhesion

**Author:**
Shirin Feghhi,Adam D. Munday,Wes W. Tooley,Shreya Rajsekar,Adriane M. Fura,John D. Kulman,Jose A. López,Nathan J. Sniadecki

**Publication:** Biophysical Journal
**Publisher:** Elsevier
**Date:** 9 August 2016



### Order Completed

Thank you for your order.

This Agreement between Emory University -- Joshua Brockman ("You") and Elsevier ("Elsevier") consists of your license details and the terms and conditions provided by Elsevier and Copyright Clearance Center.

Your confirmation email will contain your order number for future reference.

| | |
|---|---|
| License Number | 4830471276554 |
| License date | May 15, 2020 |

Printable Details

Rightslink® by Copyright Clearance Center

### Licensed Content

| | |
|---|---|
| Licensed Content Publisher | Elsevier |
| Licensed Content Publication | Biophysical Journal |
| Licensed Content Title | Glycoprotein Ib-IX-V Complex Transmits Cytoskeletal Forces That Enhance Platelet Adhesion |
| Licensed Content Author | Shirin Feghhi,Adam D. Munday,Wes W. Tooley,Shreya Rajsekar,Adriane M. Fura,John D. Kulman,Jose A. López,Nathan J. Sniadecki |
| Licensed Content Date | Aug 9, 2016 |
| Licensed Content Volume | 111 |
| Licensed Content Issue | 3 |
| Licensed Content Pages | 8 |
| Journal Type | S&T |

### Order Details

| | |
|---|---|
| Type of Use | reuse in a thesis/dissertation |
| Portion | figures/tables/illustrations |
| Number of figures/tables/illustrations | 1 |
| Format | both print and electronic |
| Are you the author of this Elsevier article? | No |
| Will you be translating? | No |

### About Your Work

| | |
|---|---|
| Title | Mapping the 3D Orientation and Nanoscale Distribution of Piconewton Receptor Forces |
| Institution name | Emory University |
| Expected presentation date | May 2020 |

### Additional Data

| | |
|---|---|
| Portions | Figure 1 |

### Requestor Location

| | |
|---|---|
| Requestor Location | Emory University<br>1515 Dickey Dr<br><br>ATLANTA, GA 30322<br>United States<br>Attn: Joshua Brockman |

### Tax Details

| | |
|---|---|
| Publisher Tax ID | 98-0397604 |

### $ Price

| | |
|---|---|
| Total | 0.00 USD |

**Total: 0.00 USD**

CLOSE WINDOW ORDER MORE

## REFERENCES


1. Brockman, J.M. & Salaita, K. Mechanical Proofreading: A General Mechanism to Enhance the Fidelity of Information Transfer Between Cells. *Front Phys* **7** (2019).

2. Ting, L.H. *et al.* Contractile forces in platelet aggregates under microfluidic shear gradients reflect platelet inhibition and bleeding risk. *Nat Commun* **10**, 1204 (2019).

3. Feghhi, S. *et al.* Glycoprotein Ib-IX-V Complex Transmits Cytoskeletal Forces That Enhance Platelet Adhesion. *Biophys J* **111**, 601-608 (2016).

4. Liang, X.M., Han, S.J., Reems, J.A., Gao, D. & Sniadecki, N.J. Platelet retraction force measurements using flexible post force sensors. *Lab Chip* **10**, 991-998 (2010).

5. Lam, W.A. *et al.* Mechanics and contraction dynamics of single platelets and implications for clot stiffening. *Nat Mater* **10**, 61-66 (2011).

6. Zhang, Y. *et al.* Platelet integrins exhibit anisotropic mechanosensing and harness piconewton forces to mediate platelet aggregation. *Proc Natl Acad Sci U S A* **115**, 325-330 (2018).

7. Qiu, Y. *et al.* Platelet mechanosensing of substrate stiffness during clot formation mediates adhesion, spreading, and activation. *Proc Natl Acad Sci U S A* (2014).

8. Liu, B., Chen, W., Evavold, B.D. & Zhu, C. Accumulation of dynamic catch bonds between TCR and agonist peptide-MHC triggers T cell signaling. *Cell* **157**, 357-368 (2014).

9. Liu, Y. *et al.* DNA-based nanoparticle tension sensors reveal that T-cell receptors transmit defined pN forces to their antigens for enhanced fidelity. *Proc Natl Acad Sci U S A* (2016).

10. Bashour, K.T. *et al.* CD28 and CD3 have complementary roles in T-cell traction forces. *Proc Natl Acad Sci U S A* **111**, 2241-2246 (2014).

11. Basu, R. *et al.* Cytotoxic T Cells Use Mechanical Force to Potentiate Target Cell Killing. *Cell* **165**, 100-110 (2016).

12. Kumar, S. & Weaver, V.M. Mechanics, malignancy, and metastasis: the force journey of a tumor cell. *Cancer Metastasis Rev* **28**, 113-127 (2009).

13. Paszek, M.J. *et al.* Tensional homeostasis and the malignant phenotype. *Cancer Cell* **8**, 241-254 (2005).

14. Engler, A.J., Sen, S., Sweeney, H.L. & Discher, D.E. Matrix elasticity directs stem cell lineage specification. *Cell* **126**, 677-689 (2006).

15. Discher, D.E., Janmey, P. & Wang, Y.L. Tissue cells feel and respond to the stiffness of their substrate. *Science* **310**, 1139-1143 (2005).

16. Kim, S.T. *et al.* The alphabeta T cell receptor is an anisotropic mechanosensor. *J Biol Chem* **284**, 31028-31037 (2009).

17. Zhu, J. *et al.* Structure of a complete integrin ectodomain in a physiologic resting state and activation and deactivation by applied forces. *Mol Cell* **32**, 849-861 (2008).

18. Dembo, M., Oliver, T., Ishihara, A. & Jacobson, K. Imaging the traction stresses exerted by locomoting cells with the elastic substratum method. *Biophys J* **70**, 2008-2022 (1996).

19. Oliver, T., Dembo, M. & Jacobson, K. Traction forces in locomoting cells. *Cell Motil Cytoskeleton* **31**, 225-240 (1995).

20. Polacheck, W.J. & Chen, C.S. Measuring cell-generated forces: a guide to the available tools. *Nat Methods* **13**, 415-423 (2016).

21. Stabley, D.R., Jurchenko, C., Marshall, S.S. & Salaita, K.S. Visualizing mechanical tension across membrane receptors with a fluorescent sensor. *Nature Methods* **9**, 64-U172 (2012).

22. Zhang, Y., Ge, C., Zhu, C. & Salaita, K. DNA-based digital tension probes reveal integrin forces during early cell adhesion. *Nat Commun* **5**, 5167 (2014).

23. Blakely, B.L. *et al.* A DNA-based molecular probe for optically reporting cellular traction forces. *Nature Methods* **11**, 1229-+ (2014).

24. Grashoff, C. *et al.* Measuring mechanical tension across vinculin reveals regulation of focal adhesion dynamics. *Nature* **466**, 263-266 (2010).

25. Wang, X. & Ha, T. Defining single molecular forces required to activate integrin and notch signaling. *Science* **340**, 991-994 (2013).

26. Wolff, J. *Das Gesetz der Transformation der Knochen*. (Berlin; 1892).

27. Wolff, J. *The Law of Bone Remodeling*. (Springer-Verlag, Berlin; 1986).

28. Thompson, D.A. *On Growth and Form*. (Cambridge University Press, UK; 1917).

29. Hudspeth, A.J. & Corey, D.P. Sensitivity, polarity, and conductance change in the response of vertebrate hair cells to controlled mechanical stimuli. *Proc Natl Acad Sci U S A* **74**, 2407-2411 (1977).

30. Kachar, B., Parakkal, M. & Fex, J. Structural basis for mechanical transduction in the frog vestibular sensory apparatus: I. The otolithic membrane. *Hear Res* **45**, 179-190 (1990).

31. Jaeger, R.G., Fex, J. & Kachar, B. Structural basis for mechanical transduction in the frog vestibular sensory apparatus: II. The role of microtubules in the organization of the cuticular plate. *Hear Res* **77**, 207-215 (1994).

32. Wilson, L.J. & Paul, D.H. Functional morphology of the telson-uropod stretch receptor in the sand crab Emerita analoga. *J Comp Neurol* **296**, 343-358 (1990).

33. Wang, N., Butler, J.P. & Ingber, D.E. Mechanotransduction across the cell surface and through the cytoskeleton. *Science* **260**, 1124-1127 (1993).

34. Bell, G.I. Models for the specific adhesion of cells to cells. *Science* **200**, 618-627 (1978).

35. Dembo, M., Torney, D.C., Saxman, K. & Hammer, D. The reaction-limited kinetics of membrane-to-surface adhesion and detachment. *Proc R Soc Lond B Biol Sci* **234**, 55-83 (1988).

36. Thomas, W.E., Trintchina, E., Forero, M., Vogel, V. & Sokurenko, E.V. Bacterial adhesion to target cells enhanced by shear force. *Cell* **109**, 913-923 (2002).

37. Yakovenko, O. *et al.* FimH forms catch bonds that are enhanced by mechanical force due to allosteric regulation. *J Biol Chem* **283**, 11596-11605 (2008).

38. Tchesnokova, V. *et al.* Integrin-like allosteric properties of the catch bond-forming FimH adhesin of Escherichia coli. *J Biol Chem* **283**, 7823-7833 (2008).

39. Kong, F., Garcia, A.J., Mould, A.P., Humphries, M.J. & Zhu, C. Demonstration of catch bonds between an integrin and its ligand. *J Cell Biol* **185**, 1275-1284 (2009).

40. Marshall, B.T. *et al.* Direct observation of catch bonds involving cell-adhesion molecules. *Nature* **423**, 190-193 (2003).

41. Chen, W., Lou, J., Evans, E.A. & Zhu, C. Observing force-regulated conformational changes and ligand dissociation from a single integrin on cells. *J Cell Biol* **199**, 497-512 (2012).

42. Das, D.K. *et al.* Force-dependent transition in the T-cell receptor beta-subunit allosterically regulates peptide discrimination and pMHC bond lifetime. *Proc Natl Acad Sci U S A* **112**, 1517-1522 (2015).

43. Zhang, W. *et al.* Identification of a juxtamembrane mechanosensitive domain in the platelet mechanosensor glycoprotein Ib-IX complex. *Blood* **125**, 562-569 (2015).

44. Ma, V.P. *et al.* Ratiometric Tension Probes for Mapping Receptor Forces and Clustering at Intermembrane Junctions. *Nano Lett* **16**, 4552-4559 (2016).

45. Natkanski, E. *et al.* B cells use mechanical energy to discriminate antigen affinities. *Science* **340**, 1587-1590 (2013).

46. Hopfield, J.J. Kinetic proofreading: a new mechanism for reducing errors in biosynthetic processes requiring high specificity. *Proc Natl Acad Sci U S A* **71**, 4135-4139 (1974).

47. Ninio, J. Kinetic amplification of enzyme discrimination. *Biochimie* **57**, 587-595 (1975).

48. Chen, W., Lou, J. & Zhu, C. Forcing switch from short- to intermediate- and long-lived states of the alphaA domain generates LFA-1/ICAM-1 catch bonds. *J Biol Chem* **285**, 35967-35978 (2010).

49. Comrie, W.A., Li, S., Boyle, S. & Burkhardt, J.K. The dendritic cell cytoskeleton promotes T cell adhesion and activation by constraining ICAM-1 mobility. *J Cell Biol* **208**, 457-473 (2015).

50. Yago, T. *et al.* Platelet glycoprotein Ibalpha forms catch bonds with human WT vWF but not with type 2B von Willebrand disease vWF. *J Clin Invest* **118**, 3195-3207 (2008).

51. Tolar, P. Cytoskeletal control of B cell responses to antigens. *Nat Rev Immunol* **17**, 621-634 (2017).

52. Wang, J. *et al.* Profiling the origin, dynamics, and function of traction force in B cell activation. *Sci Signal* **11** (2018).

53. Spillane, K.M. & Tolar, P. B cell antigen extraction is regulated by physical properties of antigen-presenting cells. *J Cell Biol* **216**, 217-230 (2017).

54. Pageon, S.V. *et al.* Functional role of T-cell receptor nanoclusters in signal initiation and antigen discrimination. *Proc Natl Acad Sci U S A* **113**, E5454-5463 (2016).

55. Jung, Y. *et al.* Three-dimensional localization of T-cell receptors in relation to microvilli using a combination of superresolution microscopies. *Proc Natl Acad Sci U S A* **113**, E5916-E5924 (2016).

56. Cai, E. *et al.* Visualizing dynamic microvillar search and stabilization during ligand detection by T cells. *Science* **356** (2017).

57. Oria, R. *et al.* Force loading explains spatial sensing of ligands by cells. *Nature* **552**, 219-224 (2017).

58. Chen, Y., Ju, L., Rushdi, M., Ge, C. & Zhu, C. Receptor-mediated cell mechanosensing. *Mol Biol Cell* **28**, 3134-3155 (2017).

59. Li, J. *et al.* Conformational equilibria and intrinsic affinities define integrin activation. *EMBO J* **36**, 629-645 (2017).

60. Li, J. & Springer, T.A. Integrin extension enables ultrasensitive regulation by cytoskeletal force. *Proc Natl Acad Sci U S A* **114**, 4685-4690 (2017).

61. Hogg, N., Patzak, I. & Willenbrock, F. The insider's guide to leukocyte integrin signalling and function. *Nat Rev Immunol* **11**, 416-426 (2011).

62. Feigelson, S.W. *et al.* Occupancy of lymphocyte LFA-1 by surface-immobilized ICAM-1 is critical for TCR- but not for chemokine-triggered LFA-1 conversion to an open headpiece high-affinity state. *J Immunol* **185**, 7394-7404 (2010).

63. Comrie, W.A., Babich, A. & Burkhardt, J.K. F-actin flow drives affinity maturation and spatial organization of LFA-1 at the immunological synapse. *J Cell Biol* **208**, 475-491 (2015).

64. Moore, T.I., Aaron, J., Chew, T.L. & Springer, T.A. Measuring Integrin Conformational Change on the Cell Surface with Super-Resolution Microscopy. *Cell Rep* **22**, 1903-1912 (2018).

65. Feng, Y., Reinherz, E.L. & Lang, M.J. alphabeta T Cell Receptor Mechanosensing Forces out Serial Engagement. *Trends Immunol* **39**, 596-609 (2018).

66. Zhang, y. *et al.* Platelet integrins exhitib anisotropic mechanosensing and harness pN forces to mediate platelet aggregation. *Proc Natl Acad Sci U S A* (2017).

67. Brockman, J.M. *et al.* Mapping the 3D orientation of piconewton integrin traction forces. *Nat Methods* **15**, 115-118 (2018).

68. Liu, Y., Galior, K., Ma, V.P. & Salaita, K. Molecular Tension Probes for Imaging Forces at the Cell Surface. *Acc Chem Res* **50**, 2915-2924 (2017).

69. Harris, A.K., Wild, P. & Stopak, D. Silicone rubber substrata: a new wrinkle in the study of cell locomotion. *Science* **208**, 177-179 (1980).

70. Evans, E., Ritchie, K. & Merkel, R. Sensitive force technique to probe molecular adhesion and structural linkages at biological interfaces. *Biophys J* **68**, 2580-2587 (1995).

71. Lee, J., Leonard, M., Oliver, T., Ishihara, A. & Jacobson, K. Traction forces generated by locomoting keratocytes. *J Cell Biol* **127**, 1957-1964 (1994).

72. Sabass, B., Gardel, M.L., Waterman, C.M. & Schwarz, U.S. High resolution traction force microscopy based on experimental and computational advances. *Biophys J* **94**, 207-220 (2008).

73. Colin-York, H. *et al.* Spatiotemporally Super-Resolved Volumetric Traction Force Microscopy. *Nano Lett* **19**, 4427-4434 (2019).

74. Colin-York, H. *et al.* Super-Resolved Traction Force Microscopy (STFM). *Nano Letters* **16**, 2633-2638 (2016).

75. Stubb, A. *et al.* Fluctuation-Based Super-Resolution Traction Force Microscopy. *Nano Lett* (2020).

76. Legant, W.R. *et al.* Measurement of mechanical tractions exerted by cells in three-dimensional matrices. *Nat Methods* **7**, 969-971 (2010).

77. Legant, W.R. *et al.* Multidimensional traction force microscopy reveals out-of-plane rotational moments about focal adhesions. *Proc Natl Acad Sci U S A* **110**, 881-886 (2013).

78. Tan, J.L. *et al.* Cells lying on a bed of microneedles: an approach to isolate mechanical force. *Proc Natl Acad Sci U S A* **100**, 1484-1489 (2003).

79. Neuman, K.C. & Nagy, A. Single-molecule force spectroscopy: optical tweezers, magnetic tweezers and atomic force microscopy. *Nat Methods* **5**, 491-505 (2008).

80. Ashkin, A., Dziedzic, J.M., Bjorkholm, J.E. & Chu, S. Observation of a single-beam gradient force optical trap for dielectric particles. *Opt Lett* **11**, 288 (1986).

81. Finer, J.T., Simmons, R.M. & Spudich, J.A. Single Myosin Molecule Mechanics - Piconewton Forces and Nanometer Steps. *Nature* **368**, 113-119 (1994).

82. Kress, H. *et al.* Filopodia act as phagocytic tentacles and pull with discrete steps and a load-dependent velocity. *Proc Natl Acad Sci U S A* **104**, 11633-11638 (2007).

83. Lemke, S.B., Weidemann, T., Cost, A.L., Grashoff, C. & Schnorrer, F. A small proportion of Talin molecules transmit forces at developing muscle attachments in vivo. *PLoS Biol* **17**, e3000057 (2019).

84. Ringer, P. *et al.* Multiplexing molecular tension sensors reveals piconewton force gradient across talin-1. *Nat Methods* **14**, 1090-1096 (2017).

85. Borghi, N. *et al.* E-cadherin is under constitutive actomyosin-generated tension that is increased at cell-cell contacts upon externally applied stretch. *Proc Natl Acad Sci U S A* **109**, 12568-12573 (2012).

86. Liu, Y., Yehl, K., Narui, Y. & Salaita, K. Tension sensing nanoparticles for mechano-imaging at the living/nonliving interface. *J Am Chem Soc* **135**, 5320-5323 (2013).

87. Galior, K., Liu, Y., Yehl, K., Vivek, S. & Salaita, K. Titin-Based Nanoparticle Tension Sensors Map High-Magnitude Integrin Forces within Focal Adhesions. *Nano Lett* **16**, 341-348 (2016).

88. Blakely, B.L. *et al.* A DNA-based molecular probe for optically reporting cellular traction forces. *Nat Methods* **11**, 1229-1232 (2014).

89. Morimatsu, M., Mekhdjian, A.H., Chang, A.C., Tan, S.J. & Dunn, A.R. Visualizing the interior architecture of focal adhesions with high-resolution traction maps. *Nano Lett* **15**, 2220-2228 (2015).

90. Morimatsu, M., Mekhdjian, A.H., Adhikari, A.S. & Dunn, A.R. Molecular tension sensors report forces generated by single integrin molecules in living cells. *Nano Lett* **13**, 3985-3989 (2013).

91. Bin Zhao, N.L., Tianfa Xie, Chungwen Liang, Yousef Bagheri, Yubing Sun, Mingxu You Quantifying Tensile Forces at Cell–Cell Junctions with a DNA-based Fluorescent Probe. *bioRxiv* (2020).

92. Zhao, B. *et al.* Visualizing Intercellular Tensile Forces by DNA-Based Membrane Molecular Probes. *J Am Chem Soc* **139**, 18182-18185 (2017).

93. Murad, Y. & Li, I.T.S. Quantifying Molecular Forces with Serially Connected Force Sensors. *Biophys J* **116**, 1282-1291 (2019).

94. Zhao, Y., Sarkar, A. & Wang, X. Peptide nucleic acid based tension sensor for cellular force imaging with strong DNase resistance. *Biosens Bioelectron* **150**, 111959 (2020).

95. Wang, Y. *et al.* Force-activatable biosensor enables single platelet force mapping directly by fluorescence imaging. *Biosens Bioelectron* **100**, 192-200 (2018).

96. Feng, Y. *et al.* Mechanosensing drives acuity of alphabeta T-cell recognition. *Proc Natl Acad Sci U S A* **114**, E8204-E8213 (2017).

97. Zhu, J., Boylan, B., Luo, B.H., Newman, P.J. & Springer, T.A. Tests of the extension and deadbolt models of integrin activation. *J Biol Chem* **282**, 11914-11920 (2007).

98. Takagi, J. & Springer, T.A. Integrin activation and structural rearrangement. *Immunol Rev* **186**, 141-163 (2002).

99. Sahl, S.J., Hell, S.W. & Jakobs, S. Fluorescence nanoscopy in cell biology. *Nat Rev Mol Cell Biol* **18**, 685-701 (2017).

100. Rust, M.J., Bates, M. & Zhuang, X. Sub-diffraction-limit imaging by stochastic optical reconstruction microscopy (STORM). *Nat Methods* **3**, 793-795 (2006).

101. Betzig, E. *et al.* Imaging intracellular fluorescent proteins at nanometer resolution. *Science* **313**, 1642-1645 (2006).

102. Jungmann, R. *et al.* Multiplexed 3D cellular super-resolution imaging with DNA-PAINT and Exchange-PAINT. *Nat Methods* **11**, 313-318 (2014).

103. Xu, K., Zhong, G. & Zhuang, X. Actin, spectrin, and associated proteins form a periodic cytoskeletal structure in axons. *Science* **339**, 452-456 (2013).

104. Kanchanawong, P. *et al.* Nanoscale architecture of integrin-based cell adhesions. *Nature* **468**, 580-584 (2010).

105. Shroff, H. *et al.* Dual-color superresolution imaging of genetically expressed probes within individual adhesion complexes. *Proc Natl Acad Sci U S A* **104**, 20308-20313 (2007).

106. Hu, S. *et al.* Structured illumination microscopy reveals focal adhesions are composed of linear subunits. *Cytoskeleton (Hoboken)* **72**, 235-245 (2015).

107. Spiess, M. *et al.* Active and inactive beta1 integrins segregate into distinct nanoclusters in focal adhesions. *J Cell Biol* **217**, 1929-1940 (2018).

108. Lakowicz, J.R. *Principles of fluorescence spectroscopy*, Edn. 3rd. (Springer, New York; 2006).

109. Kampmann, M., Atkinson, C.E., Mattheyses, A.L. & Simon, S.M. Mapping the orientation of nuclear pore proteins in living cells with polarized fluorescence microscopy. *Nat Struct Mol Biol* **18**, 643-649 (2011).

110. Mattheyses, A.L., Kampmann, M., Atkinson, C.E. & Simon, S.M. Fluorescence anisotropy reveals order and disorder of protein domains in the nuclear pore complex. *Biophys J* **99**, 1706-1717 (2010).

111. DeMay, B.S., Noda, N., Gladfelter, A.S. & Oldenbourg, R. Rapid and quantitative imaging of excitation polarized fluorescence reveals ordered septin dynamics in live yeast. *Biophys J* **101**, 985-994 (2011).

112. Sund, S.E., Swanson, J.A. & Axelrod, D. Cell membrane orientation visualized by polarized total internal reflection fluorescence. *Biophys J* **77**, 2266-2283 (1999).

113. Axelrod, D. Carbocyanine dye orientation in red cell membrane studied by microscopic fluorescence polarization. *Biophys J* **26**, 557-573 (1979).

114. Kress, A. *et al.* Mapping the local organization of cell membranes using excitation-polarization-resolved confocal fluorescence microscopy. *Biophys J* **105**, 127-136 (2013).

115. Valades Cruz, C.A. *et al.* Quantitative nanoscale imaging of orientational order in biological filaments by polarized superresolution microscopy. *Proc Natl Acad Sci U S A* **113**, E820-828 (2016).

116. Mehta, S.B. *et al.* Dissection of molecular assembly dynamics by tracking orientation and position of single molecules in live cells. *Proc Natl Acad Sci U S A* **113**, E6352-E6361 (2016).

117. Chi, Q., Wang, G. & Jiang, J. The persistence length and length per base of single-stranded DNA obtained from fluorescence correlation spectroscopy measurements using mean field theory. *Physica A*, 1072-1079 (2013).

118. Murphy, M.C., Rasnik, I., Cheng, W., Lohman, T.M. & Ha, T. Probing single-stranded DNA conformational flexibility using fluorescence spectroscopy. *Biophys J* **86**, 2530-2537 (2004).

119. Marko, J.F. & Siggia, E.D. Stretching DNA. *Macromolecules* **28**, 8759-8770 (1995).

120. Petrosyan, R. Improved approximations for some polymer extension models. *Rheologica Acta* **56**, 21-26 (2017).

121. Iqbal, A. *et al.* Orientation dependence in fluorescent energy transfer between Cy3 and Cy5 terminally attached to double-stranded nucleic acids. *Proc Natl Acad Sci U S A* **105**, 11176-11181 (2008).

122. Iqbal, A., Wang, L., Thompson, K.C., Lilley, D.M. & Norman, D.G. The structure of cyanine 5 terminally attached to double-stranded DNA: implications for FRET studies. *Biochemistry* **47**, 7857-7862 (2008).

123. Norman, D.G., Grainger, R.J., Uhrin, D. & Lilley, D.M. Location of cyanine-3 on double-stranded DNA: importance for fluorescence resonance energy transfer studies. *Biochemistry* **39**, 6317-6324 (2000).

124. Cooper, M. *et al.* Cy3B: improving the performance of cyanine dyes. *J Fluoresc* **14**, 145-150 (2004).

125. Vrabioiu, A.M. & Mitchison, T.J. Structural insights into yeast septin organization from polarized fluorescence microscopy. *Nature* **443**, 466-469 (2006).

126. Vrabioiu, A.M. & Mitchison, T.J. Symmetry of septin hourglass and ring structures. *J Mol Biol* **372**, 37-49 (2007).

127. Henriques, S.S., Sandmann, R., Strate, A. & Koster, S. Force field evolution during human blood platelet activation. *Journal of Cell Science* **125**, 3914-3920 (2012).

128. Chan, T.F. & Vese, L.A. Active contours without edges. *IEEE Trans Image Process* **10**, 266-277 (2001).

129. Sunyer, R. *et al.* Collective cell durotaxis emerges from long-range intercellular force transmission. *Science* **353**, 1157-1161 (2016).

130. Labernadie, A. *et al.* A mechanically active heterotypic E-cadherin/N-cadherin adhesion enables fibroblasts to drive cancer cell invasion. *Nat Cell Biol* **19**, 224-237 (2017).

131. Tang, X., Tofangchi, A., Anand, S.V. & Saif, T.A. A novel cell traction force microscopy to study multi-cellular system. *PLoS Comput Biol* **10**, e1003631 (2014).

132. Weisel, J.W. The mechanical properties of fibrin for basic scientists and clinicians. *Biophys Chem* **112**, 267-276 (2004).

133. Plotnikov, S.V., Pasapera, A.M., Sabass, B. & Waterman, C.M. Force fluctuations within focal adhesions mediate ECM-rigidity sensing to guide directed cell migration. *Cell* **151**, 1513-1527 (2012).

134. Mui, K.L., Chen, C.S. & Assoian, R.K. The mechanical regulation of integrin-cadherin crosstalk organizes cells, signaling and forces. *J Cell Sci* **129**, 1093-1100 (2016).

135. Blanchard, A.T., Brockman, J.M., Salaita, K. & Mattheyses, A.L. Variable incidence angle linear dichroism (VALiD): a technique for unique 3D orientation measurement of fluorescent ensembles. *Opt Express* **28**, 10039-10061 (2020).

136. Savage, B., Saldivar, E. & Ruggeri, Z.M. Initiation of platelet adhesion by arrest onto fibrinogen or translocation on von Willebrand factor. *Cell* **84**, 289-297 (1996).

137. Hanke, J., Ranke, C., Perego, E. & Koster, S. Human blood platelets contract in perpendicular direction to shear flow. *Soft Matter* **15**, 2009-2019 (2019).

138. Diagouraga, B. *et al.* Motor-driven marginal band coiling promotes cell shape change during platelet activation. *J Cell Biol* **204**, 177-185 (2014).

139. Paszek, M.J. *et al.* Scanning angle interference microscopy reveals cell dynamics at the nanoscale. *Nat Methods* **9**, 825-827 (2012).

140. Swaminathan, V. *et al.* Actin retrograde flow actively aligns and orients ligand-engaged integrins in focal adhesions. *Proc Natl Acad Sci U S A* **114**, 10648-10653 (2017).

141. Zhanghao, K. *et al.* Super-resolution imaging of fluorescent dipoles via polarized structured illumination microscopy. *Nat Commun* **10**, 4694 (2019).

142. Kronenberg, N.M. *et al.* Long-term imaging of cellular forces with high precision by elastic resonator interference stress microscopy. *Nat Cell Biol* **19**, 864-872 (2017).

143. Galush, W.J., Nye, J.A. & Groves, J.T. Quantitative fluorescence microscopy using supported lipid bilayer standards. *Biophys J* **95**, 2512-2519 (2008).

144. Vacklin, H.P., Tiberg, F. & Thomas, R.K. Formation of supported phospholipid bilayers via co-adsorption with beta-D-dodecyl maltoside. *Biochim Biophys Acta* **1668**, 17-24 (2005).

145. Ma, V.P. & Salaita, K. DNA Nanotechnology as an Emerging Tool to Study Mechanotransduction in Living Systems. *Small*, e1900961 (2019).

146. Betzig, E. *et al.* Imaging intracellular fluorescent proteins at nanometer resolution. *Science* **313**, 1642-1645 (2006).

147. Jungmann, R. *et al.* Single-molecule kinetics and super-resolution microscopy by fluorescence imaging of transient binding on DNA origami. *Nano Lett* **10**, 4756-4761 (2010).

148. Strauss, S. *et al.* Modified aptamers enable quantitative sub-10-nm cellular DNA-PAINT imaging. *Nat Methods* **15**, 685-688 (2018).

149. Schnitzbauer, J., Strauss, M.T., Schlichthaerle, T., Schueder, F. & Jungmann, R. Super-resolution microscopy with DNA-PAINT. *Nat Protoc* **12**, 1198-1228 (2017).

150. Jayasinghe, I. *et al.* True Molecular Scale Visualization of Variable Clustering Properties of Ryanodine Receptors. *Cell Rep* **22**, 557-567 (2018).

151. Schueder, F. *et al.* An order of magnitude faster DNA-PAINT imaging by optimized sequence design and buffer conditions. *Nat Methods* (2019).

152. Auer, A., Strauss, M.T., Schlichthaerle, T. & Jungmann, R. Fast, Background-Free DNA-PAINT Imaging Using FRET-Based Probes. *Nano Lett* **17**, 6428-6434 (2017).

153. Dai, M., Jungmann, R. & Yin, P. Optical imaging of individual biomolecules in densely packed clusters. *Nat Nanotechnol* **11**, 798-807 (2016).

154. Loidolt-Kruger, M. in Physics of Biological and Complex Systems, Vol. Doctor rerum naturalium (International Max Planck Research School, 2018).

155. Deng, S. *et al.* Effects of donor and acceptor's fluorescence lifetimes on the method of applying Forster resonance energy transfer in STED microscopy. *J Microsc* **269**, 59-65 (2018).

156. Holzmeister, P., Wunsch, B., Gietl, A. & Tinnefeld, P. Single-molecule photophysics of dark quenchers as non-fluorescent FRET acceptors. *Photochem Photobiol Sci* **13**, 853-858 (2014).

157. Le Reste, L., Hohlbein, J., Gryte, K. & Kapanidis, A.N. Characterization of dark quencher chromophores as nonfluorescent acceptors for single-molecule FRET. *Biophys J* **102**, 2658-2668 (2012).

158. Smith, S.B., Cui, Y. & Bustamante, C. Overstretching B-DNA: the elastic response of individual double-stranded and single-stranded DNA molecules. *Science* **271**, 795-799 (1996).

159. Hatch, K., Danilowicz, C., Coljee, V. & Prentiss, M. Demonstration that the shear force required to separate short double-stranded DNA does not increase significantly with sequence length for sequences longer than 25 base pairs. *Phys Rev E Stat Nonlin Soft Matter Phys* **78**, 011920 (2008).

160. Gennes, P.-G.d. Maximum pull out force on DNA hybrids. *Comptes Rendus de l'Academie des Sciences* **2**, 1505-1508 (2001).

161. Ho, D. *et al.* Force-driven separation of short double-stranded DNA. *Biophys J* **97**, 3158-3167 (2009).

162. Whitley, K.D., Comstock, M.J. & Chemla, Y.R. Elasticity of the transition state for oligonucleotide hybridization. *Nucleic Acids Res* **45**, 547-555 (2017).

163. Liu, Y. *et al.* Nanoparticle tension probes patterned at the nanoscale: impact of integrin clustering on force transmission. *Nano Lett* **14**, 5539-5546 (2014).

164. Woodside, M.T. *et al.* Nanomechanical measurements of the sequence-dependent folding landscapes of single nucleic acid hairpins. *Proc Natl Acad Sci U S A* **103**, 6190-6195 (2006).

165. Whitley, K.D., Comstock, M.J. & Chemla, Y.R. Elasticity of the transition state for oligonucleotide hybridization. *Nucleic Acids Res.* **45**, 547-555 (2017).

166. Heilemann, M. *et al.* Subdiffraction-resolution fluorescence imaging with conventional fluorescent probes. *Angew Chem Int Ed Engl* **47**, 6172-6176 (2008).

167. Chen, Y. *et al.* An integrin alphaIIbbeta3 intermediate affinity state mediates biomechanical platelet aggregation. *Nat Mater* **18**, 760-769 (2019).

168. Kloczewiak, M., Timmons, S. & Hawiger, J. Recognition site for the platelet receptor is present on the 15-residue carboxy-terminal fragment of the gamma chain

of human fibrinogen and is not involved in the fibrin polymerization reaction. *Thromb. Res.* **29**, 249-255 (1983).

169. Farrell, D.H., Thiagarajan, P., Chung, D.W. & Davie, E.W. Role of fibrinogen alpha and gamma chain sites in platelet aggregation. *Proc. Natl. Acad. Sci. USA* **89**, 10729-10732 (1992).

170. Xiao, T., Takagi, J., Coller, B.S., Wang, J.H. & Springer, T.A. Structural basis for allostery in integrins and binding to fibrinogen-mimetic therapeutics. *Nature* **432**, 59-67 (2004).

171. Zhang, K. & Chen, J. The regulation of integrin function by divalent cations. *Cell Adh Migr* **6**, 20-29 (2012).

172. Zhu, J. *et al.* Closed headpiece of integrin alphaIIbbeta3 and its complex with an alphaIIbbeta3-specific antagonist that does not induce opening. *Blood* **116**, 5050-5059 (2010).

173. Gawaz, M., Ott, I., Reininger, A.J. & Neumann, F.J. Effects of magnesium on platelet aggregation and adhesion. Magnesium modulates surface expression of glycoproteins on platelets in vitro and ex vivo. *Thromb. Haemost.* **72**, 912-918 (1994).

174. Ravn, H.B., Kristensen, S.D., Vissinger, H. & Husted, S.E. Magnesium inhibits human platelets. *Blood Coagul. Fibrinolysis* **7**, 241-244 (1996).

175. Gawaz, M., Reininger, A. & Neumann, F.J. Platelet function and platelet-leukocyte adhesion in symptomatic coronary heart disease. Effects of intravenous magnesium. *Thromb. Res.* **83**, 341-349 (1996).

176. Gries, A. *et al.* The effect of intravenously administered magnesium on platelet function in patients after cardiac surgery. *Anesth Analg* **88**, 1213-1219 (1999).

177. Plow, E.F., Haas, T.A., Zhang, L., Loftus, J. & Smith, J.W. Ligand binding to integrins. *J. Biol. Chem.* **275**, 21785-21788 (2000).

178. Hu, D.D., Barbas, C.F. & Smith, J.W. An allosteric Ca2+ binding site on the beta3-integrins that regulates the dissociation rate for RGD ligands. *J. Biol. Chem.* **271**, 21745-21751. (1996).

179. Takagi, J., Petre, B.M., Walz, T. & Springer, T.A. Global conformational rearrangements in integrin extracellular domains in outside-in and inside-out signaling. *Cell* **110**, 599-611 (2002).

180. Stuiver, I., Ruggeri, Z. & Smith, J.W. Divalent cations regulate the organization of integrins alpha v beta 3 and alpha v beta 5 on the cell surface. *J Cell Physiol* **168**, 521-531 (1996).

181. Endesfelder, U., Malkusch, S., Fricke, F. & Heilemann, M. A simple method to estimate the average localization precision of a single-molecule localization microscopy experiment. *Histochem Cell Biol* **141**, 629-638 (2014).

182. Jungmann, R. *et al.* Quantitative super-resolution imaging with qPAINT. *Nat Methods* **13**, 439-442 (2016).

183. Mayr, S. *et al.* Localization Microscopy of Actin Cytoskeleton in Human Platelets. *Int J Mol Sci* **19** (2018).

184. Lickert, S. *et al.* Morphometric analysis of spread platelets identifies integrin alphaIIbbeta3-specific contractile phenotype. *Sci Rep* **8**, 5428 (2018).

185. Bearer, E.L., Prakash, J.M. & Li, Z. Actin dynamics in platelets. *Int Rev Cytol* **217**, 137-182 (2002).

186. Loftus, J.C., Choate, J. & Albrecht, R.M. Platelet activation and cytoskeletal reorganization: high voltage electron microscopic examination of intact and Triton-extracted whole mounts. *J Cell Biol* **98**, 2019-2025 (1984).

187. Agasti, S.S. *et al.* DNA-barcoded labeling probes for highly multiplexed Exchange-PAINT imaging. *Chem Sci* **8**, 3080-3091 (2017).

188. Gaertner, F. *et al.* Migrating Platelets Are Mechano-scavengers that Collect and Bundle Bacteria. *Cell* **171**, 1368-1382 e1323 (2017).

189. Li, Z., Kim, E.S. & Bearer, E.L. Arp2/3 complex is required for actin polymerization during platelet shape change. *Blood* **99**, 4466-4474 (2002).

190. Wu, C. *et al.* Arp2/3 is critical for lamellipodia and response to extracellular matrix cues but is dispensable for chemotaxis. *Cell* **148**, 973-987 (2012).

191. Hetrick, B., Han, M.S., Helgeson, L.A. & Nolen, B.J. Small molecules CK-666 and CK-869 inhibit actin-related protein 2/3 complex by blocking an activating conformational change. *Chem Biol* **20**, 701-712 (2013).

192. Footer, M.J., Kerssemakers, J.W., Theriot, J.A. & Dogterom, M. Direct measurement of force generation by actin filament polymerization using an optical trap. *Proc Natl Acad Sci U S A* **104**, 2181-2186 (2007).

193. Plotnikov, S.V., Sabass, B., Schwarz, U.S. & Waterman, C.M. High-resolution traction force microscopy. *Methods Cell Biol* **123**, 367-394 (2014).

194. Sabass, B., Gardel, M.L., Waterman, C.M. & Schwarz, U.S. High resolution traction force microscopy based on experimental and computational advances. *Biophysical Journal* **94**, 207-220 (2008).

195. Zhao, Y., Pal, K., Tu, Y. & Wang, X. Cellular Force Nanoscopy with 50 nm Resolution Based on Integrin Molecular Tension Imaging and Localization. *J Am Chem Soc* **142**, 6930-6934 (2020).

196. Cox, S. *et al.* Bayesian localization microscopy reveals nanoscale podosome dynamics. *Nat Methods* **9**, 195-200 (2011).

197. Pryshchep, S., Zarnitsyna, V.I., Hong, J., Evavold, B.D. & Zhu, C. Accumulation of serial forces on TCR and CD8 frequently applied by agonist antigenic peptides embedded in MHC molecules triggers calcium in T cells. *J Immunol* **193**, 68-76 (2014).

198. Elosegui-Artola, A. *et al.* Mechanical regulation of a molecular clutch defines force transmission and transduction in response to matrix rigidity. *Nat Cell Biol* **18**, 540-548 (2016).

199. Zhang, Z., Revyakin, A., Grimm, J.B., Lavis, L.D. & Tjian, R. Single-molecule tracking of the transcription cycle by sub-second RNA detection. *eLife* **3**, e01775 (2014).

200. Pan, H., Xia, Y., Qin, M., Cao, Y. & Wang, W. A simple procedure to improve the surface passivation for single molecule fluorescence studies. *Phys Biol* **12**, 045006 (2015).

201. Hua, B. *et al.* An improved surface passivation method for single-molecule studies. *Nat. Methods* **11**, 1233-1236 (2014).

202. Levet, F. *et al.* SR-Tesseler: a method to segment and quantify localization-based super-resolution microscopy data. *Nat Methods* **12**, 1065-1071 (2015).

203. Chung, K.K., Zhang, Z., Kidd, P., Zhang, Y., Williams, N. D., Rollins, B., Yang, Y., Lin, C., Baddeley, D., Bewersdorf, J. Fluorogenic probe for fast 3D whole-cell DNA-PAINT. *BioRxiv* (2020).

204. Johnson, D.S., Toledo-Crow, R., Mattheyses, A.L. & Simon, S.M. Polarization-controlled TIRFM with focal drift and spatial field intensity correction. *Biophys J* **106**, 1008-1019 (2014).

205. Brameshuber, M. *et al.* Monomeric TCRs drive T cell antigen recognition. *Nat Immunol* **19**, 487-496 (2018).

206. Valitutti, S. The Serial Engagement Model 17 Years After: From TCR Triggering to Immunotherapy. *Front Immunol* **3**, 272 (2012).

207. Valitutti, S., Muller, S., Cella, M., Padovan, E. & Lanzavecchia, A. Serial triggering of many T-cell receptors by a few peptide-MHC complexes. *Nature* **375**, 148-151 (1995).